



저작자표시 2.0 대한민국

이용자는 아래의 조건을 따르는 경우에 한하여 자유롭게

- 이 저작물을 복제, 배포, 전송, 전시, 공연 및 방송할 수 있습니다.
- 이차적 저작물을 작성할 수 있습니다.
- 이 저작물을 영리 목적으로 이용할 수 있습니다.

다음과 같은 조건을 따라야 합니다:



저작자표시. 귀하는 원저작자를 표시하여야 합니다.

- 귀하는, 이 저작물의 재이용이나 배포의 경우, 이 저작물에 적용된 이용허락조건을 명확하게 나타내어야 합니다.
- 저작권자로부터 별도의 허가를 받으면 이러한 조건들은 적용되지 않습니다.

저작권법에 따른 이용자의 권리는 위의 내용에 의하여 영향을 받지 않습니다.

이것은 [이용허락규약\(Legal Code\)](#)을 이해하기 쉽게 요약한 것입니다.

[Disclaimer](#) 

공학박사 학위논문

**Development and Performance
Verification of Post-Tensioned Anchor
for Unbonded Single-Strand Tendon**

단일 비부착 강연선용 포스트텐션 1구 정착구의
개발 및 성능 검증

2020년 2월

서울대학교 대학원

건축학과

조 아 서

Development and Performance Verification of Post-Tensioned Anchor for Unbonded Single-Strand Tendon

지도교수 강 현 구

이 논문을 공학박사 학위논문으로 제출함

2020년 2월

서울대학교 대학원

건축학과

조 아 서

조아서의 공학박사 학위논문을 인준함

2020년 2월

위원장

홍성걸



부위원장

강현구



위원

박승근



위원

이창호



위원

김강우



Abstract

Development and Performance Verification of Post-Tensioned Anchor Using Unbonded Single-Strand Tendon

Ah Sir Cho

Department of Architecture and Architectural Engineering

College of Engineering

Seoul National University

Unlike Korea, where a 15.2-mm diameter strand is used for post-tensioning (PT) method, the United States or Europe primarily uses the strand with a diameter of 12.7 mm. An anchor using the $\text{Ø}12.7$ mm single-strand has a relatively small size, but the anchor for the $\text{Ø}15.2$ -mm strand is large and inefficient. In this dissertation, a post-tensioned anchor for $\text{Ø}15.2$ -mm unbonded single-strand tendon was developed to reflect the existing trend in domestic PT construction. In addition, its performance was verified through various tests.

The shape of the anchor is optimized to minimize the von Mises stress through finite element analysis by varying the shape of bearing plate, body, and gusset. In addition, the design is also determined in consideration of a jacking device, accessories, and workability. ACI 423.7-14, on the other hand, requires the use of encapsulation

system, which is highly resistant to corrosion. Therefore, the encapsulated anchor was developed to enhance the durability of PT tendons and buildings.

Three kinds of performance tests (static load test, fatigue test, load transfer test) were carried out in accordance with the domestic test method KCI-PS101. Static load tests were performed to verify the anchorage behavior for the load greater than 95% of the strand's nominal tensile strength. Also the fatigue test was conducted in order to confirm the long-term performance of the anchor. The load transfer test verified the change of fracture strength based on the reinforcement details of the anchorage zone. The hydrostatic tests were conducted according to ACI 423.7-14 and no water flowed into the anchorage despite maintaining the water pressure of 8.6 kPa for 24 hours.

Instead of carrying out rather complicated and time-consuming performance tests, a compression test and a jacking test were devised that could be performed easily in the field of construction. The compression test reflects the process of making the fixed end through compression, while the jacking test is a method of verifying the anchorage performance by tensioning the strands. Prior to applying the developed anchor to the building, the behavior and construction of the tendon were examined by performing a mockup test.

To observe the long-term behavior of PT tendons with developed anchors in the actual building, the stress of strand was measured using a strand with fiber Bragg grating system, and the slab deflection has been measured for three years and nine months (which will be continued). The short-term deflection is predicted using the

finite element analysis program by applying the construction load and properties of the member that is known to change frequently during the construction process. For long-term deflection, the value of time-dependent coefficient for PT slab is smaller than that for RC slab and thus proposed on the basis of measured data. The proposed equation expresses the tendency of long-term deflection of PT slab better than the conventional formula. From the long-term behavior assessment, the developed anchor performance was demonstrated to be satisfactory.

The anchorage developed in this dissertation is patented and has been applied to four actual building projects. It was also used in two previous experimental studies that examine the ultimate limit state of PT elements, which confirmed the behavior of PT structures with developed anchors.

Keywords : **Anchor, Encapsulation, Post-tensioning, Unbonded, Development, Performance, Slab, Deflection**

Student Number : **2014-21407**

Contents

Abstract	i
Contents.....	iv
List of Tables	x
List of Figures	xiii
List of Symbols	xix
Chapter 1. Introduction	1
1.1 Unbonded Post-Tensioning System.....	2
1.1.1 General	2
1.1.2 History.....	6
1.1.3 Components.....	8
1.2 Motivation for Research	15
1.3 Objectives	17
1.4 Organization.....	18
Chapter 2. Literature Review	20
2.1 Code Provision and Specifications of Unbonded Single-Strand Tendon	21
2.1.1 Strand	21
2.1.2 Sheathing.....	23
2.1.3 Grease.....	25
2.1.4 Anchor.....	26
2.1.5 Wedges.....	28

2.1.6 Sleeve	29
2.1.7 Encapsulation	29
2.2 Code Provision and Specifications for Performance Tests.....	30
2.2.1 Static Load Test.....	31
2.2.2 Fatigue Test	37
2.2.3 Load Transfer Test	41
2.2.4 Hydrostatic Test	46
2.3 Previous Studies on Anchor.....	48
2.3.1 Existing Anchors	48
2.3.2 Ductile Cast Iron	50
2.3.3 Encapsulation	52
2.3.4 Existing Wedges.....	53
2.4 Previous Studies on Performance Tests.....	54
2.4.1 Static Load Test.....	54
2.4.2 Fatigue Test	55
2.4.3 Load Transfer Test	55
2.4.4 Hydrostatic Test	56
Chapter 3. Design of Post-Tensioned Anchor	57
3.1 Modeling.....	59
3.1.1 Wedge Selection.....	59
3.1.2 Tubular Body	60
3.1.3 Bearing Plate	61
3.1.4 Materials.....	63

3.1.5 Load.....	63
3.1.6 Boundary Condition	65
3.2 Design through Finite Element Analysis	66
3.2.1 Location of Bearing Plate.....	66
3.2.2 Shape of Tubular Body	68
3.2.3 Shape of Bearing Plate	71
3.2.4 Shape of Gussets	74
3.2.5 Radii	80
3.3 Consideration for Practical Construction.....	84
3.3.1 Jacking Device	84
3.3.2 Endcap.....	85
3.3.3 Sleeve	87
3.3.4 Redesign of Gusset through Finite Element Analysis.....	88
3.3.5 Casting Fabrication	89
3.4 Bare Anchor	90
3.4.1 Bare Anchor and Accessories	90
3.4.2 Detail Changes	93
3.5 Design Modification for Encapsulated System	95
3.5.1 Needs for Encapsulation.....	95
3.5.2 Encapsulated Anchor and Accessories.....	95
3.6 Summary	99
Chapter 4. Performance Tests	100
4.1 Static Load Test for Bare Anchor	101

4.1.1 Specimen	101
4.1.2 Material Properties	106
4.1.3 Test Set-up	108
4.1.4 Test Results	113
4.2 Static Load Test for Encapsulated Anchor	121
4.2.1 Test Set-up	121
4.2.2 Test Results	123
4.3 Fatigue Test.....	127
4.3.1 Test Set-up	127
4.3.2 Test Results	129
4.4 Load Transfer Test for One Anchor	131
4.4.1 Test Set-up	131
4.4.2 Test Results	137
4.5 Load Transfer Test for Three Anchors	159
4.5.1 Test Set-up	159
4.5.2 Test Results	165
4.6 Hydrostatic Test.....	179
4.6.1 Test Method	179
4.6.2 Test Results	180
4.7 Summary.....	182
Chapter 5. Field Application Tests.....	184
5.1 Compression Test	185
5.1.1 Test Method	185

5.1.2 Test Results	187
5.2 Jacking Test	190
5.2.1 Test Method	190
5.2.2 Test Results	191
5.3 Mockup Test	194
5.3.1 Test Set-up	194
5.3.2 Test Results	198
5.4 Summary	204
Chapter 6. Behavior in Actual Post-Tensioned Slab	206
6.1 Prestressing Force Monitoring.....	208
6.1.1 Method	208
6.1.2 Initial Prestressing Force.....	213
6.1.3 Long-Term Prestressing Force	215
6.2 Deflection Monitoring	217
6.2.1 Monitoring Method	217
6.2.2 Monitoring Results.....	220
6.3 Factors Affecting Post-Tensioned Slab Deflection	224
6.3.1 Dimension and Design	224
6.3.2 Concrete	226
6.3.3 Construction Method.....	227
6.3.4 Post-Tensioning and Construction Procedure	228
6.4 Short-Term Deflection.....	230
6.4.1 Comparison between Whole and Partial Models	230

6.4.2 Cycle of Construction.....	233
6.4.3 Shoring	235
6.4.4 Compressive Strength of Concrete.....	236
6.4.5 Elastic Modulus of Concrete	238
6.4.6 Analysis Results	245
6.4.7 Comparison of Monitoring and Analysis Results	246
6.5 Long-Term Deflection	249
6.5.1 Time-Dependent Factor.....	249
6.5.2 Prediction of Long-Term Deflection.....	251
6.6 Summary.....	253
Chapter 7. Application to Actual Buildings and Additional Research	255
7.1 Application to Actual Buildings	255
7.2 Application to Research.....	257
Chapter 8. Summary and Conclusions.....	258
References	263
초록	273
Acknowledgement	276
감사의 글	277

List of Tables

Table 2-1 Mechanical properties of PC strands (KS D 7002, 2019; ASTM A416/A416M, 2018)	22
Table 2-2 Properties for sheathing (ACI 423.6, 2001; ACI 423.7, 2014)	24
Table 2-3 Testing of grease (ACI 423.7, 2014)	25
Table 2-4 Types of performance tests (Cho and Kang, 2018b)	31
Table 2-5 Comparison of minimum length between anchorages	32
Table 2-6 Checklist for static load test	35
Table 2-7 Minimum free length between anchorages	38
Table 2-8 Fatigue test methods	40
Table 2-9 Size of existing anchors	49
Table 2-10 Size of existing wedges	53
Table 3-1 Permissible compressive stress and bearing stress [unit: MPa]	62
Table 3-2 Measured material properties of GCD500-7	64
Table 3-3 Location of bearing plate [unit: mm]	67
Table 3-4 Location of bearing plate with gusset [unit: mm]	68
Table 3-5 Detailed location of bearing plate	68
Table 3-6 Shape of tubular body	70
Table 3-7 Thickness of flat bearing plate [unit: mm]	72
Table 3-8 Shape of bearing plate [unit: mm]	73
Table 3-9 Shape of gusset [unit: mm]	75
Table 3-10 Height of gusset	76

Table 3-11 Half of distance between gusset elements [unit: mm]	77
Table 3-12 Radius of gusset	78
Table 3-13 Thickness of flat gusset [unit: mm]	79
Table 3-14 Detailed thickness of gusset [unit: mm]	80
Table 3-15 Rounding radius between tubular body and bearing plate	82
Table 3-16 Rounding radius for gusset edges	83
Table 3-17 Rounding radius for bearing plate	83
Table 3-18 Height of gusset [unit: mm]	88
Table 4-1 Compressive strength of concrete [unit: MPa]	107
Table 4-2 Tensile test results	107
Table 4-3 Static load test results	116
Table 4-4 Static load test results compared to P_{pk}	116
Table 4-5 Names of load transfer test specimens	134
Table 4-6 Results of load transfer tests for one anchor	140
Table 4-7 Names of specimens	162
Table 4-8 Concrete compressive strength [unit: MPa]	165
Table 4-9 Results of load transfer tests for three anchors	170
Table 5-1 Results of compressive tests	189
Table 5-2 Jacking test results	193
Table 5-3 Tensile test results of strands	197
Table 5-4 Mockup test results of banded tendon anchors [unit: mm]	199
Table 5-5 Mockup test results of distributed tendon anchors [unit: mm]	200

Table 5-6 Slip at fixed end [unit: mm]	203
Table 6-1 Jacking force and initial prestressing force measured by smart tendon	215
Table 6-2 Maximum deflection analysis for whole and partial slab models	232
Table 6-3 Ideal dates in construction cycle of East Central Tower [unit: days]	234
Table 6-4 Material properties of shoring	236
Table 6-5 Values of constants β_{se} , α , and β	237
Table 6-6 Curing rate coefficient according to temperature	242
Table 6-7 Calculation example of cumulative equivalent curing duration	242
Table 6-8 Elastic modulus of slab concrete (35 MPa)	243
Table 6-9 Elastic modulus of column concrete (45 MPa)	244
Table 6-10 Deflection change of N th floor slab along working procedure	245
Table 6-11 Deflection prediction for 13F-A and 14F-A	247
Table 6-12 Time-dependent factor (ξ) for RC and PT slabs	250
Table 7-1 Post-tensioned buildings with developed encapsulated anchors	256

List of Figures

Figure 1-1 Concept of prestressing	3
Figure 1-2 Types of prestressing	5
Figure 1-3 History of post-tensioning system	7
Figure 1-4 Composition of PT system using unbonded single-strand tendon	8
Figure 1-5 Sheathing types	10
Figure 1-6 Bolt-nut type of pocket former	12
Figure 1-7 Encapsulation system	14
Figure 2-1 Test methods for sheathing (KCI, 2010)	24
Figure 2-2 Sheathing specimens for local or isostatic forces (KCI, 2010)	25
Figure 2-3 Example specimen for static load test (ETAG 013, 2002)	32
Figure 2-4 Measuring points for displacements	35
Figure 2-5 Displacements during testing	35
Figure 2-6 Specimen of load transfer test	42
Figure 2-7 Loading history of load transfer test	44
Figure 2-8 Strains and crack widths for stabilization formula	44
Figure 2-9 Measuring set-up for load transfer test	45
Figure 2-10 Microstructure of cast irons (Berglund, 2011)	51
Figure 2-11 Tensile stress-strain curves for cast irons (Svensson and Salomonsson, 2018)	51
Figure 3-1 Initial model of tubular body [unit: mm]	60
Figure 3-2 Bearing area [unit: mm]	62

Figure 3-3 Material property of cast iron64

Figure 3-4 Applied loading64

Figure 3-5 Boundary condition65

Figure 3-6 Location of bearing plate relative to wedge [unit: mm]68

Figure 3-7 Final shape of tubular body [unit: mm]71

Figure 3-8 Examples of gusset arrangement76

Figure 3-9 Nose of jack and mountain-shaped anchor head [unit: mm]85

Figure 3-10 Anchor head design for endcap [unit: mm]86

Figure 3-11 Redesign of lower body for sleeve [unit: mm]86

Figure 3-12 Drawings of designed bare anchor [unit: mm]90

Figure 3-13 Bare post-tensioned anchor91

Figure 3-14 Accessories for bare anchor92

Figure 3-15 Modified bare post-tensioned anchor94

Figure 3-16 Drawings of encapsulated anchor [unit: mm]97

Figure 3-17 Encapsulated anchor98

Figure 4-1 Drawing of static load test specimen [unit: mm]103

Figure 4-2 Static load test specimen104

Figure 4-3 Tensile test for single-strands107

Figure 4-4 Stress-strain curve of single-strand108

Figure 4-5 Set-up plan of static load test specimen [unit: mm]111

Figure 4-6 Static load test setting112

Figure 4-7 Static load test results115

Figure 4-8 Stress-strain curve of static load test for bare anchor	116
Figure 4-9 Settlement after static load test	117
Figure 4-10 Anchors and wedges after static load test	118
Figure 4-11 Test set-up plan [unit: mm]	122
Figure 4-13 Set-up in free length	122
Figure 4-12 Set-up at fixed end	122
Figure 4-14 Static load test results	125
Figure 4-15 Stress-strain curve of static load test for encapsulated anchor	126
Figure 4-16 Fatigue test plan [unit: mm]	128
Figure 4-17 Fatigue test set-up	128
Figure 4-18 Fatigue load	128
Figure 4-19 Maximum and minimum peak loads of each cycle	130
Figure 4-20 Tested anchor and wedges	130
Figure 4-21 Drawings of load transfer test specimens [unit: mm]	134
Figure 4-22 Reinforcement details for load transfer tests	135
Figure 4-23 Concrete strain gauges of load transfer test specimens [unit: mm]	136
Figure 4-24 Extracting anchors from concrete specimen after load transfer tests	136
Figure 4-25 Load-time	138
Figure 4-26 Failure sequences	141
Figure 4-27 Stress contour at $0.8P_{pk}$ of first cycle [unit: MPa]	148
Figure 4-28 Stress contour at $0.12P_{pk}$ of first cycle [unit: MPa]	149

Figure 4-29 Stress contour at $0.8P_{pk}$ of last cycle [unit: MPa]	150
Figure 4-30 Failure mode	152
Figure 4-31 Crack patterns of failure mode	154
Figure 4-32 Anchors after load transfer test	155
Figure 4-33 Side views of anchors after load transfer test	157
Figure 4-34 Drawing of spiral reinforcement [unit: mm]	162
Figure 4-35 Drawings of specimens [unit: mm]	163
Figure 4-36 Reinforcement details	164
Figure 4-37 Stress and strain curves of steels	166
Figure 4-38 Load transfer test results	168
Figure 4-39 Failure sequences	172
Figure 4-40 Failure modes	178
Figure 4-41 Hydrostatic pressure chamber	179
Figure 4-42 Test set-up of hydrostatic test	180
Figure 4-43 Pressure history	181
Figure 4-44 Observation after hydrostatic test	181
Figure 5-1 Test set-up plan of compression test	186
Figure 5-2 Compressive test set-up	187
Figure 5-3 Load-deformation curve	188
Figure 5-4 Change of differential seating of wedges	189
Figure 5-5 Test set-up for jacking test	191
Figure 5-6 Live end and fixed end of jacking test	191

Figure 5-7 Wedge slip	193
Figure 5-8 Drawing of mockup test specimen [unit: mm]	195
Figure 5-9 Mockup test set-up	196
Figure 5-10 Tensile test results of stands	197
Figure 5-11 Displacements of W, CW, and HW	202
Figure 6-1 Application location of smart tendon [unit: mm]	210
Figure 6-2 Sensor locations for smart tendons [unit: mm]	211
Figure 6-3 Ordinary and smart tendons	212
Figure 6-4 Jacking strand and seating	212
Figure 6-5 Prestressing force during jacking and seating (13 m)	214
Figure 6-6 Prestressing force during jacking and seating (55 m)	214
Figure 6-7 Tendon force (55 m)	216
Figure 6-8 Tendon force and temperature (13 m)	216
Figure 6-9 PT drawings of standard floor showing tendon bundle height and number [unit: mm]	218
Figure 6-10 Location of deflection measuring points on 13 th (13F) and 14 th floors (14F) [unit: mm]	219
Figure 6-11 LVDT set-up	219
Figure 6-12 Results of PT slab deflection	222
Figure 6-13 Comparison between RC and PT slabs	223
Figure 6-14 Modeling for whole slab	231
Figure 6-15 Analysis results of whole slab model	231
Figure 6-16 Modeling for partial slab	232

Figure 6-17 Main construction process related to deflection of base slab	234
Figure 6-18 Shoring plan of standard floor [unit: mm]	235
Figure 6-19 Compressive strength of concrete	237
Figure 6-20 Elastic modulus of early-aged concrete	240
Figure 6-21 Analysis result of short-term deflection	246
Figure 6-22 Comparison between analysis and measured data of 13F-A	248
Figure 6-23 Comparison between analysis and measured data of 14F-A	248
Figure 6-24 Comparison between existing and suggested time-dependent factors	250
Figure 6-25 Various methods predicting long-term deflection	252
Figure 7-1 Application of developed anchor to Raemian Seocho Estige S project	256
Figure 7-2 Unbonded tendons in specimen (Kwon, 2016)	257

List of Symbols

- a = width of cross-section of member, mm
- A_b = net bearing area of anchorage, mm²
- A_b' = maximum area of portion of concrete anchorage surface that is geometrically similar to and concentric with area of anchorage, mm²
- b = length of cross-section of member, mm
- d_g = distance between centers of two gussets, mm
- d_G = distance between gage points in static load test, mm
- d_{G1} = distance between gage point G1 and anchor in static load test, mm
- d_{G2} = distance between gage point G2 and anchor in static load test, mm
- d_{sh} = inner diameter of sheathing, mm
- d_{slab} = slab thickness, mm
- d_c = length cut horizontally from point where curve or straight line meets upper body of anchor, mm
- D_{b1} = diameter of uppermost section anchor body, mm
- D_{b2} = diameter of anchor body section contacting upside of bearing plate, mm
- D_{b3} = diameter of anchor body section contacting underside of bearing plate, mm
- D_{b4} = diameter of bottom surface of anchor body, mm
- E = modulus of elasticity, MPa
- E_a = apparent activation energy, KJ/mol
- E_c = modulus of elasticity of concrete, MPa

List of Symbols

E_{cc}	= modulus of elasticity of column concrete, MPa
E_{cs}	= modulus of elasticity of slab concrete, MPa
f_c	= specified compressive strength of concrete, MPa
f_{ci}	= specified compressive strength of concrete at time of initial prestress, MPa
f_{ck}	= designed compressive strength of concrete, MPa
f_{cp}	= permissible concrete compressive stress, MPa
f_{cu}	= average compressive strength of concrete on 28 th day, MPa
$f_{cu}(t)$	= average compressive strength of concrete at age t , MPa
f_h	= hydrostatic pressure, kPa
f_{pk}	= nominal (characteristic) tensile strength of tensile elements, MPa
f_{pu}	= specified tensile strength of prestressing reinforcement, MPa
$f_{v,max}$	= maximum Von Mises stress, MPa
h	= height of member, mm
h_{gt}	= height of gusset from top edge of bearing plate, mm
h_{gb}	= height of gusset from bottom edge of bearing plate, mm
h_p	= height of center of bearing plate, mm
k_1	= proportional constant depending on type of cement
L	= span length, mm
l_f	= free length between anchors, mm
m_c	= unit weight of concrete

n	= number of cycles in load transfer test
P	= prestressing force, N
P_{iso}	= force applied to sheathing specimen for isostatic force, N
P_{pk}	= nominal (characteristic) ultimate resisting force of tensile elements, N
P_{pu}	= specified (actual) ultimate resisting force of tensile elements, N
P_w	= wedge injection force, N
R	= gas constant, J/mol·K
r	= fillet radius, mm
r_{g1}	= fillet radius between gusset and anchor body or gusset and upside of bearing plate, mm
r_{g2}	= fillet radius at top edges of gusset, mm
r_{g3}	= fillet radius between bottom edge of gusset and upside of bearing plate, mm
r_{g4}	= fillet radius between top of gusset and anchor body, mm
r_l	= fillet radius between anchor body and lower side of bearing plate, mm
r_p	= fillet radius at top of bearing plate, mm
r_u	= fillet radius between anchor body and upside of bearing plate, mm
T_a	= concrete temperature during time Δt , K
T_s	= reference temperature, K
t	= concrete age
t_b	= lower convex thickness of bearing plate, mm
t_c	= center thickness of bearing plate, mm

List of Symbols

t_e	= equivalent age, days
t_{g1}	= thickness of gusset with outer distance of 45 mm between two gussets, mm
$t_{g1,b}$	= thickness of bottom of gusset with outer distance of 45 mm between two gussets, mm
$t_{g1,t}$	= thickness of top of gusset with outer distance of 45 mm between two gussets, mm
t_{g2}	= thickness of gusset with distance of 40 mm between centers of two gussets, mm
$t_{g2,b}$	= thickness of bottom of gusset with distance of 40 mm between centers of two gussets, mm
$t_{g2,t}$	= thickness of top of gusset with distance of 40 mm between centers of two gussets, mm
t_p	= edge thickness of bearing plate, mm
t_i	= upper convex thickness of bearing plate, mm
Δf	= correction factor
Δt	= time duration, days
Δ_L	= long-term deflection, mm
Δ_g	= wedge differential seating, mm
Δ_S	= short-term deflection, mm
Δ_s	= displacement of strand wire with respect to anchorage, mm
Δ_w	= displacement of wedge with respect to anchorage, mm
Δ_g	= wedge differential seating, mm
α	= constant for concrete compressive strength

β	= constant for concrete compressive strength
$\beta_{cc}(t)$	= correction coefficient according to age for concrete strength development
β_{sc}	= influence coefficient on dry shrinkage according to cement type
ε	= strain
ε_n	= strain at n th cycle in load transfer test
ε_t	= transverse strain
ε_v	= vertical strain
ρ'	= compression steel ratio
λ_Δ	= amplification factor
ν	= Poisson's ratio
ω	= crack width
ω_n	= crack width at n th cycle in load transfer test
ξ	= time-dependent coefficient
ξ_{PT}	= suggested time-dependent coefficient for post-tensioned slab
ξ_{RC}	= time-dependent coefficient for reinforced concrete slab

Chapter 1. Introduction

In this study, a post-tensioned (PT) anchor using unbonded single-strand was developed. A series of tests were conducted in order to verify its performance and apply it to actual buildings.

In this chapter, before mentioning the details of research, Section 1.1 outlines the concept of an unbonded post-tensioning (PT) system upon which developed anchors are applied. The motivations and objectives of this study have been summarized in Sections 1.2 and 1.3, respectively. Section 1.4 elucidates the organization of this dissertation.

1.1 Unbonded Post-Tensioning System

This section summarizes the definition and features of unbonded PT along with relevant history. In addition, it provides a brief description of the components of this system.

1.1.1 General

Unbonded PT denotes a method of PT wherein prestressing steel is not bonded to the concrete member. Since it belongs to prestressing system, it is imbued with the concept and characteristics of prestressing.

Prestressing is known to strengthen concrete by giving compression through tensioning prestressing steel (**Figure 1-1**). Notably, concrete is strong in compression, but weak in tension — the tensile strength of concrete accounts for about 10% of the compressive strength of concrete. Additional compressive force exerted due to prestressing steel is known to increase the concrete member's tensile capacity. Therefore, under the same condition, prestressed concrete member requires a smaller size as compared to the reinforced concrete (RC) member. Resultantly, the prestressing system is deemed suitable for a relatively long span with fewer cracks and deflections. Furthermore, according to Cross (2007), prestressing is more economical than RC when the span is found to exceed 7 m.

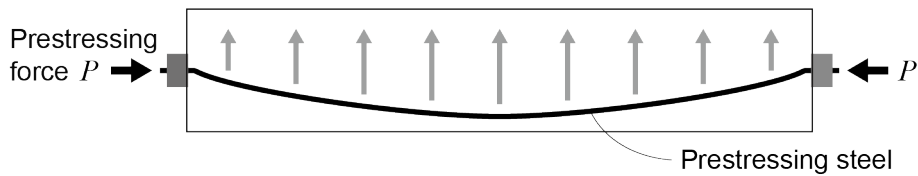


Figure 1-1 Concept of prestressing

The different types of prestressing steel include threaded bar, steel wire, strand, carbon fiber, as well as aramid fiber. Seven-wire strands are primarily used with a tensile strength of 1,860 MPa. In this study, the prestressing steel mentioned refers to the strand. Strand's tensile strength of 1,860 MPa is 3.26 times that of the universally-used steel reinforcing bar (570 MPa of SD400). Thus, it can be inferred that the prestressed concrete system has a more significant effect on tensile resistance in comparison to the conventional reinforced concrete system.

Two sub-systems are associated with prestressing, namely, pre-tensioning and post-tensioning, which is predicated on the time of stressing prestressing steel during construction (**Figure 1-2**).

In pre-tensioning, prestressing steel is strained prior to concrete pouring. When the strand gets released after the hardening of concrete, the tensile force gets converted into the compressive force of the concrete member. Meanwhile, in PT, concrete is poured on installed duct or sheath so as to avoid direct-bond between the concrete and prestressing steel. Anchorage systems are required at both ends in order to transfer the compressive force to the concrete members. The tendon can be placed into the desired profile since the prestressing steel is not jacked before pouring

concrete. Due to these characteristics, it is primarily used for the cast-in-place method.

PT system can be subdivided by location of prestressing steel and re-tensionability. If prestressing steels are installed outside the concrete structural member, it is referred to as an external PT. A deviator block is used to create the desired profile. Grout or grease can be filled either inside the duct or sheath. Owing to the fact that the tendon is not located in the member, the external PT system can be regarded as unbonded, regardless of the filling material.

The possibility of re-tension is predicated on the type of filling inside of the duct or sheath. Bonded PT uses grout to fill the void and bond bare strands (prestressed concrete steel strands, PC strands) to the concrete member. The grout provides an alkaline environment that safeguards the prestressing steel from corrosion. Meanwhile in an unbonded PT system, the void is filled with not-hardening materials, which would also form non-corrosive substances, such as grease or wax. Friction and corrosion persist without any non-corrosive substances. Upon the utilization of a single strand, a sheathed greased strand is commonly used, which is an unbonded system with or without ducts and grouting.

PT structure complementing RC structure is known to entail several advantages (Allen, 1981; Choat and Prakash, 2017; Freyssinet, 2014; PTI, 2000; Walsh and Kurama, 2009). For example, longer spans with fewer columns can be utilized and provide larger column free regions. More slender sections can be utilized for the

same load. Reduced floor thicknesses save height so that the number of stories in the building increases. Freedom of layout and increased number of stories can also pave the way for higher rental returns.

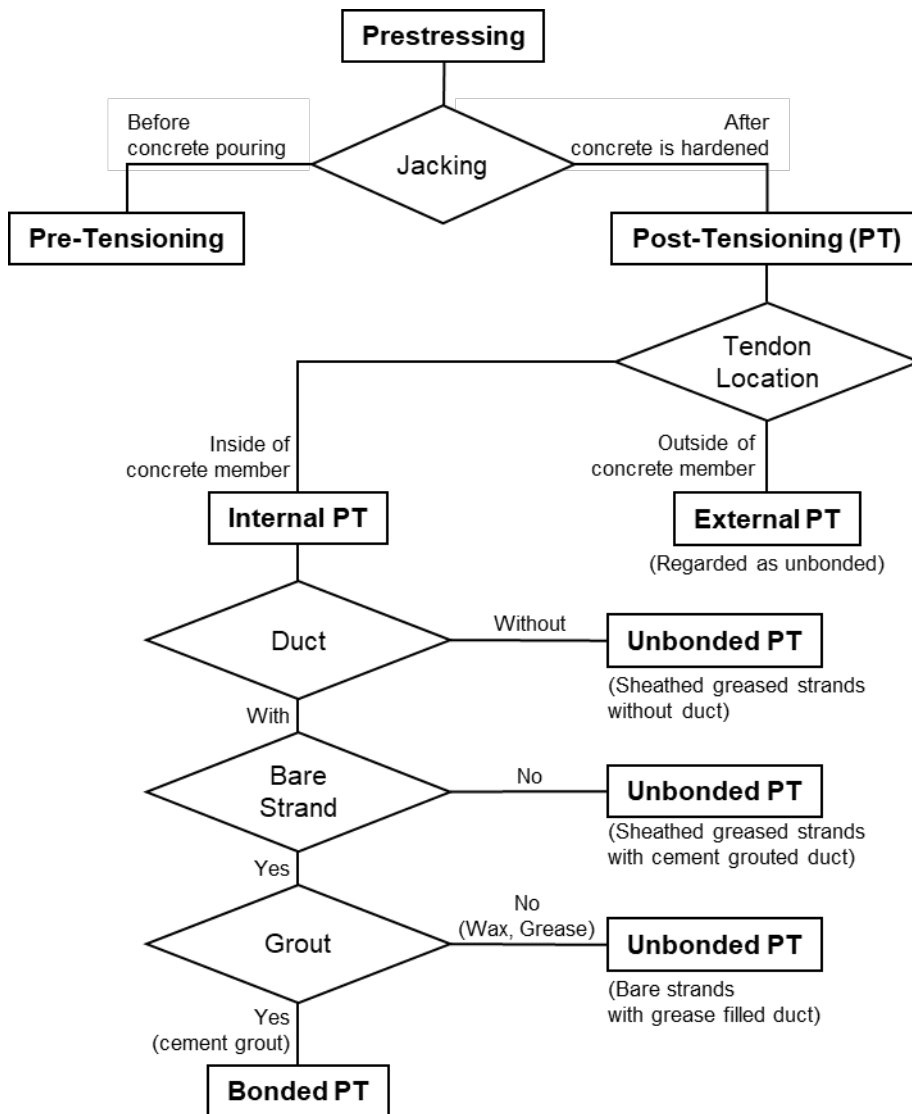


Figure 1-2 Types of prestressing

1.1.2 History

The history of prestressed concrete is less than a century and a half (**Figure 1-3**). The genesis of the concept of prestressing can be traced back to 1880, subsequent to which a patent for prestressed concrete was first filed by P. H. Jackson in 1888 (Jackson, 1888). Eugene Freyssinet developed a high-strength wire in 1928, followed by an anchorage that involved the use of wedges and a jacking device back in 1939. Correspondingly, Freyssinet and Seailles (1937) suggested tensioning high strength steel wires in concrete beams. It was the first time that prestressing steel was used in a concrete member, thereby substantially reducing the number of reinforcing bars.

In the mid-1950s, The Walnut Lane Bridge in Philadelphia, which had 47 m spans, became the first PT construction. In the mid-1950s, the PT system was extended to other buildings in the United States (U.S.) using the lift-slab construction method. In the 1960s, post-tensioned box girder bridges were extensively constructed in the western part of the country (Dinges, 2009). Simultaneously, the use of unbonded tendons in building floor systems was a ubiquitous phenomenon as well. In the 1970s, post-tensioning was applied to the foundation, after which extruded unbonded tendons started getting made use of in the 1980s (Kelley, 2001).

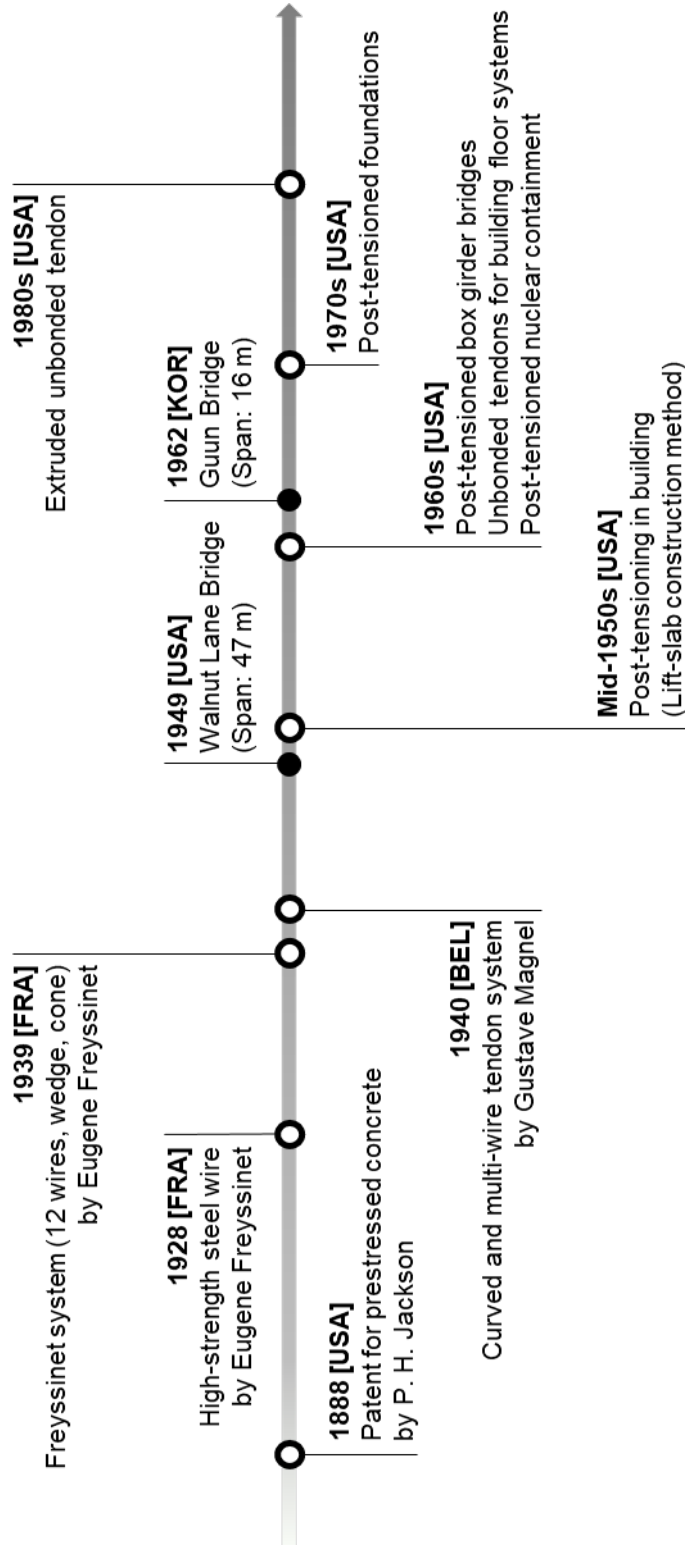


Figure 1-3 History of post-tensioning system

In Korea, the first PT bridge and building were the Guun Bridge (16 m span) in 1962 and the Kolon Hotel in 1974, respectively. It is noteworthy that the flat-slab type PT structure has been primarily applied over the past 20 years (KCI, 2013).

1.1.3 Components

A PT system using unbonded single-strand for building consists of sheathed greased strand (PC strand, sheathing, grease), anchor, wedge, and accessories (sleeve, pocket former, endcap), as illustrated in **Figure 1-4**. An encapsulation system is also applied in order to improve the water-tightness of the entire tendon.

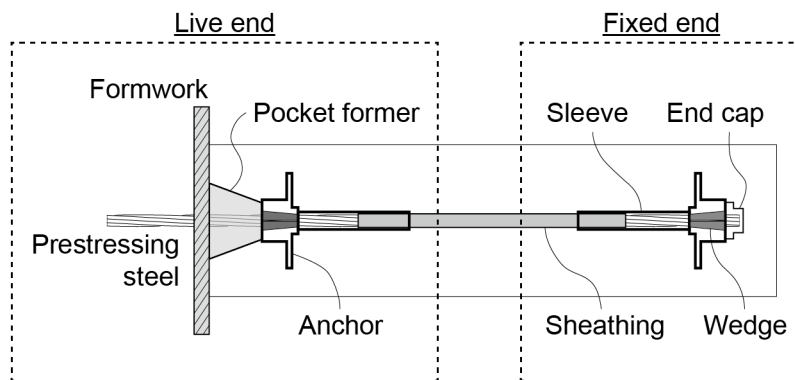


Figure 1-4 Composition of PT system using unbonded single-strand tendon

Prestressing steel

The prestressing steel for unbonded single-strand is a high-strength seven-wire strand (PC strand), something that is used for other prestressing methods as well. The raw material is a piano wire (KS D 3509, 2018), which is a hard carbon steel wire or alloy steel wire. A seven-wire strand comprises of one core wire and six helical wires twisted around the core wire.

Sheathing

The sheathing prevents the strand from coming into direct contact with the concrete. **Figure 1-5** illustrates the types of sheathing. As compared to Sisal Kraft paper sheathing, plastic sheathing has been found to significantly increase waterproof performance. Heat-sealed sheathing compensates the disadvantage of the push-through method, which could not fill grease inside the sheathing. Extruded plastic sheathing is used after being introduced in the 1980s (PTI, 2006), which has no lapped joint problem and a reduced sheathed section area. Currently, most of sheathing is made up of high-density polyethylene (HDPE) (Kelley, 2016).

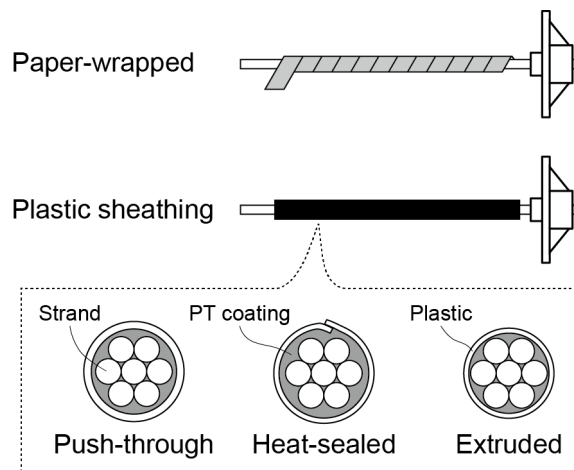


Figure 1-5 Sheathing types

Grease

The grease is filled between the strand and the sheathing, to reduce the strand's friction and waterproof. When using the paper sheathing, the grease was applied by hand. The greasing machine has been used ever since plastic tube started to get used.

Anchor

The anchor for unbonded PT in construction primarily uses a single-strand. The small cross-sectional size of the member, such as beam, slab, wall, etc. makes it challenging to focus on several strands in one place. In order to use the bundle of several strands, the size of the anchor as well as that of the member must be large. Therefore, one-hole anchors are often used to place the strands while minimizing the' dimensions of members.

Unbonded PT anchors in buildings are made of ductile cast iron. The force by only one strand is applied, whereas the anchorage buried in concrete members requires relatively little durability. Besides, it is possible to reduce the costs of material and manufacturing.

Wedge

The wedge serves to hold the strand and settle in the anchorage. The wedge is conical and has annular ridges (teeth) which is capable of biting a strand (Kelley, 2016). The minimum inside-diameter of the wedge is slightly smaller than the maximum diameter of the strand, which, in turn, can bite the strand, resulting in little loss of its cross-section.

Sleeve

The sleeve protects the space between the anchor (opposite to where the wedge is inserted) and the strand from the ingress of concrete and water. The sleeve is usually made of plastic or rubber. The plastic sleeve is rigid and durable, whereas the rubber sleeve is elastic and tight. The inner diameter is such that the sheathing can pass through. However, if it is excessively large, water and cement paste can easily pass between the sheathing and the sleeve. Additional taping may be needed to make the seal more waterproof.

Pocket former

The pocket former creates a void where the jacking device and the strand cutter can enter at the live end. It is placed between the anchor and the formwork, thus preventing concrete or cement from entering. Plastic is the primary material of the pocket former. The fact that it is lightweight and reusable means that it can be easily separated from the concrete. Depending on the type of strand jack and cutter, it is possible for the void shape to vary.

There are two ways of fixing the pocket former: using nail and bolt-nut. The nail method entails the use of nails through the bearing plate of anchor and the pocket former to the formwork. However, it is time and labor intensive because at least two nails are needed for each anchor. Depending on the shape of the pocket former, the nail may stick out in the void even after extracting the former.

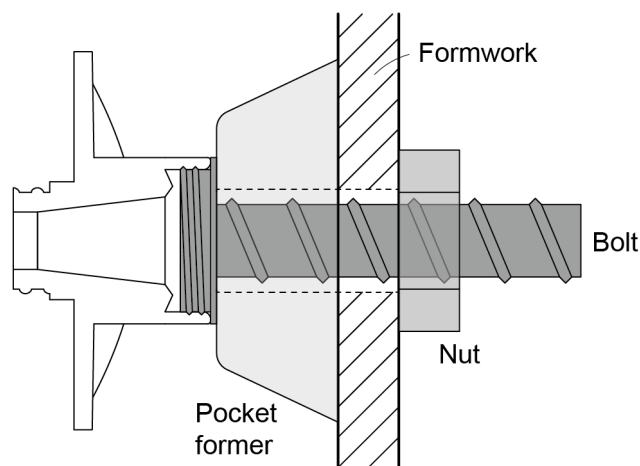


Figure 1-6 Bolt-nut type of pocket former

The bolt-nut method refers to a method of inserting a plastic bolt in the anchor head, inserting a pocket former, and then tightening a plastic nut from the outside of the formwork (**Figure 1-6**). The strand profile can be easily adjusted to the desired position because the bolt passes the hole drilled in the formwork. Additionally, the anchorage can be fixed to the formwork only using bolts and nuts without nails. The same formwork or gang-form can be reused in order to improve workability if the tendon profile remains unchanged across several floors. The pocket former, bolt, and nut are separated so that each undeformed or unbroken part can be reused.

Endcap

The purpose of endcap is to close the anchor head after cutting the strand tail. Concrete, cement, or water entering the wedge causes corrosion and a decrease of long-term durability. In particular, the void created by the pocket former is filled with cement paste. Therefore, the endcap should be used to completely block the wedge cavity with water (ACI 423.6, 2001). The grease should be filled to obtain the effect of secondary waterproof even if the endcap is broken.

Encapsulation system

Encapsulation system is a system in which a tendon entirely blocks the inflow of water, concrete, and cement from the outside (**Figure 1-7**). An unbonded single-

strand and an anchor are covered with sheathing and plastic, respectively. A sleeve is used between the strand and the anchor. The strand tail and the wedge cavity are closed with a watertight endcap at the anchor head.

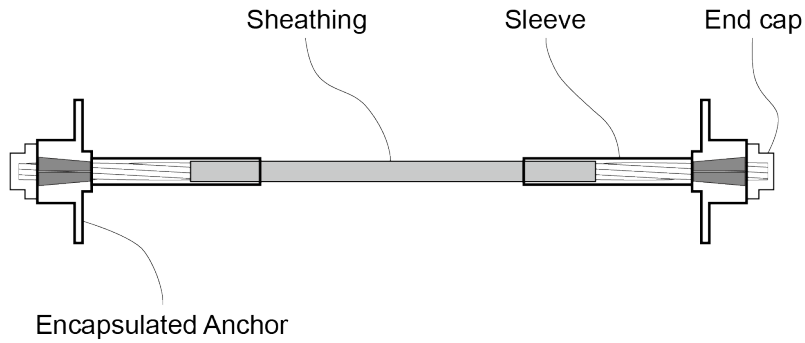


Figure 1-7 Encapsulation system

1.2 Motivation for Research

In Korea, the use of the PT method has been gradually increasing to reduce the thickness of the slab as well as to acquire enough span, height, and the number of layers since the 2000s. However, all products of PT anchorage were created using the overseas technology until the anchorage mentioned in this study was developed in 2013 (Cho et al., 2015). Notably, four major companies, overseas anchor development companies, operate Korean branches; DYWIDAG Systems International (DSI), Soletanche Freyssinet (Freyssinet), General Technologies, Inc. (GTI), VSL International (VSL).

Domestic PT construction primarily comprises of 15.2 mm diameter strands, while overseas prefers to use $\text{Ø}12.7$ mm strand. The size of anchors for $\text{Ø}12.7$ mm tendons is well optimized abroad, albeit not for $\text{Ø}15.2$ mm strands. Despite the proclivity to reduce the thickness of the slab, the anchor with large dimensions inhibits it. Put succinctly, imported anchorages are found to be less efficient in domestic PT construction.

Until the enforcement of the encapsulation system in ACI 423.7 in 2014, encapsulated tendons were used only in hazardous environments. Encapsulation is not yet required in domestic specifications. However, according to Slamova (2012), Korea, with its three sides surrounded by the sea, faces a high risk of potential corrosion. Encapsulation is applied while developing the anchor in order to improve the long-term durability of the PT structures.

Furthermore, producing developed anchorage in Korea is expected to reduce direct costs. When a span exceeds 7 m, PT flat slabs have a 5~20% cost saving as compared to RC flat slabs (Chung, 2003). However, high direct costs from importing anchorages negate this advantage and impedes the activation of domestic PT construction.

No previous study has shown regarding the design procedure of PT anchor for unbonded single-strand tendon except the papers published by the author, although there are many researches related to performance tests on existing anchorages. This dissertation, containing anchor design through finite element analysis and performance verification tests, will impart knowledge to engineers and make in-depth contribution to the PT method.

1.3 Objectives

The primary purpose of this study is to develop a post-tensioned anchor. In particular, it is a one-hole anchor for the building that uses an unbonded single-strand with a diameter of 15.2 mm.

The performance of developed anchorage was evaluated through an experimental study. The behavior of both the anchorage and the anchorage zone was analyzed with performance tests.

In addition, the behavior of the PT slab, which is also the most common member in the PT building, was monitored. The ultimate objective was to examine whether or not the developed anchorage can be utilized in actual PT construction.

1.4 Organization

Chapter 1 introduces the unbonded PT system. It also summarizes the motivation and objectives for developing PT anchor that uses the unbonded single-strand.

Chapter 2 reviews and compares codes or specifications for unbonded PT tendon and performance tests. In addition, the related preceding researches are summarized.

Chapter 3 elucidates the process of designing the PT anchor through finite element analysis. In this chapter, bare (casting) anchor with an optimized design is developed and improved to encapsulated anchor.

Chapter 4 details the methods and results of mandatory performance tests; static load test, fatigue test, as well as load transfer test. Additionally, the water-tightness of encapsulated anchors is verified by hydrostatic test.

In Chapter 5, simple experiments (compressive test and jacking test) are designed and performed, as opposed to time and cost-intensive tests by specifications. Mock-up test is conducted prior to applying the anchor to the construction site.

Chapter 6 describes the short- and long-term behavior of PT slabs with developed anchors. The prestressing force was estimated by using the strand with fiber bragg grating (FBG) system. The deflection of the PT slab was also measured. Furthermore, this chapter illustrates the prediction methods and results for deflection of PT slab.

Chapter 7 introduces application cases of the developed anchor for building constructions. In addition, the experimental studies using the anchors for PT structures are alluded to.

Finally, Chapter 8 summarizes and concludes this dissertation.

Chapter 2. Literature Review

As mentioned before, the main purpose of this study is to develop a post-tensioned anchor and experimentally verify its performance. Section 2.1 describes the specifications that must be satisfied by the unbonded single-strand tendon. Section 2.2 elucidates the methods and criteria for the performance tests for anchorage. These include static load test, fatigue test, and load transfer test. Sections 2.3 and 2.4 meanwhile summarize previous studies related to unbonded PT anchorage and its performances, respectively.

2.1 Code Provision and Specifications of Unbonded Single-Strand Tendon

This section describes the criteria for the components of the unbonded single-strand tendon based on both Korean and American specifications. The focus is on shapes or properties, and descriptive details on storage/construction are excluded.

2.1.1 Strand

KCI (2010) and ACI 423.7 (2014) require the strand to conform to KS D 7002 (2019) and ASTM A416/A416M (2018), respectively. The mechanical properties of Ø12.7 mm and Ø15.2 mm strands have been summarized in **Table 2-1**.

Normal-relaxation (stress-relieving) and low-relaxation prestressing steels are distinguished using after-heat treatment (KCI, 2013). The stress-relieving strand is heated to about 350 °C before being slowly cooled to produce. The low-relaxation strand is strain-tempered, and heated to about 350 °C, after which a tensile force is applied. Low-relaxation strand is preferable because about 10% less quantity is required than normal-relaxation strand. Moreover, it also requires less initial overstress in the concrete (Kelley, 2016).

Table 2-1 Mechanical properties of PC strands (KS D 7002, 2019; ASTM A416/A416M, 2018)

Type	Nominal Tensile strength [MPa]	Diameter [mm]	Tolerance of diameter [mm]	Nominal cross-sectional area [mm ²]	Nominal mass [kg/km]	Minimum tensile load [kN]	Minimum 0.2% offset yield load [kN]	Minimum elongation [%]	Minimum relaxation [%]
SWPC7AN	1720	12.4		92.9	729	160	136	3.5	8.0
		15.2		138.7	1,101	240	204	3.5	8.0
SWPC7AL	1720	12.4		92.9	729	160	136	3.5	2.5
		15.2		138.7	1,101	240	204	3.5	2.5
SWPC7BN	1860	12.7	+0.40	98.7	774	183	156	3.5	8.0
		15.2		138.7	1,101	261	222	3.5	8.0
SWPC7BL	1860	12.7	-0.20	98.7	774	183	156	3.5	2.5
		15.2		138.7	1,101	261	222	3.5	2.5
SWPC7CL	2160	12.7		98.7	774	214	182	3.5	2.5
		15.2		138.7	1,101	300	255	3.5	2.5
SWPC7DL	2360	12.7		98.7	774	233	198	3.5	2.5
		15.2		138.7	1,101	327	278	3.5	2.5
ASTM A416/A416	1725	12.7	±0.40	92.9	730	160	144.1*	3.5	2.5**
		15.2		139.0	1,090	240	216.2*	3.5	3.5***
	1860	12.7	+0.65	98.7	780	184	165.3*	3.5	3.5***
		15.2		140.0	1,100	261	234.6*	3.5	3.5

SWPC: Steel wires for prestressed concrete;

7: Seven-wire;

A / B / C / D: Nominal tensile strength of 1,720 / 1,860 / 2,160 / 2,360 MPa, respectively;

N / L: Normal (stress-relieving) / Low-relaxation;

*: Minimum load at 1.0% Extension [kN];

**: When initially loaded to 70% of specified minimum breaking strength;

***: When loaded to 80% of specified minimum breaking strength of strand after 1,000 hours of testing.

Most commonly used low-relaxation strands in buildings are known to impart a strength of 1,860 MPa with 12.7 mm or 15.2 mm diameters. In the context of Korean construction, there is a tendency to use Ø15.2 mm strands in order to reduce the number of tendons. This study made use of SWPC7BL, which had a diameter of 15.2 mm.

2.1.2 Sheathing

The sheath must have a strength that is capable of withstanding it, given that it may be stepped on before placing the concrete or bumped into vibrators or other tools. In addition, the shape should be maintained against the pressure caused by the poured concrete; otherwise, the cement paste in the concrete should not flow into the sheathing. The criteria for the sheathing are listed in ACI 423.6 (2001) and ACI 423.7 (2014), as depicted in **Table 2-2**.

The commentary of KCI (2010) suggests test methods to ascertain the quality of the sheathing. Cement pastes with water-cement ratio of 50% are injected into the straight and curved sheathing specimens (**Figure 2-1**). The length of both sheathing specimens is four times that of the inner diameter (d_{sh}). For curved specimen, the radius of curvature is $30d_{sh}$. The cement paste should not leak for 30 minutes (but water may leak) after pouring the cement paste.

The specimens are fabricated as shown in **Figure 2-2**, depending on whether they are tested for resistance to local or isostatic forces. With regard to a locally forced case, after placing $0.8d_{sh}$ diameter circular steel inside of sheath, a load of 1 kN is applied for a short time using a $\text{Ø}9$ mm circular steel perpendicular to the center of the sheathing. In case the hardness of sheathing material changes significantly with temperature, each test specimen should be loaded at -10, 20, and 50 °C, respectively. For the specimen for isostatic force, a load $P_{iso} = 100\pi d_{sh}^2$ [N] is applied for 10 minutes using a test set-up at room temperature, as illustrated in **Figure 2-2(b)**.

Table 2-2 Properties for sheathing (ACI 423.6, 2001; ACI 423.7, 2014)

	Acceptance criteria
Thickness	≥ 1.27 mm
Density	≥ 941 kg/m ³
Inside diameter	\geq (maximum diameter of strand + 0.76 mm)
Surface	- Smooth circular outside surface - Not visibly reveal lay of strand

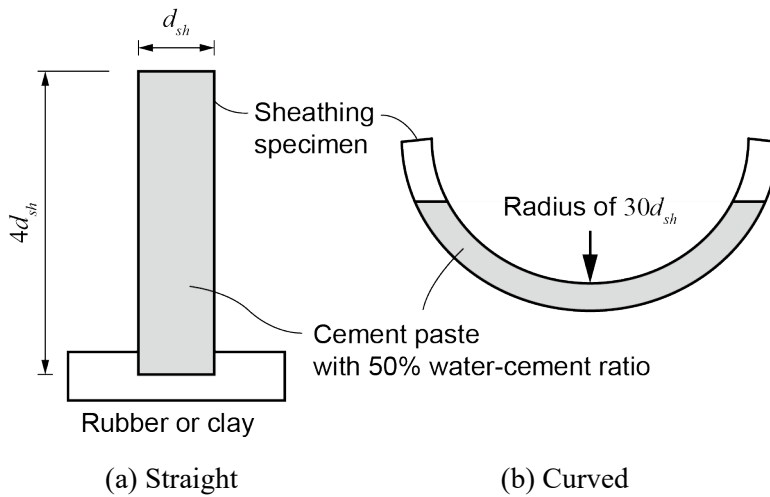


Figure 2-1 Test methods for sheathing (KCI, 2010)

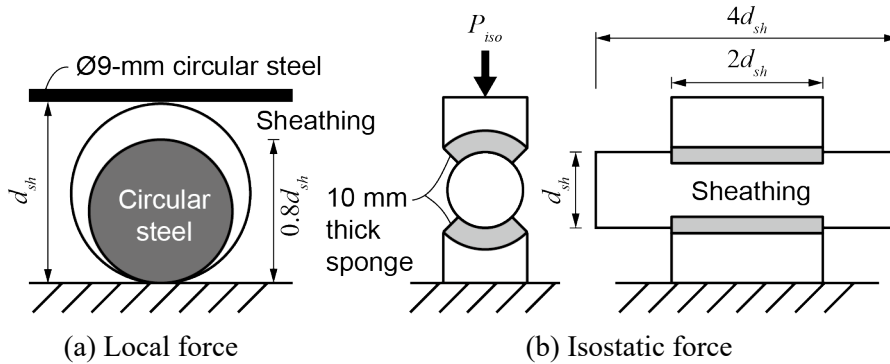


Figure 2-2 Sheathing specimens for local or isostatic forces (KCI, 2010)

Table 2-3 Testing of grease (ACI 423.7, 2014)

Test description	Acceptance criteria	Test method	
Dropping point	≥ 149 °C	ASTM D556 or D2265	
Oil separation	$\leq 0.5\%$ by mass	ASTM D6184	
Water content	$\leq 0.1\%$	ASTM D95	
Flashpoint	≥ 149 °C	ASTM D92	
Corrosion	Rust grade 7 or better	ASTM B117	
Water-soluble ions	Chlorides	≤ 10 ppm	ASTM D512
	Nitrates	≤ 10 ppm	ASTM D3867
	Sulfides	≤ 10 ppm	ASTM D4658
Soak	No emulsification	ASTM B117	
Compatibility with sheathing	Hardness change	$\leq 15\%$	ASTM D4289
	Volume change	$\leq 10\%$	ASTM D4289
	Tensile strength change	$\leq 30\%$	ASTM D638

2.1.3 Grease

The criteria for grease are strictly complied with in order to improve the persistence of the unbonded post-tensioned system, as shown in **Table 2-3**. The sheathed strand

with Ø15.2 mm should be filled with more than 1.36 kg per 30.5 m (ACI 423.6, 2001) or 0.0446 kg/m (ACI 423.7, 2014). The corrosion-inhibiting ability of this grease should be demonstrated in accordance with ASTM D610 (2008).

2.1.4 Anchor

When tested in an unbonded condition, anchorages for tendons should develop at least 95% of f_{pu} , specified tensile strength of prestressing reinforcement, without exceeding the anticipated set (AASHTO, 2017a; ACI 301, 2016; ACI 318, 2019; ACI 350, 2006; ACI 423.3R, 2017; ACI 423.6, 2001; PTI, 2006). This requirement is substantially more pronounced than the maximum design stress for unbonded tendons ensures the provision of a safety margin (PTI, 2006).

A bearing plate transfers the tendon force from the anchor body to concrete. PTI (1998) and AASHTO (2017a) aid down basic bearing plate design criteria and testing for special bearing plates. Similarly, PTI (2000) provided elaborate guidance concerning the design of bearing plates and anchorages. Additional information and requirements can be found in AASHTO (2017b).

Anchorage dimensions should be such that the average bearing stresses on concrete created by an anchorage should not exceed the values computed by the following equations unless a test performed by a certified independent laboratory clearly

indicates that anchorage performance is equal or superior to anchorages, thereby satisfying the requirements of this section (ACI 423.6, 2001; ACI 423.7, 2014).

a) At transfer load

$$f_{cp} = 0.83 f_{ci} \sqrt{\frac{A_b'}{A_b}} - 0.2 \leq 1.25 f_{ci} \quad (\text{ACI 423.6, 2001}) \quad (2-1)$$

$$f_{cp} = 0.75 f_{ci} \sqrt{\frac{A_b'}{A_b}} \leq 1.25 f_{ci} \quad (\text{ACI 423.7, 2014}) \quad (2-2)$$

b) At service load

$$f_{cp} = 0.6 f_c \sqrt{\frac{A_b'}{A_b}} \leq f_c \quad (\text{ACI 423.6, 2001; ACI 423.7, 2014}) \quad (2-3)$$

where f_{cp} denotes permissible concrete compressive stress; f_c refers to specified concrete compressive strength; f_{ci} represents specified concrete compressive strength at the time of initial prestress; A_b signifies the net bearing area of anchorage; and A_b' denotes the maximum area of the concrete anchorage surface's portion that is geometrically similar to and concentric with the area of the anchorage.

A special bearing plate is commonly used for unbonded single-strand tendon. Its performance should be verified through testing even if it is designed to meet specific design criteria based on the distribution area (PTI, 2006).

In addition to being nonporous, castings should be free of sand, blowholes, voids, and other defects (ACI 423.6, 2001; ACI 423.7, 2014). Essential considerations in

the design of castings are inclusive of the following: the raw material grade, surface roughness, surface hardness, flatness of conical angle, compatible angle geometry, as well as tolerance in conjunction with the wedge and specified strand (ACI 423.6, 2001). SAE J449 (2011) is the reference for standard surface conditions of castings.

The performance tests required for the anchor have been discussed in detail in Section 2.2. Investigations of existing anchors and other information for anchors find mention in Section 2.3.

2.1.5 Wedges

As mentioned in Section 2.1.4, ACI 318 (2019) requires that the anchorage develops at least $0.95f_{pu}$. Prior to ACI 318 (1989), the anchorage was required to develop 100% of the tensile strength of the strand. However, this was reduced to 95% due to the stress-riser effect by the wedge teeth gripping the strand (Kelley, 2016).

The material and shape of the wedge are not mentioned in the specifications. Existing wedge products and related literatures have been reviewed in Section 2.3.

2.1.6 Sleeve

For the wedge to be able to bite the strand, the sheathing and grease should be removed. Since the covers are removed to some distance from the anchorage, the concrete and water may enter, thus accelerating the progress of corrosion. It is also noteworthy that the stress of the strand is concentrated near one specific part of the anchorage. The strand wire corrosion occurs, especially when water or foreign matter in the vicinity of the wedge occurs. The tensile stress is sharply lowered, which means that the strand may even break. Therefore, the sleeve should be used in order to safeguard this part. The sleeve and the sheathing should overlap at least 100 mm (ACI 423.6, 2001; ACI 423.7, 2014). The minimum thickness is 1.27 mm (ACI 423.6, 2001).

2.1.7 Encapsulation

Previously, encapsulation system was applied in environments that were vulnerable to corrosion. Since 2014 implementing this system to all anchorages, when designed for ACI 318 and ACI 350 (ACI 423.7, 2014), was made mandatory. For these anchorages, hydrostatic tests should be confirmed, as detailed in Section 2.2.

2.2 Code Provision and Specifications for Performance Tests

Table 2-4 shows the types of performance tests offered by each country's regulations (Cho and Kang, 2018b). In Korea, the anchor test methods ensure compliance with KCI-PS101, which is the appendix No. 15 of KCI (2010). A static load test, fatigue test, and load transfer test are required. This regulation is modified based on the European specification, ETAG 013 (2002), which also requires the above three tests to be performed as deemed necessary. Moreover, it provides additional performance test methods for frictional coefficient, horizontal displacement, electrical resistance, as well as water tightness so as to facilitate its performance as necessary.

Contrastingly, U.S. regulations only mention static and fatigue tests, wherein load transfer tests are not presented as test items. ACI 423.7 (2014) follows the test method of ICC-ES AC303 (2011). ACI 350 (2006) is required to follow the test methods of ACI 423.3R (1996) and ACI 301 (1989). ACI 318 (2019) refers to ICC-ES AC303, ACI 423.3R, and ACI 301. ACI 423.3R (1996) has been amended to ACI 423.3R (2017), with ACI 423.6 (2001) mentioning static load testing and fatigue testing as well. Additionally, ACI 423.7 (2014) proposes a hydrostatic test method to verify the waterproof performance of encapsulated anchor using an unbonded tendon.

Table 2-4 Types of performance tests (Cho and Kang, 2018b)

	Static load test	Fatigue test	Load transfer test	Hydrostatic test
KCI-PS101 (2010)	○	○	○	
ETAG 013 (2002)	○	○	○	
ACI 301 (2016)	○			
ACI 318 (2019)	○	○		
ACI 350 (2006)	○			
ACI 423.3R (2017)	○			
ACI 423.6 (2001)	○			
ACI 423.7 (2014)	○	○		○
ICC-ES AC303 (2011)	○	○		

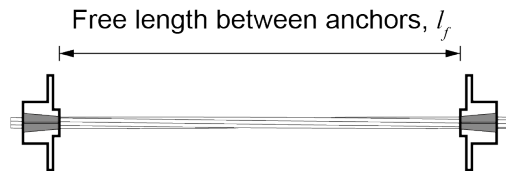
2.2.1 Static Load Test

Specimen

In ACI 318 (2019), Section R25.8.1, the static load test of anchorages aims to ensure compliance with ICC-ES AC303 (2011), according to which the distance between the anchorages at both ends is at least 1,067 mm.

Furthermore, Section R25.8.3 of ACI 318 (2019) refers to the static load test method of ACI 423.3R (2014), according to which the minimum distance between the anchorages at both ends is 1,100 mm. Meanwhile ACI 423.6 (2001) and ACI 423.7 (2014) specify a minimum distance of 1,100 mm. It is different from 1,067 mm of ICC-ES AC303 (2011) and occurs in converting 3.5 ft, which has been found to be the same in every specification, namely, SI units in each document.

Table 2-5 Comparison of minimum length between anchorages



Specification	Minimum l_f
ICC-ES AC303 (2011)	1,067 mm (3.5 ft)
ACI 423.3R (2017)	
ACI 423.6 (2001)	1,100 mm (3.5 ft)
ACI 423.7 (2014)	
KCI-PS101 (2010)	3,000 mm (10 ft)
ETAG 013 (2002)	

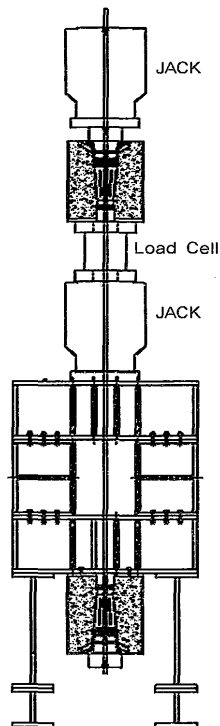


Figure 2-3 Example specimen for static load test (ETAG 013, 2002)

ACI 350 (2006), Section R18.21.3, refers to the static load methods in ACI 423.3R (1996) and ACI 301 (1989). On the other hand, no changes are observed in ACI 423.3R (1996) and ACI 423.3R (2017) when it comes to identifying yield strength, tensile strength, and final elongation. However, it is notable that the minimum distances between the two anchorages are different. For example, 3,000 mm (10 ft) in ACI 423.3R (1996) changed to 1,100 mm (3.5 ft) in ACI 423.3R (2005, 2017). ACI 301 (1989) is replaced by ACI 301 (2016) so that components of unbonded tendon systems are ensured compliance with ACI 423.7 (2014).

Both KCI-PS101 (2010) and European code, ETAG 013 (2002), do not specify the length of the entire specimen but point out that strand's free length should be at least three meters long. The total number of tests is mentioned only in ETAG 013 (2002) and is five for a static load test.

The distance suggested by each criterion is illustrated in **Table 2-5**. Although the shape of the test specimen is not explicitly defined, an example specimen is provided in KCI-PS101 (2010), as shown in **Figure 2-3**.

Loading

According to ICC-ES AC303 (2011), the initial tensile force, whose purpose is to prevent the wedge from falling before the test, should not exceed 4.45 kN. The tensioning speed should be between 5.0 and 22.5 mm/min. According to ACI 423.7

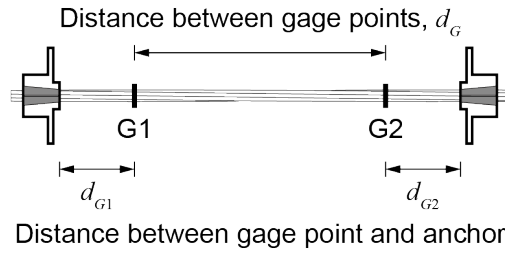
(2014), the anchorage should be able to withstand 95% of the tensile strength of the strand. Importantly, the load should be applied to satisfy the condition. Meanwhile other U.S. regulations do not entail specific methods or restrictions.

Contrastingly, ETAG 013 (2002) presents a specific method. The tendon is tensioned at one end in steps corresponding to 20%, 40%, 60% and 80% of the characteristic tensile strength of the tensile elements, f_{pk} . The load gets increased at a constant rate that corresponds to about 100 MPa/min. The load is transferred from the equipment to the anchorage and test rig at the 80% level.

Loads should be maintained with a maximum tolerance of 2%. It is necessary to adjust the load measured in the jack for estimated friction losses in the anchorages so as to assure that the specified load has been applied to the anchor head that is used for measurement.

KCI-PS101 (2010) offers a simplified method based on ETAG 013 (2002). Importantly, 10% of f_{pk} is applied as an initial tensile force and is about 26 kN (based on the 1,860 MPa strand with 15.2 mm diameter), which is greater than ICC-ES AC303 (2011). The displacement meters are installed, and the after-process remains the same as ETAG 013 (2002).

Table 2-6 Checklist for static load test



	Yield strength	Tensile strength	Fracture	Min. d_G	Min. d_{G1}, d_{G2}	Elongation
ICC-ES AC303 (2011)				914 mm (3 ft)	76 mm (3 in.)	
ACI 423.3R (2005)	Check	Check	Not less than $0.95f_{pu}$	900 mm (3 ft)	75 mm (3 in.)	Not less than 2%
ACI 423.6 (2017)				915 mm (3 ft)	75 mm (3 in.)	
ACI 423.7 (2014)						

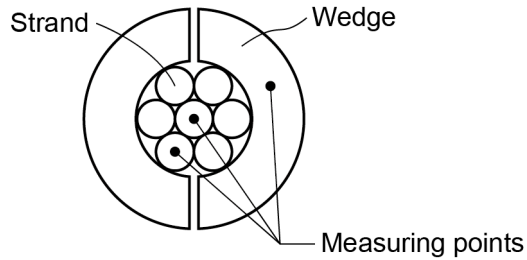


Figure 2-4 Measuring points for displacements

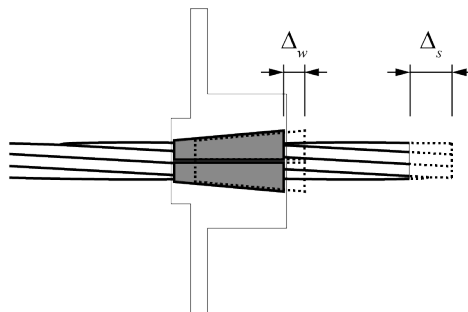


Figure 2-5 Displacements during testing

Measurements

U.S. regulations (ACI 423.3R, 2017; ACI 423.6, 2001; ACI 423.7, 2014; ICC-ES AC303, 2011) mandate a static load test to determine the yield strength and tensile strength of tension members. Additionally, the strength at break must not be less than 95% of the strand's tensile strength. However, it does not mean that the strand must be strained to break. Even in the absence of a break, it is evident that the strength at break exceeds the maximum load.

The maximum elongation of the strand is supposed to be at least 2%. Elongation is measured at two points in the free length between the anchorages. **Table 2-6** shows the conditions for the distance between two measuring points, d_G , as well as the distance from each point to the anchorage, d_{G1} and d_{G2} . Depending on the standards, the suggested distances are known to vary slightly. Nevertheless, they have the same value in the USCS unit, which appears to be a problem caused by its conversion into SI units. The distance between two anchors and the free length can be inferred by the sum of d_G , d_{G1} and d_{G2} . As far as the USCS unit is concerned, the sum is the same as the free length, whereas the difference in the SI unit is 1 to 50 mm.

On the other hand, the elongation measuring points are not mentioned in KCI-PS101 (2010) and ETAG 013 (2002). However, they do require more detailed data as compared to U.S. specifications. Displacements are measured at three points at the fixed end (**Figure 2-4**); core wire, a wire of the six helical wire, and a piece of the

wedge pieces. Relative load- and time-dependent displacements Δ_s and Δ_w with respect to the anchorage (**Figure 2-5**) are required as well.

During the course of one hour at $0.8f_{pk}$, it is important for the measured displacements to be stable within the first 30 minutes, which, in turn, signifies the fact that the strand and wedge are settled at the anchor. Otherwise, it can be inferred that the wedge and the strand are not entirely settled. There is a possibility of the strand sliding from the wedge, or the wedge falling out of the anchor.

The maximum load and elongation will be checked at the breaking after an hour. Additionally, the location and failure mode of the strand are recorded using photographic documentation or comments.

The anchor should be taken out of the specimen and visually checked after performing the test. The anchor should not be broken. However, the wedge may be partially broken, depending on the specific attributes of the product or the surface condition of the anchor.

2.2.2 Fatigue Test

Specimen

According to ACI 318 (2019), the static load test and the fatigue test are in compliance with the method of ICC-ES AC303 (2011). The distance between both

anchorage should be at least 914 mm (3 ft). Details of cyclic loading tests in ACI 318 (2019) find mention in ACI 423.3R (2005) and ACI 301 (1989). In ACI 423.3R (2005), the free length l_f is not less than 900 mm (3 ft), whereas it is not described by ACI 301 (1989). On the other hand, ACI 423.6R (2001) and ACI 423.7 (2014) require at least one meter (**Table 2-7**).

ACI 350 (2006), Section R18.21.3, refers to Section 4.1.3 of ACI 423.3R (1996) and Section 15.2.2 of ACI 301 (1989). As mentioned above, the minimum free length is 900 mm in ACI 423.3R (2005), but ACI 423.3R (1996) does not specify it since “the specimen used for the static load test in Section 4.1.3.1 does not need to be the same that is used for the fatigue test.” Thus, it can be inferred that the specimen length of the fatigue test is also at least 3.0 m (10 ft).

According to U.S. regulations, the minimum distances appear to be different, but they remain the same at 3 ft in USCS units. The difference can be up to 100 mm, but this is an error caused by the conversion of USCS units into SI units.

ETAG 013 (2002) requires a test specimen of 3 m. While PTI (2006) and KCI-PS101 (2010) do describe the test method, they do not mention the length of the specimen.

Table 2-7 Minimum free length between anchorages

Specification	Minimum l_f
ICC-ES AC303 (2011)	914 mm (3 ft)
ACI 423.3R (2017)	900 mm (3 ft)
ACI 423.6 (2001)	1,000 mm (3 ft)
ACI 423.7 (2014)	1,000 mm (3 ft)
ETAG 013 (2002)	3,000 mm (10 ft)

Loading

There are two types of fatigue tests defined in the U.S.; 50 cycles and 500,000 cycles (**Table 2-8**). One cycle entails a change from the lower stress level to the upper stress level and back to the lower. The sinusoidal loading function helps ensure a smooth connection (ICC-ES AC303, 2011). The 50-cycle test with a high stress range aims to simulate the effect of a severe earthquake on the tendon. The 500,000-cycle test with a low stress range simulates the tendon behavior due to service loads and vibrations that may occur in a commercial building (ACI 423.6, 2001). Otherwise, tendons in prestressed concrete structures do not typically experience cycling stresses, which cause fatigue problems.

The load range of 50 cycles is 40 to 80% of the minimum specified tensile strength (ACI 423.3R, 2017; ACI 423.6, 2001; ICC-ES AC303, 2011; PTI, 2006). Importantly, only ACI 423.7 (2014) has a more conservative range, 40~85%. ICC-ES AC303 (2011) curtails the cycling speed to 1 ~ 3 Hz. As many as 500,000 cycles have a stress range of 60 ~ 66% of minimum specified tensile strength (ACI 423.3, 2017; ACI 423.6, 2001; ACI 423.7, 2014; ICC-ES AC303, 2011; PTI, 2006).

ETAG 013 (2002) and KCI-PS101 (2010) have suggested the 2,000,000-cycle test. The range is 80 MPa, with the highest stress of the cycle being 65% of the nominal tensile stress. The cycle is designed to be fast at 1 to 10 Hz. Whereas, the load range of 80 MPa can be replaced with the range from 60.7 to 65% for the most commonly used strand with 1,860 MPa.

Table 2-8 Fatigue test methods

	Test 1			Test 2		
	Number of cycles	Loading range	Speed	Number of cycles	Loading range	Speed
ICC-ES AC303 (2011)			1 ~ 3 Hz			1 ~ 10 Hz
ACI 423.3 (2005)	50	40 ~ 80% of f_{pu}	-	500,000	60 ~ 66% of f_{pu}	-
ACI 423.6 (2001)						
PTI (2006)						
ACI 423.7 (2014)		40 ~ 85% of f_{pu}				
KCI-PS101 (2009)	2 million	80 MPa (0.65 f_{pk} at peak)	≤ 10 Hz			-
ETAG 013 (2002)						

When the magnitudes of load ranges are expressed in % and MPa, 50 cycles, 500,000 cycles, and 2,000,000 cycles denote 40% (744 MPa), 6% (111.6 MPa), and 4.3% (80 MPa), respectively, based on the 1,860 MPa strand. The size of the range gradually decreases as the number of cycles increases.

Measurements

According to U.S. specifications, fatigue tests only need to confirm that specimens are capable of withstanding cyclic loading without the failure of either the strand or the anchor.

Specific data are required by KCI-PS101 (2010) and ETAG 013 (2002). Relative displacements, Δ_s and Δ_w , are measured during the test, as shown in **Figure 2-5**. The deformation of anchorage components is noted after the test is checked, whereas the fracture location of the tensile element gets recorded after its failure.

2.2.3 Load Transfer Test

Specimen

U.S. regulations do not include the load transfer test. Only ETAG 013 (2002) and KCI-PS101 (2010) are present, and they both have an identical test method. According to ETAG 013 (2002), the load transfer test must be conducted on at least four occasions.

The specimen is illustrated in **Figure 2-6**. The height of the specimen h should be at least twice the length of the two sides, a and b . Sections from the bottom of the specimen to a half of the height should not be subject to reinforcement details, with the exception of basic reinforcing bars, which are auxiliary to resist the bursting effect. It does not need technical approval in case the following conditions are met: Total cross-section of longitudinal bars is not more than 0.3 percent of the concrete section, whereas the weight of uniformly distributed stirrups is not more than 50 kg per cubic meter of concrete.

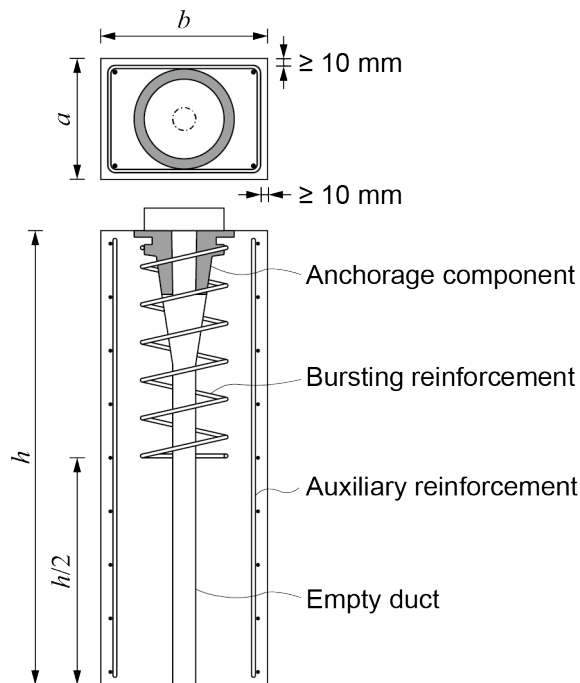


Figure 2-6 Specimen of load transfer test

After pouring concrete, the specimen molds are removed one day later, subsequent to which wet curing is performed. It minimizes the cracks by the concrete shrinkage and helps facilitate an accurate measurement of the crack width and strain during the test.

Loading

The load is applied to anchorages, not concrete, up to 80% of the nominal tensile strength. Subsequently, cyclic loads are applied between $0.12f_{pk}$ and $0.8f_{pk}$. The number of cycles should be at least ten until the stabilization criteria are met, which

in turn are premised on concrete strain and crack widths that are measured in both longitudinal and transverse directions on at least two sides. The compressive deformation of concrete is measured in the longitudinal direction, whereas the crack width is measured in the lateral direction. The strain (ε) and the crack width (ω) that are to be ascertained during the experiment are used in the following stabilization formula.

$$\omega_n - \omega_{n-4} \leq \frac{1}{3}(\omega_{n-4} - \omega_0), \quad n \geq 10 \quad (2-4)$$

$$\varepsilon_n - \varepsilon_{n-4} \leq \frac{1}{3}(\varepsilon_{n-4} - \varepsilon_0), \quad n \geq 10 \quad (2-5)$$

where n denotes the number of cycles on at least ten occasions.

After satisfying both **Eqs. (2-4)** and **(2-5)**, the load is applied up to the specimen fracture. As the cyclic loading progresses, the increasing rate of the strain and the crack width decreases gradually (**Figure 2-8**). This, in turn, implies that the interaction between the anchorage, the reinforcement, as well as the concrete is stabilized. Cyclic loads of not less than ten times are sufficient enough to adequately damage the specimen and to gain the crack width/strain in a conservative manner.

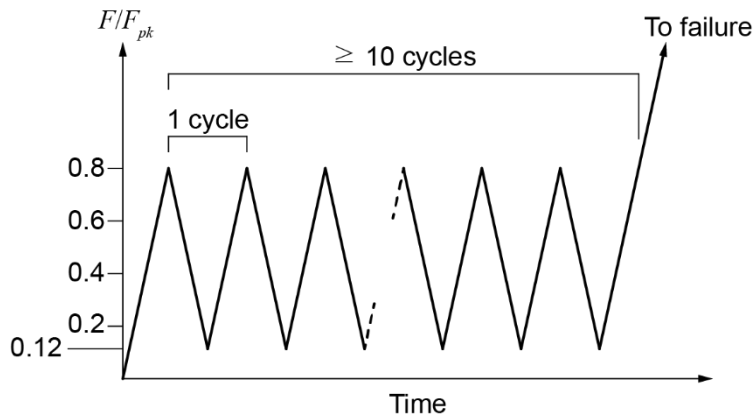


Figure 2-7 Loading history of load transfer test

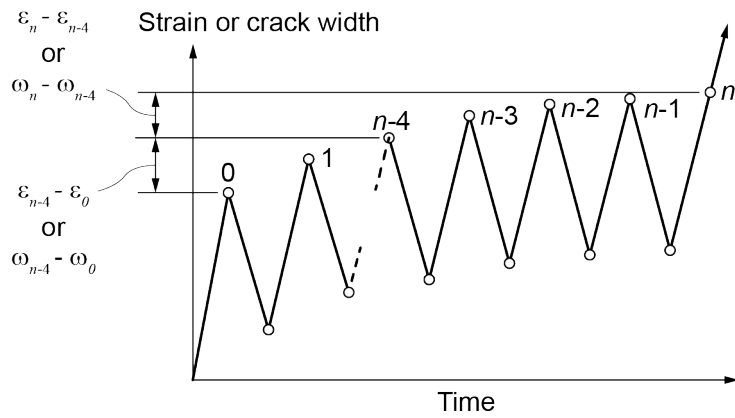


Figure 2-8 Strains and crack widths for stabilization formula

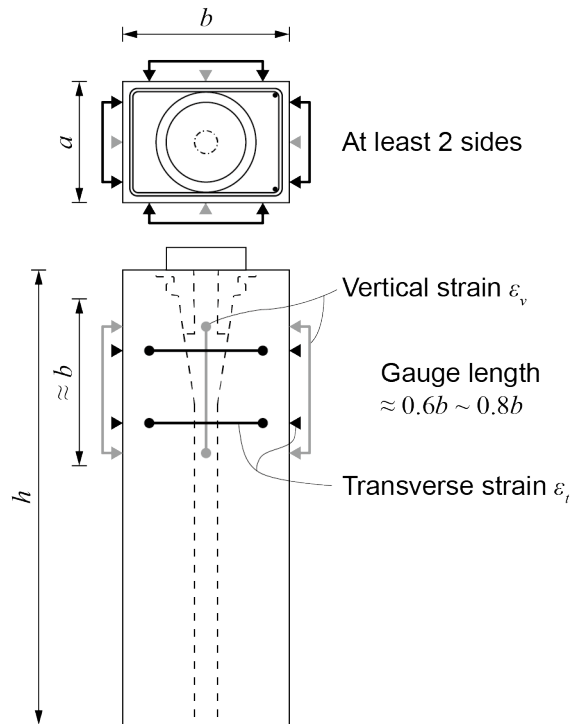


Figure 2-9 Measuring set-up for load transfer test

Measurements

As mentioned above, the crack width and strain are measured on at least two sides, which is illustrated in **Figure 2-9**. The values are used in the stabilization formula.

KCI-PS101 (2010) requires the limitation of the crack widths at several points. The maximum crack width should be 0.15 mm or less when the first $0.8f_{pk}$ after which the last $0.12f_{pk}$ are reached. At the last $0.8f_{pk}$, it should be 0.25 mm or less. The maximum crack width over the limit implies that the specimen is weak in terms of bursting force. In such cases, the reinforcement for anchorage zone should be increased or the bearing area of the anchor should be enlarged.

2.2.4 Hydrostatic Test

In the past, watertight tests were carried out for extreme environments (ACI 423.6, 2001). However, ACI 423.7 (2007) was revised in 2014 to ensure that the use of an encapsulation system is required when ACI 318 and ACI 350 are applied (ACI 423.7, 2014).

Specimen

Representative anchorage from production runs, selected and assembled by the manufacturer, should be used for testing purposes. Stressing, intermediate, and fixed anchorage assemblies should be tested individually.

ACI 423.6 (2001) and ACI 423.7 (2014) suggest the same conditions for detecting the presence of moisture. Three tests are necessiated for each assembly. Pigment is added to the post-tensioning coating, whereas a colored dye is mixed in the water to contrast with the white color of the post-tensioning coating.

Loading

ACI 423.7 (2014) set the minimum uniform hydrostatic pressure, f_h , as the following equation:

$$f_h \geq \begin{cases} 8.6 & \text{kPa (governed by ACI 318)} \\ 68.8 & \text{kPa (governed by ACI 350)} \end{cases} \quad (2-6)$$

In ACI 423.6 (2001), Section R2.2.6.1, and PTI M10.2 (2017), Section 2.2.6, the pressure is found to be at least 8.6 kPa throughout the specimen. Considering the worst case of beams or slabs, it is found to correspond to a water pressure of about 1 m (3 ft). More rigorous testing is required for the structures having above one-meter water pressure, such as in swimming pools, water tanks, basement beams, and slabs.

According to ACI 350 (2006), Section 18.16.3, unbonded single-strand tendon systems are subjected to a watertight test in accordance with the test method of ACI 423.6 (2001), albeit with a water pressure of 70 kPa rather than 8.6 kPa. According to Section 18.16.4, unbonded single-strand tendons should comply with the “aggressive environment” chapter of ACI 423.6 (2001). The duration of test is 24 hours (ACI 350, 2006; ACI 423.6, 2001; ACI 423.7, 2014).

Measurements

After 24 hours, it is important to remove the encapsulation system, after which the color of the coating should be noted (ACI 423.7, 2014). Moreover, while colored dye should not be found inside the encapsulation system, it is indeed permissible on the white grease (ACI 423.6, 2001; ACI 423.7, 2014).

2.3 Previous Studies on Anchor

2.3.1 Existing Anchors

The sizes of post-tensioned anchors sold by major companies are listed in **Table 2-9** (Alga, 2001; Amsysco, 2010; DSI, 2004, 2009; ICC-ES, 2018, 2019; PHI, 2016; VSL, 2015; WJE, 2006). In an endeavor to distinguish the characteristics of each product, the product names are redefined in the following manner: The first letter signifies the first letter of each company name; 12 and 15 represent strand diameters of 12.7 mm and 15.2 mm, respectively, and 12/15 can be used in conjunction with each other. The alphabet following the number represents a separate feature. T and E indicate two (double) bearing plate system and encapsulated system, respectively. O refers to the anchor having optimized height. G means that the gusset locates below the bearing plate.

Companies are largely based in the United States or Europe. In the United States, unbonded post-tensioning method has been preferred, which is evidenced in the fact that companies such as GTI and Hayes International were already using encapsulation systems before 2014. On the other hand, the bonded post-tensioned system using grouting was preferred in Europe. However, Freyssinet, DSI, and VSL also released encapsulated products after 2014 to satisfy ACI 423.7 (2014). Alga also forms part of the Soletanche-Freyssinet group and uses the same products as Freyssinet.

Table 2-9 Size of existing anchors

Company	Product	Strand size [mm]	Height [mm]	Bearing Plate		
				Length [mm]	Width [mm]	Area [mm ²]
Precision-Hayes International	P12	12.7	38.1	127.0	57.2	7,264.4
	P12O	12.7	33.0	127.0	57.2	7,264.4
	P15	15.2	40.1	148.1	75.9	11,240.8
Amsysco	A12	12.7	38.1	127.0	57.2	7,264.4
	A15	15.2	41.4	149.4	76.2	11,384.3
	A12E	12.7	38.1	133.4	63.5	8,470.9
	A15E	15.2	44.5	155.7	85.9	13,374.6
DSI	D12	12.7	-	127.0	57.2	7,264.4
	D12/15	12.7	-	130.0	55.0	7,150.0
		15.2	-			
	D15T	15.2	110.0	105.0	75.0	7,875.0
	D12E	12.7	-	131.6	62.7	8,251.3
	D15E	15.2	-	153.2	81.3	12,455.2
Freyssinet, Alga	F12/15	12.7	86.0	130.0	70.0	9,100.0
		15.2				
VSL	V12	12.7	38.1	127.0	57.2	7,264.4
	V12G	12.7	63.5	127.0	57.2	7,264.4
	V15	15.2	47.8	117.6	88.9	10,454.6
	V15T	15.2	110.0 95.0	104.9	74.9	7,857.0
	V15E	15.2	70.0	122.0	94.0	11,468.0

Overall, it can be seen that the anchors using $\text{Ø}15.2$ mm strand are larger in size than using $\text{Ø}12.7$ mm strand since the prestressing force is proportional to the diameter. The average dimensions of the anchors using $\text{Ø}12.7$ mm and $\text{Ø}15.2$ mm are as follows: $129 \text{ mm} \times 59 \text{ mm} \times 48 \text{ mm}$ and $131 \text{ mm} \times 76 \text{ mm} \times 69 \text{ mm}$, respectively.

P12O reduced the height of P12 by about 5 mm. Since the D15T and V15T have two bearing plates, the size of the main bearing plate is smaller than the other products. However, its height is more than twice as much. The dimensions of the sub bearing

plate are not presented, which means that the main bearing plate is taken into consideration when estimating the bearing plate area. Typically, gussets are above the bearing plate, while V12G has gussets below the plate. It is inefficient because the gusset is in tension under prestressing, which is why the anchor height should be increased to compensate for this.

In the case of applying encapsulation, the total sizes of the bearing plate are increased. Considering the fact that the thickness of the plastic cover is about 2~3 mm, it can be inferred that the casting size is the same as the other bare anchor of that company. Although not shown in **Table 2-9**, other types of post-tensioned anchorages also exist. An anchor using $\text{Ø}15.2$ mm strands with 2,400 MPa was used by Kim (2018). Additionally, Kim et al. (2019) used an anchor with a circular bearing plate for the experiment.

2.3.2 Ductile Cast Iron

Casting of the anchor is commonly made of ductile cast iron, one of three classes of cast iron. Ductile cast iron is applied extensively in constructive and automobile industries (Kasvayee, 2015). Anchors are typically made of Grade 80-55-06 of ASTM A536 (1984) or GCD400~600 of SPS-KFCA-D4302-5016 (2017).

Cast irons are primarily classified into three classes by graphite morphology (**Figure 2-10**); lamellar graphite iron (LGI, flake graphite iron, gray cast iron), compacted

graphite iron (CGI, vermicular graphite cast iron), as well as spheroidal graphite iron (SGI, nodular cast iron, ductile cast iron). Graphical illustrations of tensile stress-strain curves for those three types of cast irons (Svensson and Salomonsson, 2018) are shown in **Figure 2-11**.

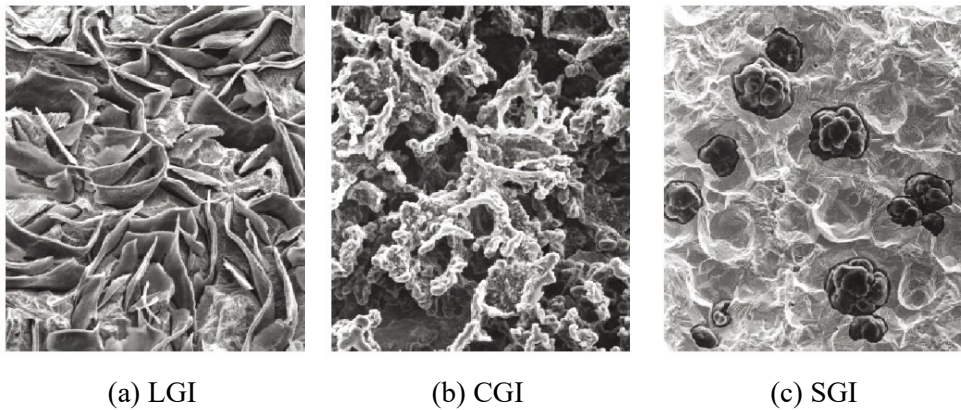


Figure 2-10 Microstructure of cast irons (Berglund, 2011)

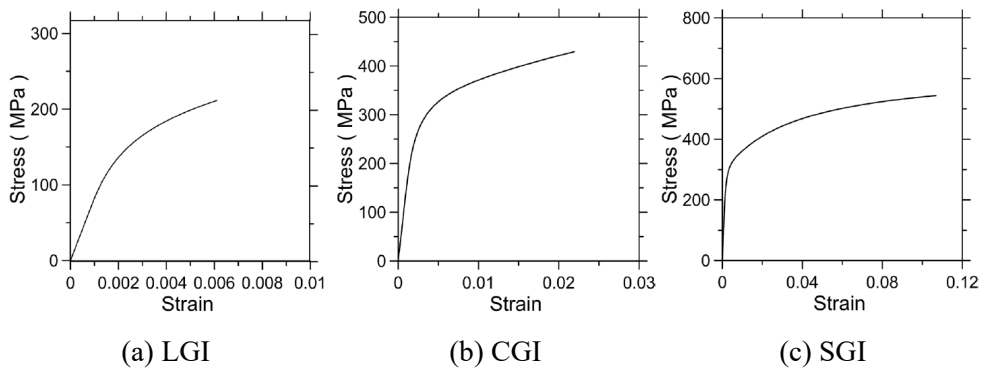


Figure 2-11 Tensile stress-strain curves for cast irons (Svensson and Salomonsson, 2018)

Corrosion resistance is better than with gray cast iron (Grilec et al., 2010). Unalloyed cast irons generally exhibit good resistance to alkalis. In calm seawaters, the corrosion resistance of cast iron is not greatly affected by the presence of crevices. However, intermittent exposure to seawater is very corrosive to unalloyed cast irons (Cramer and Covino, 2005).

Graphitic (gray and ductile) cast iron has the greatest fluidity and the least shrinkage (less than 1%) of any ferrous metal. This allows products to be made to exact dimensions much more easily using ductile cast iron, posing very few challenges in obtaining pressure tightness.

In addition, cast irons have good welding capability (Pascual et al., 2009) and are more machinable than cast steels (Chiang et al., 2007). They are also relatively more wear-resistant due to the self-lubricating behavior of graphite (Lampman and DiMateo, 1996; Unkic et al., 2008). It is possible to reduce the costs by 30 to 40% relative to cast steel (Kasvayee, 2015; Lampman and DiMateo, 1996).

2.3.3 Encapsulation

Krauser (2007) summarized the criteria for encapsulation systems required by ACI and PTI. Correspondingly, Khosa (2010) reported that the material and labor costs for encapsulation system had been reduced and emphasized the long-term corrosion protection effect of this system.

However, with the exception of the anchor developed in this study, no encapsulation application case or research has been found for post-tensioned anchor using a single-strand.

2.3.4 Existing Wedges

Information on wedges is limited compared to anchors. Maximum length and diameter of the wedge are proportional to the diameter of the strand. Sufficient length of teeth should be secured in order to grip the prestressed strand, and sufficient thickness is needed to sustain the force without distortion.

Taper angle serves to transfer the prestressing force through the wedge to the anchor. The taper angles of P12 and D15T are 7.5° and 7.0° , respectively (**Table 2-10**). It can be determined that P12O with a wedge length smaller than P12 will have a taper angle greater than 7.5° , while that of P15 is smaller than 7.5° based on the ratio of the length and the diameter.

Table 2-10 Size of existing wedges

Company	Anchor	Max. strand size [mm]	Max. wedge length [mm]	Max. wedge diameter [mm]	Taper angle [°]
Precision-Hayes	P12	12.7	33.0	25.4	7.5
	P12O	12.7	30.5	25.4	-
International	P15	15.2	40.6	28.4	-
DSI	D15T	15.2	45.0	29.0	7.0

2.4 Previous Studies on Performance Tests

While Section 2.2 addressed the criteria related to anchorage performance tests, this section examines extant studies about performance tests. Unlike the multistrand system, relatively few performance tests have been performed on post-tensioned anchors using single-strand so far.

Performance tests for the anchor developed in this dissertation are also included in other papers written by the author (Cho et al., 2015; Cho and Kang, 2017, 2018a; Kang et al., 2015), although they are excluded from this section because they are covered in greater detail in other chapters.

2.4.1 Static Load Test

WJE (2006) conducted three static load tests for each anchorage and coupler setup. The minimum strand length was 1,448 mm. Similarly, the maximum load for all setups was above 176.6 kN, which exceeds 95% of tensile strength of Ø12.7 mm strand (173.9 kN).

Walsh and Kurama (2009) performed monotonic testing of unbonded PT systems using casting and barrel anchors. According to ICC-ES AC303 (2007), the free length between anchors was 1,829 mm and a preload of 3.34 kN was applied. Instead

of verifying the performance of a particular anchorage, they examined the effects of each condition by changing the types of anchorage or wedge.

2.4.2 Fatigue Test

WJE (2006) performed 50 cycles and 500,000 cycles with cycle frequencies of 2 and 6 Hz, respectively. The stress ranges were found to be between 40 to 85 percent for 50 cycles, and between 60 to 66 percent for 500,000 cycles. Strand minimum length was the same as static load test specimen (1,448 mm)

Walsh and Kurama (2009) ran three fifty-cycle fatigue tests in accordance with ICC-ES AC303 (2007). The loading speed was found to be 0.056 mm/mm/min. However, 500,000-cycle test was not conducted.

2.4.3 Load Transfer Test

The load transfer test is a test that verifies the performance of reinforcement details of the anchorage zone. Anchors using single-strands, which are commonly used in building post-tensioning system, are frequently used in the U.S., although it is not essential to conduct load transfer tests. Unlike the multistrand anchorage used for bridges, the safety details can be expected only with the reinforcement details

presented by PTI (2006) without carrying out additional performance tests. Therefore, while many load transfer test studies have been conducted for multistrand anchorage according to ETAG 013 (2002), no transfer test study has been conducted for anchorage using a single-strand.

Kim et al. (2018) used circular anchorage to verify the details of reinforcement for the anchorage zone. It was not a load transfer test but a static compression test, and five specimens with three anchors each were used. In the experimental results, when the concrete compressive strength is less than 17.5 MPa, an additional reinforcement is required.

2.4.4 Hydrostatic Test

Hayes Industries (2014) conducted the watertight test in accordance with PTI (2010). The water tightness was verified at the pressure of 44-inch H₂O pressure, which is 11.0 kPa, 2.4 kPa higher than the reference (8.6 kPa).

PSI (2015) performed the test under 68.8 kPa for a duration of 24 hours. The report claims to satisfy ACI 423.7 (2007), but this appears to be misleading. ACI 423.7 (2007) provides a pressure of 8.6 kPa, whereas ACI 350 (2001) Section 18.14.3 specifies that testing should be conducted at 103.2 kPa or higher. Therefore, PSI (2015) fails to meet both criteria. Based on the test pressure, PSI (2015) seems to be examined following ACI 423.7 (2014) that is governed by ACI 350 (2006).

Chapter 3. Design of Post-Tensioned Anchor

This chapter elucidates the design process of the post-tensioned anchor using a single-strand. Rather than imitating existing products, the design in this study was optimized through finite element analysis. The anchor is a single casting, which can be sectioned into three parts: a tubular body, a bearing plate, and gussets. The location and shape of each element are analyzed as variables. The overall size of the anchorage is proportional to the size and strength of the strand. In addition to using the strength of 1,860 MPa, two size-types of unbonded strands are also commonly used in buildings; $\text{Ø}12.7$ mm and $\text{Ø}15.2$ mm. Recent construction norms in Korean PT entails the use of a 15.2mm diameter unbonded tendon. For this reason, an anchor using a 15.2mm diameter unbonded single-strand was designed.

In this study, ABAQUS 6.10, a finite element analysis program, was used. Structural optimization was performed after considering its shape, strength, and weight. The design was completed simultaneously, thus reflecting the product fabrication and construction process.

All PT anchors that are governed by either ACI 318 (2019) or ACI 350 (2006) should be applied with encapsulation in accordance with ACI 423.7 (2014). Although it is not reflected in Korean regulations, developed bare anchor was improved into the encapsulated anchor in order to have better long-term durability. The casting of bare

anchors was redesigned in order to consider the method of assembling accessories and the plastic cover.

3.1 Modeling

3.1.1 Wedge Selection

The wedge requires advanced technology, such as treads, material strength, and heat treatment. Since wedge production is not aligned with the purpose of this study, ready-made products were used.

According to Leonhardt (1964), when the wedge taper angle is within 5.7° to 6.33° , it yields effective results. On the other hand, Walsh and Kurama (2010) experimentally confirmed that the optimal angle at the wedge thickness of 13.9 mm for the 15.2 mm strand was 8.10° . In **Table 2-10**, it can be seen that the angles of existing wedges for PT anchors are within $7 \sim 7.5^\circ$. Therefore, when selecting the wedge, it was considered whether a taper angle is between 6° and 8° .

In order to reduce the cost, domestic wedges for $\text{Ø}15.2$ mm strand produced by Shinsung PC, Inc. were selected. Its taper angle is 6.47° . This recyclable wedge is for the pre-tensioning method. Although it is impossible to reuse the wedge in the post-tensioning system due to the construction method (buried in the concrete member), the reason why the wedge was selected because it was found to satisfy both performance and price competitiveness.

3.1.2 Tubular Body

The tubular body denotes the main part where the strand and wedges are settled and the tensile stress gets transmitted. It has a hole whose shape resembles that of a truncated cone. The strand can pass through a smaller hole. After the wedge bites the strand, it gets fixed on the sloped side of the hole. The wider the contact area, the less distributed the stress. Therefore, the shape of the inside body must be considered as the wedge shape.

The initial model of the tubular body follows the shape of the existing barrel anchor using the selected wedge (**Figure 3-1**). Given that the slope of the hole assumes significance, it was set as immutable even if the design of the anchorage was altered in the subsequent optimization process.

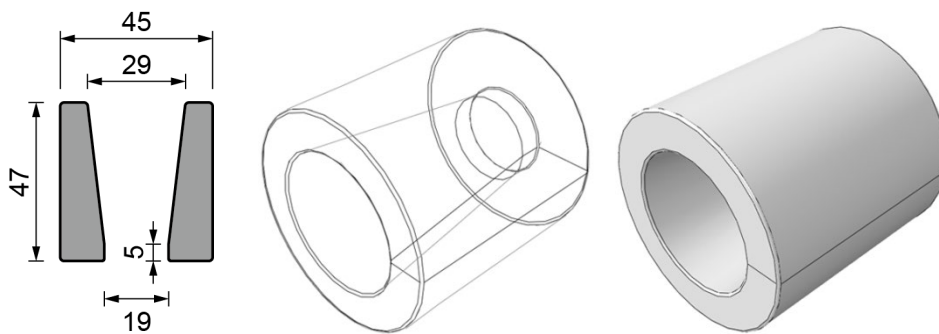


Figure 3-1 Initial model of tubular body [unit: mm]

3.1.3 Bearing Plate

The bearing plate disperses and transfers the compressive force by the tensioned strand from the tubular body or gussets to the concrete. This concrete could be easily obliterated if a barrel anchor with a small bottom area is used. The plate serves to extend the bearing area in order to reduce the stress transmitted to the concrete.

Table 2-9 shows the size of the bearing plate of the existing anchors selling on the market. For the anchors using Ø15.2 mm strand, the length is 105 to 149 mm and the width is 55 to 89 mm, whereas the ratio of the length to the width is 1.40 to 2.36. D12/15 has the smallest size but the largest thickness of bearing plate. V15T has the shortest length, albeit with an additional small bearing plate. This double-plate anchor owns a large total bearing area, but is way too high and big.

The design length of the anchor was determined to be 125 mm, which is shorter than P12 and V12. Since the thickness of the slab has recently been minimized, the shorter length is deemed more advantageous. The width was determined to be 70 mm, which is the same as F12/15. Meanwhile the area of the anchor plate, A_b , is 8,750 mm², which is smaller than existing anchors for Ø15.2 mm strand, with the exception of D12/15, D15T, and V15T.

Assuming that the slab thickness d_{slab} is 200 mm, A_b' can be estimated regarding **Figure 3-2** when the anchorage is placed vertically and horizontally, where A_b' denotes the maximum area of portion of concrete anchorage surface that is geometrically similar to and concentric with the area of anchorage. The concrete

strength at jacking is set at 25 MPa, which is the minimum, as suggested by KCI (2010), Section 3.5.3. When the service load was applied, the concrete strength was found to be 35 MPa, which is commonly used for post-tensioned slabs.

Permissible compressive stress f_{cp} calculated by Eqs. (2-2) and (2-3) is illustrated in Table 3-1. Average bearing stress can be estimated by dividing the strand force P by the bearing plate area A_b . Meanwhile f_{cp} exceeds the average bearing stresses under both transfer and service loads. The conditions are met even at nominal tensile strength, the average bearing stress of 29.8 MPa.

Therefore, the length and width of the bearing plate were deemed appropriate. The initial thickness of the plate was assumed as 7 mm based on the average of other products. The thickness was optimized during the design process.

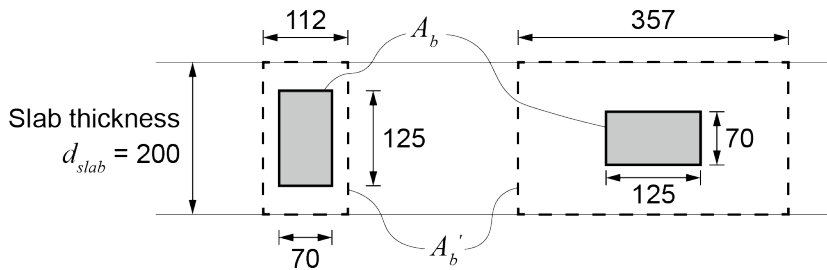


Figure 3-2 Bearing area [unit: mm]

Table 3-1 Permissible compressive stress and bearing stress [unit: MPa]

	Permissible concrete compressive stress, f_{cp}		Average bearing stress
	Horizontal	Vertical	
Transfer load	31.3	30.0	23.9
Service load	35.0	33.6	20.9

3.1.4 Materials

Generally, spheroidal graphite cast iron GCD 400~500 is used as the anchor material. However, GCD 500-7 was used in this study. According to SPS-KFCA-D4302-5016 (2017), GCD 500-7 must satisfy the tensile strength of 500 N/mm², yield strength of 320 N/mm², and elongation of 7%. The test results of three specimens are illustrated in **Table 3-2**.

In the analysis, the material yields at 400 N/mm², which accounts for 80% of the specified tensile strength, with the elastic modulus being 200,000 MPa. The Poisson's ratio ν is 0.3. The anchor may get deformed after yielding under excessive load. However, only elastic state is considered for safety purposes, and the stresses over 400 MPa are ignored from the analysis. The material property is defined as illustrated in **Figure 3-3**.

3.1.5 Load

The anchor must not be destroyed or largely deformed before reaching 95% of the nominal tensile strength of the strand (ACI 318, 2019). Considering the fact that the actual strength of the strand is larger than the nominal strength, the total input load for finite element analysis is set conservatively as $P_{pk} = 261$ kN.

Table 3-2 Measured material properties of GCD500-7

Properties	SPS-KFCA-D4302-5016 (2017)	Test results		
		1	2	3
Tensile strength [N/mm ²]	≥ 500	612	602	616
Elongation [%]	≥ 7.0	9.6	9.8	9.6
Brinell hardness	150~230	207	201	207

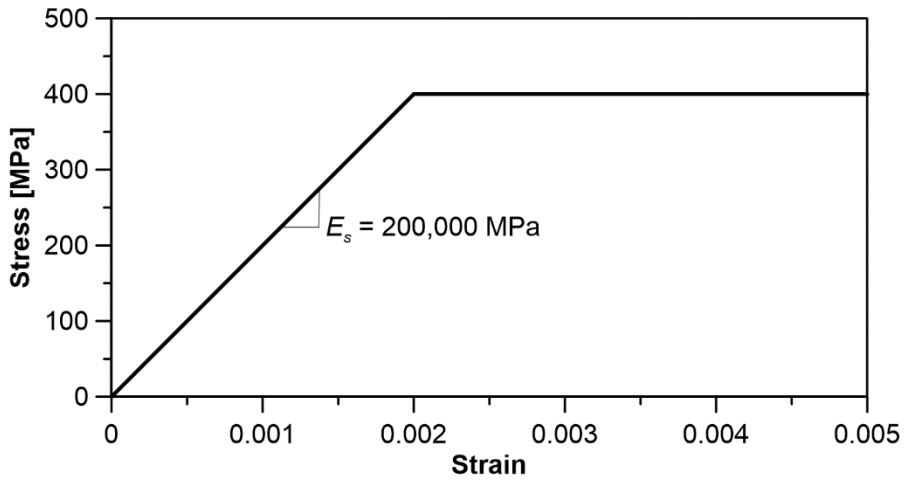


Figure 3-3 Material property of cast iron

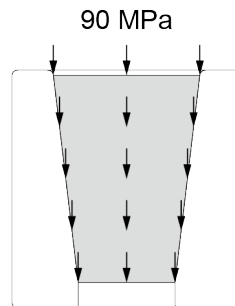


Figure 3-4 Applied loading

The prestressed load is transmitted from the wedge to the anchor through the surface where the wedge and anchor come into contact. The area of the wedge-contact surface is 2,872.6 mm², whereas the uniform stress is 90.86 MPa. Therefore, the analysis reveals that 90 MPa of surface traction is input to the entire wedge-contact surface with a direction parallel to the strand.

3.1.6 Boundary Condition

The post-tensioned anchor is embedded in concrete. The anchor does not move or rotate until the concrete begins to crack. However, an analysis reveals that if most of the outer surfaces are fixed, it is deemed advantageous for deformation and stress of the anchor. The fixed boundary condition is applied to the bottom surfaces of the tubular body and bearing plates in order to consider the deformation of the anchorage (**Figure 3-5**). In Abaqus, the boundary condition was set to “Encastre (U1 = U2 = U3 = UR1 = UR2 = UR3 = 0)”.

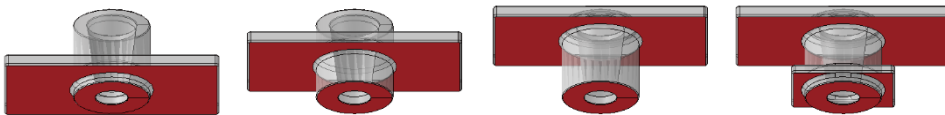


Figure 3-5 Boundary condition

3.2 Design through Finite Element Analysis

The objective is to design the anchor having minimum stress under the same load. The von Mises stress is a value that represents the magnitude of the torsional energy caused by the stress components at each point of the object, and is also known as a criterion for accurately predicting the destruction. Therefore, the design having the minimum of the maximum von Mises stress ($f_{v,max}$) is selected at each design step. Simultaneously, the practical reasons are considered in order to determine the design.

3.2.1 Location of Bearing Plate

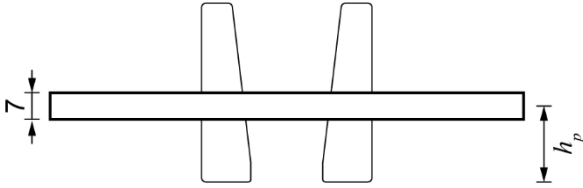
The location of the bearing plate relative to the wedge-contact surface is shown to have the greatest influence on the stress distribution. It may minimize the anchor size along with the casting amount. The wedge-contact surface is inclined for the wedge to settle in the cylinder body. The strand force is transferred diagonally inside the cylinder through the wedge. The bearing plate and the gusset resist the force spreading outward and change its direction that is parallel to the strand.

Table 3-3 shows analysis results when the bearing plate locates 8.5 mm, 23.5 mm, 40 mm from the bottom, respectively. It appears to be most effective when the bearing plate is in the middle of the cylinder body. The bearing plate at the bottom performs in a similar manner. With the bearing plate located at the top, the stress gets

concentrated at where the bearing plate and the cylindrical part meet. The maximum stress is significantly reduced when the square plate (60 mm × 60 mm) is added at the height of 8.5 mm.

The inclusion of gussets, which contribute to the dispersion of stress, changes the optimal position of the bearing plate. Since the gussets are located above the bearing plate, it is possible for the bearing plate to move slightly lower. Two gussets are triangular and have a thickness of 10 mm. The detailed form of gussets will be discussed later. According to **Table 3-4**, the maximum von Mises stress is the smallest when the height of the center of bearing plate, h_p , is 20 mm. In order to determine the detailed height, the stress is analyzed at 1 mm intervals in the range of 17 to 23 mm (**Table 3-5**). The selected height of 20 mm with the minimum value is where the wedge-contact area gets divided by 5:9. In subsequent analysis, it is revealed that the height of the wedge-contact area remains unchanged even if the length of the lower tubular part (not inclined) changes.

Table 3-3 Location of bearing plate [unit: mm]



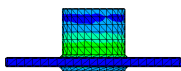
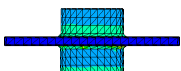
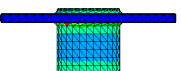
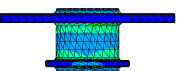
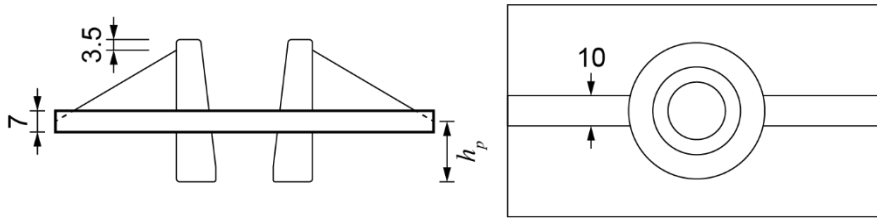
Location	Bottom (8.5 mm)	Middle (23.5 mm)	Top (40 mm)	Top & Bottom (40 & 8.5 mm)
				
$f_{v,max}$ [MPa]	229.3	223.5	281.1	225.4

Table 3-4 Location of bearing plate with gusset [unit: mm]



h_p [mm]	16.5	20	23.5	27	30.5
$f_{v,max}$ [MPa]	224.1	201.6	208.6	225.5	293.0

Table 3-5 Detailed location of bearing plate

h_p [mm]	16.5	17	18	19	20	21	22	23	23.5
$f_{v,max}$ [MPa]	224.1	229.7	210.4	208.4	201.6	206.5	232.0	245.6	208.6

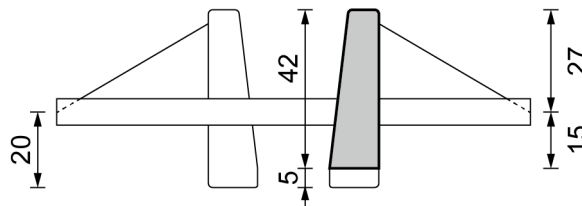


Figure 3-6 Location of bearing plate relative to wedge [unit: mm]

3.2.2 Shape of Tubular Body

Next, the external shape of the tubular body is taken into consideration (**Table 3-6**).

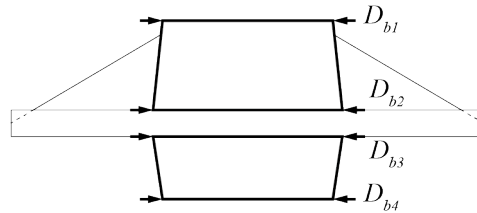
The body is divided into upper and lower parts based on the bearing plate, whereas the top and bottom diameters of each part are used as variables. The diameter ranges

from 45 mm to 55 mm, considering the size of the bearing plate, and has 5 mm intervals in consideration of the practicality of the manufacturing.

D_{b1} , which is the diameter of the uppermost section, is not found to significantly impact the stress distribution since it is above the position where the load is applied. D_{b2} is contacting the top of the bearing plate. As D_{b2} increases, the amount of upper body which acts like gussets increases as well, thus reducing the maximum stress. D_{b3} refers to a diameter where lower body contacts with the underside of the bearing plate. The smaller D_{b3} is, the larger the bottom area of the bearing plate. In other words, the more fixed parts are, the smaller the stress in the anchor is. D_{b4} is the diameter of the lower body's bottom, whereas the bottom surface except the hole is fixed. As D_{b4} increases, the fixed area increases correspondingly while the maximum stress decreases.

It is notable that 55-55-45-55 ($D_{b1} - D_{b2} - D_{b3} - D_{b4}$) has the smallest value, followed by 45-55-45-55, because the fixed boundary condition is the largest when D_{b3} is 45 mm and D_{b4} is 55 mm. However, if D_{b4} is found to be larger than D_{b3} , then it is difficult to manufacture using a mold. As shown in **Figure 3-7**, the set of 45-55-45-45, which is the third smallest stress, was selected.

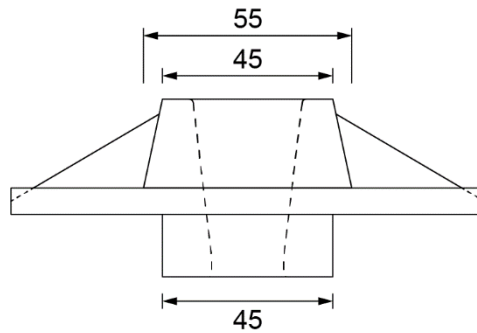
Table 3-6 Shape of tubular body



D_{b1} [mm]	D_{b2} [mm]	D_{b3} [mm]	D_{b4} [mm]	$f_{v,max}$ [MPa]	
45	45	45	45	207.6	
			50	196.3	
		55	202.3		
		45	217.8		
		50	197.2		
		55	270.7		
	50	50	45	45	205.8
				55	191.8
			45	193.7	
			50	219.5	
		55	55	45	195.8
				50	186.6
			45	184.3	
			55	252.9	
Continuous linear slope			50	193.5	
Continuous linear slope			55	196.3	
50	45	45	45	203.7	
			50	199.7	
		45	216.8		
		50	190.4		
	50	50	45	201.8	
			50	218.7	
		45	203.3		
		50	197.5		
Continuous linear slope			45	199.7	

Table 3-6 Shape of tubular body (continued)

D_{b1} [mm]	D_{b2} [mm]	D_{b3} [mm]	D_{b4} [mm]	$f_{v,max}$ [MPa]	
55	45	45	45	198.5	
			55	188.0	
		55	45	270.6	
			55	190.2	
	55	45	45	188.3	
			55	182.2	
		55	45	226.4	
			55	189.6	
	Continuous linear slope			45	211.1

**Figure 3-7** Final shape of tubular body [unit: mm]

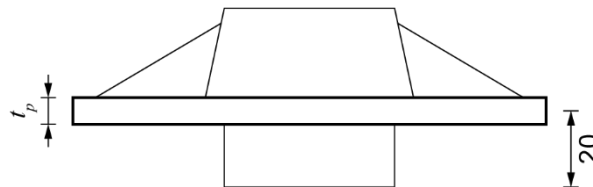
3.2.3 Shape of Bearing Plate

Until the previous step, the thickness of the bearing plate was assumed to be 7 mm. In order to determine the optimized thickness, it is analyzed in the range of 3 to 14 mm (**Table 3-7**). The anchor, which has the 13 mm thickness of the bearing plate, has the smallest maximum stress. However, the anchor eventually becomes bulky

and uneconomical if the bearing plate is too thick. Conversely, if the thickness is too thin, the risk of breaking begins to assume significance. It is consistent with the high stress in the results of 3 to 5 mm. The second smallest maximum stress was found to occur when the thickness of the bearing plate was 7 mm.

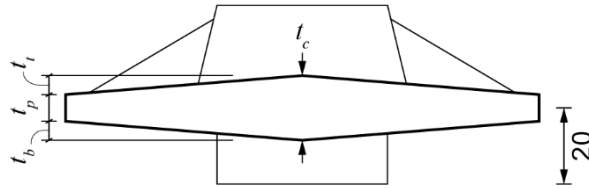
Typically, mold-filling problems are rarely an issue when the wall thickness exceeds 9.5 mm (0.375 in.). Alternately, when the wall thickness is reduced below 3.2 mm (0.125 in.), adequate mold filling is virtually impossible, except for short distances. Premature freezing of the molten metal poses a problem. In such instances, a designer can allow for certain geometric features on the casing that can ensure the molten metal's fluidity for the entire length of the mold cavity.

Table 3-7 Thickness of flat bearing plate [unit: mm]



t_p [mm]	$f_{v,max}$ [MPa]
3	215.2
4	219.1
5	232.7
6	187.0
7	184.2
8	188.2
9	189.8
10	199.0
11	199.9
12	192.5
13	178.8
14	181.9

Table 3-8 Shape of bearing plate [unit: mm]



t_p [mm]	t_c [mm]	t_i [mm]	t_b [mm]	$f_{v,max}$ [MPa]	
6	6	0	0	186.9	
	7	0	0	1	400.0
			1	0	191.9
	8	0	0.5	0.5	317.0
			0	2	268.3
			2	0	186.9
			1	1	378.5
	9	0	0	3	265.1
			3	0	191.5
			1.5	1.5	296.4
7	7	0	0	184.2	
			1	292.9	
	8	0	1	202.0	
			0.5	0.5	353.4
	9	0	0	2	257.9
			2	0	193.5
			1	1	400.0
	10	3	0	195.3	

The shape of the bearing plate does not necessarily have to be flat. **Table 3-8** illustrates the manner in which the maximum stress varies, depending on the plate shape in the range of 6 to 8 mm, which is the appropriate thickness range having a relatively low stress.

The flat plates have lower stress than other convex shapes. The top convex shape, $t_i > 0$, is found to be effective in reducing stress. The stress increases in case of the

bottom convex. The bottom of the bearing plate is V-shaped and fixed so that the stress gets concentrated in the middle of the plate. For the exact same reason, the maximum stress is also high in the convex shape, both up and down.

Flat bearing plates of 7 mm and 6 mm are confronted with the first and second smallest maximum stress, respectively. However, the inclination of the plate makes it easier to remove the mold during the fabrication process as compared to the flat form. Therefore, the selected shape is the top convex, 6 mm at both ends and 8 mm at the center.

3.2.4 Shape of Gussets

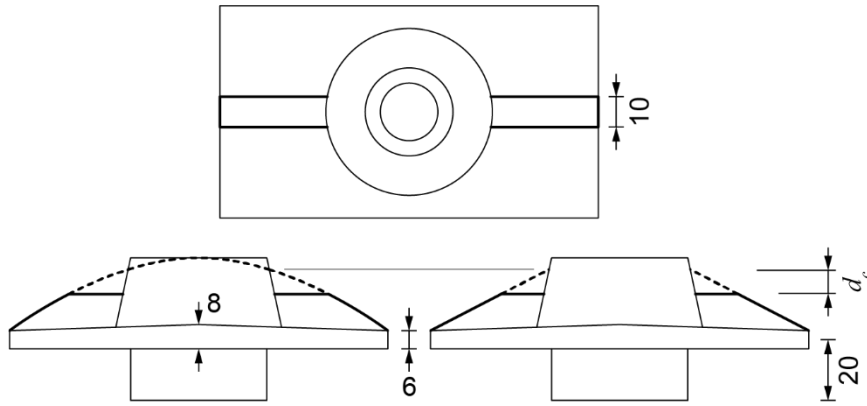
Subsequently, the stress distribution is examined, depending on the gusset shape. First, the shape of the gusset from the front is considered (**Table 3-9**); curve, straight, and top cut curve or straight. The 3-point curve connects both top ends of the bearing plate in addition to the top center of the upper tubular body. The straight lines are from the points where the curve meets the upper body to either top end of the bearing plate. d_c denotes the length cut horizontally from the point where the curve or straight line meets the upper body.

According to the results of our analysis, curved gussets perform slightly better than straight gussets. Although the curved length is similar to the straight length due to the large curvature, the curve shape exhibits greater efficiency on the stress

distribution. The larger the value of d_c in the curved gusset, the lower the maximum stress; however, this is not the case in the straight gusset.

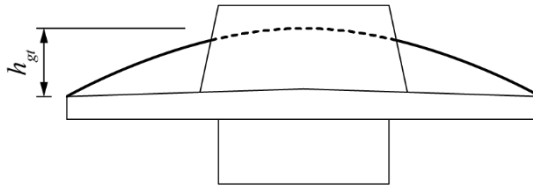
Since no significant difference is found in the maximum stress, the optimum height of the curved gusset is found rather than the height cutting top of the gusset (**Table 3-10**). The maximum stress appears to be the smallest when h_{gt} is 12.5 mm, where h_{gt} is the height of gusset from the top edge of the bearing plate.

Table 3-9 Shape of gusset [unit: mm]



Shape	d_c [mm]	$f_{v,max}$ [MPa]
Round	0	186.9
	2.5	186.2
	5	185.9
Triangle	0	193.9
	2.5	190.3
	5	191.0

Table 3-10 Height of gusset



h_{gt} [mm]	12	13	14	15	16	17	18	19	20	20.5	24
$f_{v,max}$ [MPa]	190.4	189.2	196.4	189.5	192.2	191.1	190.5	192.8	192.9	197.7	224.1

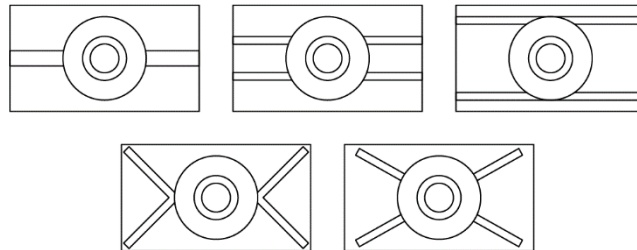


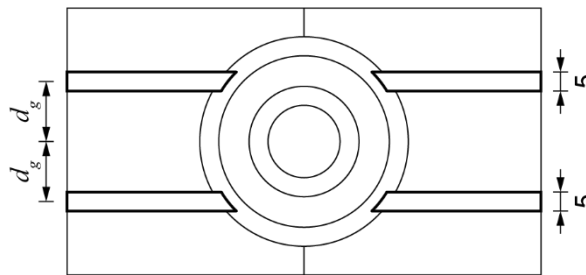
Figure 3-8 Examples of gusset arrangement

Second, when viewed from above, the arrangement of the gusset is taken into consideration. Examples of gusset arrangement are illustrated in **Figure 3-8**. One thick straight line (two-gusset) is used in the previous analysis. Each thick gusset can be separated into two parallel thin gussets (total four gussets), whereas the parallel distance can be as far as the diameter of the upper tubular body. There are also shapes with a diagonal arrangement. The two gussets on either side intersect at the outer of the tubular body, which is the same part where the thick straight gusset meets. It has the advantage of transferring the load to the edge of the bearing plate. In case all four gussets are placed toward the edge of the bearing plate from the center, it is possible to distribute the load from the tubular body throughout the bearing plate. However,

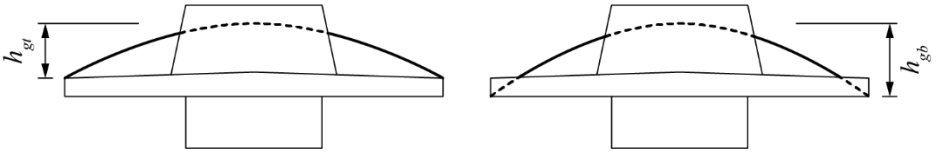
it is difficult to manufacture the diagonal layout, thus implying that the straight or parallel gusset arrangement is chosen.

One 10 mm thick straight can be divided into two 5 mm thick straight lines, and the stress change is analyzed based on the difference between the centers of two lines. The results are shown in **Table 3-11**. If the distance between the half of the centers of two gussets, d_g , is 2.5 mm, it denotes a gusset with the thickness of 10 mm. When compared with their concentrated counterparts, widely separated gussets are more efficient and distribute the stress more evenly over the bearing plate. The result is most efficient when the distance is 12.5 mm. However, the 20 mm, the next best option, is selected in consideration of the load eccentricity that can occur at the end of the bearing plate. On the other hand, the 12.5 mm is relatively concentrated in the middle of the plate.

Table 3-11 Half of distance between gusset elements [unit: mm]



d_g [mm]	2.5	5	7.5	10	12.5	15	17.5	20	22.5	25
$f_{v,max}$ [MPa]	189.2	196.3	187.8	192.0	185.3	187.9	189.1	186.2	187.9	186.6

Table 3-12 Radius of gusset


h_{gt} [mm]	$f_{v,max}$ [MPa]	h_{gb} [mm]	$f_{v,max}$ [MPa]
12	190.4	18	189.1
13	189.2	19	193.5
14	196.4	20	191.9
15	189.5	21	186.6
16	192.2	22	192.2
17	191.1	23	189.5
18	190.5	24	190.3
19	192.8	25	189.4
20	192.9	26	191.7
20.5	197.7	26.5	195.2
24	224.1	30	191.7

Since the position of gussets has changed with respect to the tubular body and bearing plate, the optimized height of the gusset is found again. On this occasion, all cases where both ends of the 3-point curve meet the upper or lower edges of ends of the bearing plate are taken into consideration. The gusset height, h_{gt} or h_{gb} , is defined as the vertical distance between the endpoint and the midpoint of the 3-point curve. The h_{gb} is 6 mm (the thickness of the bearing plate) higher than h_{gt} . According to the results in **Table 3-12**, the curve from bottom edge of the bearing plate is more efficient than that from top edge. Since the bottom surface of the bearing plate contacts with the concrete, it is found to be more efficient than the force transferred from the tubular body, which is then directed to the lower edges of the bearing plate. The shape where h_{gb} is 21 mm is selected due the smallest maximum stress.

The thickness of the flat gusset is determined (**Table 3-13**). As evidenced in the previous analysis, the distance between the centers of the gussets was 40 mm, and the outer distance is 45 mm when the gusset thickness is 5 mm. It is similar to the upper outer diameter of the body. Accordingly, the thickness of flat gusset t_{g1} is changed inward. Meanwhile, as shown in the previous analysis, the half distance between the gussets was fixed at 20 mm, whereas the thickness of the gusset for that case (t_{g2}) was changed. The optimum results were obtained when the gusset thicknesses t_{g1} and t_{g2} for both cases were 5 mm (same state).

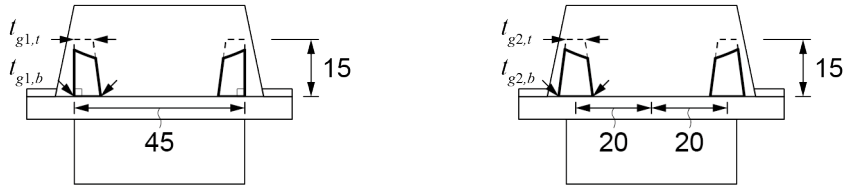
To elaborate, the upper and lower thicknesses of the gusset are determined. Both cases of the gussets' outer distance of 45 mm and 40 mm are taken into consideration. Since the optimized thickness of the flat gusset is 5 mm, it is analyzed in the range of 4 to 7 mm (**Table 3-14**). Notably, the smallest peak stress in the results is with a distance of 40 mm, a thickness of 6 mm on the top and 5 mm on the bottom.

Table 3-13 Thickness of flat gusset [unit: mm]



t_{g1} [mm]	$f_{v,max}$ [MPa]	t_{g2} [mm]	$f_{v,max}$ [MPa]
4	197.3	4	189.0
5	186.6	5	186.6
6	187.0	6	199.3
7	197.7	7	191.0
8	188.2	8	189.9
9	187.0	9	189.5

Table 3-14 Detailed thickness of gusset [unit: mm]



$t_{g1,t}$ [mm]	$t_{g1,b}$ [mm]	$f_{v,max}$ [MPa]	$t_{g2,t}$ [mm]	$t_{g2,b}$ [mm]	$f_{v,max}$ [MPa]
4	6	190.4	4	6	188.7
	5	186.6		5	5
5	6	187.8	5		6
	7	190.2		6	7
6	4	190.9	6		4
	5	194.4		7	5
7	5	191.1	7		5

3.2.5 Radii

A fillet radius r redirect stresses from being concentrated at sharp corner. It also minimizes turbulence in the metal in order to inhibit formation defects from oxides and trapped gas. Furthermore, radii dissipate heat, which improves solidification. For the aforementioned reasons, the corners or edges should be rounded. The radii are also optimized with the finite element analysis.

First, the boundary between the body and the anchor plate was taken into consideration (**Table 3-15**). This pertains to the efficacy with which the body's power can be distributed to the anchor plate. It is found to be the most efficient when r_u is 2.5 mm, while r_l is 2 mm, where r_u is the boundary radius between the

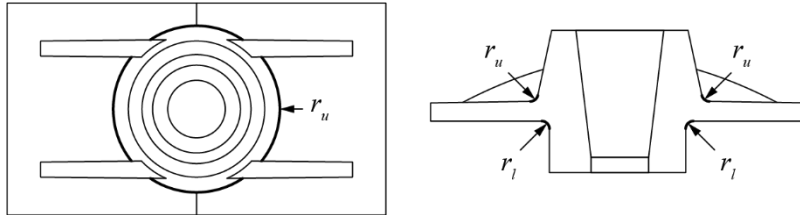
bearing plate and the upper body and r_l is the boundary radius between the bearing plate and the lower body.

Next, the edges of gussets are taken into consideration (**Table 3-16**). The part that crosses the gusset, the body, as well as the bearing plate, is optimized at 5 mm (r_{g1}). The upper edge of the gusset (r_{g2}) was found to be most effective at 8 mm, but the thickness of the gusset was between 5 mm and 6 mm, which is why 2 mm was chosen. The optimum radius between the gusset and the bearing plate (r_{g3}) was 2 mm. The stress was also the smallest at r_{g4} of 2 mm, where r_{g4} is the radius between the gusset and the upper body.

Finally, the curvature of the bent portion of the upper convex bearing plate r_p is analyzed (**Table 3-17**). No significant differences are found in the curvature with the naked eye. It was found that 2 mm of them appeared most effectively.

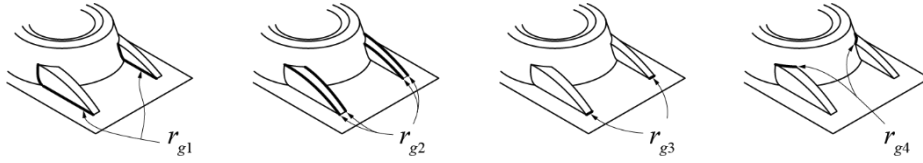
In most cases, the corner curvature of 2 mm is found to be most useful. Accordingly, the edges or boundaries not previously determined by the analysis are applied on a 2 mm radius.

Table 3-15 Rounding radius between tubular body and bearing plate



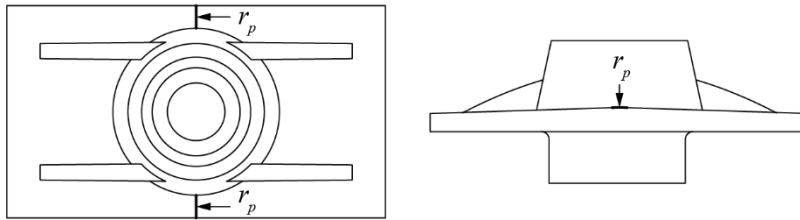
r_u [mm]	$f_{v,max}$ [MPa]	r_l [mm]	$f_{v,max}$ [MPa]
0.5	186.8	0.5	340.0
1.0	192.1	1.0	291.0
1.5	189.6	1.5	186.2
2.0	194.4	2.0	183.8
2.5	186.6	2.5	192.7
3.0	191.7	3.0	198.1
3.5	189.9	3.5	193.4
4.0	183.8	4.0	195.9
4.5	185.9	4.5	196.6
5.0	189.6	5.0	200.3
5.5	193.0	5.5	196.0
6.0	186.5	6.0	204.5
6.5	186.8	6.5	203.0
7.0	189.4	7.0	209.9
7.5	191.0	7.5	243.1
8.0	192.2	8.0	239.4
8.5	188.2	8.5	243.1
		9.0	238.8
		9.5	236.5
		10.0	250.2
		10.5	246.3
		11.0	253.2
		11.5	255.6

Table 3-16 Rounding radius for gusset edges



r_{g1} [mm]	$f_{v,max}$ [MPa]	r_{g2} [mm]	$f_{v,max}$ [MPa]	r_{g3} [mm]	$f_{v,max}$ [MPa]	r_{g4} [mm]	$f_{v,max}$ [MPa]
1	280.5	1	183.1	1	188.6	1	188.6
2	212.4	2	186.9	2	185.1	2	188.2
3	208.8	3	188.4	3	216.1	3	192.4
4	191.5	4	196.0	4	194.3	4	212.3
5	181.1	5	191.4	5	189.2	5	201.2
6	186.8	6	192.4	6	191.8	6	200.5
7	185.1	7	190.7	7	184.9	7	194.6
8	191.7	8	181.3	8	198.5	8	278.9
9	191.3	9	190.8	9	185.6	9	224.9
10	186.9	10	194.0	10	189.7	10	187.3

Table 3-17 Rounding radius for bearing plate



r_p [mm]	$f_{v,max}$ [MPa]
1	208.4
2	187.5
3	209.0
4	189.8
5	189.7
10	197.8
15	205.7
20	190.2
25	192.6

3.3 Consideration for Practical Construction

The anchor is designed by conducting a finite element analysis. However, it still needs to be determined whether or not the designed anchor can be used in actual construction. Under this section, the anchor design is changed to take the following points into consideration.

3.3.1 Jacking Device

When jacking the strand, the nose of the jacking device lends support to the anchor. A mountain-shape may be required on the top of the tubular body. A mountain-shape similar to SURE-LOCK's anchor is utilized in order to ensure versatility with existing jacks. The SURE-LOCK's anchor using $\text{Ø}12.7$ mm strand (not $\text{Ø}15.2$ mm) is taken into consideration so as to avoid increasing the size of the anchor. Its mount diameter is 34 mm. However, since the wedge hole diameter of the developing anchor is 29 mm, the mount diameter is determined as 36 mm (**Figure 3-9**). The height of the mountain is 2.5 mm, which is the same as that of the SURE-LOCK's anchor.

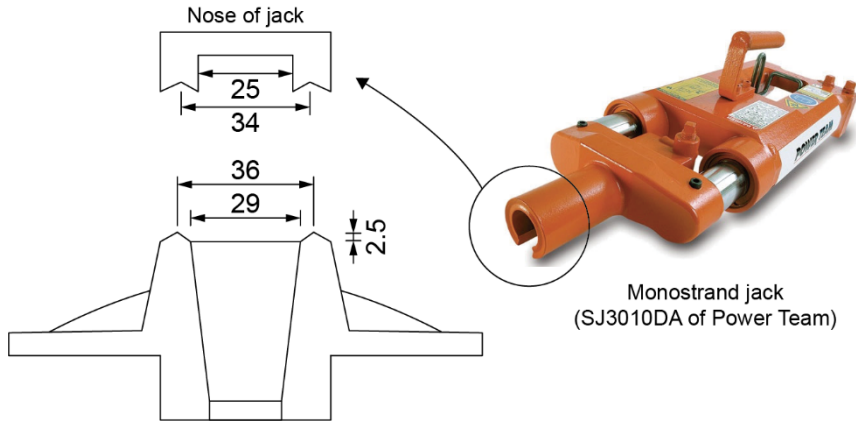


Figure 3-9 Nose of jack and mountain-shaped anchor head [unit: mm]

3.3.2 Endcap

There are several ways of fitting the endcap to safeguard the tendon tail and wedge hole from corrosion. Most anchors use the screw method, which is time and energy-intensive, depending on the number of threads. By using the push-in method, the worker can not only easily insert it, but also drastically shorten the construction time. Based on existing 12.7 mm diameter cap, the inner diameter required for capping is 47 mm, whereas the minimum required thickness is 4 mm to clean the casting surface. The upper body is a cylinder with a diameter of 55 mm, which is already analyzed in **Table 3-6**. The end edges of the casting are rounded, thus implying that the endcap can be easily inserted.

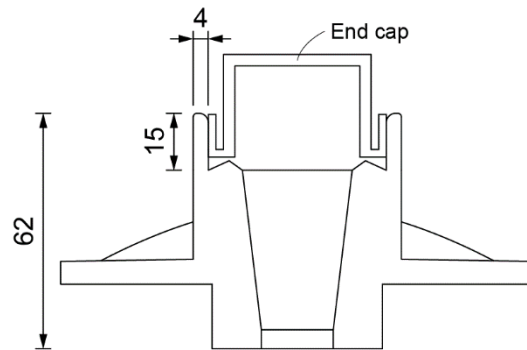


Figure 3-10 Anchor head design for endcap [unit: mm]

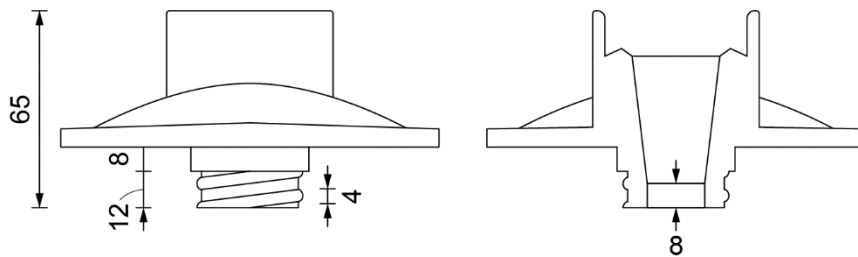


Figure 3-11 Redesign of lower body for sleeve [unit: mm]

The minimum wall thickness that can be achieved is contingent on the material and the distance the molten metal is required to traverse. Metal is poured at higher temperatures than the mold it is entering. Metal entering a mold is constantly losing heat. If the metal loses enough heat, it will solidify before it has an opportunity to fill out all the details of the mold.

3.3.3 Sleeve

The screw-in type can securely fix the sleeve to prevent it from falling out. In addition, it is excellent when it comes to waterproofing since it is formed to cover the inside of the anchor.

Water-tightness improves when there are many threads with small gaps, but the workability is greatly reduced. The round thread is applied so that the sleeve can be easily inserted even when the casting finishing may not be clean. Screw length is 12 mm and the distance between thread pitches is 8 mm. The sleeve can be fitted with only 1.5 rotation, thus reducing the work time.

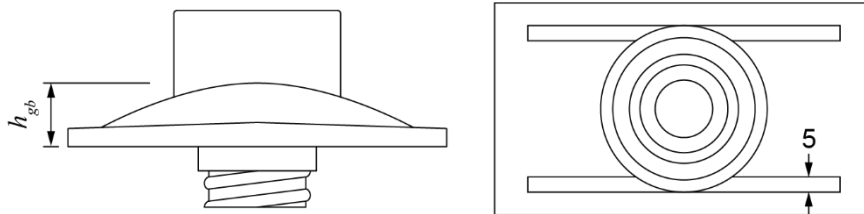
Applying threads for the sleeve, the vertical section of the wedge cavity increased from 5 mm to 8 mm. Increasing this interval is simply an increase in the free length of the strand. In this regard, Walsh and Kurama (2010) found that the change in free length does not affect anchorage settlement.

On the other hand, as the outer part of the lower body is changed into a screw shape. There is a possibility of stress concentration occurring here, which was verified through analysis in Section 3.3.4.

3.3.4 Redesign of Gusset through Finite Element Analysis

In light of the aforementioned changes, the finite element analysis is performed on the size of the gusset. At this time, gusset is circumscribed the tubular body in the same manner and analyzed only by altering the height and length. As evidenced in the results in **Table 3-18**, the optimal h_{gb} is 21 mm, which is non-different from the previous analysis.

Table 3-18 Height of gusset [unit: mm]



h_{gb} [mm]	$f_{v,max}$ [MPa]
18	258.7
19	276.9
20	264.8
21	257.6
22	259.9
23	281.9
24	275.0
25	261.1
26	278.9
26.5	266.0
30	291.6

3.3.5 Casting Fabrication

The mold must be able to easily fall out of the casting. Therefore, the middle part of the anchor is thick and becomes thinner toward the end in the direction of removing the mold frame, so as to form the inclined surface. Since the product to be developed has a screw shape in the part where the sleeve is fitted, it should be designed in order to separate the mold from one side to another about the surface perpendicular to the bearing plate. At this time, the gusset part is inclined as a result of finite element analysis, but this becomes problematic because the inner surface of the bearing part is horizontal. The shape of the anchor plate selected through the finite element analysis is thin at both ends and thick in the middle, flat at the bottom, and convex at the top. However, it is changed to be convex at the top and bottom in order to form the slope. Given that there is no significant difference in the efficiency of the anchor depending on the type, the thickness of both ends and the middle part remain the same as that of the finite element analysis, which implies that the amount of casting hardly changes.

3.4 Bare Anchor

3.4.1 Bare Anchor and Accessories

Figure 3-12 illustrates a drawing of bare anchor developed by considering finite element analysis results and constructability. The overall shape, with the exception of screw threads, is symmetrical and is slightly tapered outwards for fabrication.

The prototype is shown in **Figure 3-13**. The material of casting is GCD 500-7.

Figure 3-14 depicts the accessories used as sets and their fittings in the anchorage.

The sleeve is threaded as previously designed. The pocket former is inserted into anchor head and fixed by nail through to holes. The endcap can be fitted to the anchor head and remains tight without any additional fixing.

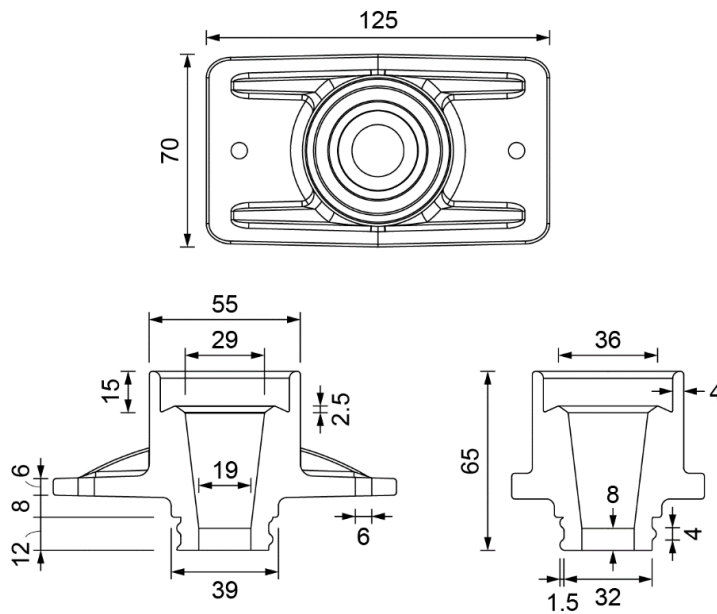


Figure 3-12 Drawings of designed bare anchor [unit: mm]



Figure 3-13 Bare post-tensioned anchor



(a) Endcap



(b) Pocket former



(c) Sleeve



(d) Live end set-up

Figure 3-14 Accessories for bare anchor

3.4.2 Detail Changes

The conventional method for fixing pocket former has been found to be inefficient, thus underpinning the need for preferring the bolt nut method (**Figure 1-6**) for the gang-form system. Accordingly, the pocket former is modified to consist of bolts, nuts, and pockets. As shown in **Figure 3-15**, threads are further machined inside the anchor head in order to secure the bolts to the anchor.

A groove was formed in the center of both ends of the bearing plate so as to fix it by nails or screws. Such classical methods can be applied, when deemed necessary.

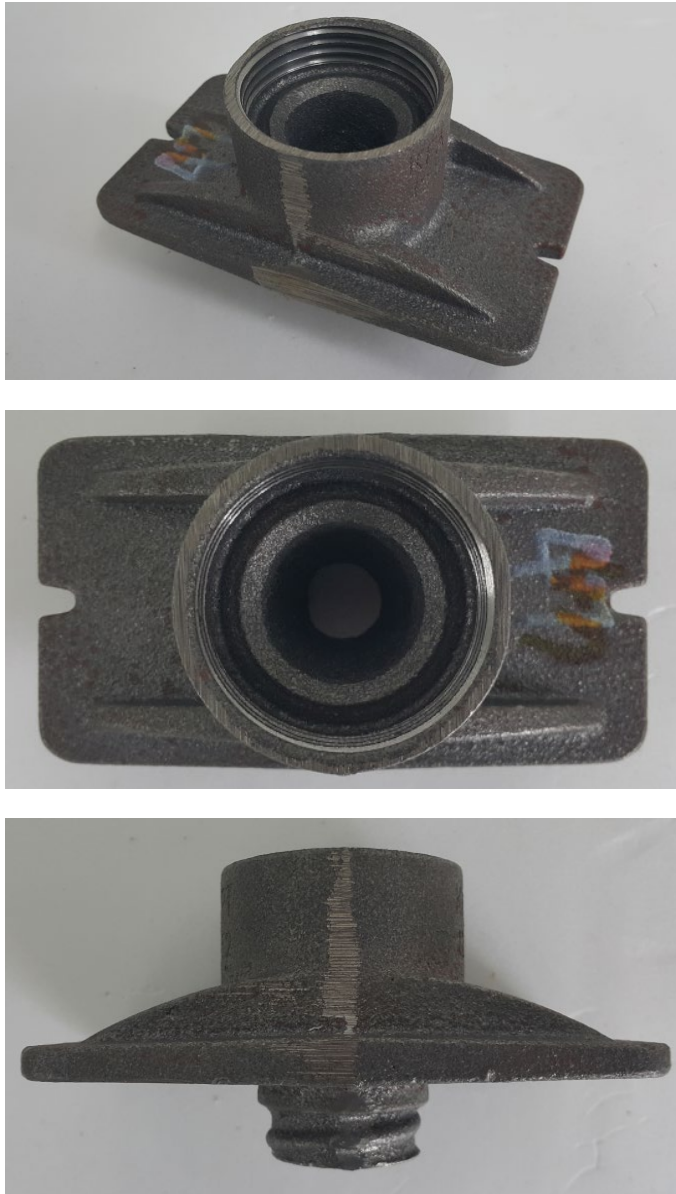


Figure 3-15 Modified bare post-tensioned anchor

3.5 Design Modification for Encapsulated System

3.5.1 Needs for Encapsulation

ACI 423.7 (2014) mandates the use of encapsulation. Encapsulation refers to the plastic coating, which is a method of minimizing the corrosion of the casting that directly comes into contact with concrete and water. This is especially true in environments that are susceptible to corrosion. However, the use of encapsulation anchorages is strongly recommended for the tendon's long-term sustained effects since the strands and anchorages are exposed to moisture even under normal conditions.

Unlike the U.S., encapsulation is not yet necessary in Korea. However, that situation is likely to change in the long-term, thus underpinning the importance of encapsulation. As mentioned above, the application of encapsulation is essential to improve the durability and post-safety of buildings.

3.5.2 Encapsulated Anchor and Accessories

In addition to structural parts, bare anchor requires additional castings in order to apply accessories. However, unnecessary parts of casting can be minimized by replacing them with plastic.

The drawings of modified bare anchor are depicted in **Figure 3-16**. The threaded portion for inserting the pocket former or endcap is cut. Screw for the sleeve is removed, which reduces the height of the lower body. Therefore, the total height of casting is only 47.5 mm. Unlike the original bare anchor, the modified anchor cannot use accessories by casting itself, and must undergo the encapsulation process.

Figure 3-17 illustrates the encapsulated anchor. The plastic material is linear low-density polyethylene (LLDPE) and the thickness of plastic cover is 2 mm. When the cover is hard, it is strong in scratching, but the cracks easily occur even in cases of small deformation. Otherwise, it is not broken by impact or various deformations with soft plastic. However, the workability may deteriorate because the parts for the sleeve, the pocket former, or the endcap is bent under a weak force. Therefore, proper compounding of the plastic material is found and verified through mock-up test in Section 5.3. In addition to encapsulation, this can also be applied on the plastic-formed pocket formers and endcaps, thereby increasing the applicability of accessories.

The sleeve is plastic-molded along with the plastic cover of an anchor as an integrated encapsulation. The length of the sleeve is 145 mm, which is longer than minimum length of 100 mm in ACI 423.7 (2010), Section 6.5.2.b). The diameter decreases towards the end, along with a reduction in thickness. The thickness at the sleeve tip is 1.5 mm, thus exceeding the minimum thickness of 1.27 mm specified in Section 8.4.1 of ACI 423.7 (2010).

In order to fit the pocket former and endcap, the cylindrical cover extends about 12 mm from the anchor head. The protruding portion has a thickness of up to 6 mm. The inside has a thread about 2 mm thick to screw the pocket former bolt along with the endcap.

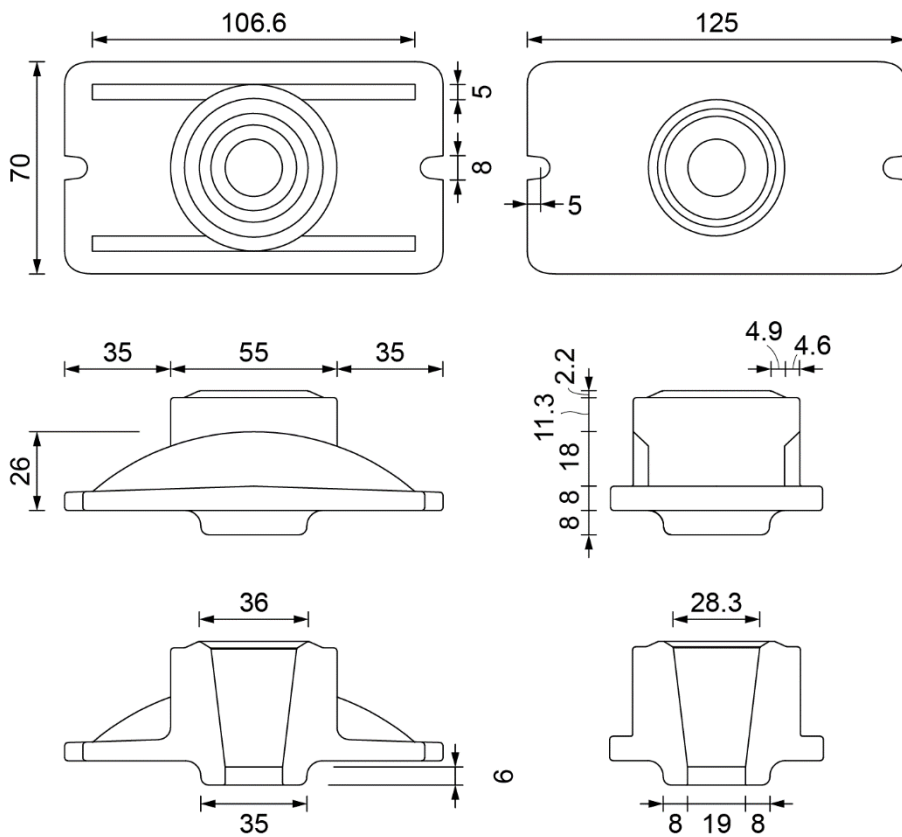


Figure 3-16 Drawings of encapsulated anchor [unit: mm]

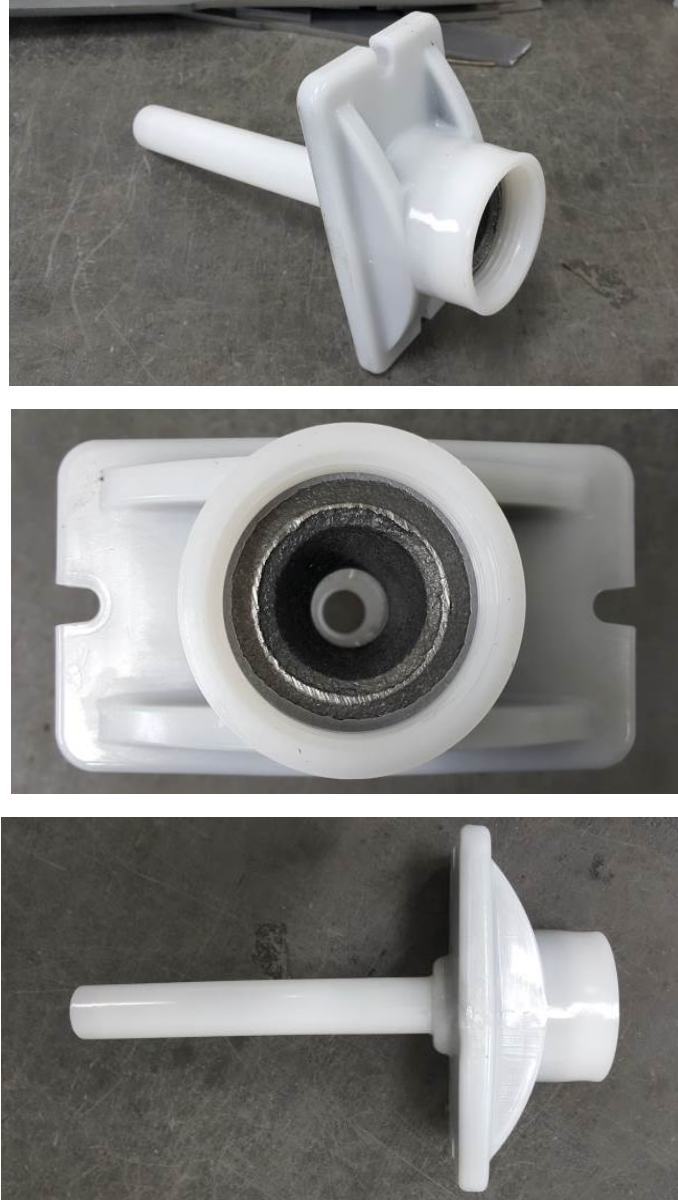


Figure 3-17 Encapsulated anchor

3.6 Summary

For designing the anchor, finite element analysis is performed to investigate the maximum von Mises stress by varying the shape of bearing plate, body, and gusset. The shape is optimized to minimize this stress. In addition, the design is also determined in consideration of a jacking device, accessories, and workability. ACI 423.7-14, on the other hand, requires the use of encapsulation system that is highly resistant to corrosion. Despite not being mandatory in Korea, the encapsulated anchor was developed to enhance the durability of PT tendons and buildings.

The design results of the bare and encapsulated anchors are summarized as follows.

- 1) Developed bare anchor has the bearing plate of 125 mm × 70 mm, with its height being 65 mm.
- 2) Casting material is GCD500-7 and the sleeve can be fixed with threads.
- 3) For the encapsulated anchor, unnecessary parts of casting were eliminated because the plastic cover can be used to either substitute or fix the accessory. The height of encapsulated anchor was reduced to 47.5 mm by removing the threaded portion for the sleeve and the cylindrical portion for the pocket former/end cap.
- 4) The plastic cover had a thickness of about 2 mm and was made in a single piece, including a 145 mm long sleeve. The pocket former and the end cap can be screwed on the anchor head.

Chapter 4. Performance Tests

In this chapter, the performance of the developed anchor in Chapter 3 was verified after conducting several experiments. The three tests (static load test, fatigue test, and load transfer test) were conducted based on the Korean specifications, KCI-PS101 (2010).

In Korea, a hydrostatic test is not yet necessary. However, in order to verify the watertight performance of developed encapsulated anchor, the hydrostatic test is performed following ACI 423.7 (2014).

4.1 Static Load Test for Bare Anchor

The static load test is performed to check the performance of the anchor and behavior of the tensile element when a static load applied. In this section, a static load test was performed on the bare anchor that was initially developed.

4.1.1 Specimen

Three specimens of the same specification (SB1, SB2, and SB3) were fabricated. S and B indicate the static load test and the bare anchor, respectively. They were designed with reinforced concrete to reduce the buckling effect due to the strand as well as the cost, while the example specimen in ETAG 013 (2002) was made of a steel frame.

The drawing of the specimen is shown in **Figure 4-1**. The length of the concrete specimen was 3,120 mm which includes the free length of the strand (3,000 mm) as well as the height of two anchors at each end. The cross-section was a square of 400 mm. The concrete design strength was 80 MPa. SD400 D16 was used as the longitudinal steels, whereas SD400 D13 was used as the stirrup. The concrete cover was 10 mm.

Two anchors were placed at either end of the specimen and the center of the cross-section. The anchor head at the fixed end and the surface of the specimen were

arranged on the same line. On the live end, the anchor head was protruded 10 mm from the concrete specimen so that the tensile force could be directly transmitted to the anchor. In addition, two holes were drilled in each anchor's bearing plate to fix the anchors to the wooden formwork with bolts and nuts (**Figure 4-2(b), (c), and (d)**).

In the middle of the specimen, a concrete pocket was created 100 mm in width, 242 mm in depth, and 1,500 mm in length to expose the strand. In the portion other than the pocket, polyvinyl chloride (PVC) pipes with a diameter of 40 mm were provided from each bearing plate to the pocket.

The fabrication process of the specimen is shown in **Figure 4-2**. For each specimen, two steel hooks of 200 mm long were made for transportation and installed in two points on the upper part of the specimen. In order to ascertain the compressive strength of the concrete, 15 concrete cylinders were made at the same time of concrete pouring. The static load test was carried out after a period of one month for ensuring sufficient strength of the concrete.



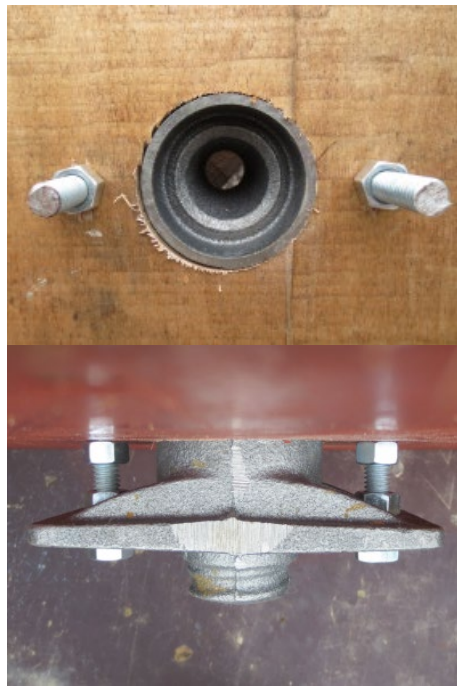
(a) Steel reinforcement



(b) Drilled anchors



(c) Fixed end



(d) Live end

Figure 4-2 Static load test specimen



(e) Framework



(f) Lifting ring



(g) Concrete pouring



(h) Aging



(i) Specimens

Figure 4-2 Static load test specimen (continued)

4.1.2 Material Properties

The static load test was performed on the 35th day from the concrete pouring. The compressive strength of six cylinder specimens on the day of testing is illustrated in **Table 4-1**. The average compressive strength was found to be 73.1 MPa.

Five tensile test specimens of the strand used in the static load test were carried out by Korea Testing & Research Institute (KTR) (**Figure 4-3**). The results are shown in **Table 4-2**, whereas the stress-strain curves are shown in **Figure 4-4**. The average tensile strength was 267.2 kN, 2.4% greater than f_{pk} , where f_{pk} is the nominal tensile strength of strand. The average yield strength calculated by the 0.2% offset strain method was 236.0 kN, which was 6.3% larger than the nominal yield strength. This corresponds to 90.4% of f_{pk} . In terms of comparing the yield points, the actual average yield strength was 88.3% of the mean tensile strength, while the nominal yield strength is 85.1% of the nominal tensile strength. The average elongation was 8.8%, which was more than twice the minimum requirement of 3.5% for KS D 7002 (2018).

Table 4-1 Compressive strength of concrete [unit: MPa]

Avg.	Specimen					
	1	2	3	4	5	6
73.1	67.0	73.3	66.2	76.7	79.6	75.9

**Figure 4-3** Tensile test for single-strands**Table 4-2** Tensile test results

	KS D 7002 (2018)	Specimen					
		Avg.	1	2	3	4	5
Tensile load [kN]	≥ 261.0	267.2	266.0	266.0	265.0	270.8	268.3
Yield strength [kN]	≥ 222.0	236.0	233.0	234.0	234.0	240.1	239.1
Elongation [%]	≥ 3.5	8.7	9.5	8.5	8.9	8.6	8.1

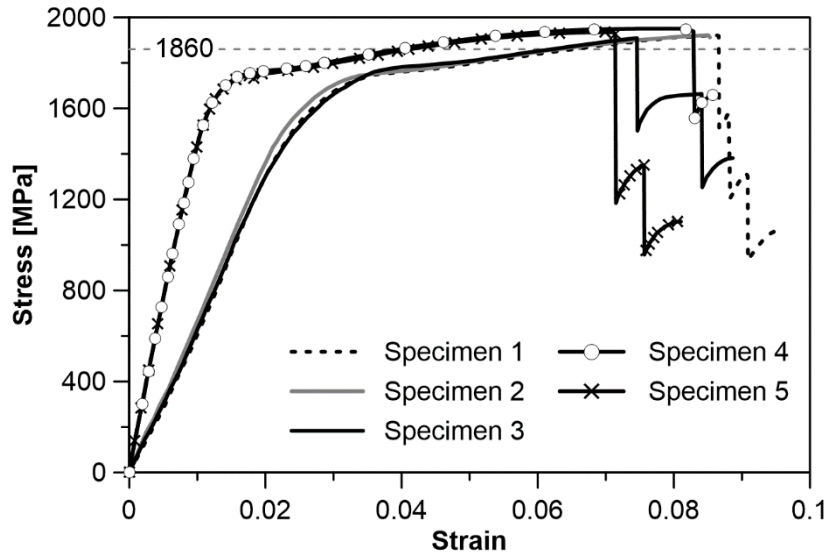


Figure 4-4 Stress-strain curve of single-strand

4.1.3 Test Set-up

Figure 4-5 illustrates the set-up plan of static load test specimen. After passing a PC strand through the specimen, the wedges were inserted into the fixed-end anchor. A load cell was then installed on the anchor head on the jacking side (Figure 4-6(a)). Two steel plates were attached to both sides of the load cell in order to prevent the equipment from getting damaged and to allow the jacking force to be transmitted only to the anchor head.

In accordance with KCI-PS101 (2010), the wedges at the fixed end should be hooked with a load of $0.1P_{pk}$, where P_{pk} is the force at the nominal tensile strength of strand (261 kN). In this experiment, a jacking device used in practice was used, with

only one load limit. This limit was set at 80% of the nominal tensile strength, which means that a technician manually operated a 10% load.

After applying the load, a total of five LVDTs were installed. Two (G1 and G2) measured the elongation in the free length as **Figure 4-6(c) and (d)**. Two special steel plates were fixed on the strand to measure the horizontal displacement, and the displacement meters gauged the displacement of each plate. The distance between G1 and G2 was 1,200 mm.

The remaining three LVDTs (W, CW, and HW) measured the displacements of the wedge and strand wires at the fixed end (see **Figure 4-6(e)**). W, CW, and HW denote wedge, central wire, and helical wire, respectively. W measured the displacement of the top surface of a piece of the wedge pieces. Similarly, HW measured the displacement of a wire that was arbitrarily selected among six helical wires, while CW measured that of the center wire. Since the measuring points were close to each other, needle-shaped steels were attached to the end of the displacement meters.

The magnitude of the force is neither related to the durability of the anchor nor the time of stabilization of the wedge and the strand, but it affects the elongation of the free field measured by the displacement gauge, which is why it is considered that the wedge of the fixed end starts to grip the strand.

After all the displacement gauges were installed, the strand was pulled to $0.8P_{pk}$ with the prescribed speed of 100 MPa/min. However, it was jacked through three steps because the jack could not control the tensile speed. While maintaining 80% of

the nominal tensile strength for an hour, the machine pressure was not kept constant. If the load fell, additional tension was applied so that the force could be maintained within the tolerance of $\pm 2\%$. The displacement of the wedge and wires should be stabilized within the first 30 minutes of one hour.

After one hour, the load should be applied until the strand breaks. However, the load was applied only up to 95% of the nominal tensile strength. The maximum load and elongation were supposed to be supplemented by the strand tensile test.

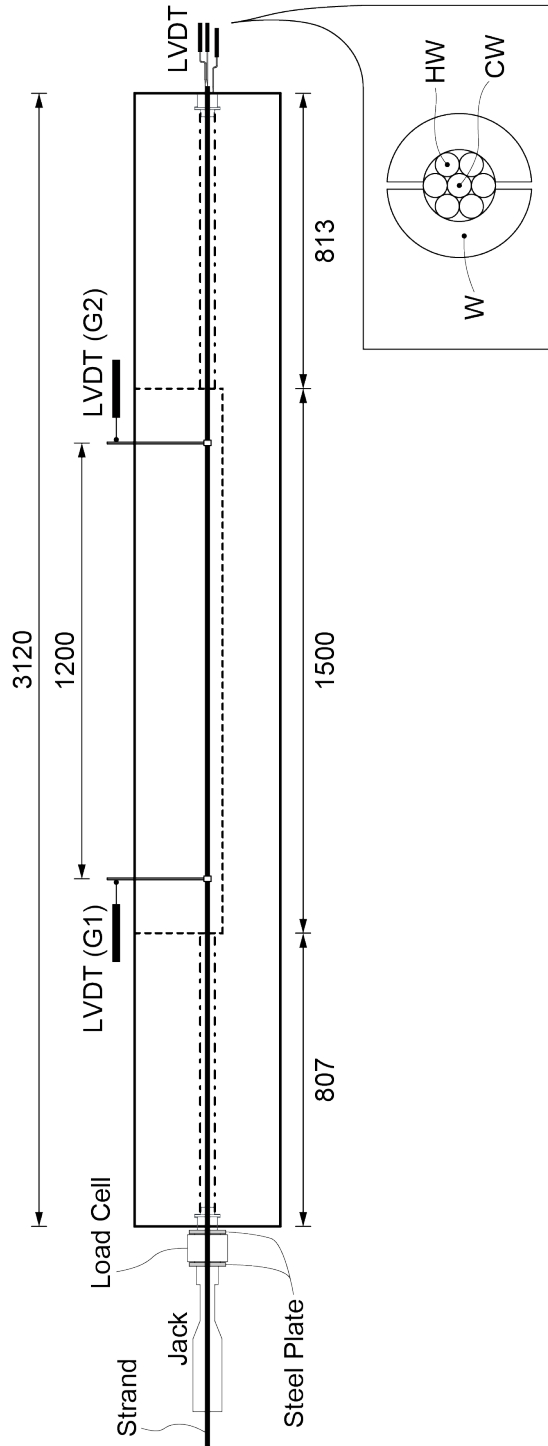


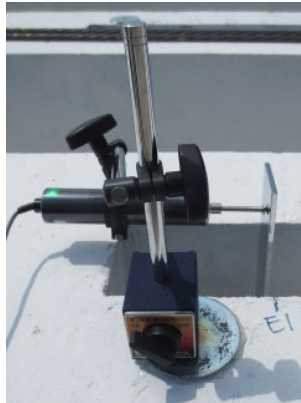
Figure 4-5 Set-up plan of static load test specimen [unit: mm]



(a) Test set-up



(b) Load cell



(c) Live end (G1)



(d) Fixed end (G2)



(e) Fixed end (W, CW, and HW)

Figure 4-6 Static load test setting

4.1.4 Test Results

The results for each specimen are shown in **Figure 4-7** and summarized in **Table 4-3**. Due to equipment problems encountered during the test, no results were measured for SB2 from 0:05:11 to 0:26:23 and for SB3 from 0:13:08 to 0:24:36 (marked as dashed lines).

The measured maximum loads of SB1, SB2, and SB3 were 253.9 kN, 234.5 kN, and 228.4 kN, corresponding to 98%, 91%, and 89% of P_{pk} , respectively. In the process of maintaining up to 80% of the P_{pk} for one hour, the displacements of CW, HW, and W of SB2 and SB3 were stabilized immediately after the force. Meanwhile, displacements of SB1 were continuously fluctuated within early 30 minutes and became stable during the latter minutes.

The amount of the strand elongation measured in the free field can be calculated by G1-G2. Given that 2% elongation is required by KCI-PS101 (2010), ETAG 013 (2002), and ACI 423.7 (2014), the minimum elongation should be not less than 24 mm. However, the elongation results were less than 2% because the experiment did not proceed until strand breaking. As depicted by **Figure 4-4**, the strain of strands rapidly increased by 6% before breaking. Since all strands of the tensile tests and the static load tests belonged to the same product line, it can be inferred that the elongation would have exceeded 2% if the experiment had been conducted until the strand break.

Figure 4-8 shows the relation between the stresses measured by the load cell and the strains calculated by G1 and G2. The dashed lines in the SB1 and SB3 denote the displacements measured after the initial jacking for inserting the wedges. In addition, the solid lines were not straight because slippage occurs during each interval of loading. In the case of SB2, the data was recorded after the load reached the level of $0.8P_{pk}$.

Immediately after the test, the fixed and live ends of all the specimens were well settled, as shown in **Figure 4-9**, even though the strands were broken. According to the KCI-PS101 (2010), the anchors and wedges used for the tests were taken out and checked (**Figure 4-10**). The only exception that it was exposed to the outdoors before the experiment and rusted in the anchorage. There were no deformations or cracks in the wedge-contact surfaces and the bearing plates in all the anchors. Additionally, the conditions of wedges were clean.

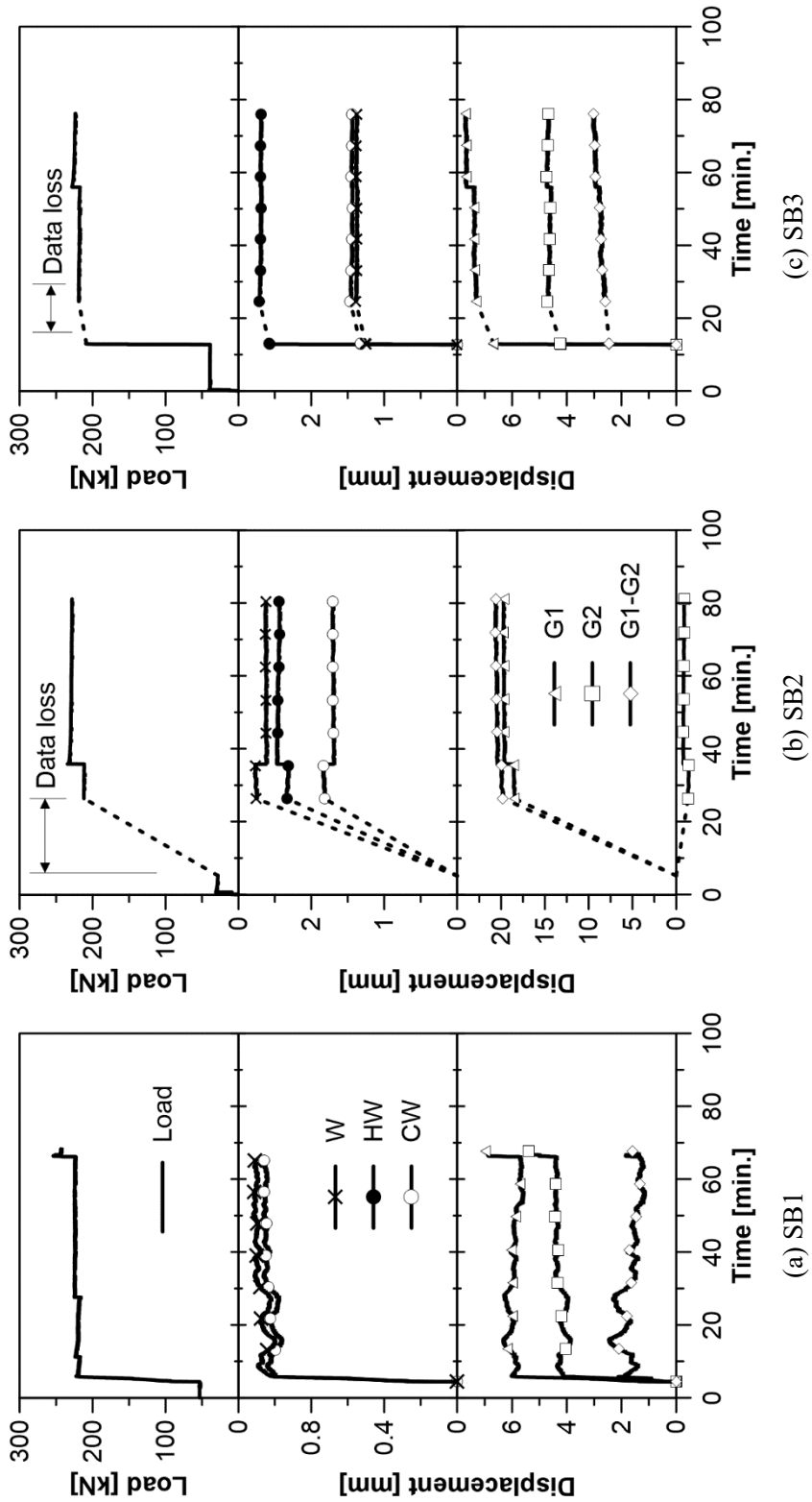


Figure 4-7 Static load test results

Table 4-3 Static load test results

	SB1	SB2	SB3
Load at $0.1P_{pk}$ [kN]	53.4	28.2	39.0
Max. Load [kN]	253.9	234.5	228.4
CW [mm]	At least 1.06	1.70	1.44
HW [mm]	N. A.	2.46	2.69
W [mm]	At least 1.11	2.63	1.38
G1 [mm]	N. A.	19.62	7.68
G2 [mm]	N. A.	-0.82	4.73
G1-G2 [mm]	N. A.	20.44	2.95

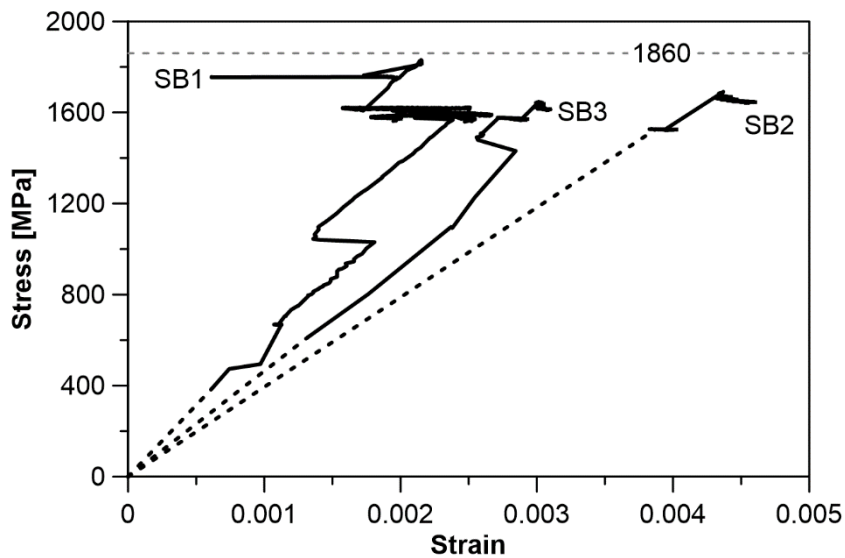


Figure 4-8 Stress-strain curve of static load test for bare anchor

Table 4-4 Static load test results compared to P_{pk}

	SB1	SB2	SB3
Min. load during 1hr. [kN]	216.2	211.3	217.1
Ratio to nominal tensile force (P_{pk})	0.84	0.82	0.84
Ratio to measured tensile load	0.81	0.79	0.81

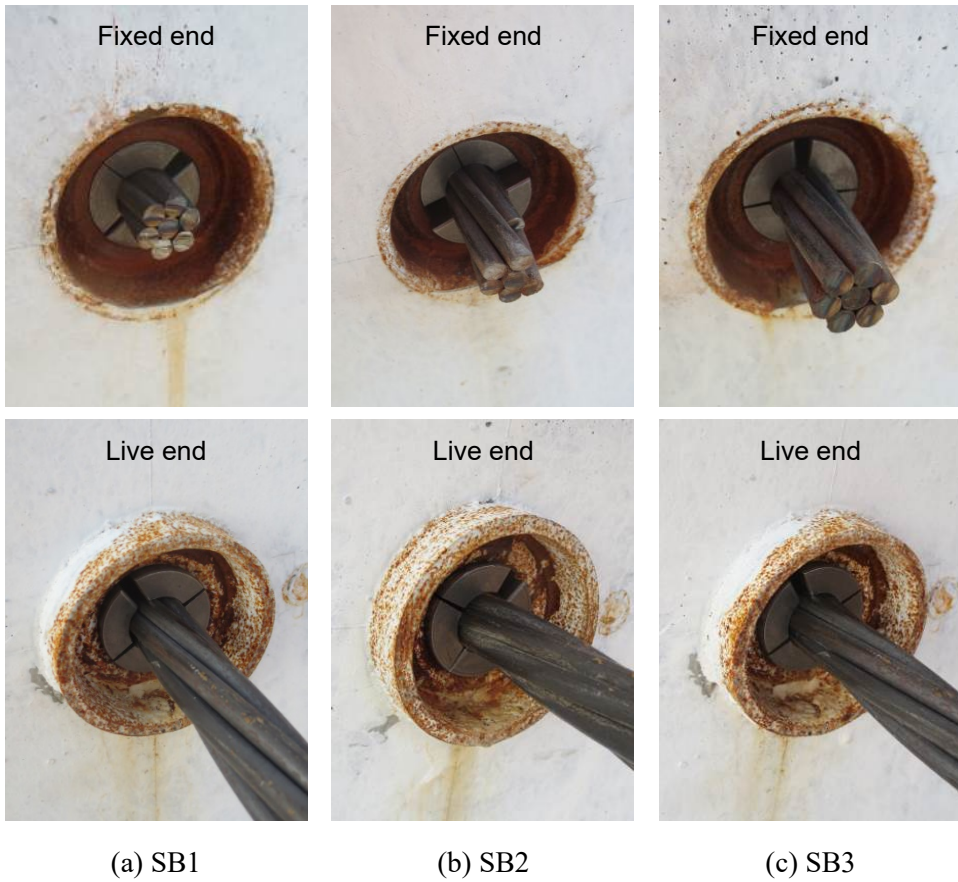


Figure 4-9 Settlement after static load test



Anchor (at fixed end)



Anchor (at live end)



Wedges (at fixed end)



Wedges (at live end)



(a) SB1

Figure 4-10 Anchors and wedges after static load test



Anchor (at fixed end)



Anchor (at live end)



Wedges (at fixed end)



Wedges (at live end)

(b) SB2

Figure 4-10 Anchors and wedges after static load test (continued)



Anchor (at fixed end)



Anchor (at live end)



Wedges (at fixed end)

Wedges (at live end)

(c) SB3

Figure 4-10 Anchors and wedges after static load test (continued)

4.2 Static Load Test for Encapsulated Anchor

Although encapsulated anchors have structural similarities with bare anchors, there are some differences as well. Therefore, static load tests for encapsulation system were performed separately.

During the development of the encapsulation anchor, the wedge-producing company made static load test equipment, using which the tests were performed more accurately and conveniently than the tests for the bare anchor system.

4.2.1 Test Set-up

Three specimens (SE1, SE2, and SE3) were tested with test set-up of **Figure 4-11**. E indicates encapsulated anchor. In order to control both load and displacement, the live-end anchor was set onto a steel frame, which was moved by an actuator, rather than a jacking device.

At about 26 kN (10% of P_{pk}), four LVDTs (**Figure 4-12**) were set in order to measure the displacements of an anchor plate (A), core wire (CW), one of the six helical wires (HW), and one set of the wedges (W).

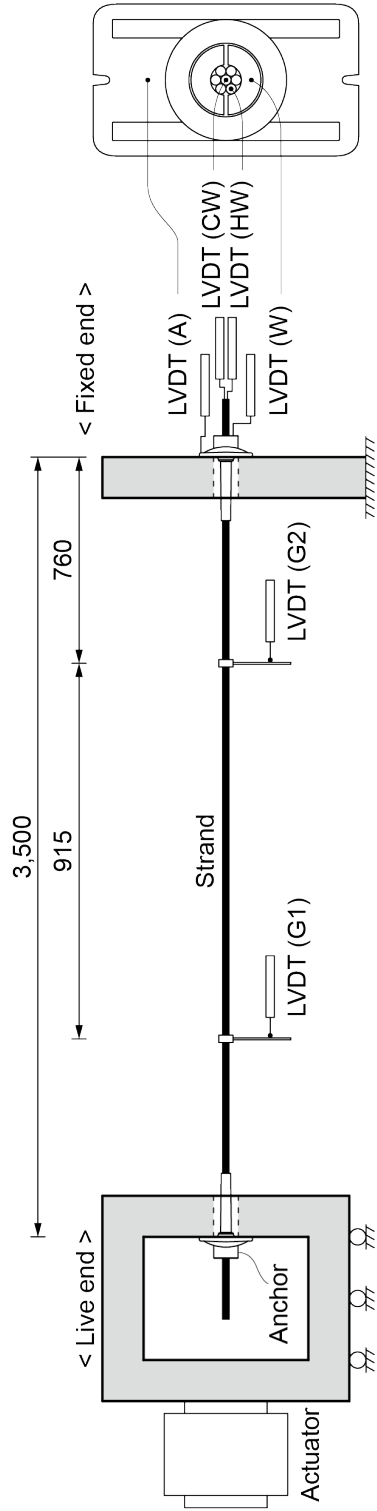


Figure 4-11 Test set-up plan [unit: mm]

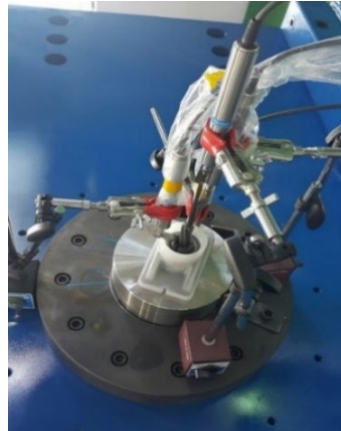


Figure 4-12 Set-up at fixed end



Figure 4-13 Set-up in free length

The free length of the strand was 3,500 mm. For SE3, two LVDTs (G1 and G2), as shown in **Figure 4-13**, were added in order to measure the elongation in the middle of the strand, thus satisfying the stipulations in ACI 423.7 (2014).

For safety purposes, the loading was stopped just before the fracture of the strand. Only the test for SE3 was carried out until the strand fractured, but the LVDTs were removed before strand breaking due to the risk of breakage or failure.

4.2.2 Test Results

For all specimens, the load of 80% of P_{pk} was maintained for one hour, after which the load was increased up to over 260 kN (**Figure 4-14**). Only the SE3 specimen was tested up to strand fracture; however, the LVDTs were removed after one hour to ensure compliance with equipment safety guidelines. The measured maximum loads (268.5, 266.6, and 270.5 kN) exceeded 100% (260 kN) of P_{pk} for all specimens, thus indicating that the load-carrying capacity has been confirmed.

The displacements of the CW, HW, and W were calibrated by subtracting the value of A. At 80% of P_{pk} , the anchorage slip displacement was only approximately 3 mm, which is within the wedge draw-in range of 3 to 5 mm for fixed end mentioned in EOTA (2013). This, in turn, demonstrated the stabilized performance of the tendon assembly.

The relationship between the elongation percentage (strain) and stress is plotted in **Figure 4-15**. The strain increased rapidly to over 0.03 beyond 1,860 MPa. Fracture occurred at about 0.04 of strain in the SE3 specimen. The elongation percentage results demonstrate the sufficient ductility of the tested strands before fracture and satisfactory performance of the tested tendon assemblies.

The partial elongation of the SE3 specimen was obtained using the difference between the displacements of G1 and G2. The measured portion was much closer to the fixed end. The partial elongation for the SE3 specimen was approximately 75% of the total elongation. The fact that the tensile strain increased more at the jacking end than at the fixed end was a new finding.

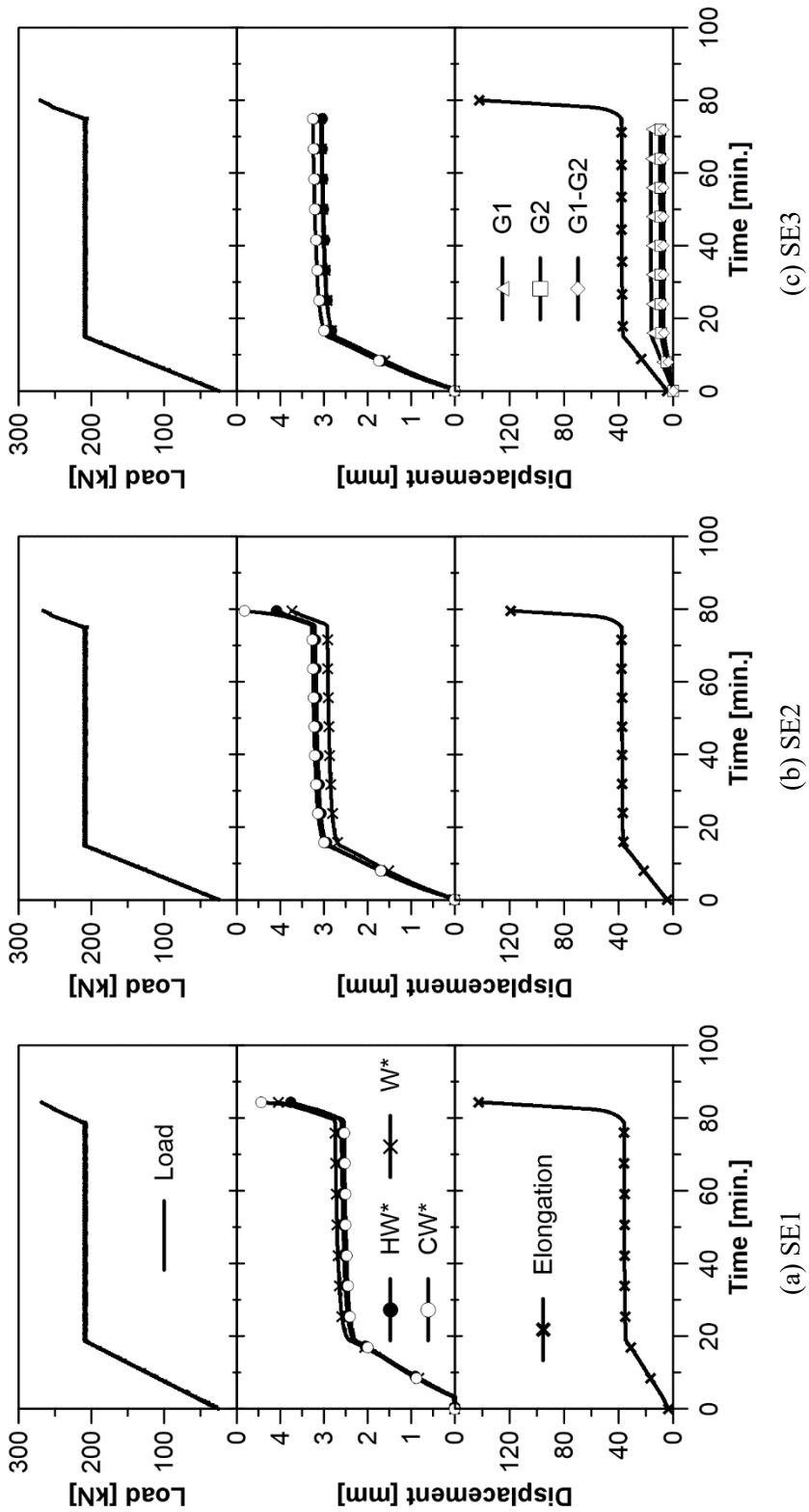


Figure 4-14 Static load test results

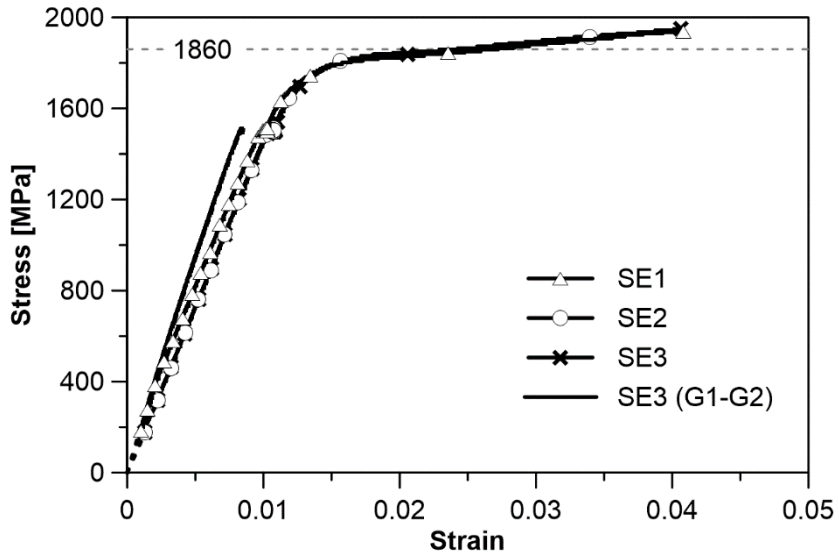


Figure 4-15 Stress-strain curve of static load test for encapsulated anchor

4.3 Fatigue Test

The objective of fatigue test is to verify behavior of the anchor, wedges, and the strands under cyclic loads. The experiment for encapsulated anchor was performed with the equipment developed at Korea Conformity Laboratories (KCL). However, due to limitations of the device, only the casting (removed encapsulating plastic) was used to secure the free length of the strand.

4.3.1 Test Set-up

The test method was in accordance with KCI-PS101 (2010). The anchorages without plastic coating were used at both ends, with the free length of the strand being 1 m (**Figure 4-16**). The 3-piece wedges were used.

The strand was inserted into the anchors with 3-piece wedges, and each anchor was hanged to the steel jigs, as shown in **Figure 4-17**. Both ends were fixed with hinges so that the longitudinal axis was maintained parallel to the ground plane when the strand was elongated.

According to the test method (KCI-PS101, 2010), the repetitive load with range from 156.6 kN to 167.7 kN was planned to be two million times at 3 Hz. After increasing slowly over about one minute to 162.2 kN, the middle value of the range, the cyclic load was exerted in the form of a sin wave (**Figure 4-18**).

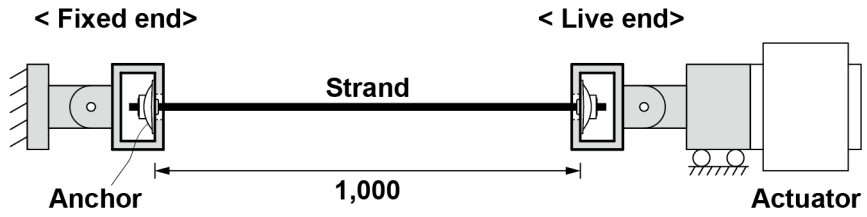


Figure 4-16 Fatigue test plan [unit: mm]

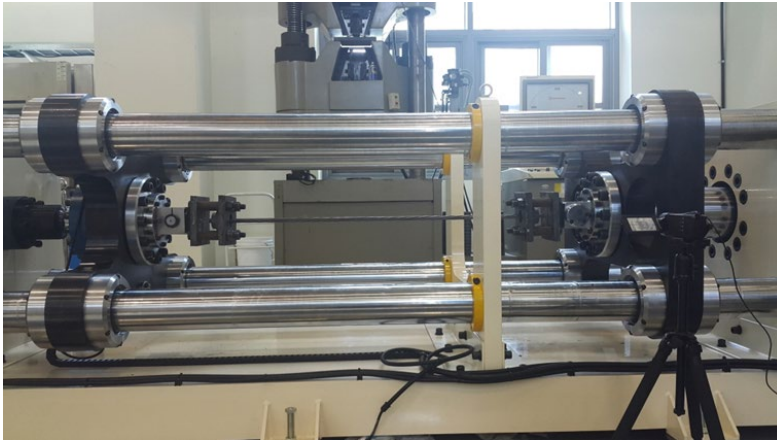


Figure 4-17 Fatigue test set-up

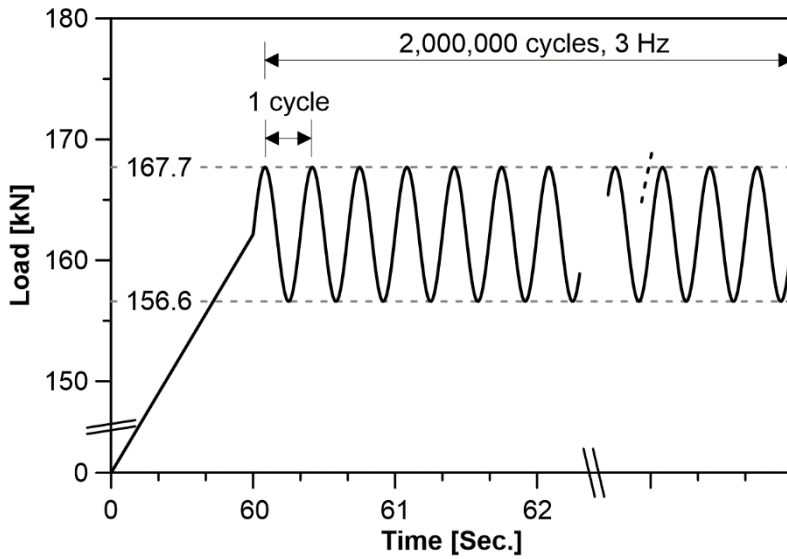


Figure 4-18 Fatigue load

4.3.2 Test Results

The maximum and minimum peaks of applied cyclic loads are shown in **Figure 4-19**. The test was conducted in approximately 7.7 days. There were slight variations in load amplitude since a hydraulic pump operated the actuator. Despite the amplitude variations by a hydraulic pump, the loading range was maintained evenly. The average peaks were found to be slightly higher than designed load. The data from day four to seven were not obtained due to the equipment's recording storage problem.

After the test, no cracks were observed in the anchors and wedges (**Figure 4-20**). The tendon was stretched due to fatigue loads, but no fracture of the strand was found to occur. These results prove the long-term performance of the developed anchorages.

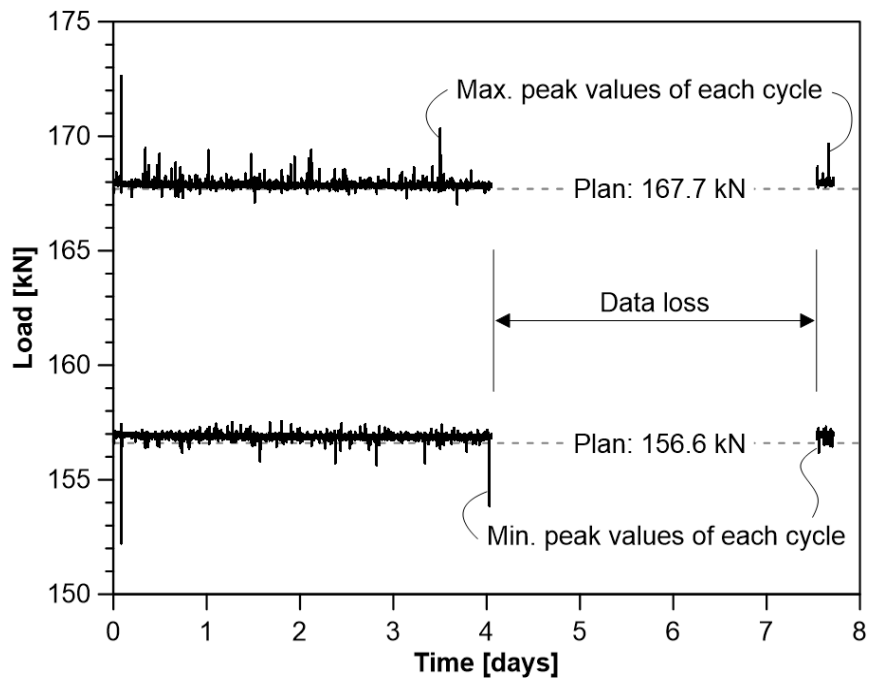


Figure 4-19 Maximum and minimum peak loads of each cycle



Figure 4-20 Tested anchor and wedges

4.4 Load Transfer Test for One Anchor

The load transfer test is a method of confirming the load of supporting the ability of the anchorage. It is mainly aimed at verifying the details of the anchorage zone reinforcement. A load transfer test including only one anchor was performed in accordance with the test method of KCI-PS101 (2010). Bare anchors were used because the tests were confirmed before the encapsulated anchor was developed.

4.4.1 Test Set-up

The test specimen was made of concrete square column for uniaxial compression test, considering the general slab thickness and the anchor size, the length and width of the cross-section were set to 300 mm and 250 mm, respectively. The specimen height was determined to be 600 mm because it should be more than twice the length of the two sides (KCI-PS101, 2010).

The two sets (A and B) of specimens were manufactured, but the concrete was poured on different day for each set. Designed concrete compressive strength was 27 MPa. The specimen was demolded after one day from pouring and then coated with curing agent to replace the wet curing.

The test specimens do not contain the strands because they were tested by compression, and not by tensioning the strand. It is also notable that the presence of

strands creates resistance in the compression process. A sheathing tube of $\text{Ø}15.2$ mm strand was inserted at the center of the member to render the concrete void.

The auxiliary reinforcement was included in each specimen. Four longitudinal bars were SD400 D13, and three stirrups of SD400 D10 were placed with intervals of 170 mm in order to stimulate the condition of the continuous concrete member. The additional steel for lifting specimen may affect the test results. Therefore, two of four longitudinal bars located at the corner was made of one reinforcing bar to be connected to the outside of the member. The specimens were lifted and moved with this part.

To confirm the performance change in accordance with the reinforcement details, a total of 18 specimens were manufactured as listed in **Table 4-5**. B refers to two reinforcing bars placed directly in front of the bearing plate. P signifies two hairpin bars for resisting the bursting force. MB is reinforcing bars that is parallel to B, but the location inside of P. N indicates the specimen with no reinforcement for anchorage zone. The numbers indicate the following reinforcing bar (SD400) specifications: 10, 13, and 16 mean D10, D13, and D16, respectively.

Figure 4-21 shows the detailed drawing of the specimens. B should be extended 150 mm both outside from the anchor group in the slab (ACI 423.3R, 2017). However, Since B and MB could not be placed in a straight line due to the specimen size, B and MB were made in the form of a 90-degree bent hook, and the length of the hook was 150 mm in order to ensure sufficient bond length.

ACI 423.3R (2017) also suggests that the minimum vertical length of the P is 230 mm. On the other hand, KCI-PS101 (2010) regulates that the reinforcement details should not be placed below the middle height of the specimen. Therefore, P was extended only to the middle height of the specimen.

The reinforcement of each specimen before pouring concrete has been shown in **Figure 4-22**. A total of 45 concrete cylinder specimens were prepared to check the concrete strength every day, and tests were conducted on the day when the concrete strength was about 21 MPa. Prior to the test, the concrete strain gauges were attached as shown in **Figure 4-23**, which was used in the stabilization formula, **Eq. (2-5)**.

The load was applied following procedure of **Figure 2-7**. After reaching 208.8 kN, cycle loads with range from 31.3 kN to 208.8 kN were input at least 10 times until the stabilization condition was met. Subsequently, the load was increased until the specimen was fractured. After the experiment, the anchor was extracted from the concrete member to check the condition, as shown in **Figure 4-24**.

Table 4-5 Names of load transfer test specimens

		Hairpin bars (P)			
		N	P10	P13	P16
Horizontal bars (B)	N	A-N B-N	-	-	-
	B13	A-B13 B-B13	A-B13P10 B-B13P10	A-B13P13 B-B13P13	-
	MB13	A-MB13 B-MB13	A-MB13P10 B-MB13P10	-	-
	B16	A-B16 B-B16	-	A-B13P13 B-B13P13	A-B13P16 B-B13P16

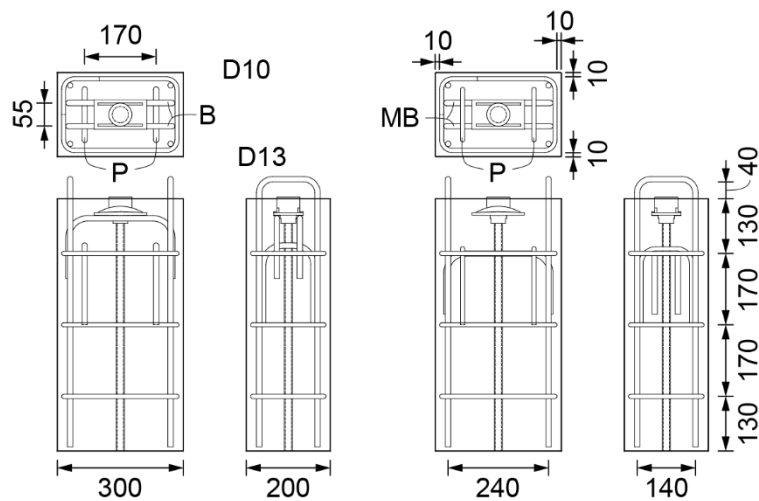


Figure 4-21 Drawings of load transfer test specimens [unit: mm]



(a) N



(b) MB13



(c) MB13P10



(d) B13



(e) B13P10



(f) B13P13



(g) B16



(h) B16P13



(i) B16P16

Figure 4-22 Reinforcement details for load transfer tests

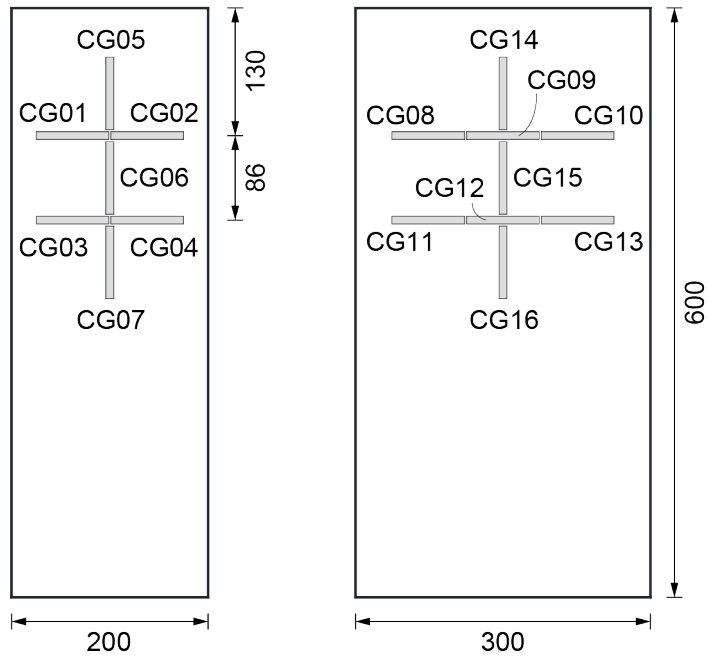


Figure 4-23 Concrete strain gauges of load transfer test specimens [unit: mm]



Figure 4-24 Extracting anchors from concrete specimen after load transfer tests

4.4.2 Test Results

The compressive strengths of set A and B were 20.0 MPa and 21.5 MPa, respectively.

The concrete strength was measured with randomly selected three specimens of cylinder for each set on the test day.

The input load has been illustrated in **Figure 4-25**. The number of cycles and measured maximum load has been summarized in **Table 4-6**. B-N was found to have the operation problem of equipment. A-B13 stabilized after 15 cyclic loads. Three specimens (A-B13P13, A-B16, B-B13P10) and two specimens (A-B16P13 and B-MB13) needed 11 and 12 cycles to be stabilized, respectively. Ten cyclic loads were applied for other specimens. Only the strain value of the concrete gauge was used to determine the stabilization state, because there were no visible cracks up to $0.8P_{pk}$.

B-N was found to have the smallest fracture load (422.2 kN), while B-B16 had the largest value (559.6 kN). They are 1.62 times and 2.14 times the nominal tensile strength of strand, respectively. With an increase in the amount of reinforcement steels, the magnitude of the failure load increased proportionally. B displayed 4.7% higher performance than MB, which seems to be more effective in order to reinforce closer to anchorage.

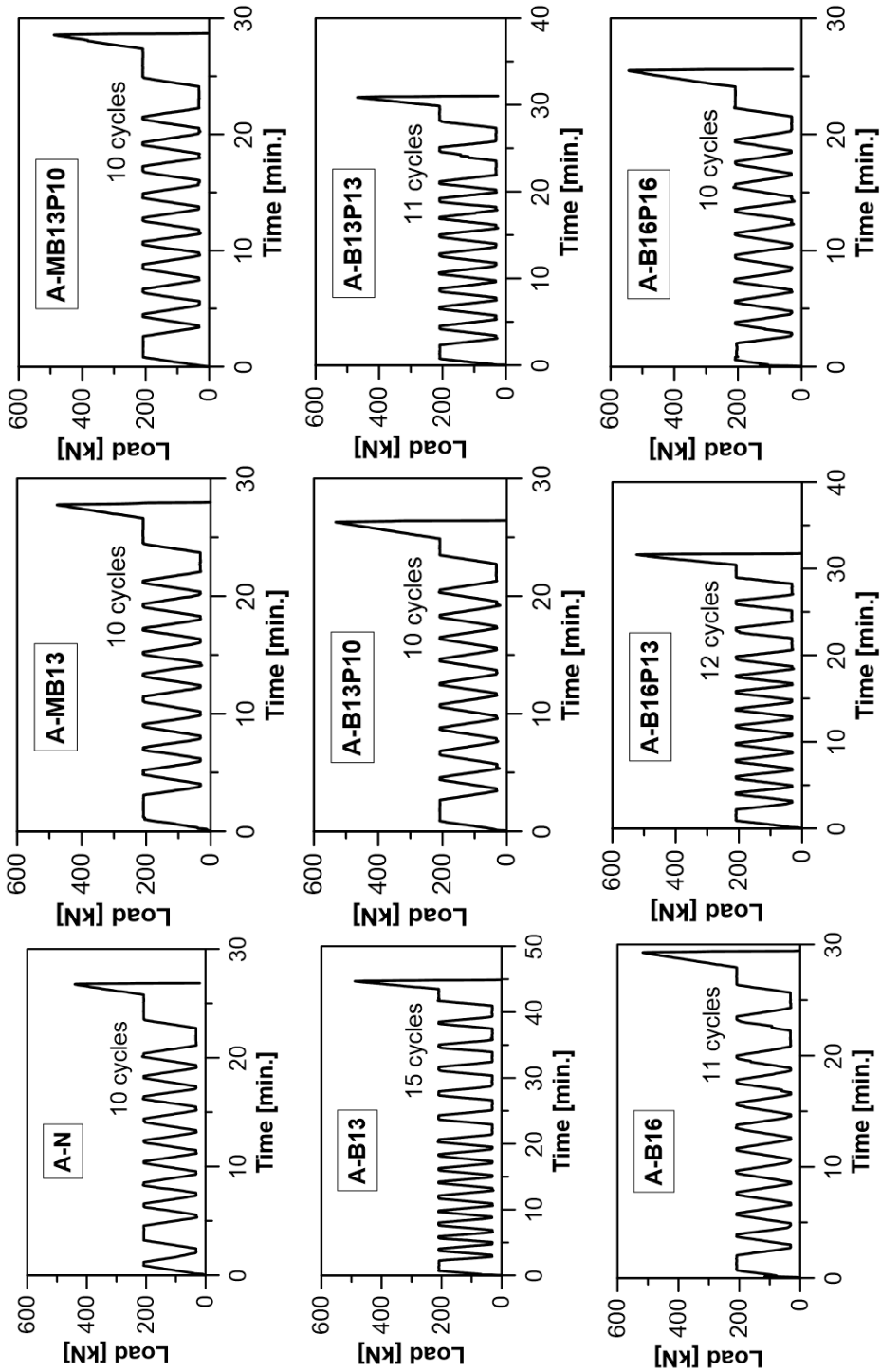


Figure 4-25 Load-time

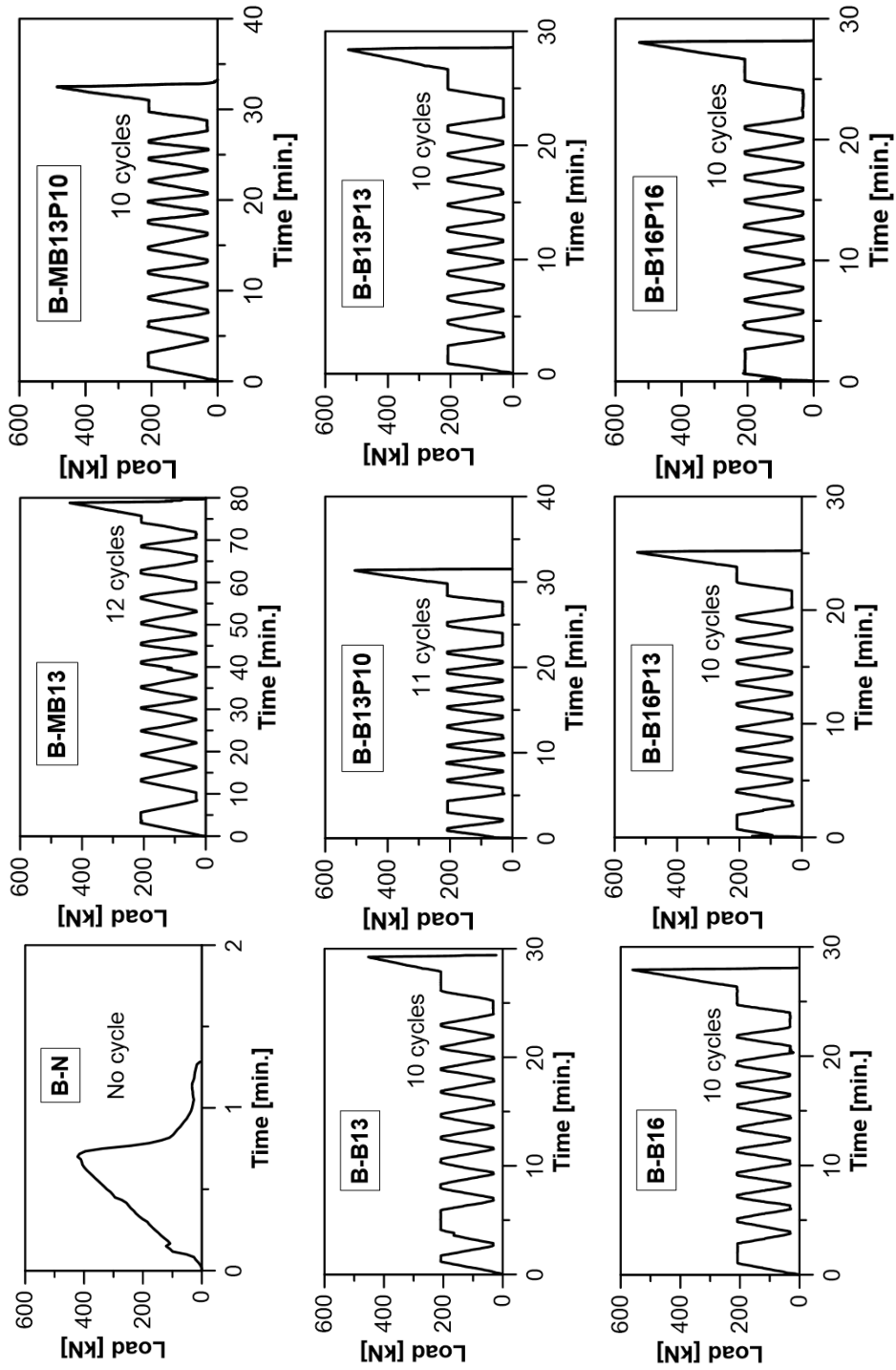
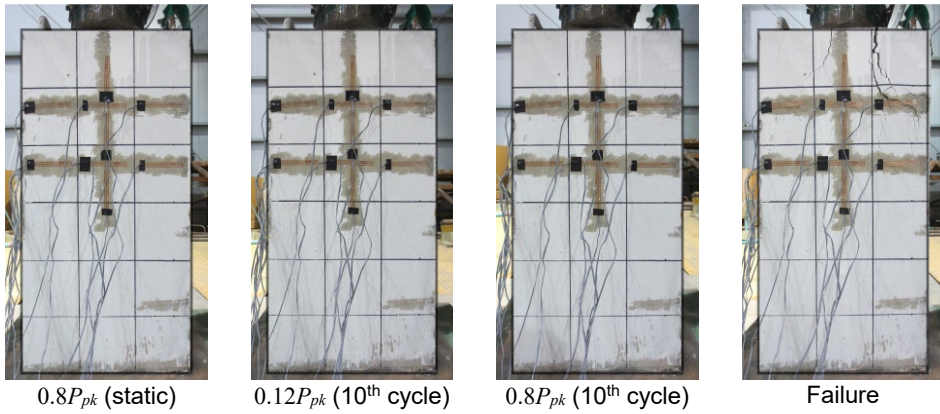


Figure 4-25 Load-time (continued)

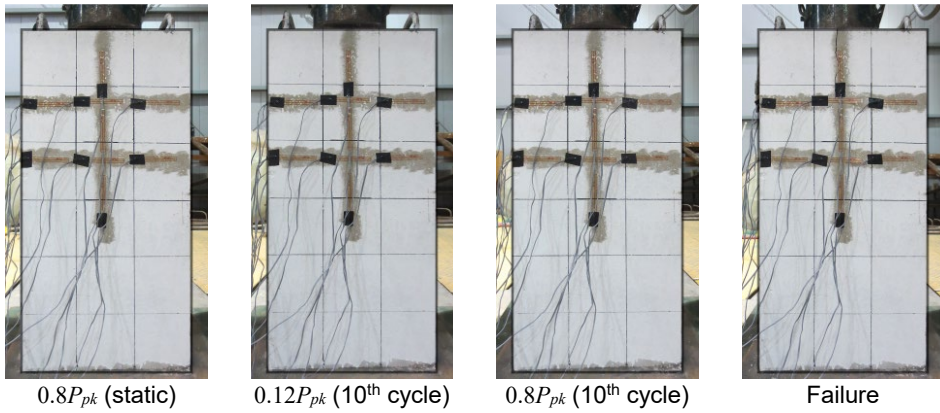
Table 4-6 Results of load transfer tests for one anchor

Specimen	<i>n</i>	Maximum load [kN]	Specimen	<i>n</i>	Maximum load [kN]
A-N	10	440.1	B-N	0	422.2
A-MB13	10	476.4	B-MB13	12	439.8
A-MB13P10	10	488.6	B-MB13P10	10	485.8
A-B13	15	488.6	B-B13	10	452.6
A-B13P10	10	532.4	B-B13P10	11	505.2
A-B13P13	11	468.6	B-B13P13	10	526.8
A-B16	11	517.1	B-B16	10	559.6
A-B16P13	12	523.0	B-B16P13	10	527.1
A-B16P16	10	543.1	B-B16P16	10	527.7

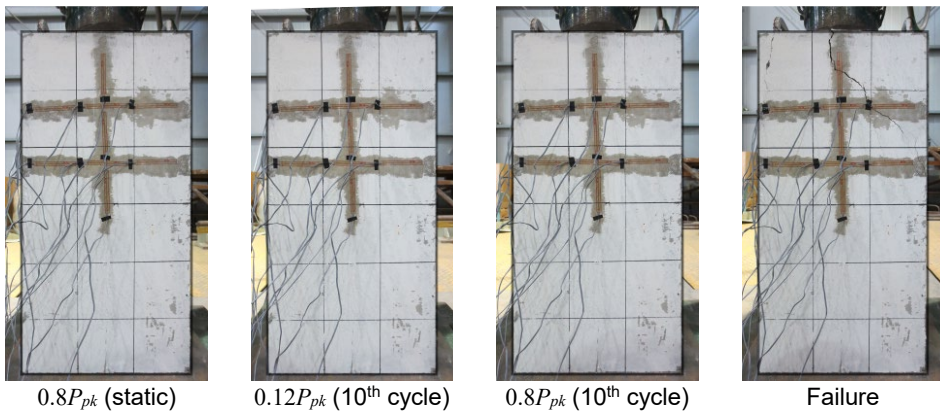
Figure 4-26 shows the crack shape of each specimen at the time point of loading. Almost no cracks were found during cyclic loading. Due to the fact that the magnitudes of the break loads were all different and some specimens were excessively stressed after the fracture, it is difficult to equally compare the size and number of cracks. However, the tendency or overall shape of cracks was meaningful. The first crack occurred near the anchor or in the middle of the anchorage zone and became parabolic as the crack expanded. The inflection point of the parabola was located about 50 ~ 100 mm from the top of the specimen (below the bearing plate). The greater the capacity of the hairpin reinforcement (P), the smaller the parabola's width. It was found that horizontal rebars located just in front of the anchor (B) did not affect the parabolic width, while the steels away from the anchorage (HB) contributed to reducing the width.



(a) A-N

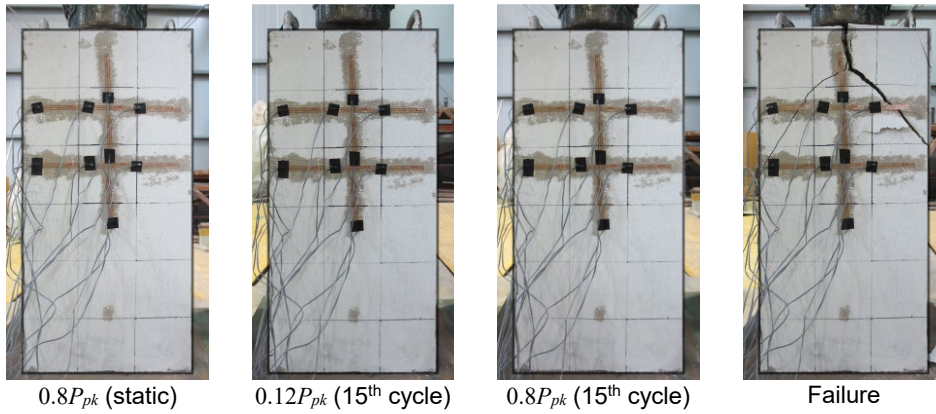


(b) A-MB13

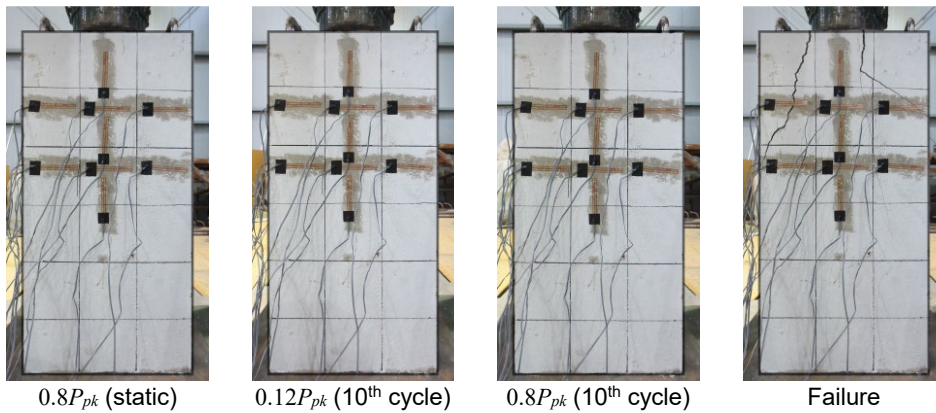


(c) A-MB13P10

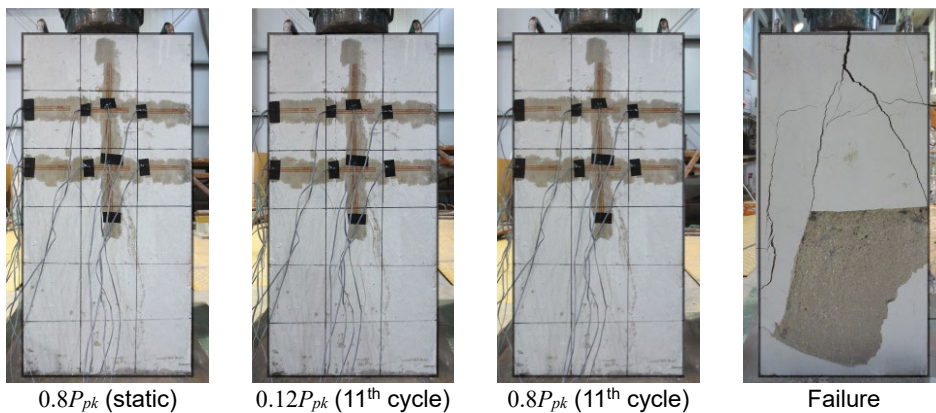
Figure 4-26 Failure sequences



(d) A-B13

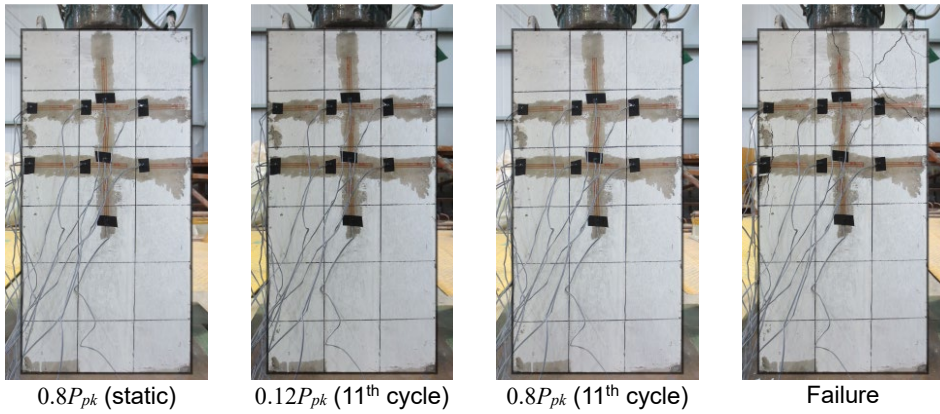


(e) A-B13P10

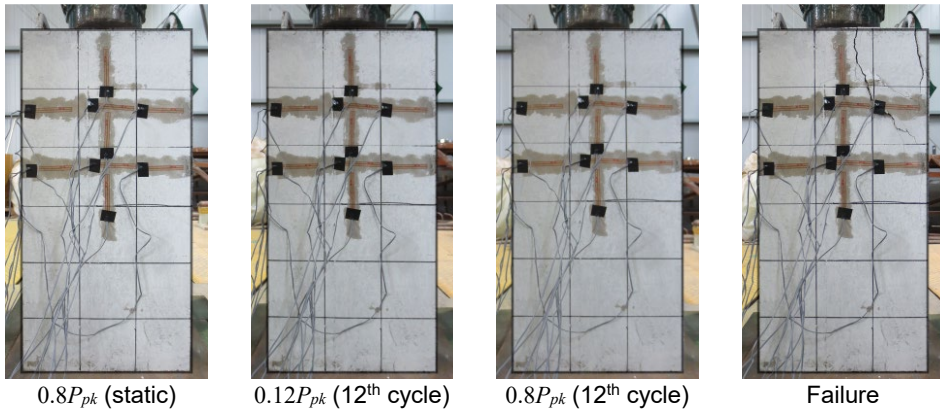


(f) A-B13P13

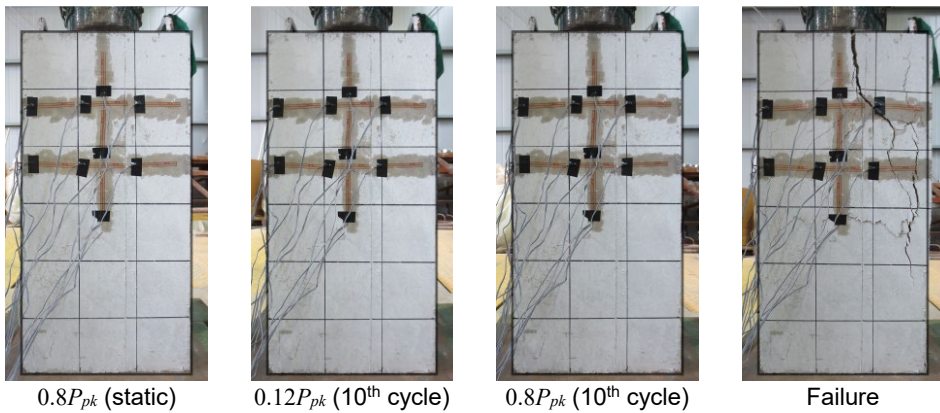
Figure 4-26 Failure sequences (continued)



(g) A-B16



(h) A-B16P13



(i) A-B16P16

Figure 4-26 Failure sequences (continued)

(No picture)

(No picture)

(No picture)



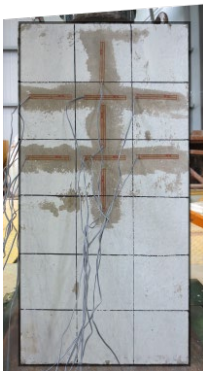
Failure

$0.8P_{pk}$ (static)

$0.12P_{pk}$ (10th cycle)

$0.8P_{pk}$ (10th cycle)

(j) B-N



$0.8P_{pk}$ (static)



$0.12P_{pk}$ (12th cycle)

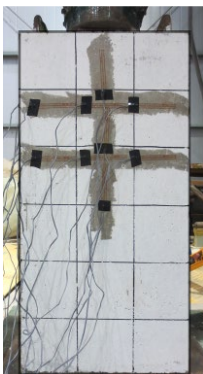


$0.8P_{pk}$ (12th cycle)

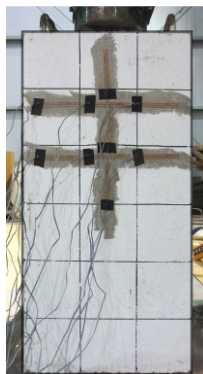


Failure

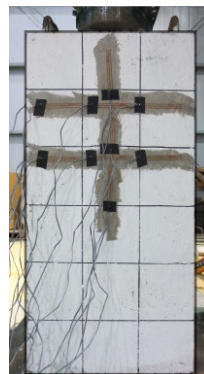
(k) B-MB13



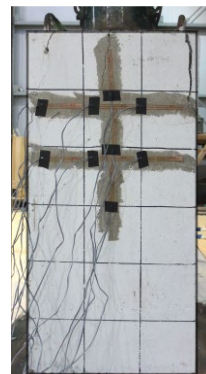
$0.8P_{pk}$ (static)



$0.12P_{pk}$ (10th cycle)



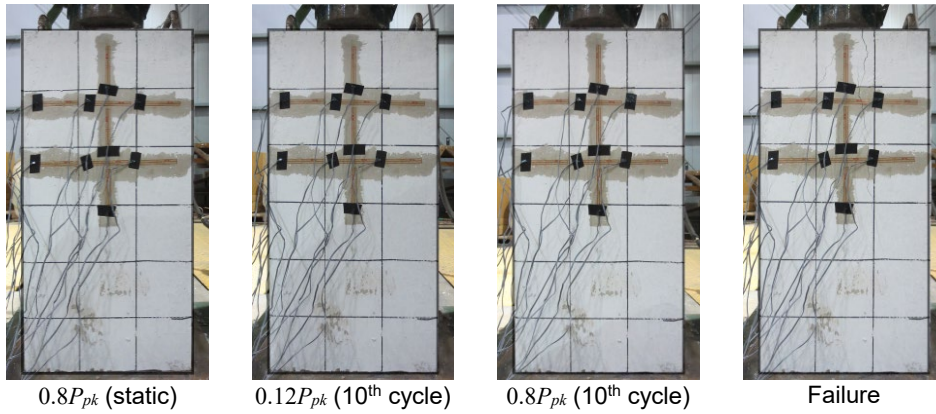
$0.8P_{pk}$ (10th cycle)



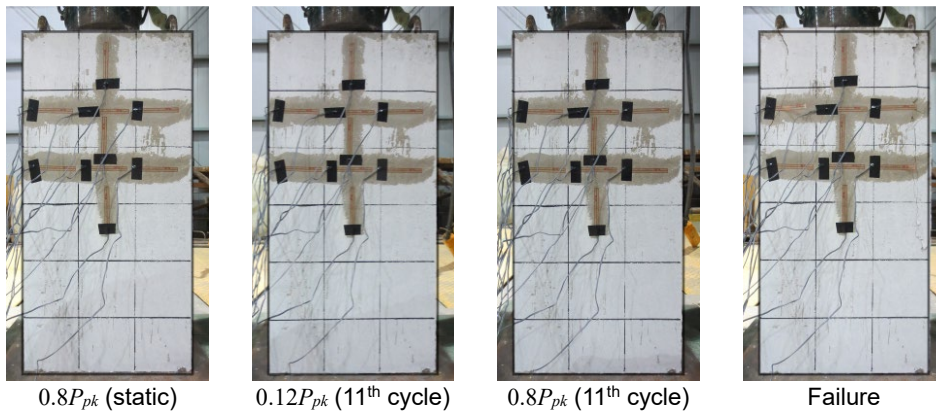
Failure

(l) B-MB13P10

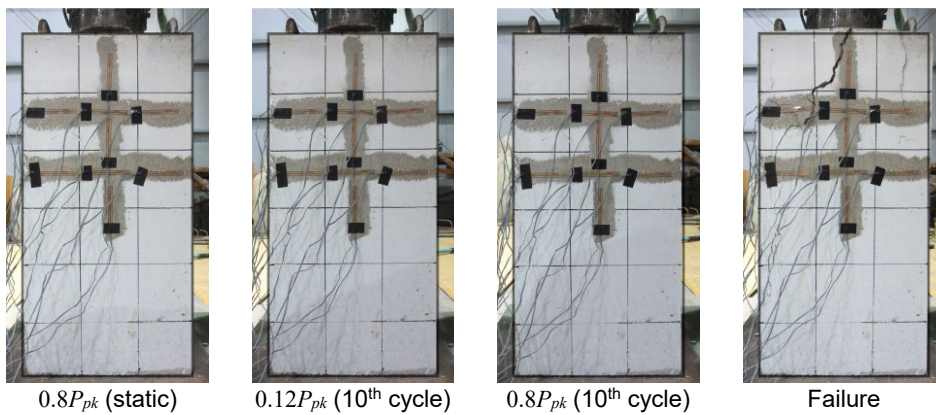
Figure 4-26 Failure sequences (continued)



(m) B-B13

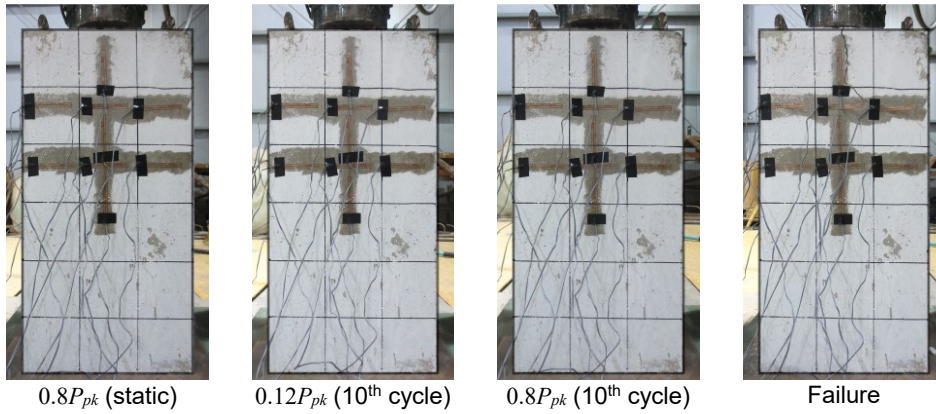


(n) B-B13P10

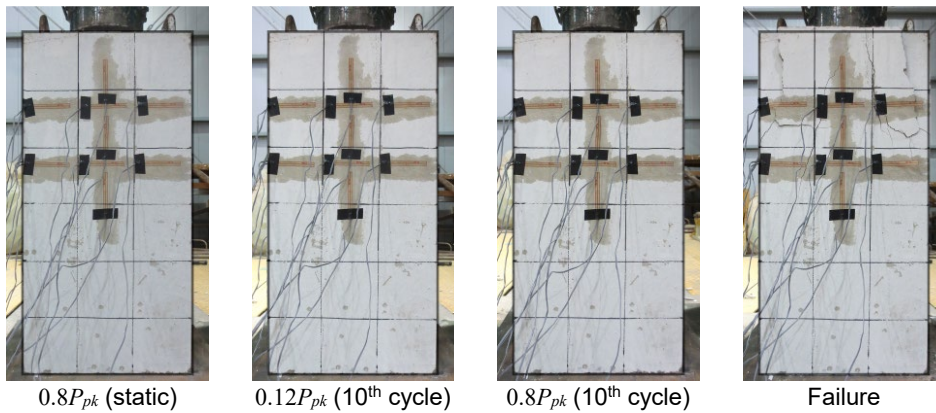


(o) B-B13P13

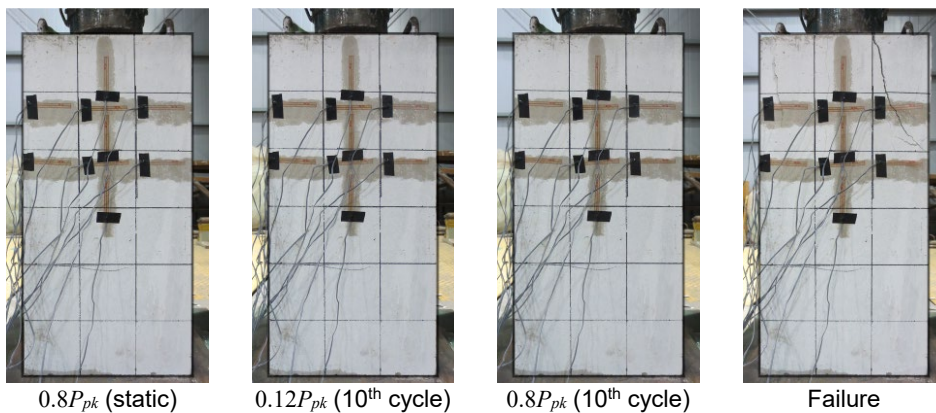
Figure 4-26 Failure sequences (continued)



(p) B-B16



(q) B-B16P13



(r) B-B16P16

Figure 4-26 Failure sequences (continued)

Figures 4-27, 4-28, and 4-29 illustrate stress contours using concrete strain gauge results of $0.8P_{pk}$ of the first cycle, $0.12P_{pk}$ of the last cycle, and $0.8P_{pk}$ of the last cycle, respectively, and the predicted modulus of elasticity (26,702 MPa) using the following equation and designed concrete strength (27 MPa).

$$E_c = 8500\sqrt[3]{f_{cu}} \text{ [MPa]} \quad (4-1)$$

where E_c is elastic modulus of concrete; and f_{cu} is the average compressive strength of concrete on the 28th day.

Solid and dashed lines signify the stresses distribution of tension and compression. The magnitudes of both compressive and tensile stress were found to be greater when the load was large ($0.8P_{pk}$) than when the load was small ($0.12P_{pk}$).

Given that the failure load and the number of reinforcing bars was proportional to each other, the higher the amount of rebar in the anchorage zone, the better the load carrying capacity. B-B13 had measured values of the strains and stresses that were found to be small because the deformations primarily occurred on the opposite side of the measured surface due to eccentricity.

Bursting stress was observed to be the greatest at about 100 mm away from the bearing plate, regardless of the type of reinforcement details or the magnitude of the load. This is where CG09 is located. Bursting force acted transversely, and P resisted to the bursting effect.

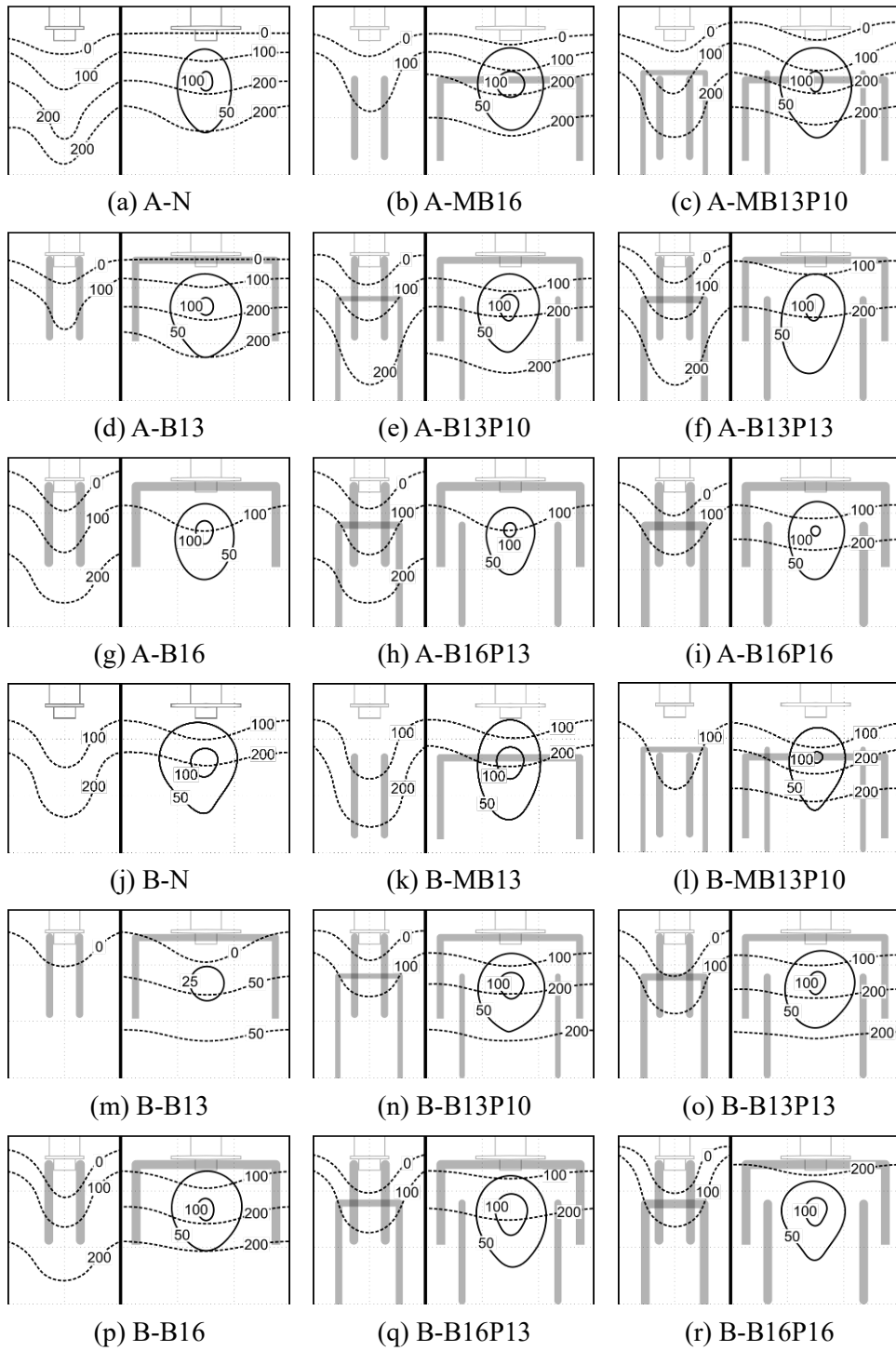


Figure 4-27 Stress contour at $0.8P_{pk}$ of first cycle [unit: MPa]

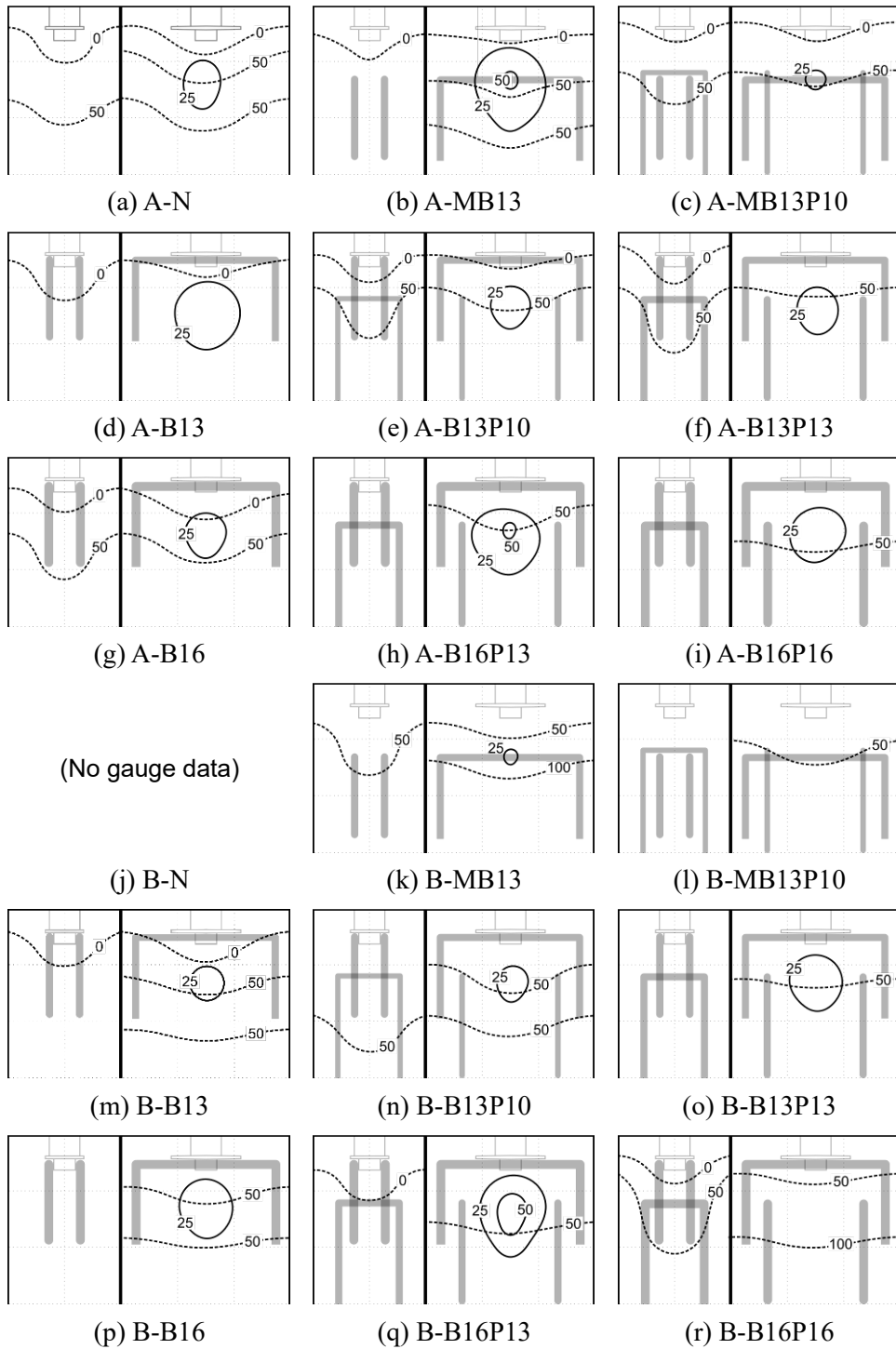


Figure 4-28 Stress contour at $0.12P_{pk}$ of first cycle [unit: MPa]

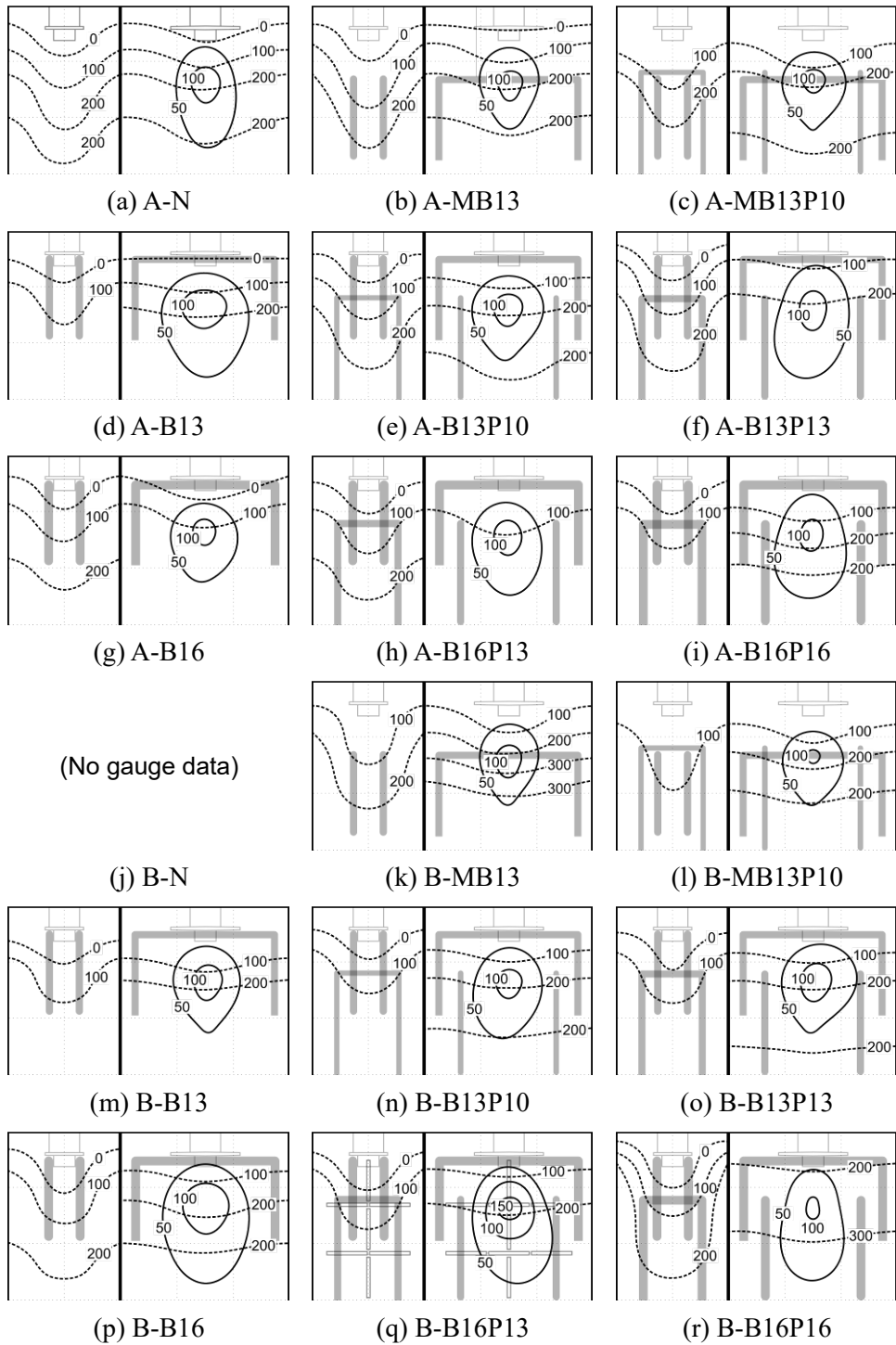


Figure 4-29 Stress contour at $0.8P_{pk}$ of last cycle [unit: MPa]

The top view of the specimen after the test has been shown in **Figure 4-30**. Initially, the anchor only 10 mm protrusion was pressed by a square shape steel plate. However, as displacements increased with the increase in load, the steel plate contacted to the top surface of concrete specimen. The steel plate inhibited the expansion of the cracks which were already occurred in the inner region of the plate. The widths of other cracks were increased as there was an increase in the applied load.

The crack patterns of all specimens around the anchor were collected and expressed in **Figure 4-31**. The crack proceeded from the center of the anchor toward the vertex of the bearing plate. The average angle of cracks was 29.4° , and $\tan 29.4^\circ$ is 0.56, corresponding to the ratio of the width and length of the bearing plate. However, as the concrete members began to be loaded by the square steel plate, the cracks expanded about 45° from the vertexes of the plate.

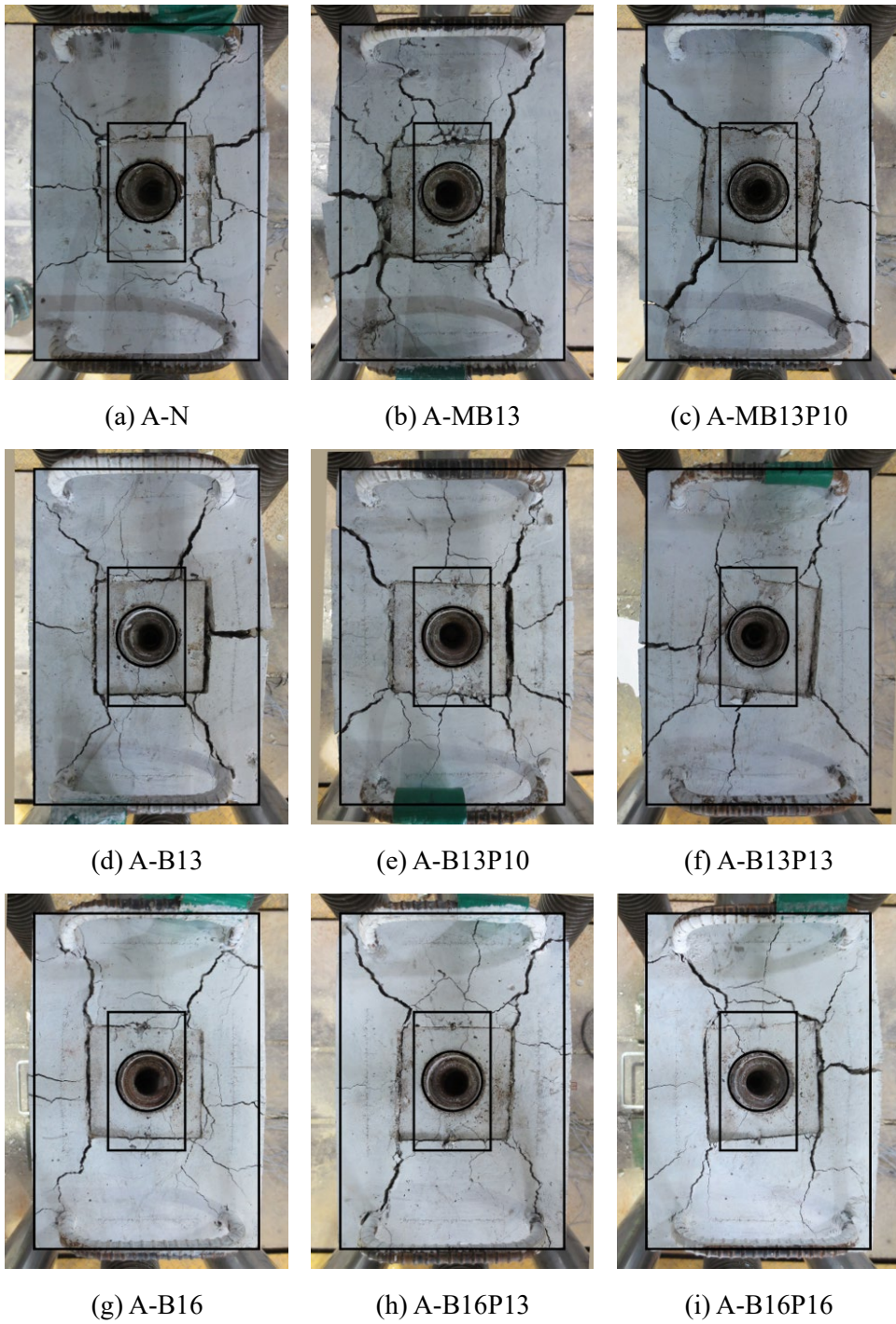


Figure 4-30 Failure mode

(No picture)



(j) B-N

(k) B-MB13

(l) B-MB13P10



(m) B-B13

(n) B-B13P10

(o) B-B13P13



(p) B-B16

(q) B-B16P13

(r) B-B16P16

Figure 4-30 Failure mode (continued)

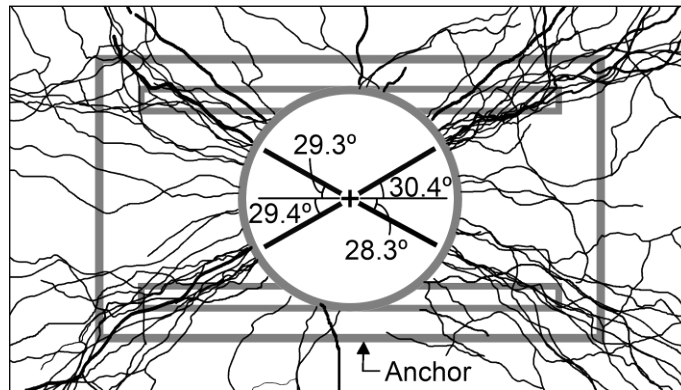


Figure 4-31 Crack patterns of failure mode

After the anchor was taken out from each test specimen, the condition was confirmed. **Figure 4-32** and **Figure 4-33** illustrate the state of the head and the side, respectively, after the test. No cracks or deformation were found at the anchor head and wedge cavity, except the rust. In most of the specimens, the bearing plate had no deformation or slight warpage, but no cracks were found. A slight warpage did occur, indicating that the anchor was ductile, as was the purpose of using the anchor material as the ductile cast iron.

For A-B13P10, B-B13P10, and B-B16P13, the cracks occurred on the bottom of one side of bearing plate. It seems to be caused by excessive fracture load or continued loading after fracture, and it is believed that cracking did not occur under service load. The bearing plate of B-MB13P10 was broken by the impact of the equipment while taking out the anchor from the concrete member.

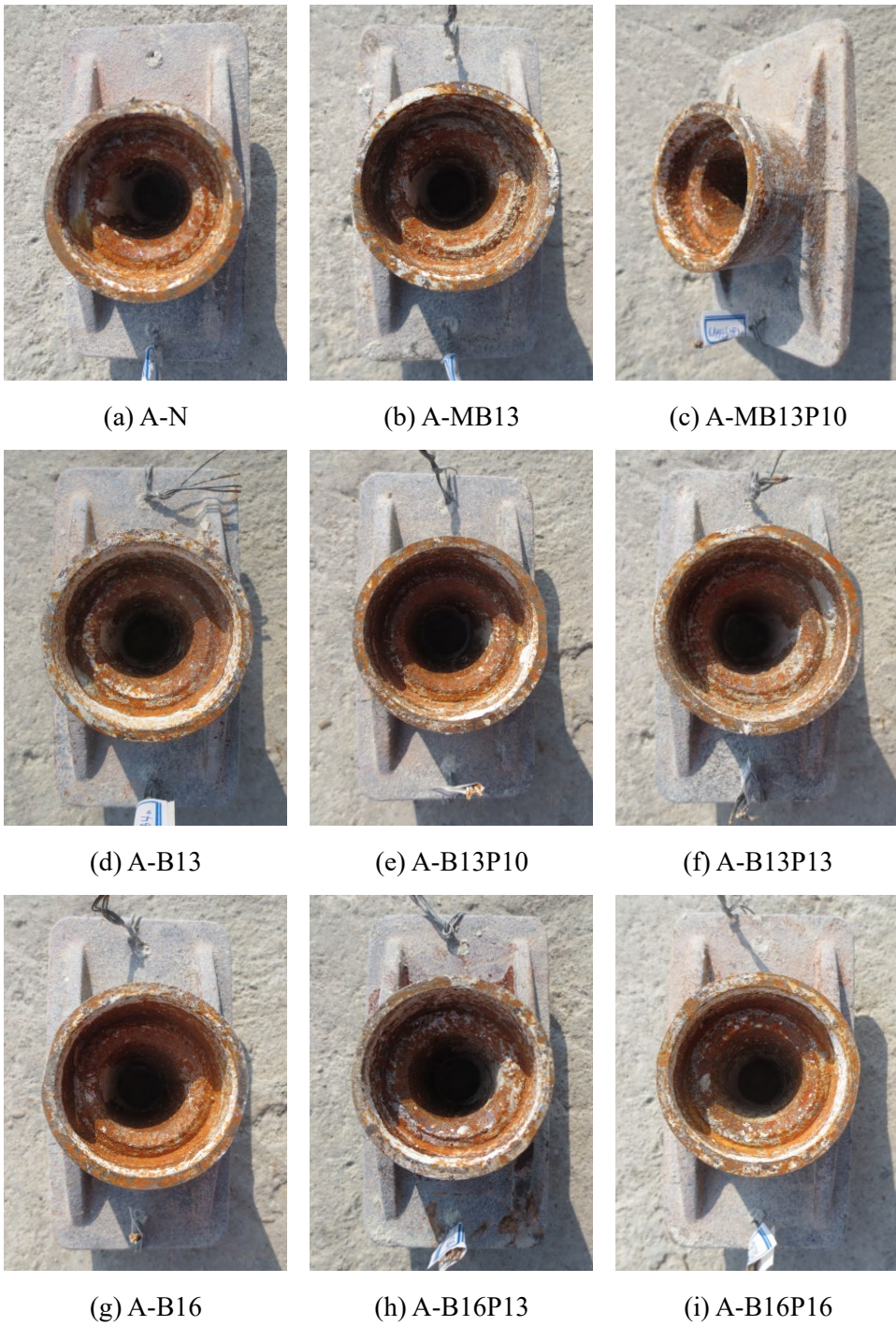


Figure 4-32 Anchors after load transfer test



(j) B-N



(k) B-MB13



(l) B-MB13P10



(m) B-B13



(n) B-B13P10



(o) B-B13P13



(p) B-B16



(q) B-B16P13



(r) B-B16P16

Figure 4-32 Anchors after load transfer test (continued)

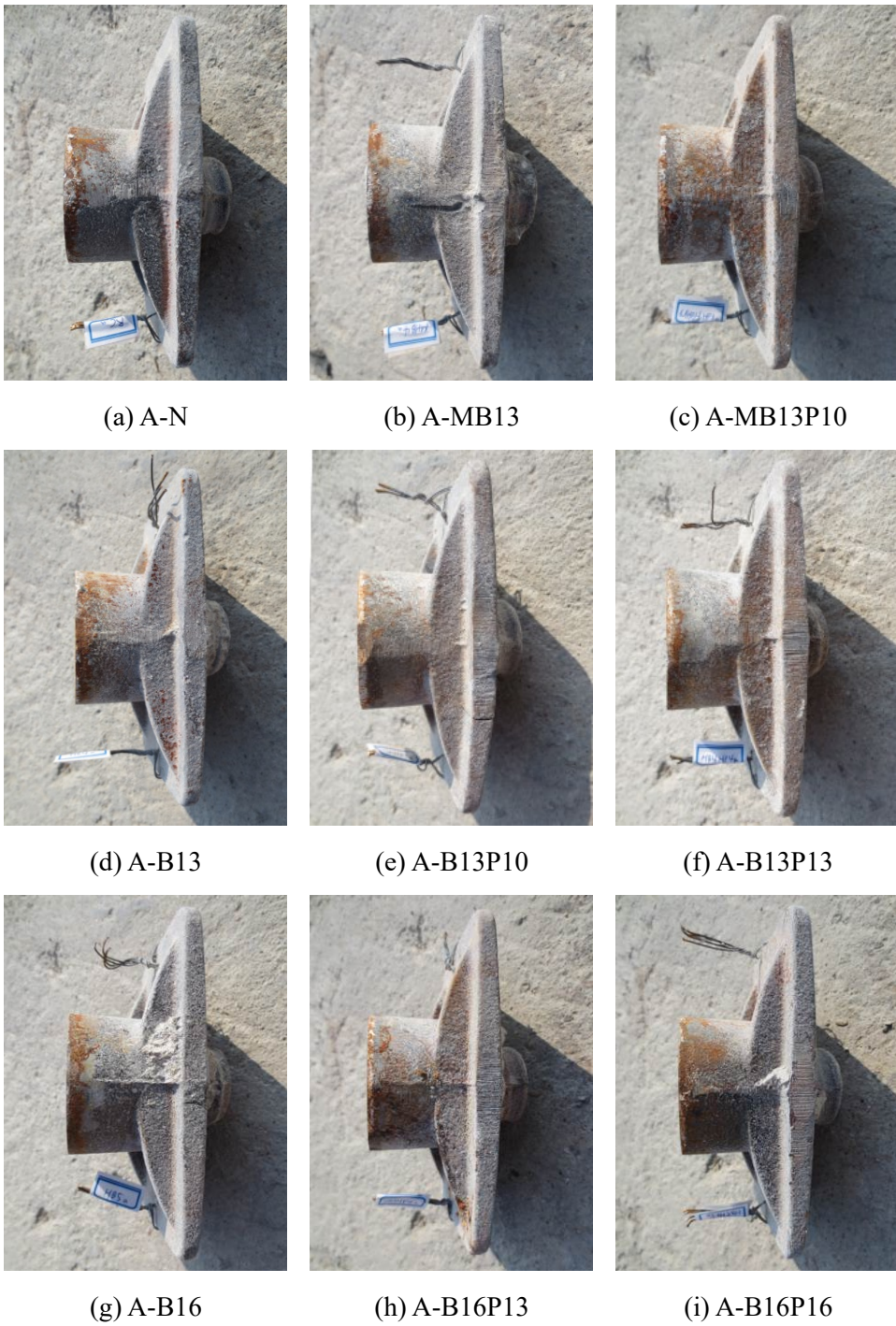


Figure 4-33 Side views of anchors after load transfer test



(j) B-N



(k) B-MB13



(l) B-MB13P10



(m) B-B13



(n) B-B13P10



(o) B-B13P13



(p) B-B16



(q) B-B16P13



(r) B-B16P16

Figure 4-33 Side views of anchors after load transfer test (continued)

4.5 Load Transfer Test for Three Anchors

For two-way slabs, banded tendons, two or more anchorages are commonly used. When using more than one anchorage, one more hairpin reinforcement should be placed than the number of anchorages in accordance with ACI 423.3R (2017). In this section, a load transfer test was performed in order to verify the reinforcement details in anchorage zone for a banded group of three anchorages.

4.5.1 Test Set-up

The specimen was designed in the form of rectangular column. The length and width of the cross-section were 550 mm and 210 mm in consideration of the minimum thickness of PT slab. The minimum height should be 1,100 mm in accordance with KCI-PS101 (2010). In the load transfer test for one anchor, the effect of auxiliary reinforcement was considered to be excessive compared to the nominal tensile strength of one strand. Therefore, the height was decided to be 400 mm without the auxiliary reinforcement.

The number of test specimens was 24, listed in **Table 4-7**, considering the following three factors as variables: concrete strengths, reinforcement details, and anchors. Two types of concrete strengths were applied: low strength of about 15 MPa (Set L) and high strength of about 24 MPa (Set H). In order to confirm the performance of

the developed bare anchor (C), one of commercially available anchors (D) was selected as the control group. Additionally, four kinds of reinforcement details for anchorage zone were set as variables: the most basic method of placing two horizontal bars (B13), reinforcing additional hairpin bars to two horizontal bars (B13P13), a spiral reinforcing bar (S) detailed in **Figure 4-34**, as well as a spiral reinforcement with extended bar for corners (SC) in order to reduce the occurrence of concrete dropout at the end or corner in consideration of bent end reinforcement by extending both horizontal bars in the spiral reinforcement details.

For flat slab-column connections, S was originally used as the punching shear reinforcement. The spiral shape was found to significantly increase the binding effect of concrete, which is beneficial for the improvement of punching shear strength and securing ductility. It was thought that it would be effective to use S with such characteristics for reinforcing anchorage zone, and the performance was verified experimentally.

The specimen drawings have been illustrated in **Figure 4-35**. The spacing between the anchorage centers was 75 mm. The reinforcement of B13 was placed in accordance with PTI (2006). One rebar was placed 40 mm away from the bearing plate and the other one was placed opposite the plastic sheathings so that the distance between two rebars was 40 mm. The length of horizontal bars was 505 mm, extending 150 mm from the end of the anchorage to both ends of the member. In B13P13, two horizontal rebars were located 95 mm from the bearing plate and four hairpin reinforcements were placed at 75 mm intervals.

The center of the spiral of S and SC was 95 mm from the bearing plate. A 35-mm high chair was welded so that the Ø12-mm bar could contact the bottom of the sheathing. An SD400 D13 was added to provide two-horizontal-rebar system, which was positioned just below the bearing plate.

According to KCI-PS101 (2010), reinforcing details should not be included below half the height of the specimen. However, because these specimens did not have any auxiliary reinforcement, all reinforcing details were contained even below half the height. **Figure 4-36** illustrates the reinforcement details of each specimen before concrete pouring.

Table 4-7 Names of specimens

Concrete strength	15 MPa (L)		24 MPa (H)	
Anchor type	C	D	C	D
Two horizontal bars (B)	LC-B13	LD-B13	HC-B13	HD-B13
Two horizontal bars and hairpin bars (BP)	LC-B13P13a LC-B13P13b	LD-B13P13a LD-B13P13b	HC-B13P13a HC-B13P13b	HD-B13P13a HD-B13P13b
Helical reinforcement (H)	LC-Sa LC-Sb	LD-Sa LD-Sb	HC-Sa HC-Sb	HD-Sa HD-Sb
Helical reinforcement extended to corners (HC)	LC-SC	LD-SC	HC-SC	HD-SC

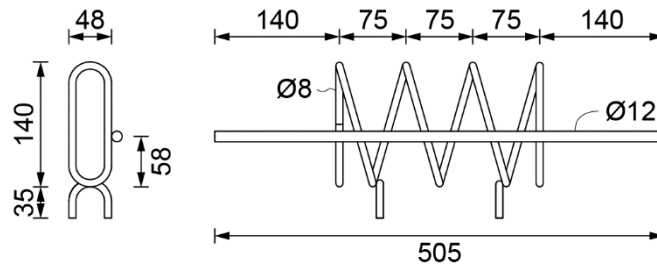


Figure 4-34 Drawing of spiral reinforcement [unit: mm]

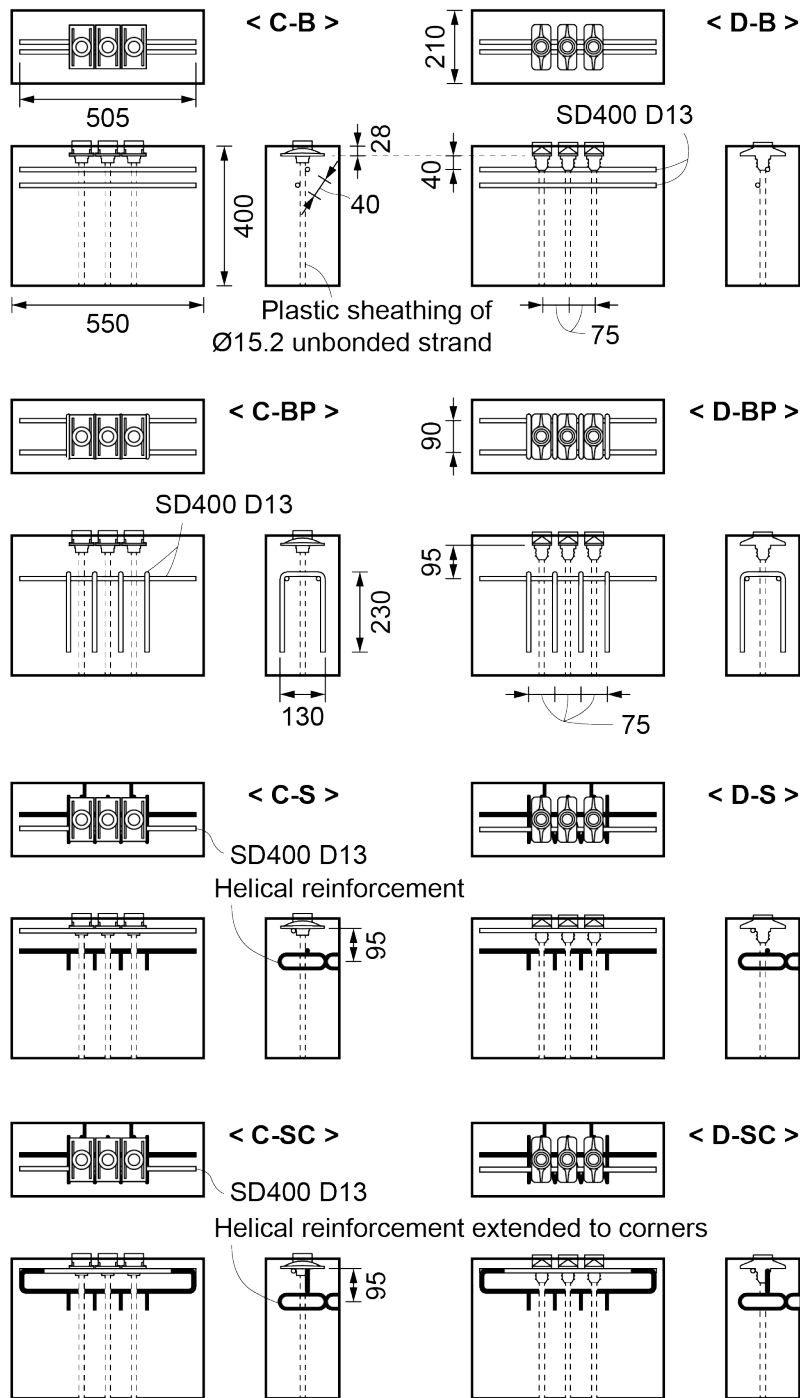


Figure 4-35 Drawings of specimens [unit: mm]

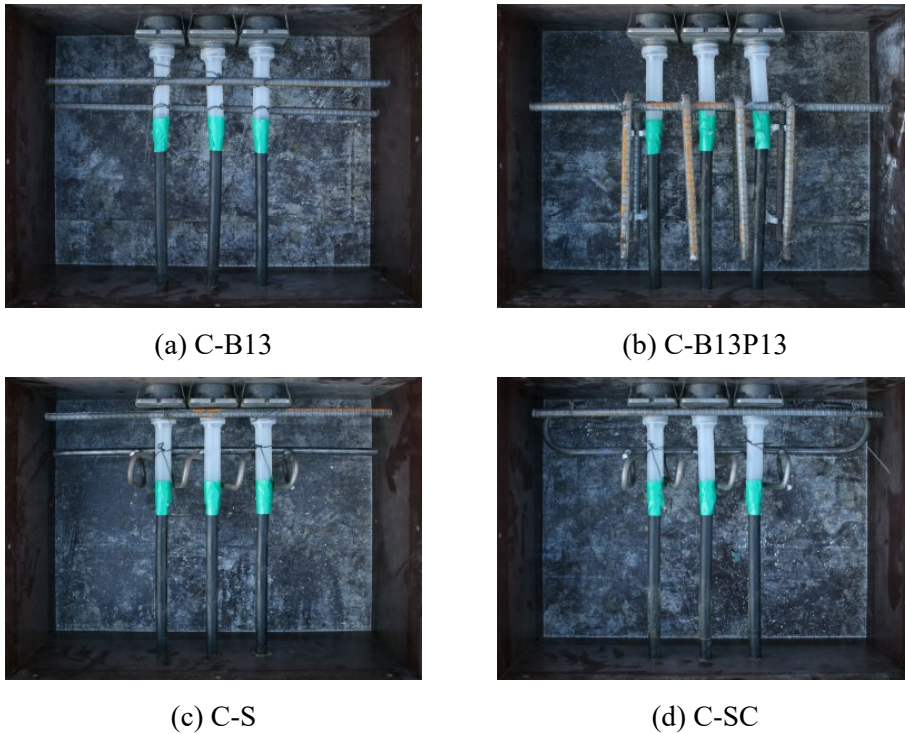


Figure 4-36 Reinforcement details

The loading procedure was basically in compliance with the KCI-PS101 (2010). For the cyclic load in the manual, 80% of nominal tensile strength denotes $2.4P_{pk}$ (626.4 kN) for three anchors. However, in this test, there is no auxiliary reinforcement, which means that the maximum value of the cyclic load was set to only $0.8P_{pk}$ (208.8 kN). The load applied to a steel plate contacting the anchor heads, which were protruded 10 mm from the top section of the specimen.

4.5.2 Test Results

The compressive strength results of the specimens tested were the same as **Table 4-8**. All 12 specimens of Set L (14.7 MPa) were tested on a day, and 10 specimens of Set H with the exception of HC-B13P13a and HC-Sa were examined on another day. The HC-B13P13a and HC-Sa (Set H*), which were tested one day prior to the experiment of Set H, and had an average strength of 22.1 MPa, which was 2.2 MPa less than measured the next day.

There were two types of reinforcing bars: SD400 D13 and circular reinforcing bars for S or SC (**Figure 4-37**). The spiral reinforcing bar has a similar yield strength and ductility as SD400 D13, but its tensile strength is found to be smaller than that of SD400 D13. In addition, there was no horizontal yield section and deformation hardened.

Table 4-8 Concrete compressive strength [unit: MPa]

	Average	Cylinder					
		1	2	3	4	5	6
Set L	14.7	15.4	15.3	14.6	13.4	15.2	14.4
Set H	24.3	25.3	22.1	25.6	-	-	-
Set H*	22.1	21.0	20.9	24.3	-	-	-

* Tests were conducted one day before other specimens of Set H were tested.

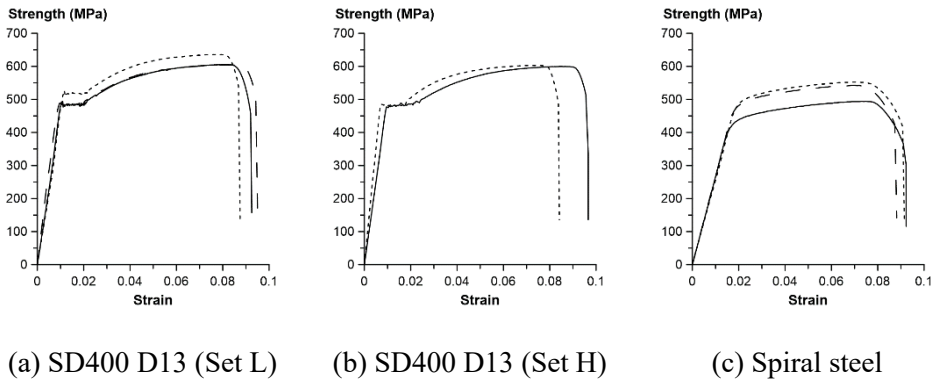


Figure 4-37 Stress and strain curves of steels

The results of the load transfer test for three anchors are presented in **Figure 4-38** and summarized in **Table 4-9**. LD-SC was one of four specimens tested at the beginning of the experiment, which had 15 cycles in order to satisfy the stabilization formula. In addition, others in the four specimens (LC-B13P13b, LD-B13P13a, and LD-B13P13b) could not be subjected to cyclic loads due to equipment operation problems, and were even destroyed at one time. Among them, the data of LC-B13P13b was found to be unreliable because the measuring equipment malfunctioned. Furthermore, the stabilization formula through crack width and strain could not be accurately measured, such as the attached concrete gauge cut or dropped during cyclic loading. Therefore, all other specimens were tested with 10-cycle loads.

According to the results of Set H, all specimens except HC-Sa showed compressive strengths greater than the nominal tensile strength of three strands. On the other hand, all the specimens of Set L were found to have cracks under the nominal tensile strength of one strand. HC-Sa also showed relatively low fracture strength due to the

low compressive strength of concrete as compared to other specimens tested after one day. This suggests that the concrete strength greatly contributes to the performance of anchorage zone.

In particular, when S and SC were used, the compressive strengths were 7.4% and 12.0% higher, respectively, than in using the B13P13. The SC was found to have the highest compressive strength and about two-thirds of the steel amount of B13P13. SC did not show significant differences in efficiency as compared to S, but it seems to be required where there is a concern about member dropout, such as slab corners.

Additionally, the spiral reinforcement had better workability through the fabrication process than traditional reinforcement. The spiral reinforcement is an all-in-one product that is capable of being pre-fabricated in the factory. It is possible to reduce the construction time incurred in rebar processing, chair installation, and rebar assembly, unlike existing methods that require on-site work.

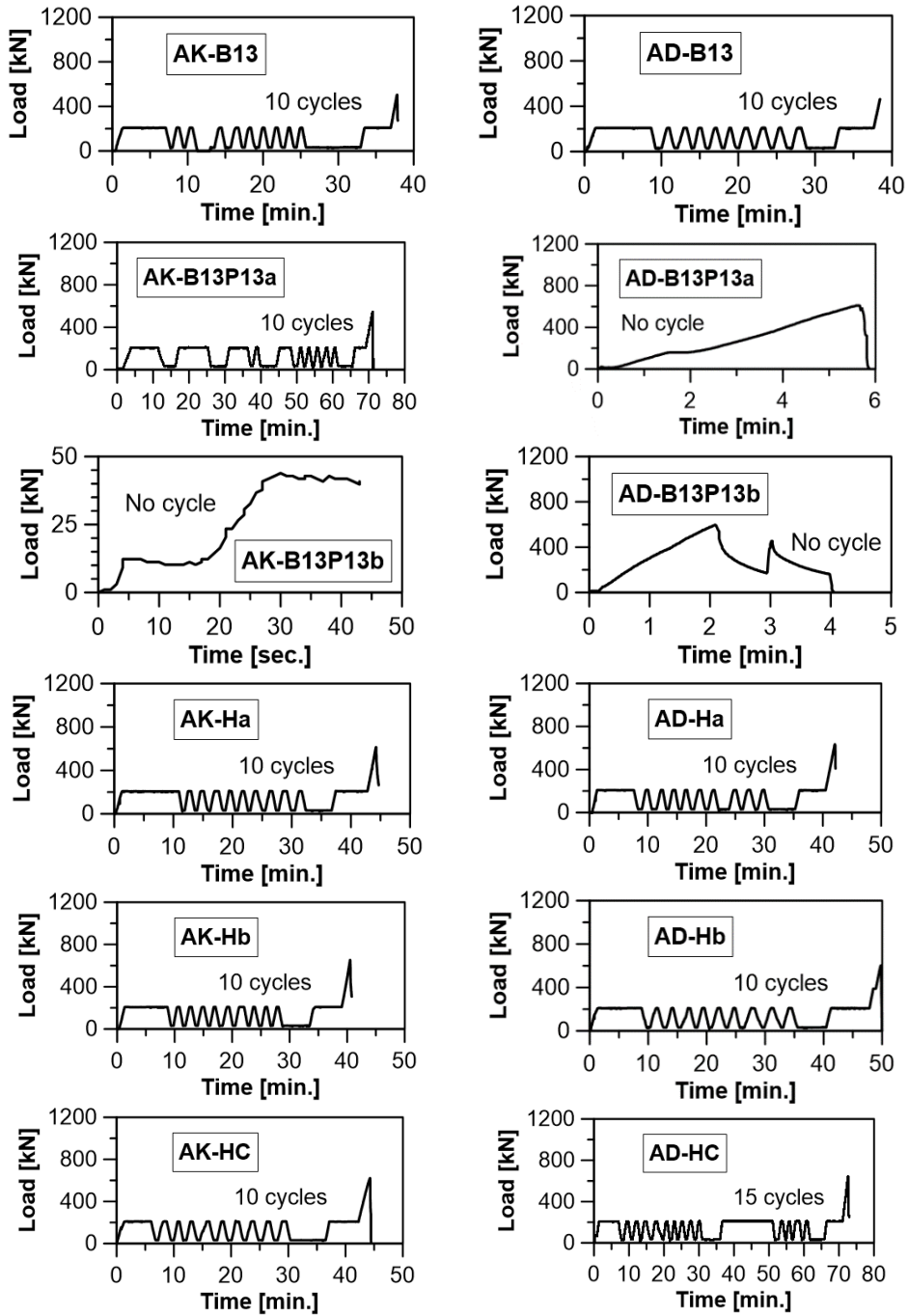


Figure 4-38 Load transfer test results

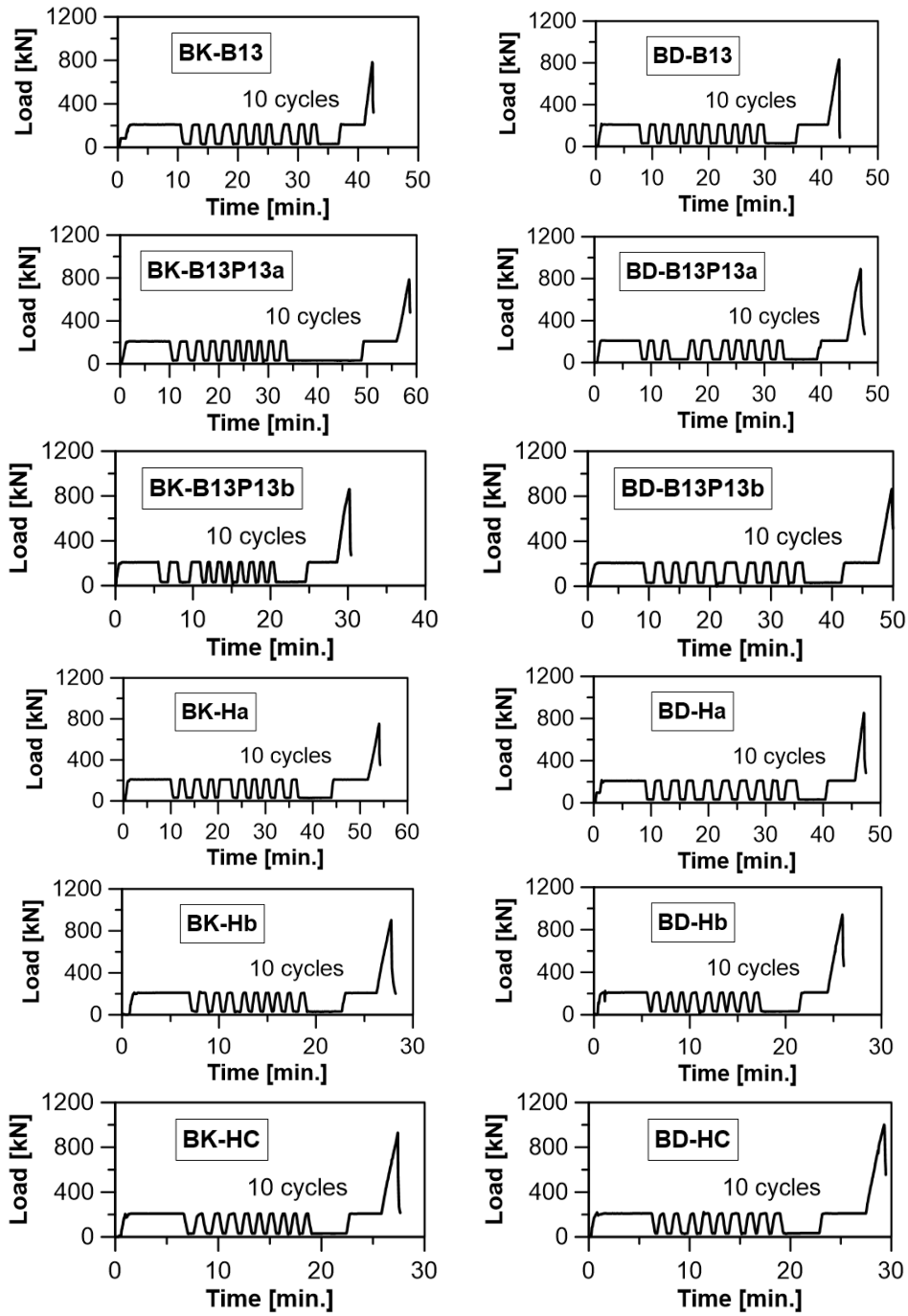


Figure 4-38 Load transfer test results (continued)

Table 4-9 Results of load transfer tests for three anchors

Specimen	Max. load [kN]	Max. load relative to $3P_{pk}$	Volume of steel [mm ³]	Max. load / volume of steel [N/mm ³]
LC-B13	503.9	0.64	127,967	3.9
LC-B13P13a	544.9	0.70	399,663	1.4
LC-B13P13b	N.A.	N.A.	399,663	N.A.
LC-Sa	614.0	0.79	206,146	3.0
LC-Sb	653.8	0.84	206,146	3.2
LC-SC	621.2	0.79	228,054	2.7
LD-B13	463.1	0.59	127,967	3.6
LD-B13P13a	611.0	0.78	399,663	1.5
LD-B13P13b	596.7	0.76	399,663	1.5
LD-Sa	634.4	0.81	206,146	3.1
LD-Sb	601.8	0.77	206,146	2.9
LD-SC	644.6	0.82	228,054	2.8
HC-S13	782.3	1.00	127,967	6.1
HC-B13P13a*	785.4	1.00	399,663	2.0
HC-B13P13b	860.9	1.10	399,663	2.2
HC-Sa*	752.8	0.96	206,146	3.7
HC-Sb	902.7	1.15	206,146	4.4
HC-SC	929.2	1.19	228,054	4.1
HD-B13	832.3	1.06	127,967	6.5
HD-B13P13a	891.5	1.14	399,663	2.2
HD-B13P13b	861.9	1.10	399,663	2.2
HD-Sa	852.7	1.09	206,146	4.1
HD-Sb	942.5	1.21	206,146	4.6
HD-SC	1,001.6	1.28	228,054	4.4

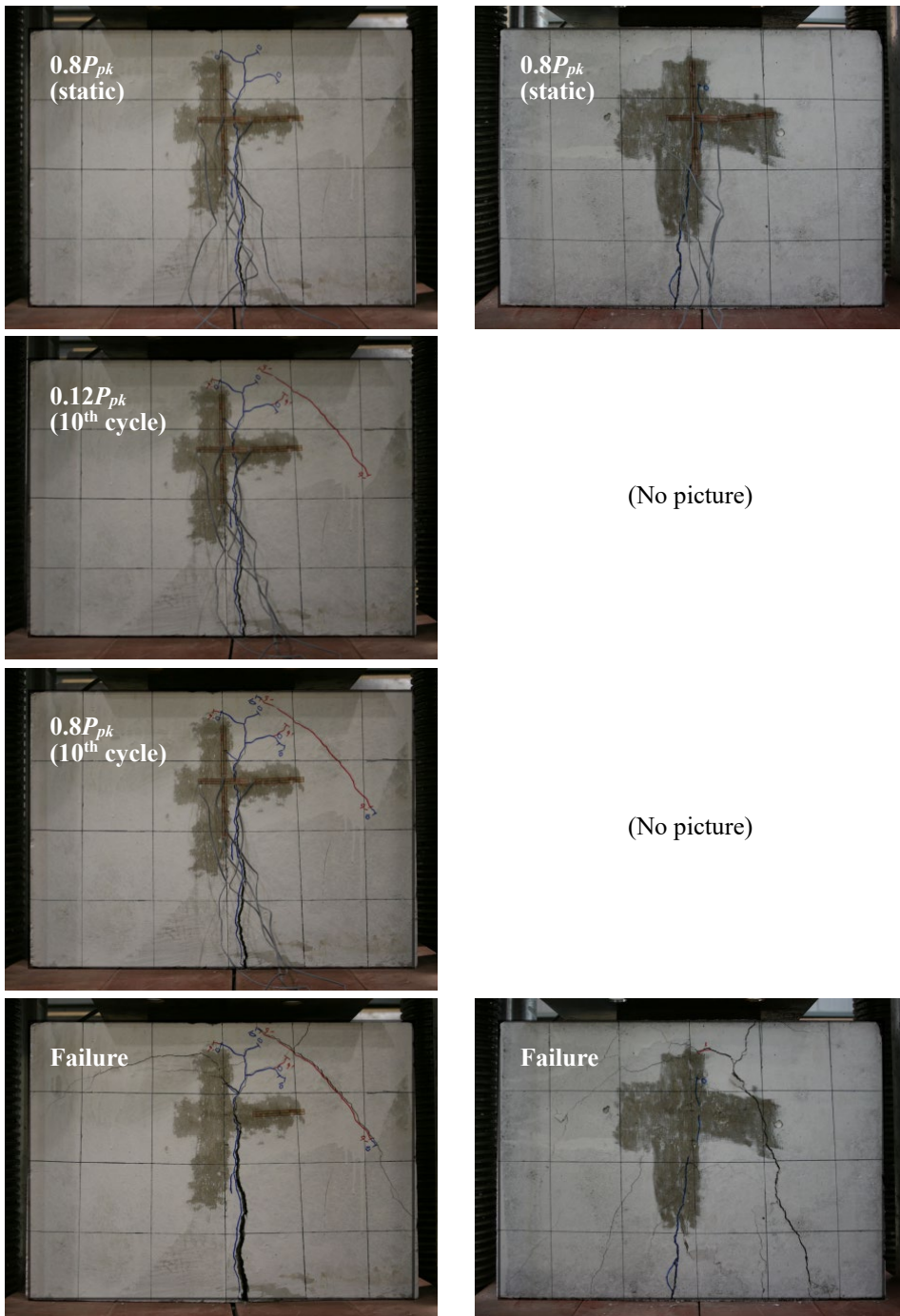
* Test was conducted when the concrete strength was 22.1 MPa (examined one day before other specimens of Set H were tested).

The crack pattern at each major loading point is illustrated in **Figure 4-39**. Contrary to the load transfer test results for one anchor with auxiliary reinforcement, cracking occurred under the first $0.8P_{pk}$ in the load transfer test of three anchorages without auxiliary reinforcement. The crack started at the bottom center of the test specimen.

During cyclic loads, vertical cracks extended from the crack start point to near the anchor. In some specimens, the cracks also occurred as a portion of the parabola and its position was 5 to 15 mm from the top of the specimen.

Subsequent introduction of fracture loads resulted in parabolic cracks throughout the specimen. Parabolic widths were smaller with S or SC than with B13 or B13P13. This implies that the spiral reinforcement with good concrete restraint was highly resistant to bursting force.

The crack in the top surface of the specimen was shown in **Figure 4-40**. Cracks penetrated the anchorage and the cross-section of the member horizontally. This was attributed to the fact that the concrete was vulnerable to tension in the vertical direction, since the width of the cross-section was short and the anchorage zone was primarily reinforced in the horizontal direction. In addition, diagonal cracks occurred from the anchor head or bearing plate. Excessive load caused the concrete to drop out, but the inside of the concrete member was confirmed to be well constrained by means of reinforcement.



(a) LC-B13

(b) LC-B13P13a

Figure 4-39 Failure sequences

(No picture)



(No picture)



(No picture)

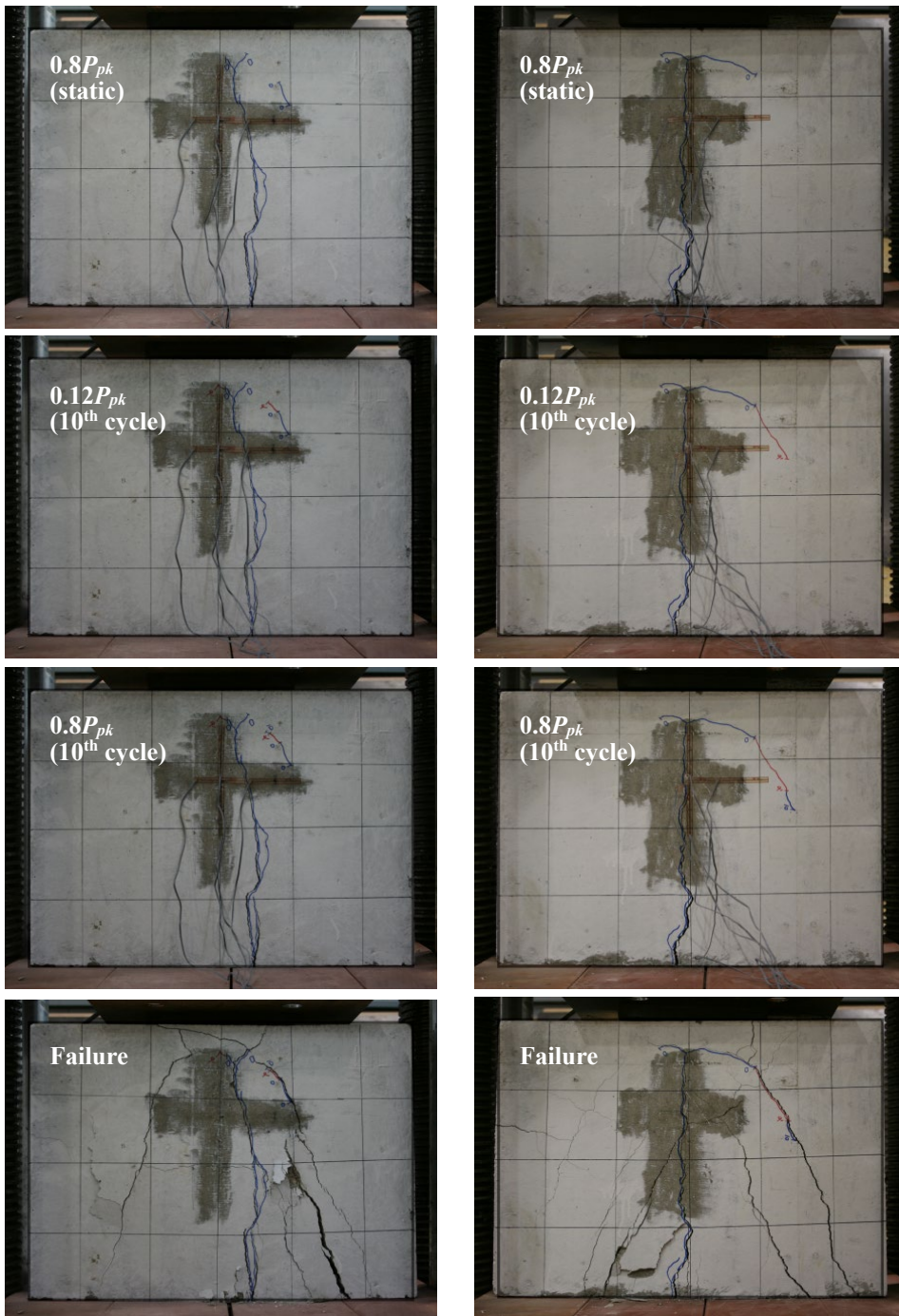


(c) LC-B13P13b



(d) LC-Sa

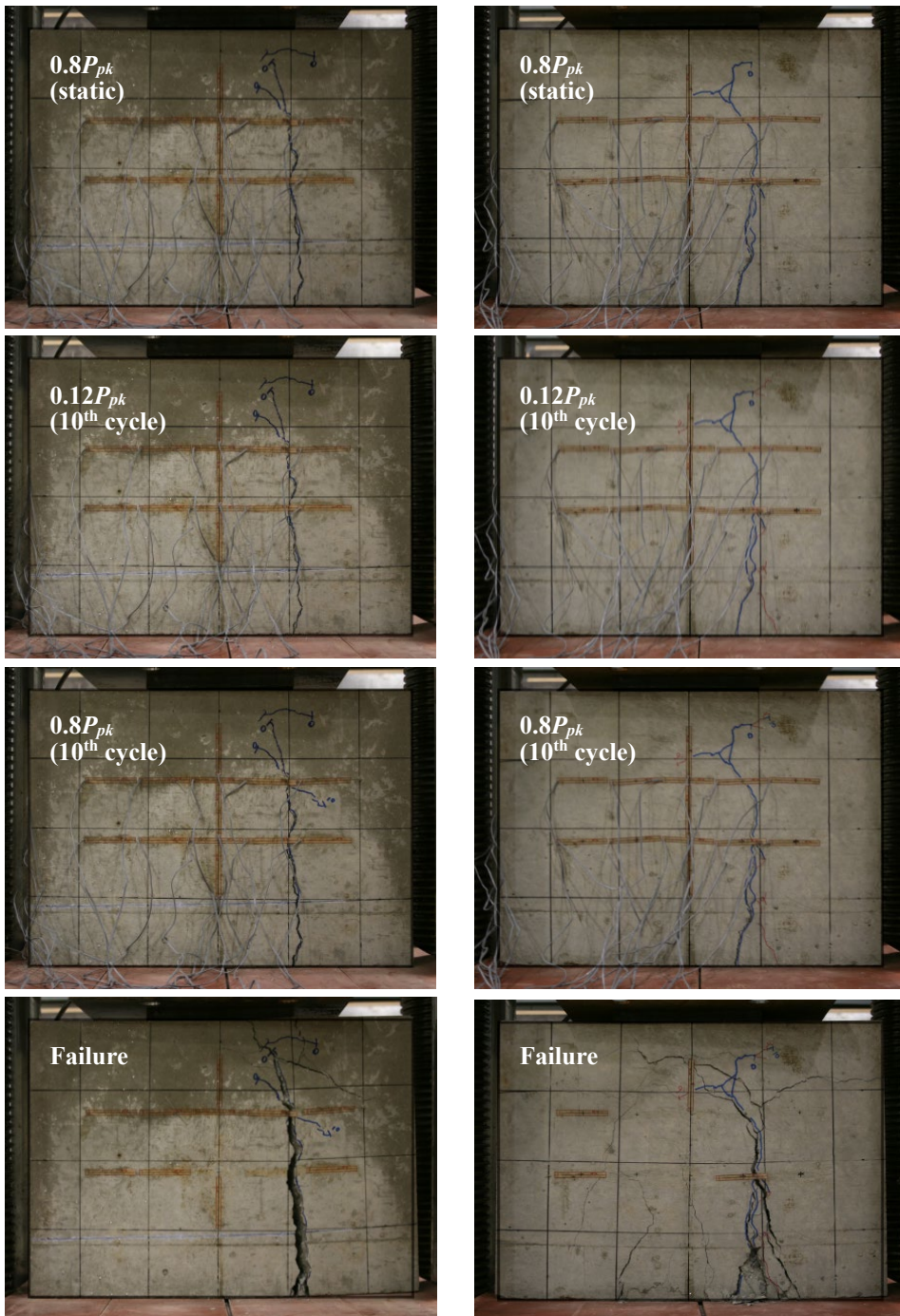
Figure 4-39 Failure sequences (continued)



(e) LC-Sb

(f) LC-SC

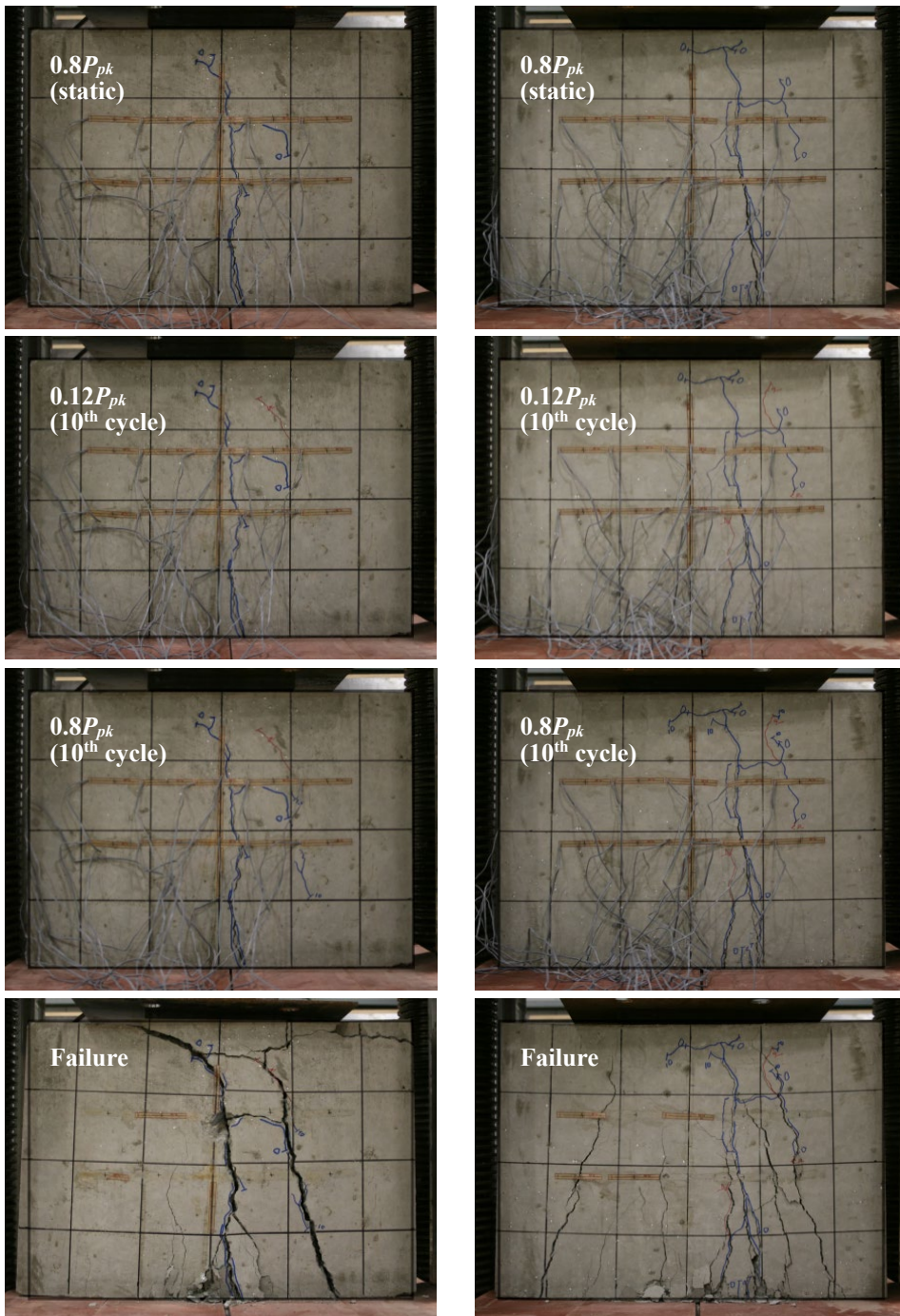
Figure 4-39 Failure sequences (continued)



(m) HC-B13

(n) HC-B13P13a

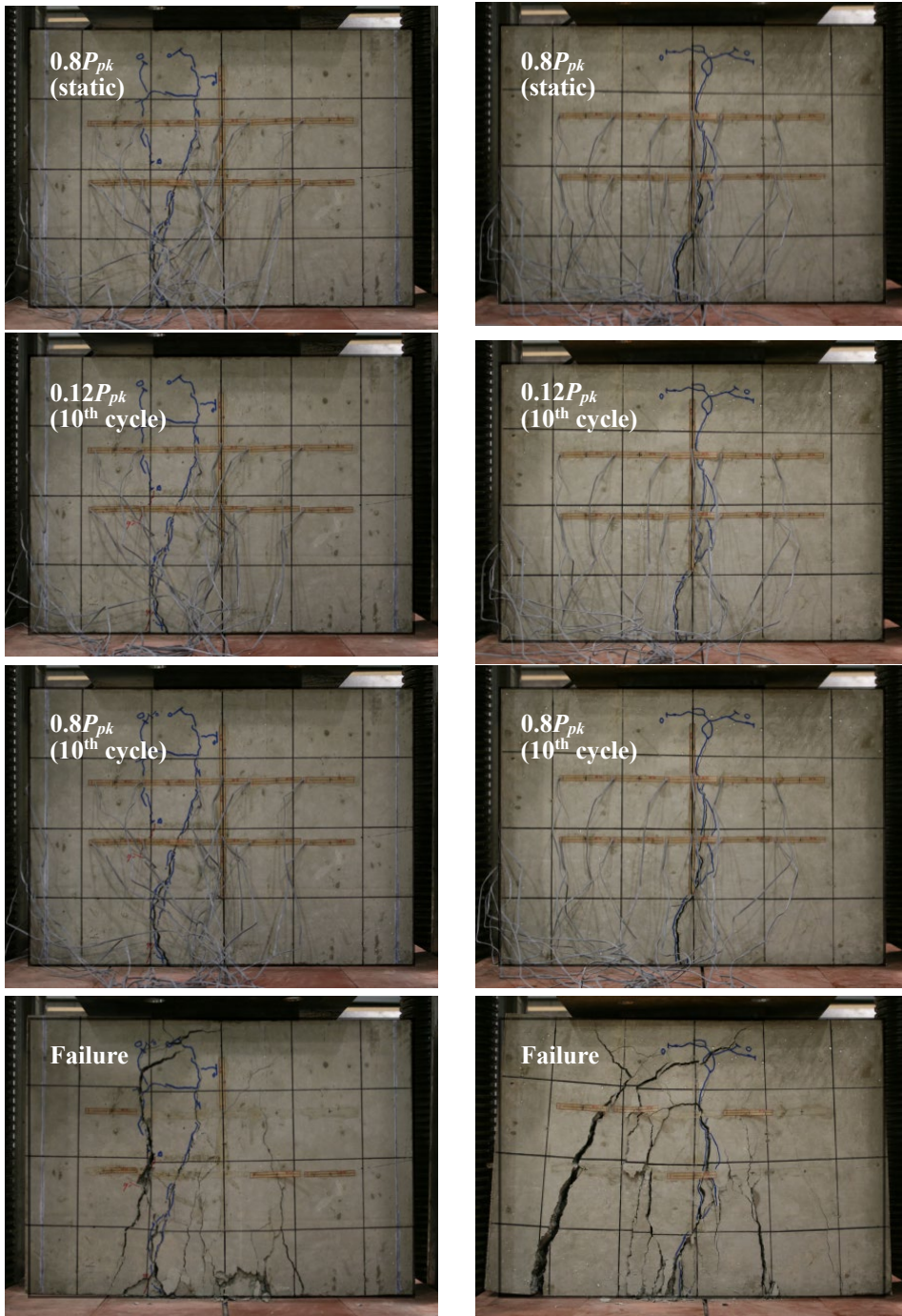
Figure 4-39 Failure sequences (continued)



(o) HC-B13P13b

(p) HC-Sa

Figure 4-39 Failure sequences (continued)



(q) HC-Sb

(r) HC-SC

Figure 4-39 Failure sequences (continued)

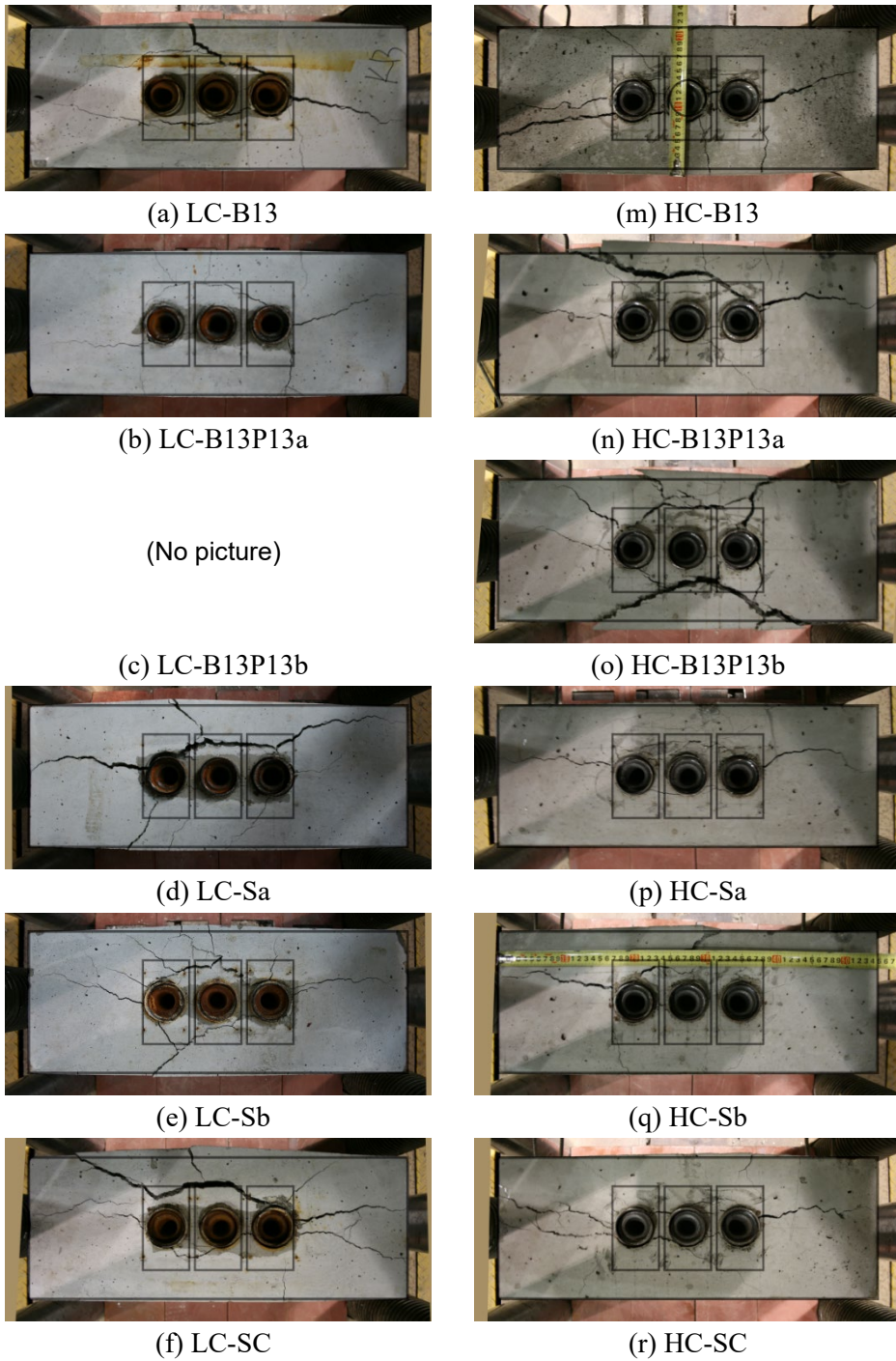


Figure 4-40 Failure modes

4.6 Hydrostatic Test

It is noteworthy that the main purpose of the encapsulation system is to prevent water from entering the interior of the anchorage so that corrosion can be prevented. In order to confirm the water tightness performance of the developed encapsulated anchor, hydrostatic test was performed in accordance with the method outlined in ACI 423.7 (2014).

4.6.1 Test Method

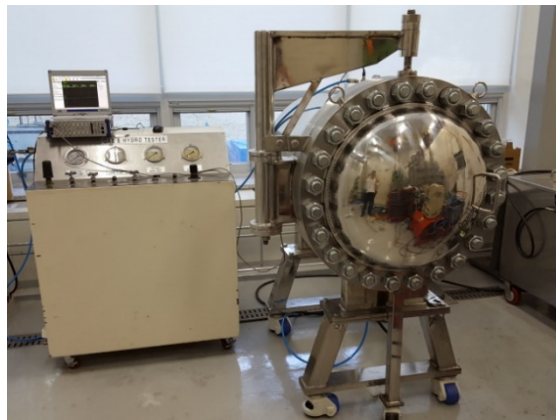


Figure 4-41 Hydrostatic pressure chamber



Figure 4-42 Test set-up of hydrostatic test

Rather than a wedge, a white tissue was placed inside the wedge cavity, which was covered by an endcap. The end of the sleeve was sealed with tape, as used in the field of construction. A blue dye was added to the water in order to examine whether the water entered the void after the experiment. In a hydrostatic pressure chamber (**Figure 4-41**), four encapsulated anchor specimens (**Figure 4-42**) were placed with a hydrostatic pressure of over 8.6 kPa for 24 hours.

4.6.2 Test Results

The hydraulic pressure in the equipment was maintained between 9.3 and 9.8 kPa for 24 hours, as illustrated in **Figure 4-43**, which was found to exceed the minimum pressure of 8.6 kPa specified in ACI 423.7 (2014).

After the hydrostatic test for 24 hours, the entire moisture on the outside surface of the anchorage was removed, subsequent to which the endcap was opened. No paint or water was observed, whereas the white tissues were clean and dry (**Figure 4-44**).

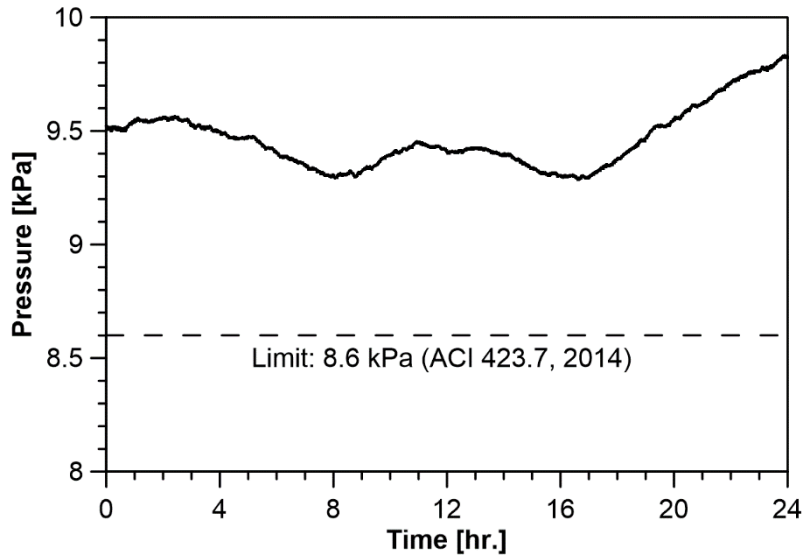


Figure 4-43 Pressure history



Figure 4-44 Observation after hydrostatic test

4.7 Summary

The three kinds of performance tests (static load test, fatigue test, load transfer test) were carried out in accordance with the domestic test method KCI-PS101. Currently, there is no test that verifies the water tightness of the encapsulation system in Korea, which is why hydrostatic tests were conducted according to ACI 423.7-14. The results of performance tests are summarized as follows.

- 1) Static load tests were performed on the bare anchor and encapsulated anchor, respectively, so as to verify the anchorage behavior for the load that is greater than 95% of the strand's nominal tensile strength.
- 2) The displacement of the wedge and the two wires of strand measured at the fixed end was found to be less than 6 mm.
- 3) In the fatigue test, two million times of cyclic loads in the range of 156.6 kN and 167.7 kN at 3 Hz were applied to confirm the long-term performance of the anchor.
- 4) The load transfer test with rectangular concrete specimens verified the change of fracture strength in accordance with the reinforcement details of the anchorage zone.
- 5) A specimen which only has the auxiliary reinforcement withstands 1.62 times the nominal tensile strength of the strand. The reinforcement

performance of the existing horizontal and U-shaped reinforcement was confirmed in the experiment using three anchors.

- 6) In addition, it is experimentally verified that the use of spiral circular reinforcement increases the concrete binding force in the anchorage zone, thus resisting the bursting force better.
- 7) Despite maintaining the water pressure of 8.6 kPa for 24 hours, no water flowed into the anchorage.

Chapter 5. Field Application Tests

The performance tests in Chapter 4 are essential and regulated by specifications; however, they are time-consuming and expensive.

Compression and jacking tests are presented in Sections 5.1 and 5.2, respectively, as a means of easily verifying the performance of the anchorage even in the construction field. It is important to re-verify the performance of the anchor system though the system is already certified. The proposed methods are expected to make this possible.

In Section 5.3, the mock-up test not only confirmed the performance of the anchorage but also its construction ability, before applying the developed anchor to the actual building.

A mock-up test was conducted to determine if the anchor could be used in practice. All procedures from the installation of anchorages, accessories, and tendons to jacking strands were verified.

5.1 Compression Test

When placing the tendon in the PT slab, one side is a fixed end and the other is a live end. Fabricating the fixed end, the wedges are pushed and settled (not by pulling the strand). The anchorage behavior by pushing method cannot be judged by the performance tests conducted in Chapter 4. In addition, unlike the jacking device, the compression test equipment is common in each construction site, and so the compression test can be easily organized.

5.1.1 Test Method

The strands and wedges were inserted in the anchor, and the anchorage was placed on a steel block, as shown in **Figure 5-1**. A total of 10 specimens were tested; five bare anchors (B) and five encapsulated anchors (E). For the bare anchor, a wooden board was added to allow the bearing stress to be evenly distributed. E-N1 was also compressed with a wooden plate as the control group. A two-piece wedge was used to grip the strand, and the differential seating Δ_g was set as variable. Three of the bare anchors and two of the encapsulated anchors had evenly-seated wedges (N), while pieces of wedges were out of alignment (O) in the other specimens. The height difference between the two pieces was measured at both sides of the top surface of the wedges.

The test set-up is shown in **Figure 5-2**. The load was applied to the strand, and not on the wedge. This is suitable for measuring the maximum capacity of an anchor system itself with the actual wedge pieces seated in. For safety, the test was stopped before reaching 400 kN, which is over 1.5 times the nominal tensile strength of strand and is enough to verify the anchorage performance under service load.

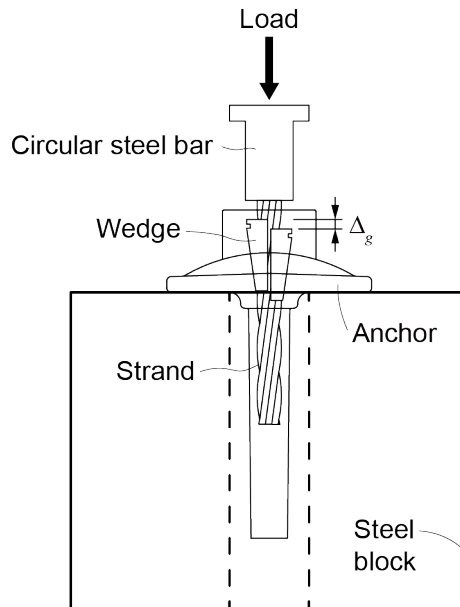


Figure 5-1 Test set-up plan of compression test



Figure 5-2 Compressive test set-up

5.1.2 Test Results

In **Figure 5-3**, a Slip occurred at the beginning of loading. It included both the wedge seating and the squeeze of the wooden board or plastic cover. Since the displacement by pressing the 2-mm plastic cover was very small, the slip because of the encapsulated anchors could be regarded as the anchorage slip. On the other hand, a large slip occurred in the bare anchor while using the wooden plate.

The results of the compression tests are summarized in **Table 5-1**. No cracks were observed even at loads of 1.2 to 1.57 times the nominal tensile strength of the strand. The bearing plate was slightly bent after the test, which means that the bearing plate

and gusset dissipated some of the energy under the force, indicating that it is operating normally.

As the wedge seating occurred, the height difference between the two pieces of wedges decreased in all specimens except B-O1. Based on the measured Δ_g , the relative angles of the two pieces before and after the loading are shown in **Figure 5-4**, where Δ_g is the differential seating of wedge pieces. B-O1 had the largest angle (8.40°), excessively misaligned, but decreased to 4.30° after the experiment. However, the height difference became rather larger. On the other hand, the angle of B-O2 and E-O3 increased, while the height differences decreased. During the wedge seating process, the wedge pieces were found to move themselves to effectively transmit the force. The angles after seating were not more than 4.10 degrees.

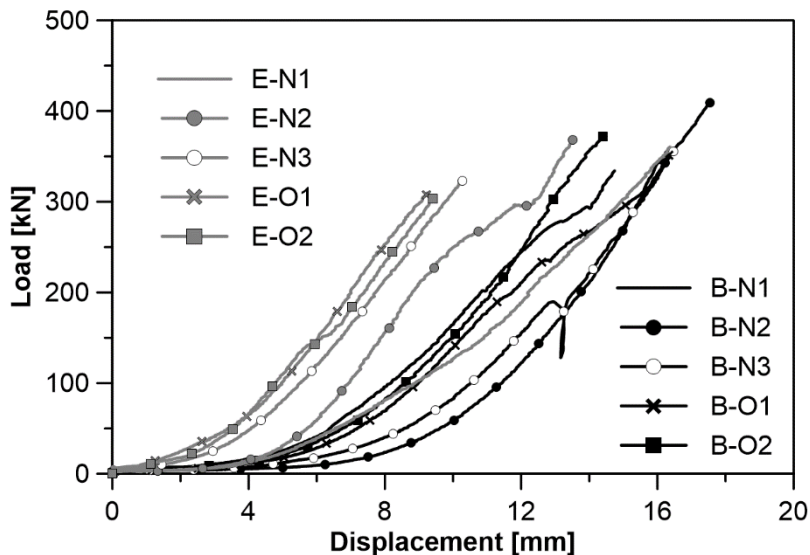


Figure 5-3 Load-deformation curve

Table 5-1 Results of compressive tests

Specimen	Max. load [kN]	Δ_g [mm]			Remarks
		Before	After	Change	
B-N1	332.6	-	-	-	
B-N2	411.1	-	-	-	
B-N3	356.8	Avg. (Left / Right)			With wooden plate
B-O1	351.8	5.60 (4.53 / 6.67)	6.41 (5.89 / 6.93)	+0.81 (+1.36 / +0.26)	
B-O2	373.0	5.92 (5.63 / 6.21)	5.30 (4.81 / 5.78)	-0.62 (-0.82 / -0.43)	
E-N1	359.3				
E-N2	30.3				
E-O1	324.3	7.84 (7.74 / 7.94)	6.56 (6.49 / 6.63)	-1.28 (-1.25 / -1.31)	Without wooden plate
E-O2	311.8	7.41 (6.99 / 7.82)	6.17 (6.10 / 6.23)	-1.24 (-0.89 / -1.59)	
E-O3	304.7	6.70 (6.34 / 7.06)	6.10 (5.71 / 6.48)	-0.60 (-0.63 / -0.58)	

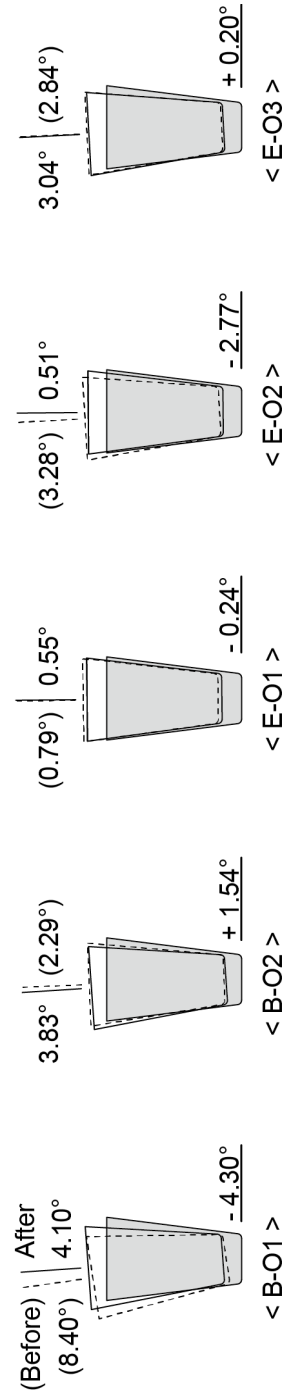


Figure 5-4 Change of differential seating of wedges

5.2 Jacking Test

Although the compression test in Section 5.1 considers the fabrication of the fixed end, the strand is tensioned from the live end. The anchorage behavior by jacking the strand might be different from that by pushing the wedge. Therefore, the jacking test was conducted in this section with a simple method that can be easily performed in the field of construction.

5.2.1 Test Method

The test set-up of the jacking test is as simple as **Figure 5-5**. A strand passed through a reaction wall, and the anchor and wedges were placed on one side. On the other side, a load cell with two steel plates was inserted and the strand was strained by the jacking device.

As shown in **Figure 5-6**, the jacking device for the precast prestressed concrete in the plant was used, and the load was increased up to $0.8P_{pk}$ at one time, which is the same as the tensioning method in the actual PT slab. For the strand with a long free length, the load might be applied in steps of two or three times.

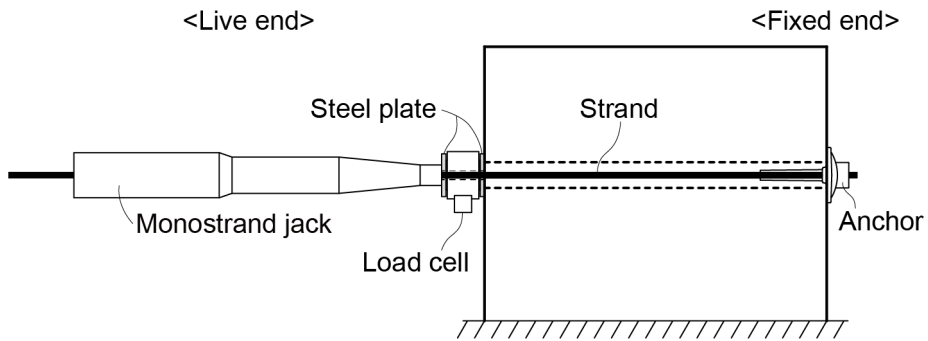


Figure 5-5 Test set-up for jacking test



Figure 5-6 Live end and fixed end of jacking test

5.2.2 Test Results

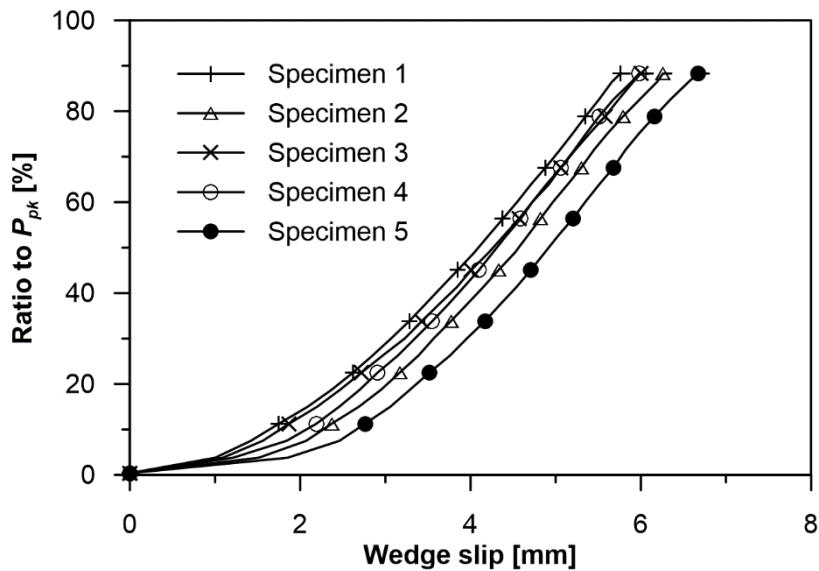
The experimental results are shown in **Table 5-2**. A load of jack's maximum capacity was applied, but the strand was not fractured except in case of one specimen in which the wedge pieces were severely misaligned (about 13 mm).

The maximum loads were 263.5 ~ 275.3 kN, 1.1 ~ 5.6% more than the nominal tensile strength of strand. The performance of anchorage was irrelevant to the type of wedge (two- and three-piece) or whether the encapsulation system was applied.

The wedge slip was measured through a precise and static jacking test. The experiment was conducted by a professional technician, and the displacement of the wedge according to the load is expressed in **Figure 5-7**. At a load of about 10% of the nominal tensile strength of the strand, the wedge slipped about 2 mm. Thereafter, the displacement increased in proportion to the load and was less than 6 mm at $0.8P_{pk}$.

Table 5-2 Jacking test results

		Pre-jacking load [kN]	Max. load [kN]	Max. load relative to P_{pk} [%]	Remark
Bare anchor	Normal	-	272.0	104.3	
		-	270.5	103.8	
	(3-piece wedge)	-	273.0	104.7	
		-	267.5	102.6	
		Out of alignment	-	272.0	104.3
	Out of alignment	-	275.3	105.6	Failure by wedge
Encapsulated anchor	Normal	27.3	265.0	101.6	Without wooden plate
		37.5	265.8	102.0	
	Out of alignment	19.6	263.3	101.0	
		26.8	263.5	101.1	

**Figure 5-7** Wedge slip

5.3 Mockup Test

Developed encapsulated anchors were decided to be used for the PT slabs of Jayang-dong Raemian Premier Palace constructed by Samsung C&T. Through the mockup test before application, the performance and constructability of the tendon were confirmed.

5.3.1 Test Set-up

The width and length of the mockup specimen were 6 m each, which was shorter than the actual span but sufficient to observe the behavior of the PT tendon. The slab thickness was 230 mm, which was the same as the actual thickness. As a two-way slab, the tendon was designed with a distributed arrangement (D) in one direction and a banded arrangement (B) in the other (**Figure 5-8**). Six sets of two anchors were placed in the D, while one set of three anchors and one set of 10 anchors were placed in B (**Figure 5-9**).

D1 ~ D4 were bare anchors and only D6 used the three-piece wedge. Usually, a fixed end of each tendon was made by using the push-in method, seating wedges by compression. In this test, however, the push-in method was not applied for measuring the displacement of the wedge and strand like static load test.

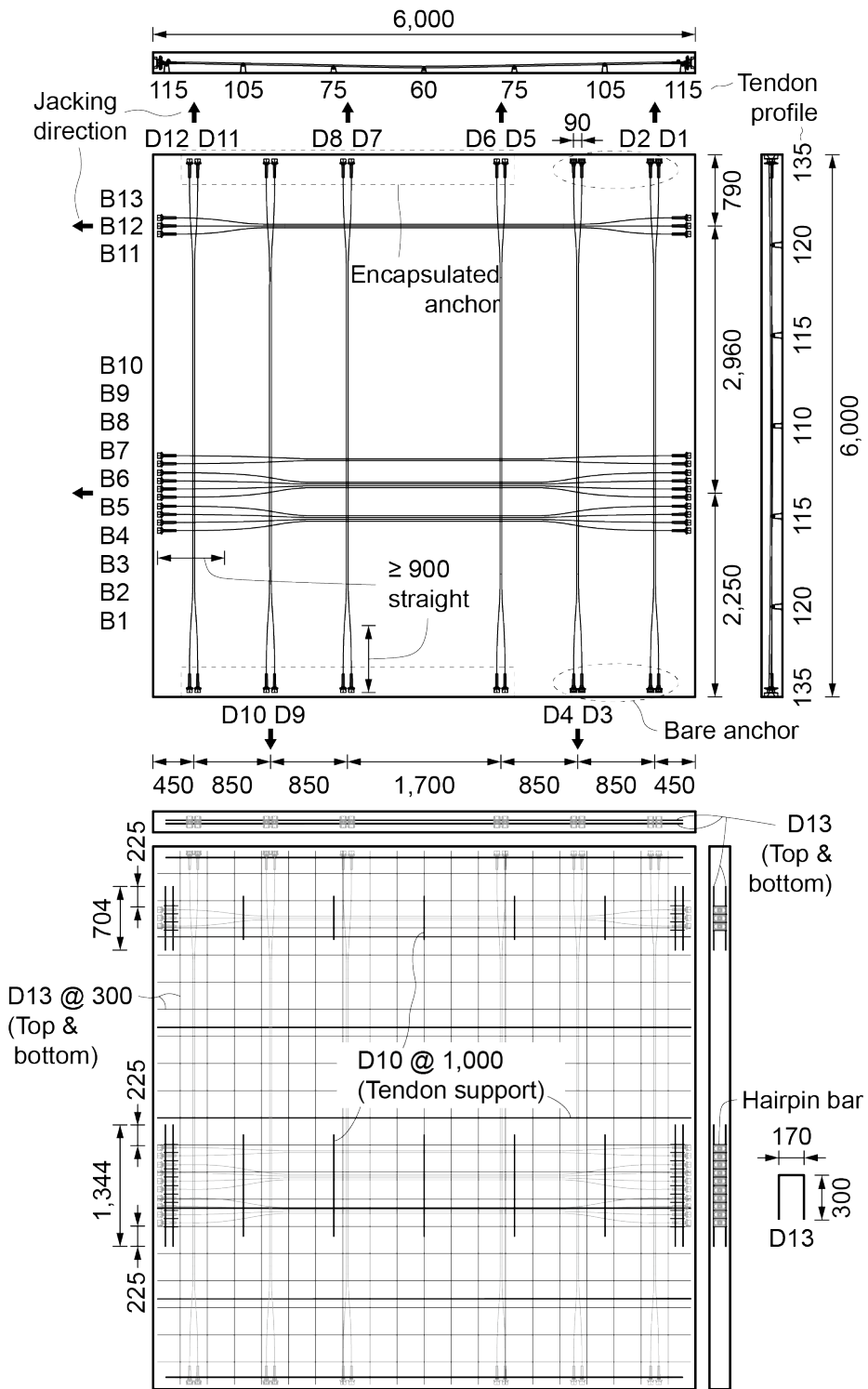


Figure 5-8 Drawing of mockup test specimen [unit: mm]

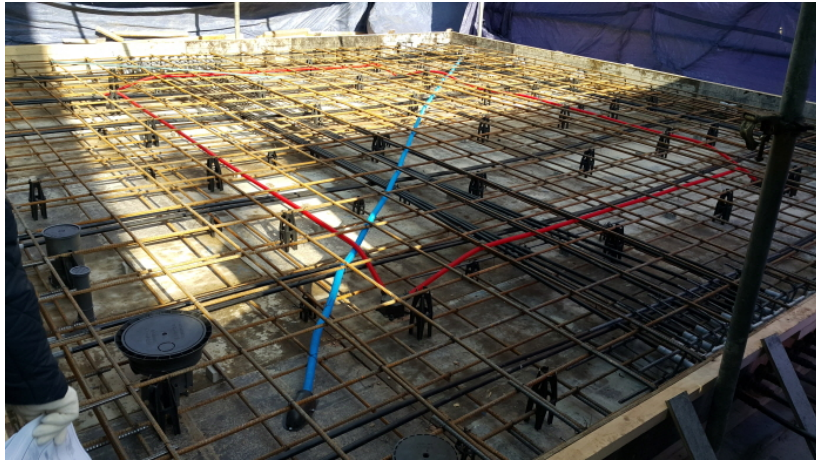


Figure 5-9 Mockup test set-up

The prestressing load was applied with four steps; $0.25P_{pk}$, $0.5P_{pk}$, $0.75P_{pk}$, and $0.8P_{pk}$. The displacement was measured at D5, D6, B1, B10, B11, and B13, which were anchors located at both edges of each kind of tendon sets (two-, three-, ten-anchors). Especially, for B13, the load $0.8P_{pk}$ was maintained during one hour and increased to the maximum capacity of the jacking device. This was the same procedure as that of static load test according to KCI-PS101 (2010).

The material properties of the strand used in the mockup test are summarized in **Table 5-3**. The stress-strain curves through the tensile test are shown in **Figure 5-10**.

Table 5-3 Tensile test results of strands

	Avg.	Specimen		
		1	2	3
Tensile load [kN]	271	272	270	271
Yield strength [kN]	221	217	223	224
Elongation [%]	9.8	9.8	10.9	8.6
Cross-sectional area [mm ²]	141.4	141.3	141.5	141.4

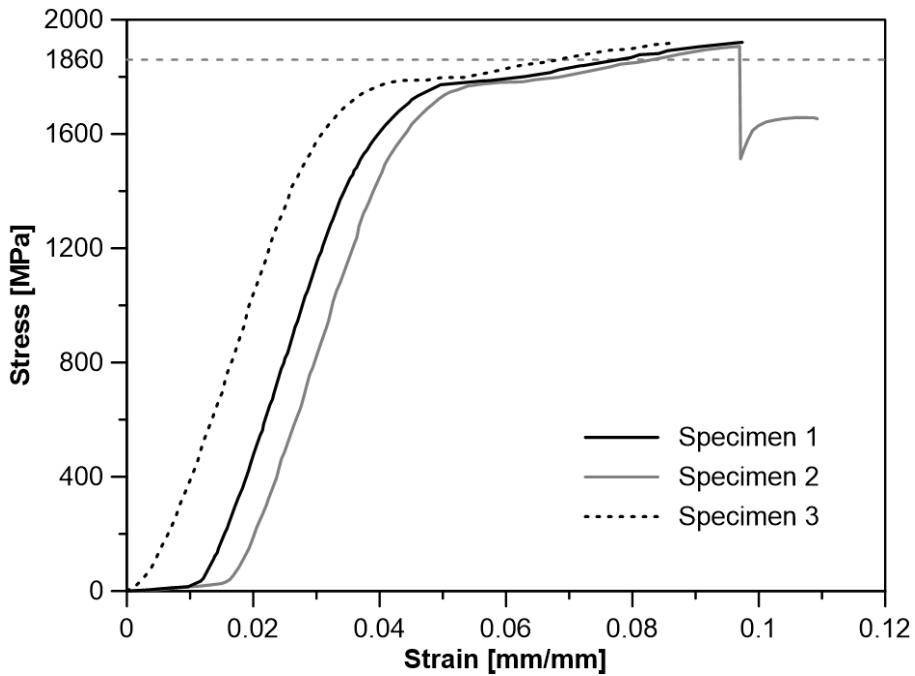


Figure 5-10 Tensile test results of stands

5.3.2 Test Results

The test results of banded and distributed tendons are summarized in **Tables 5-4** and **5-5**, respectively. The displacement of the inner pipe of the jacking device was measured at each loading stage. The distance from the concrete surface to the end of the strand tail was recorded before and after jacking. With the measured values, the tendon elongation was calculated. In addition, a point was marked with paint 100 mm from the concrete surface, and its displacement was also measured.

The elongation varied according to the method, and the value measured with paint marking was the smallest. The elongation results of D1-D6 and B1-B10 seemed to be larger than the expectation, so the nose of the jacking device was changed to fit more to the anchor head. After the nose was amended, the error was relatively reduced.

Although no structural problems occurred during the construction process, some defects were found in terms of constructability. The plastic material was too hard because of which it was difficult to remove the pocket former during the demolding process. In addition, the rotation number of the thread for inserting the pocket former or endcap was too many. In order to improve these points, softer HDPE was applied to the accessories, and the number of threads was decreased to reduce the construction time even during installation and demolding.

Table 5-4 Mockup test results of banded tendon anchors [unit: mm]

Jacking force	B1	B2	B3	B4	B5	B6	B7	B8	B9	B10	B11	B12	B13
$0.25P_{pk}$	39.0	36.0	36.0	31.0	38.0	37.0	41.0	38.0	33.0	37.0	39.0	34.0	36.0
$0.5P_{pk}$	53.0	53.0	53.0	47.0	54.0	53.0	58.0	54.0	48.0	53.0	55.0	52.0	52.0
$0.75P_{pk}$	69.0	69.0	69.0	64.0	70.0	69.0	75.0	71.0	64.0	70.0	72.0	70.0	70.0
$0.8P_{pk}$	71.0	72.0	72.0	66.0	73.0	72.0	78.0	73.0	67.0	73.0	75.0	73.0	73.0
$0.5P_{pk}$	28.0	34.0	34.0	32.0	32.0	32.0	34.0	32.0	30.0	32.0	32.0	36.0	32.0
$0.75P_{pk}$	45.0	49.5	49.5	49.5	48.0	48.0	51.0	49.5	46.5	49.5	49.5	54.0	51.0
$0.8P_{pk}$	47.0	52.9	52.9	51.4	51.4	51.4	54.4	51.4	50.0	52.9	52.9	57.3	54.4
Length of tendon tail	0	355.0	538.0	511.0	412.0	516.0	397.0	428.0	415.0	531.0	433.0	467.0	455.0
	$0.8P_{pk}$	387.0	567.0	541.0	450.0	554.0	437.0	462.0	451.0	561.0	477.0	506.0	482.0
Elongation by tendon tail	$0.8P_{pk}$	32.0	29.0	30.0	38.0	38.0	40.0	34.0	36.0	30.0	44.0	39.0	37.0
Marking slip	$0.8P_{pk}$	13.4	22.3	21.3	11.8	11.8	9.8	18.8	13.8	18.4	7.3	12.3	18.7
Anchor type	Encapsulated anchor												
Wedge type	2-piece												
Nose of jacking device	Before nose modification											Modified	

Table 5-5 Mockup test results of distributed tendon anchors [unit: mm]

Jacking force	D1	D2	D3	D4	D5	D6	D7	D8	D9	D10	D11	D12
$0.25P_{pk}$	33.0	33.0	41.0	32.0	40.0	31.0	33.0	35.0	33.0	35.0	36.0	36.0
$0.5P_{pk}$	48.0	49.0	58.0	50.0	58.0	47.0	50.0	52.0	49.0	51.0	52.0	53.0
$0.75P_{pk}$	64.0	66.0	75.0	69.0	75.0	64.0	68.0	72.0	67.0	69.0	71.0	72.0
$0.8P_{pk}$	67.0	69.0	70.0	72.0	77.0	67.0	70.0	75.0	70.0	72.0	74.0	74.0
$0.5P_{pk}$	30.0	32.0	34.0	36.0	36.0	32.0	34.0	38.0	32.0	36.0	38.0	40.0
$0.75P_{pk}$	46.5	49.5	51.0	55.5	52.5	49.5	52.5	58.5	51.0	54.0	57.0	58.5
$0.8P_{pk}$	50.0	52.9	55.8	58.8	54.4	52.9	54.4	61.7	54.4	57.3	60.2	60.2
0	531.0	388.0	471.0	452.0	410.0	405.0	300.0	331.0	318.0	323.0	333.0	440.0
$0.8P_{pk}$	561.0	430.0	499.0	497.0	455.0	450.0	340.0	372.0	359.0	366.0	376.0	482.0
Elongation by tendon tail	30.0	42.0	28.0	45.0	45.0	45.0	40.0	41.0	41.0	43.0	43.0	42.0
Marking slip	18.4	9.3	26.2	12.2	7.8	6.3	12.8	19.1	11.8	12.7	15.6	16.6
Anchor type	Bare anchor						Encapsulated anchor					
Wedge type	2-piece						3-piece	2-piece				
Nose of jacking device	Before nose modification						After nose modification					

At the fixed ends of six anchors (D5, D6, B1, B10, B11, and B13), the measured displacement results are illustrated in **Figure 5-11**. The wedge slips measured at four loading stages are summarized in **Table 5-6**. In the case of D5, the displacement of the wedge occurred over 10 mm. Because the sheathing was not removed clearly in the wedge cavity, the wedge gripped the strand and extruded sheathing so that it could not be fully seated.

The amount of wedge slip was between 4 and 6 mm, which was adequate to use. All displacements, including B13, became stable as soon as the load was introduced. B13 was maintained at 208.6 kN for one hour and was finally jacked to 260.7 kN with wedge displacement of 6.2 mm.

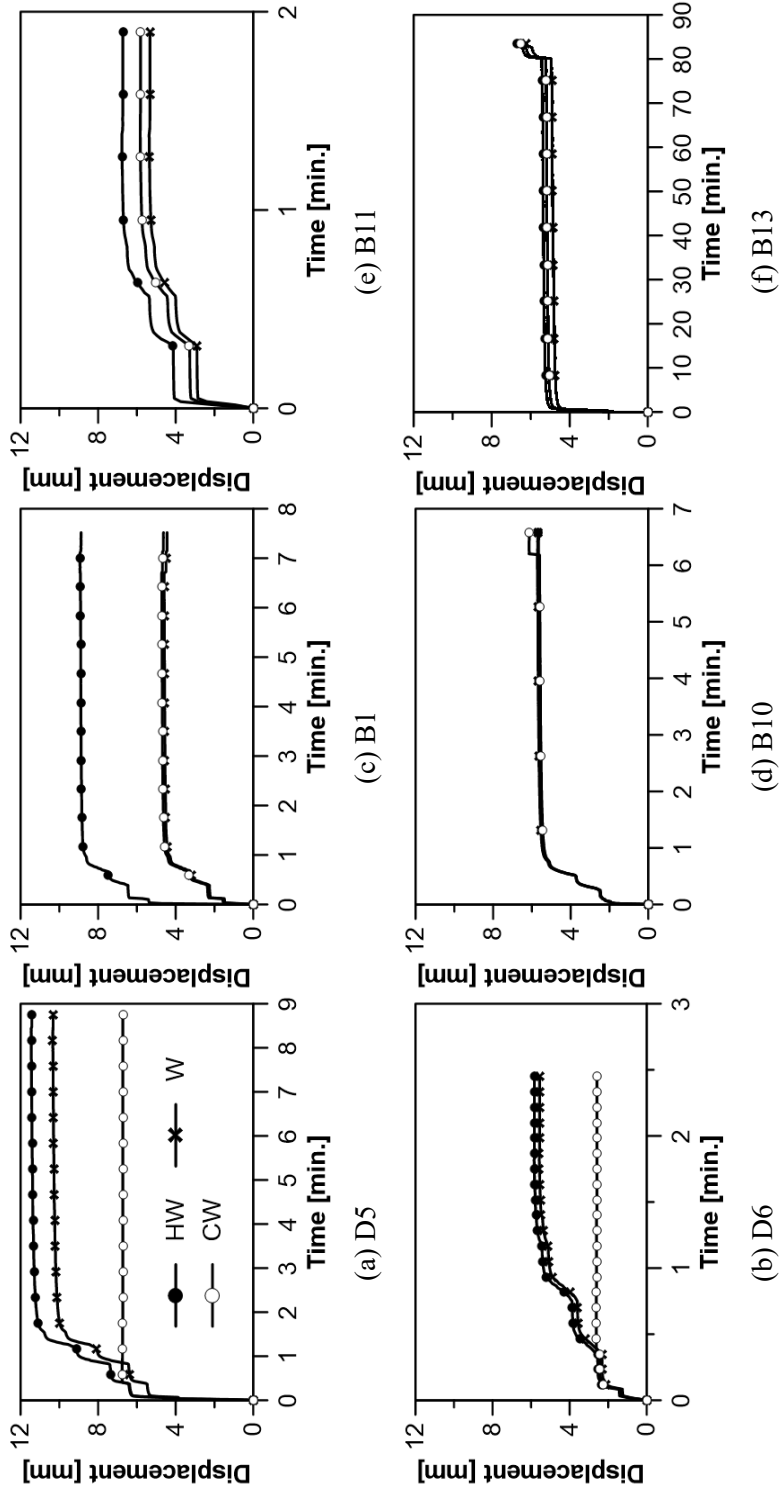


Figure 5-11 Displacements of W, CW, and HW

Table 5-6 Slip at fixed end [unit: mm]

		Jacking force					Avg. slip at $0.8P_{pk}$
		66.9 kN	133.7 kN	200.5 kN	208.6 kN	260.7 kN	
D5	W	3.6	8.1	9.6	10.3	N.A.	9.5
	CW	2.6	6.7	6.7	6.8	N.A.	
	HW	3.9	9.1	10.7	11.5	N.A.	
D6	W	1.3	2.3	3.6	5.6	N.A.	4.7
	CW	1.3	2.5	2.6	2.6	N.A.	
	HW	1.4	2.6	3.9	5.8	N.A.	
B1	W	2.3	3.2	4.3	4.6	N.A.	6.1
	CW	2.4	3.4	4.4	4.7	N.A.	
	HW	6.5	7.5	8.6	8.9	N.A.	
B10	W	2.5	3.7	5.2	5.7	N.A.	5.8
	CW	2.5	3.7	5.1	6.1	N.A.	
	HW	2.5	3.7	5.1	5.7	N.A.	
B11	W	2.9	4.0	5.1	5.4	N.A.	6.0
	CW	3.3	4.4	5.5	5.8	N.A.	
	HW	4.1	5.3	6.5	6.8	N.A.	
B13	W	2.0	3.1	4.2	4.7	6.2	5.1 (6.5 at P_{pk})
	CW	2.2	3.3	4.5	5.2	6.5	
	HW	2.3	3.5	4.7	5.4	6.7	

5.4 Summary

Instead of rather complicated and time-consuming performance tests, a compression test and a jacking test were devised that could be easily conducted in the field of construction.

The compression test reflects the process of making the fixed end through compression, supporting the bearing plate and pushing the strand. However, for safety reasons, the test was stopped before reaching 400 kN. Unlike the compression test, the jacking test is a method of verifying the anchorage performance by tensioning the strands.

Before applying the developed anchor to the building, the behavior and construction of the tendon were examined by conducting a mockup test with 6-m square two-way slab specimen. The thickness of the slab was 230 mm. In one direction, six sets of two anchors were distributed, with three and ten anchors being placed with banded arrangement in the other direction.

The results of field application tests are summarized as follows.

- 1) In compression test, the misaligned wedges leveled themselves during seating and the final angle between two pieces of the wedge was within 4.1° .
- 2) In the jacking test, the load was applied to the maximum capacity of device, and all the specimens withstood the load above the nominal tensile strength.

However, the strand in one of specimens was fractured due to the excessively shifted (13 mm) wedges at a jacking force of 275.3 kN.

- 3) Tendon's performance did not find any problem in the mockup test, and the wedge slip measured at some fixed ends was 4 to 6 mm.
- 4) Plastic breakage occurred during the construction, which is why the material of plastic cover and accessories was made softer to improve workability.

Chapter 6. Behavior in Actual Post-Tensioned Slab

Ultimately, the developed anchor is utilized for PT slabs. The previous tests conducted in Chapters 4 and 5 were deemed sufficient to ascertain/validate the performance of the anchorage. However, they were unable to confirm the behavior in the actual PT slab.

Against this backdrop, Chapter 6 aims to examine the strand and anchor behavior in PT slab from the time of installation till the stage when it is actually used in the building. In order to examine long-term behaviors, there is an urgent need to conduct research on a building that is actually built and used.

The target building was East Central Tower constructed by Samsung C&T in Seoul, Korea. The measuring plan was schemed prior to the beginning of construction. The prestressing force has been observed. The deflection of PT slab has been measured to determine the long-term effect of PT tendons with developed anchors.

Accurate prediction of short-term deflection and total deflection enables to better assess the performance of developed anchors, though only used for four tendons, and to eventually assist in the optimization of the design, thus reducing construction costs.

In the practical field, the short-term and long-term deflection of PT slab are predicted by conducting simple analysis with a combination of loads. However, the

construction process is particularly complicated, and the load changes frequently. Therefore, the method that only uses load combination will not accurately predict short-term deflection. Minor errors in short-term deflection can also result in variations in long-term deflection.

This chapter summarizes the factors which affects the deflection of PT slab and predicts the deflection change over time by reflecting on load change and member stiffness according to the construction procedure.

6.1 Prestressing Force Monitoring

Even to this day, a great deal of research needs to be conducted into the distribution of prestressing stresses or forces in strands that are buried in concrete members. In particular, there is paucity of academic research on the PT method using the unbonded single-strand.

To fill this gap in literature, the present section explains the process and results of measuring prestressing force applied into the PT slab using optical sensors.

6.1.1 Method

The post-tensioning method was used to cover the entire slab from 3rd to 36th floors. More specifically, the tendons were banded in the North-South direction and then distributed in the East-West direction. Meanwhile, the anchor of DSI was used with the Ø15.2-mm unbonded single strand for all tendons, except four tendons with the currently developed anchors.

For these four tendons, the measurement of the stress was undertaken using a single strand using fiber Bragg grating (FBG) system, developed by Korea Institute of Civil Engineering and Building Technology (KICT). In addition, the center wire of the 7-wire strand was replaced with carbon fiber steel, including optical fiber. The strength

of this strand was same as that of a 1,860 MPa low-relaxation strand, albeit with slightly reduced ductility.

As shown in **Figure 6-1**, the fiber-optic strands were installed on the 13th floor: one 13-m strand, two 27-m strands, and one 55-m strand. However, it was very difficult to measure 27-m strands because the sensor was broken and disconnected while pouring concrete. Therefore, the prestressing forces were observed only with the 13-m and 55-m strands. The 13-m and 55-m strands had one and five sensors, respectively, where the sensing points were located at the center of each span (**Figure 6-2**).

Figure 6-3 shows that the FGB strand (also called as smart strand or tendon) with developed encapsulated anchor was placed. At the live end, after taking into consideration the length of strands, the 13-m strand was jacked at once, whereas the 55-m strand was strained with three steps of loading (**Figure 6-4**).

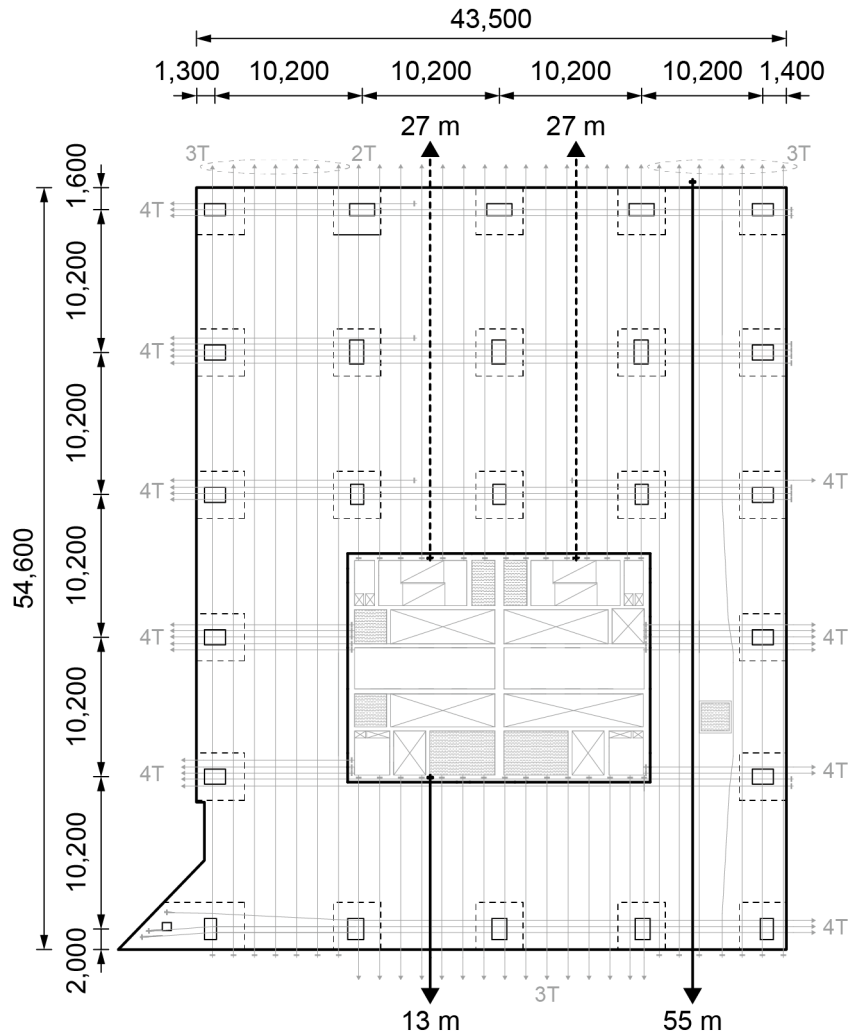


Figure 6-1 Application location of smart tendon [unit: mm]

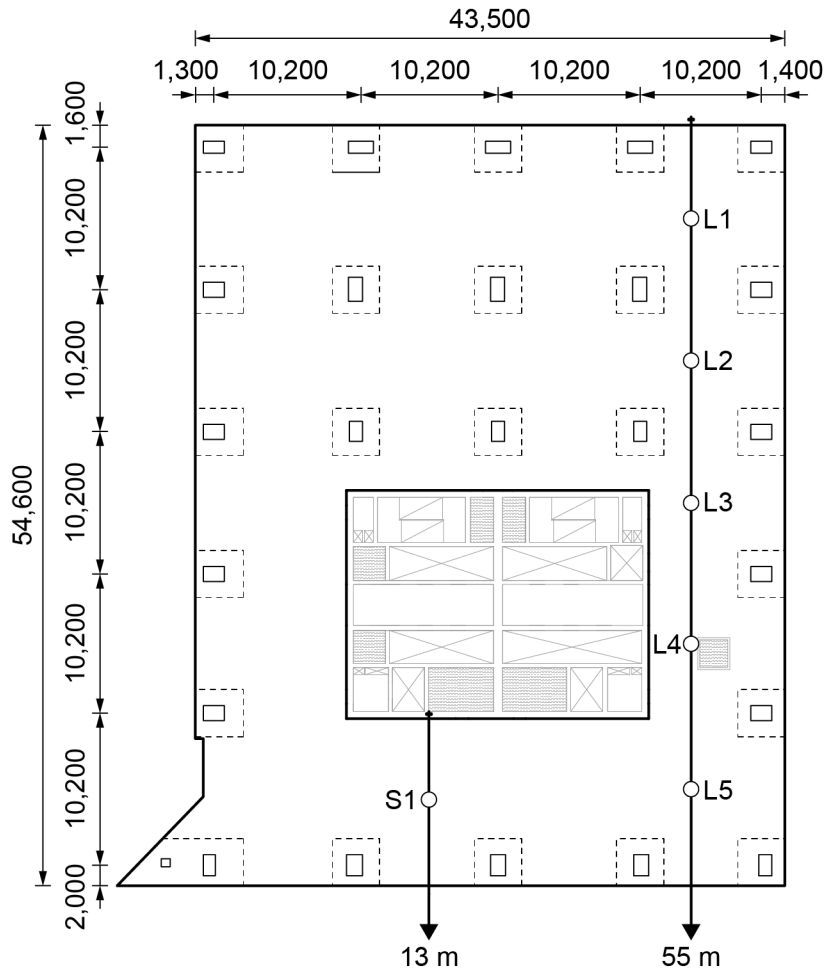


Figure 6-2 Sensor locations for smart tendons [unit: mm]



Figure 6-3 Ordinary and smart tendons



Figure 6-4 Jacking strand and seating

6.1.2 Initial Prestressing Force

The change in prestressing force during jacking was then measured. The results of 13-m and 55-m strands are illustrated in **Figures 6-5** and **6-6**, respectively. The measured values at $0.8P_{pk}$ and after releasing the strand have been summarized in **Table 6-1**.

The force was set as 80% of the nominal tensile strength by the jacking device, but only $0.49P_{pk}$ was applied to the S1, because of its short length. The full jacking force for other long tendons was not transferred to the entire tendon due to the curvature of the tendon profile and the friction inside the sheathing.

For the 55-m strand, the prestressing force was found to be greater closer to the live end (L5) than to the fixed end (L1). This is attributed to the curvature and wobble friction. In particular, as the jacking force began to exceed 60 kN, the prestressing forces of each sensors varied, based on the distance from the live end. Put differently, the friction effect caused by tendon profile began to manifest at loads above 60 kN.

While the jacking force was set as 80% of the nominal tensile strength with a jacking device, $0.78P_{pk}$ (204 kN) was measured at L5 and then reduced to $0.75P_{pk}$ (196 kN) when the strand was released. Put succinctly, the anchor set loss was about 3% of the nominal tensile strength, which was converted into 3-mm anchorage slip. On the other hand, L1 ~ L4 were not affected at all after the removal of the jacking force.

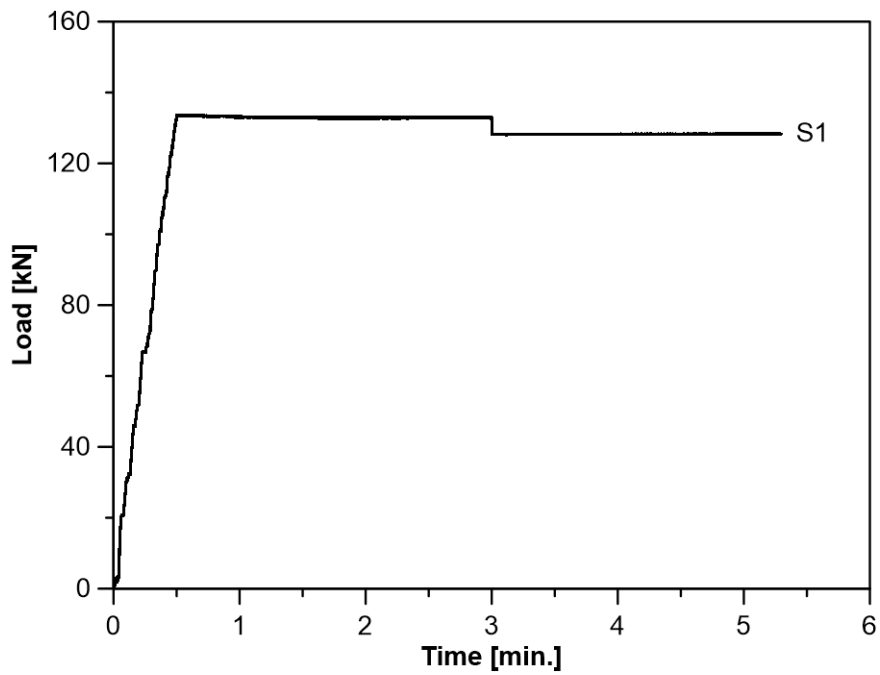


Figure 6-5 Prestressing force during jacking and seating (13 m)

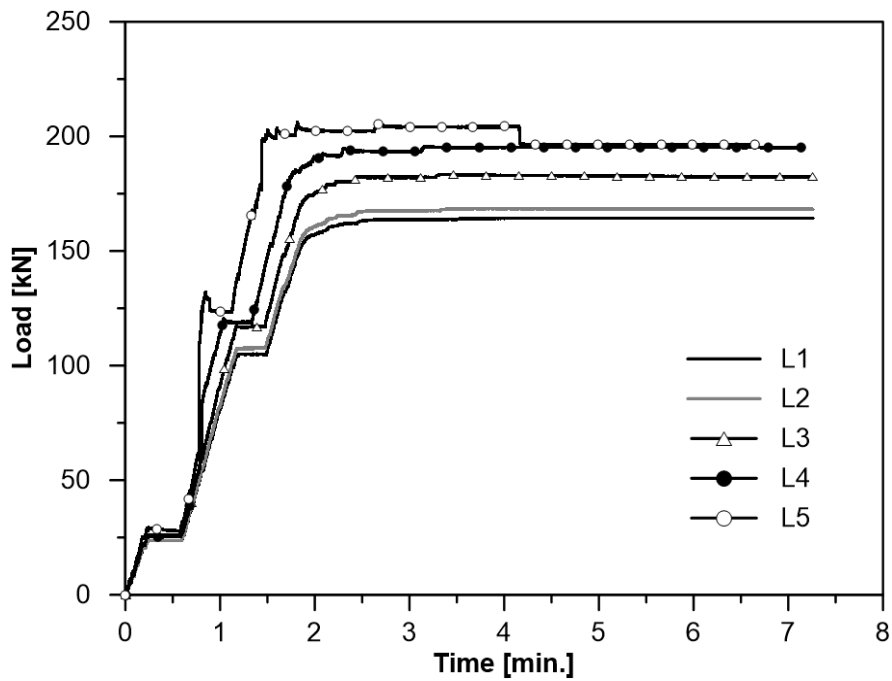


Figure 6-6 Prestressing force during jacking and seating (55 m)

Table 6-1 Jacking force and initial prestressing force measured by smart tendon

Sensor	Jacking force [kN]	Initial prestressing force [kN]
S1	133 (51%)	128 (49%)
L1	164 (63%)	164 (63%)
L2	168 (65%)	168 (65%)
L3	182 (70%)	182 (70%)
L4	195 (75%)	195 (75%)
L5	204 (78%)	196 (75%)

6.1.3 Long-Term Prestressing Force

In order to determine the long-term behavior of tendons with developed anchors in the PT slab, prestressing forces were continuously measured since jacking the strand, as mentioned in Section 6.1.2.

Close to three months' data of the 55-m strand are illustrated in **Figure 6-7**. The values measured at five points witnessed a similar trend over time. In the case of L5 and L4, the magnitude of the load became almost similar after one month because it was redistributed in the two-span section, including both these points after removal of shoring on top of slab. The 55-m strand has not been measured since the fiber was disconnected while concluding the work in April 2016.

The S1, on the other hand, collected long-term data over a three-year period (**Figure 6-8**). For that tendon, less than 50% of the nominal tensile strength was initially loaded due to short length. Though, the long-term behavior was meaningful. When compared with the average temperature, the optical fiber was found to be greatly

affected by temperature, as known. However, it remains to be seen whether the impact is caused by the temperature sensitivity of the fiber that oscillates with changes in temperature or the shrinkage and expansion of concrete members.

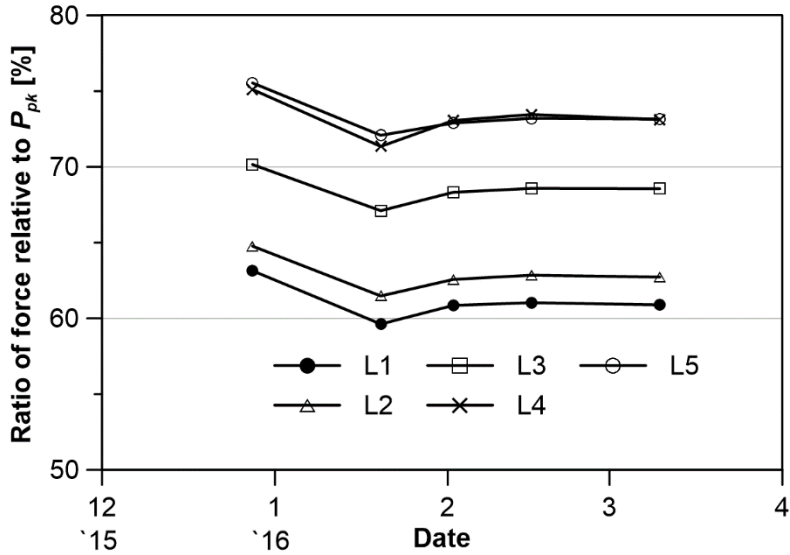


Figure 6-7 Tendon force (55 m)

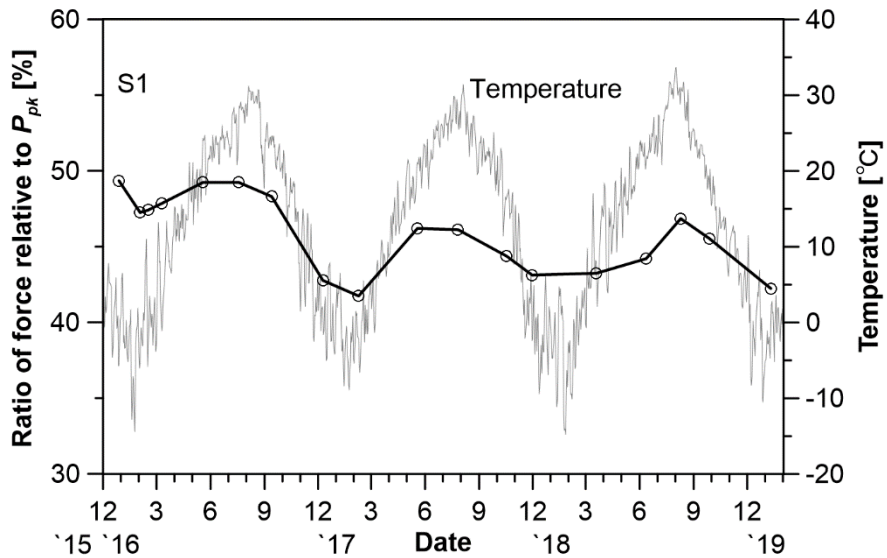


Figure 6-8 Tendon force and temperature (13 m)

6.2 Deflection Monitoring

In both theory and experiments with beam members, it has already been proven that PT system has a better deflection effect than RC. However, with regard to real buildings with various loads, very few experiments have revealed their efficacy. In this section, slab deflections were measured in the same building where the prestressing force was identified for developed anchors in Section 6.1.

6.2.1 Monitoring Method

The East Central Tower is a flat slab structure using curtain walls, wherein each column has a rectangular drop panel. The measurements of floor height, slab thickness, and the drop panel thickness was 3.9 m, 210 mm, and 190 mm, respectively. The span of each square shaped slab was about 10 m. **Figure 6-9** depicts the PT layout.

The deflections were measured at a total of six points, comprising of three points each on the 13th and 14th floors (**Figure 6-10**). The three points represent three different types of slab: a slab at the corner (A), a slab on the edge (B), and interior slab (C).

Deflection measuring equipment was installed as illustrated in **Figure 6-11**. Both ends of the steel wire were suspended on drop panels and pretensioned with springs

and turnbuckles in order to prevent the wire from sagging caused by temperature change during long-term measurement. LVDT was 100 mm long and springless. In the presence of a spring, a reaction force causes the steel wire to be affected, thus resulting in measurement errors.

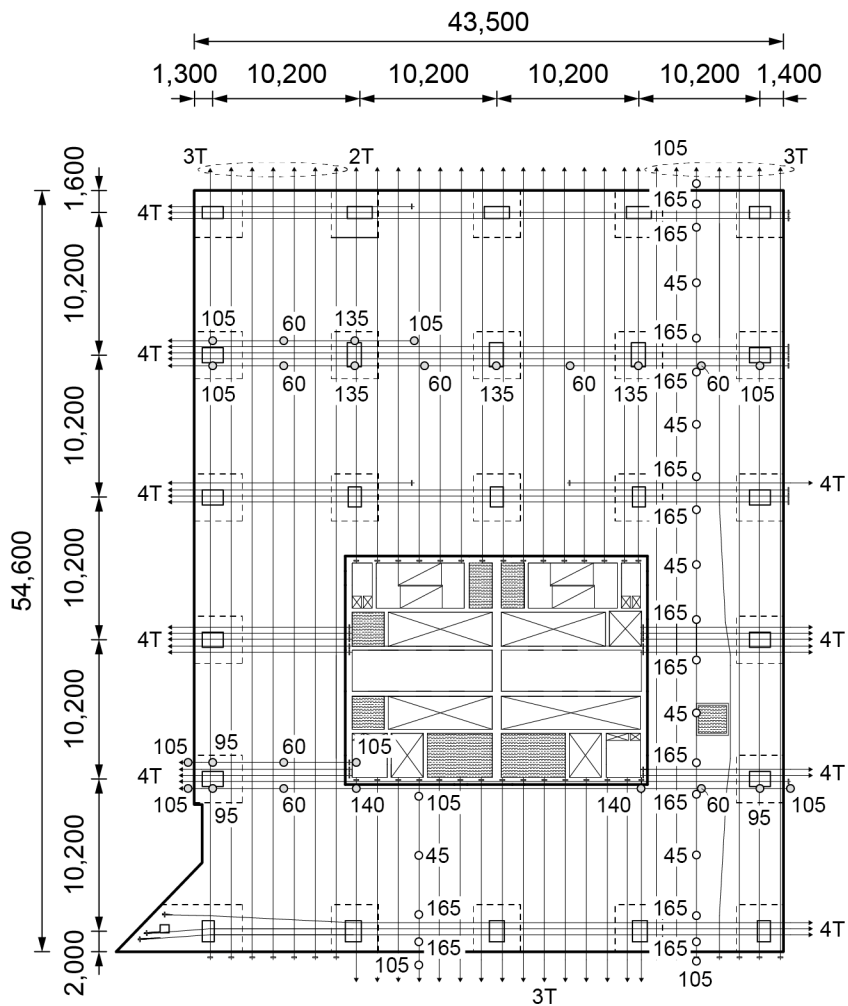


Figure 6-9 PT drawings of standard floor showing tendon bundle height and number [unit: mm]

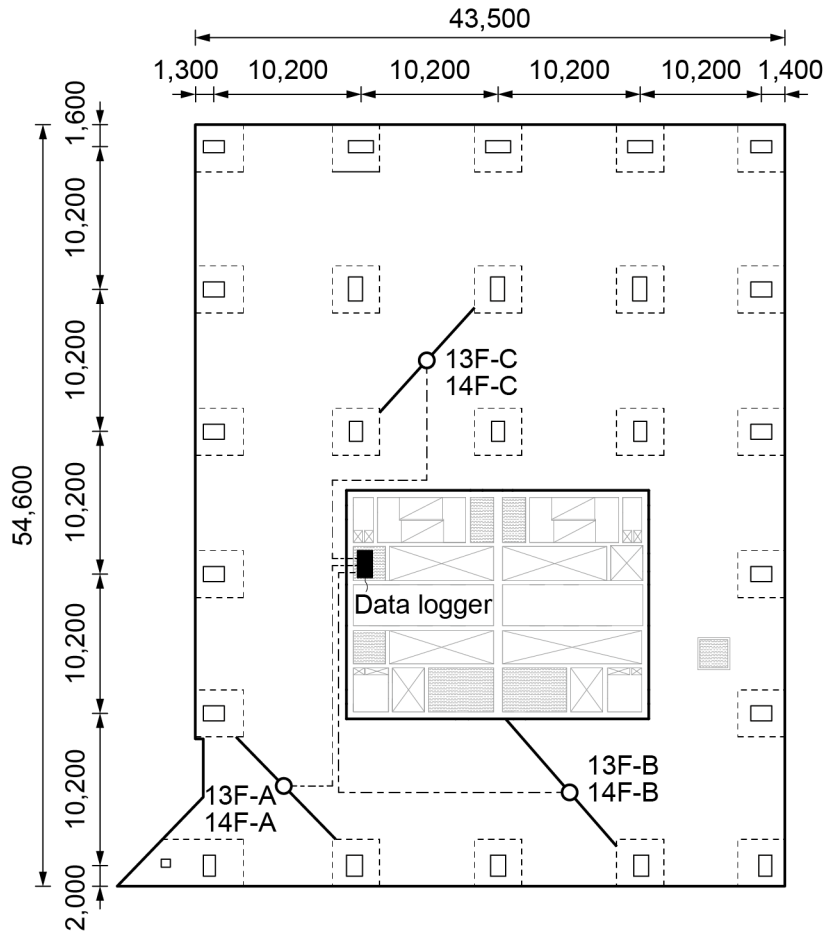


Figure 6-10 Location of deflection measuring points on 13th (13F) and 14th floors (14F) [unit: mm]

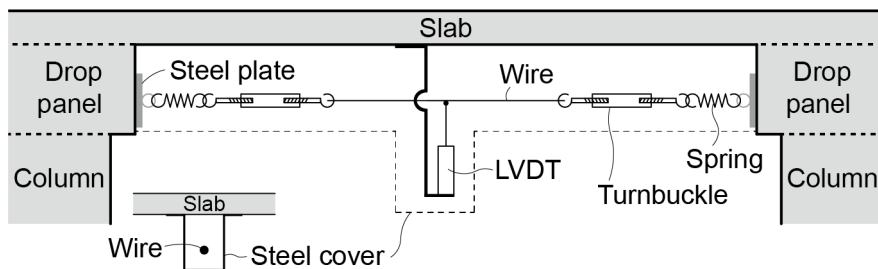


Figure 6-11 LVDT set-up

6.2.2 Monitoring Results

Deflection data of about four years is shown in **Figure 6-12**. The measurement device was unable to install when the concrete poured due to the concrete mold. The deflection started to get measured just after the mold was removed. When the strand was jacked, the deflection was found to decrease. Removing the bottom group of three floor shoring sets increased the deflection.

It is noteworthy that these stages mainly affected the deflection of slab. During the same procedure in the next floors, the deflection of the target slab changed in consonance with a similar trend. However, as the target slab was indirectly affected by shoring and its concrete stiffness increased over time, the range of deflection change was smaller.

The deflection decreased radically after the removal of the shoring group directly above the slab. The deflection value at this time is called the short-term deflection. During previous process, about 10 to 15 mm was restored from the maximum deflection.

Since no shoring was associated with the slab, the deflection only was affected by time and additional loads. The deflection, early after short-term deflection, increased drastically owing to insufficient stiffness and the loads attributed to finishing materials. In May and June 2016, the finishing was completed and the live load was removed, which, in turn, helped lower the deflection. The sag increased slightly over time and has converged without much alteration since 2018. Unlike the slabs located

at the corners or edges, the inner slab with all four constrained edges witnessed the smallest deflection results.

Figure 6-13 compares the measured deflection of PT slabs with those of RC slabs that were measured from different flat plate buildings. Among the results measured in this study, 13F-A and 14F-A, which were at the corner slab, were selected. The RC results were measured in two apartment buildings in Seoul, Korea.

No significant difference was found between PT and RC structure before removing shoring group above the slab. However, after its removal, PT slab largely restored due to the effect of tension, while the deflection decreased only 7 mm in the RC slab.

Long-term deflection is proportional to short-term deflection. Since the short-term deflection was much smaller in PT slab than RC slab, it can be inferred that the long-term deflection is also smaller in PT slab. On 100th day of concrete pouring, RC-A and RC-B were 25 mm, 5 mm more than 13F-A and 14F-A. RC-A was 30 mm on the 120th day, but 14F-A reached 30 mm on the 450th day. On the other hand, 13F-A still maintained less than 30 mm for about four years. Overall, there were no signs of abnormal long-term behavior of developed anchors.

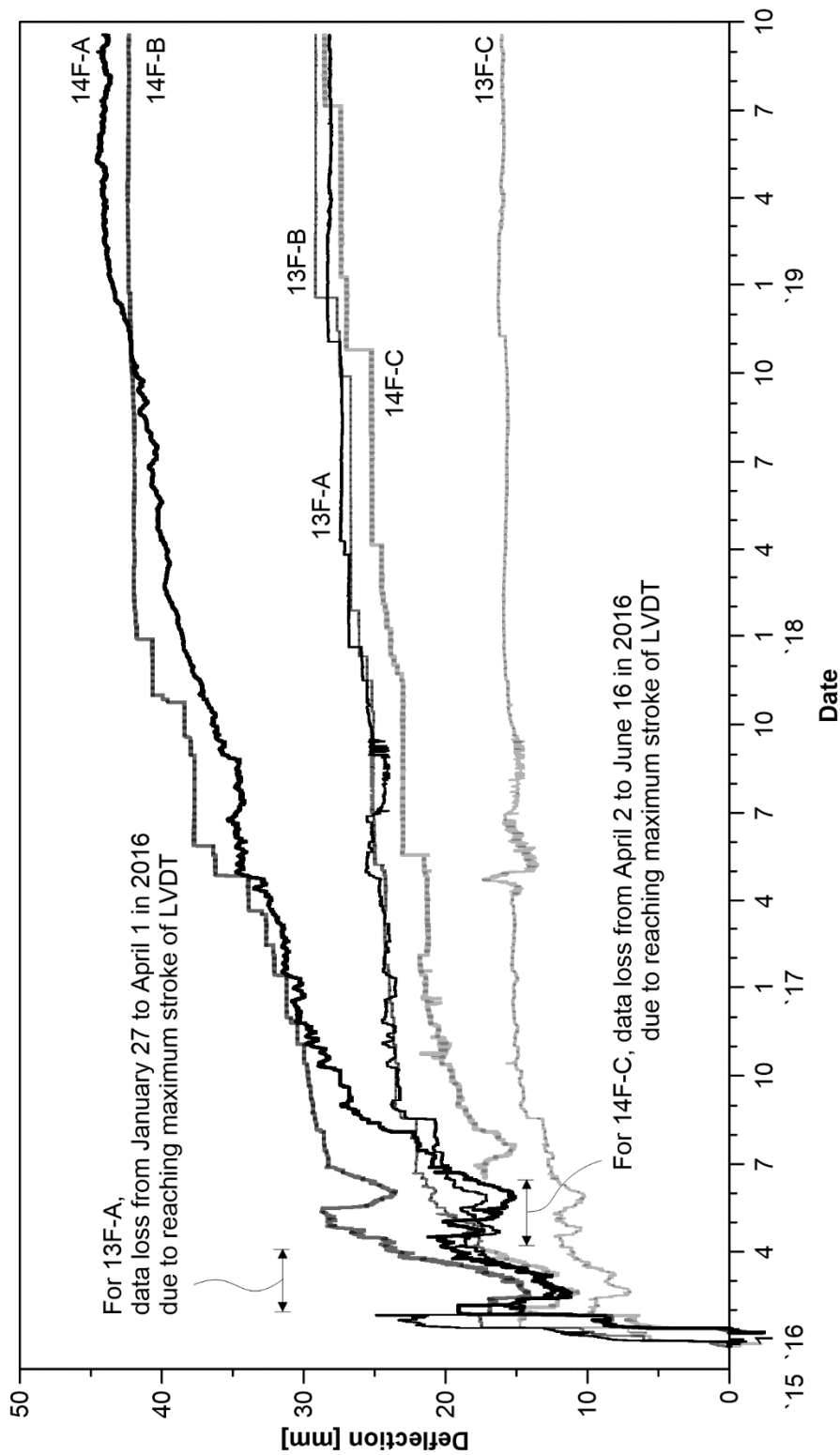


Figure 6-12 Results of PT slab deflection

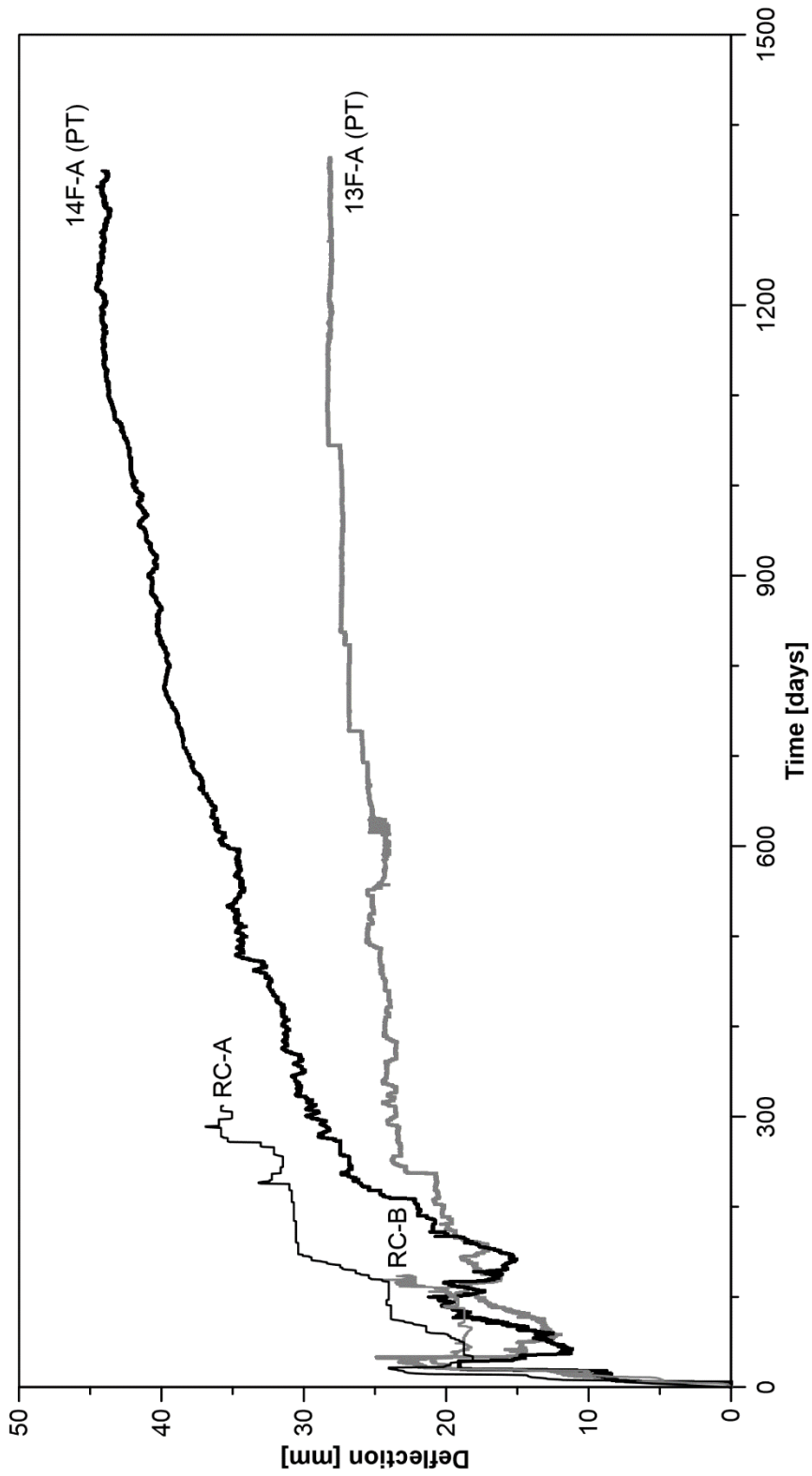


Figure 6-13 Comparison between RC and PT slabs

6.3 Factors Affecting Post-Tensioned Slab Deflection

Before predicting slab deflection, the factors that affect it were discussed. In addition to the construction methods, the composition of the members and the material properties of the concrete are well known deflection-related factors.

6.3.1 Dimension and Design

Span length

The slab is a curved member with a surface shape. The longer its span, the greater the deflection. This is especially proportional to the net span, which can be reduced by adding members such as drop panels, brackets, and walls.

Slab thickness

The slab thickness is directly related to the member's rigidity. The slab's stiffness is proportional to its thickness, and the deflection decreases with higher stiffness. As the thickness increases, however, the weight increases and more rebars are needed to resist flexure. Thinner slabs can help acquire a larger number of floors in buildings, so slab thickness should be set for economic considerations. In general, the thickness of the PT slab is 200 ~ 230 mm.

Beam and wall

A beam—a horizontal member that crosses between columns—shares the load of the slab and transmits it to the column, which greatly increases the rigidity as the secondary moment of the cross-section increases. However, the use of beams does not take advantage of the flat plate structure. When a wall is used instead of a column, it is designed by a one-way slab, which reduces the deflection.

Tendon profile

A tendon provides a compressive and upward force to concrete along the profile. The compression reduces the incidence of cracks and creeps, while the upward force directly reduces deflection. The number of tendons can be determined according to the allowable stress range of the concrete, and it is good to economically calculate it keeping in mind the construction cost along with the quantity of the rebar and tendon. Because of the small slab thickness, however, there is a limit to the varying tendon profiles.

Camber

Camber refers to the bending member that convexes upward when pouring concrete, taking into account that short- and long-term deflection occurs due to gravity. The convexly-manufactured members deflect over time resulting in lesser deflection.

However, it is practically very difficult to form a camber by deforming the formwork. In the PT slab, the amount of deflection is relatively smaller as compared to that of the RC slab due to the prestressing force. But at the same time, the deflection reduction can be maximized by using the camber optimally.

6.3.2 Concrete

Concrete strength does not directly affect deflection estimation. Stiffness is related to the modulus of elasticity, which is proportional to concrete strength, and therefore, the higher the concrete strength, the greater the resistance to deflection.

The elastic modulus is proportional to the rigidity of the member. As the shape of the cross-section is fixed, the change that occurs to the stiffness with time is due to the elastic modulus, unless there are no cracks. It is important to acquire the elastic modulus sufficiently early because the deflection continues to accumulate over time.

The concrete strength increases over time and is considerably affected by the curing temperature. In general, the ideal curing temperature suggested in the specification for strength is 20 °C. When the temperature is lower than 20 °C, the strength development slows down, and when the temperature is higher, the development speed increases. Sufficient curing temperature needs to be secured until enough strength is obtained. In cold winter, it is better to carry out heat curing.

6.3.3 Construction Method

The number of floors supported by shores during construction has a direct impact on the deflection. Applied loads, such as concrete pouring or stacking up of materials, are distributed to the lower slabs that are connected by shores. The total load on the uppermost slab is lower, but the load on the bottom slab is higher, which may result in an increase in the deflection. Since some time has already passed for the bottom concrete, it has a certain amount of stiffness and a better bending resistance as compared to the top concrete that has just been poured. However, care should be taken if the stiffness of the underlying concrete is not sufficiently developed.

The number of shores used on one floor is determined by considering the load that may occur during construction. Simply, a point load at shoring is calculated by dividing the total load with the number of shores. The weight of the shores, however, should be considered as the live load. In addition, when the number of shores increases, the workspace is shortened and the construction time increases.

Removing shorings that are at the bottom of the slab increases the deflection. In order to minimize this, the concrete strength of the slab linked to the shorings should be enough to resist additional loads due to the elimination of shorings.

As mentioned, deflection is directly affected by the rigidity of the member. Since the design strength of concrete is already determined, the speed at which the initial strength is developed is important for deflection control. Concrete strength at the time of formwork removal is generally less than the design strength, and so there is

a high probability that large deflections will occur even at light loads. It is best to maintain the formwork until the concrete is fully hardened.

Furthermore, sag can be drastically reduced by using curing methods, such as wet and steam curing. In particular, when the temperature is low in winter, the curing speed of the concrete drops sharply, which makes heat supply curing essential.

6.3.4 Post-Tensioning and Construction Procedure

The concrete receives upward force due to the tension of the strand in the parabolic tendon profile. The upward movement prevents or delays the occurrences of cracks or creeps. The minimum concrete strength required for jacking the strand is basically 24 MPa. As the stiffness of the concrete increases over time, the effect of the prestressing force decreases. Therefore, tensioning the strand as early as possible is better to minimize deflection.

During construction, various kinds of loads, such as equipment, material, and workers are applied. A large degree of cracking and creep may be generated even through temporarily applied loads, thereby increasing the amount of residual deflection.

If there is more deflection at the time of the finishing process than what was planned, it will be hard to acquire the designed height of the floor with ducts, pipes, or other

materials that have a fixed dimension. In addition, these installations used for finishing can be treated as dead load, which may result in an increase in the deflection. Even after attaching the materials, various problems, such as cracking of the tiles, detachment of materials, and deformation of panels, may occur due to deflection. Therefore, it is recommended to install the finishing member after about three months of the short-term deflection occurrence.

6.4 Short-Term Deflection

The short-term deflection for the slab of the East Central Tower was predicted with analysis. The deflection change was tracked based on the load and material properties that varied with the construction process. Also, the analytic procedure using ADAPT-Floor Pro, a specialized PT slab design software, was introduced.

6.4.1 Comparison between Whole and Partial Models

A model for the target slab, which includes columns, drop panels, and PT tendons, is shown in **Figure 6-14**. In the analysis with self-weight (**Figure 6-15**), the maximum deflection is observed at the corner slab, which is the same location as 13F-A or 14F-A in **Figure 6-10**.

To save the modeling and computing time, a partial model of the corner slab is designed as **Figure 6-16**. Partial modeling requires the proper division of the compartments and the appropriate boundary conditions for the cutouts. For the two sides where the slab continues, the displacement is free in the Z direction and the rotation is fixed only along the edge of X-X or Y-Y.

The analysis results of the whole and partial models are compared in **Table 6-2**. The two models show similar deflections for each load combination; the differences are

0.01 mm under dead load and 0.07 mm while considering prestressing. Therefore, the partial model is used for the remaining prediction process in this section.

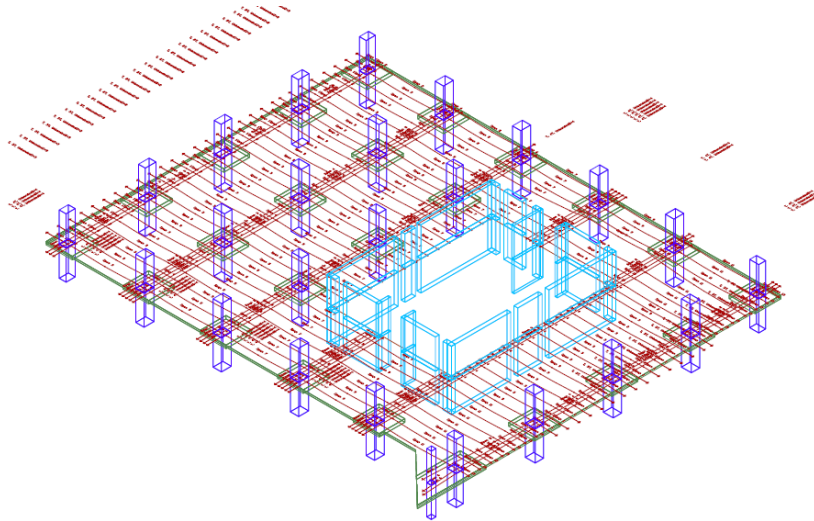


Figure 6-14 Modeling for whole slab

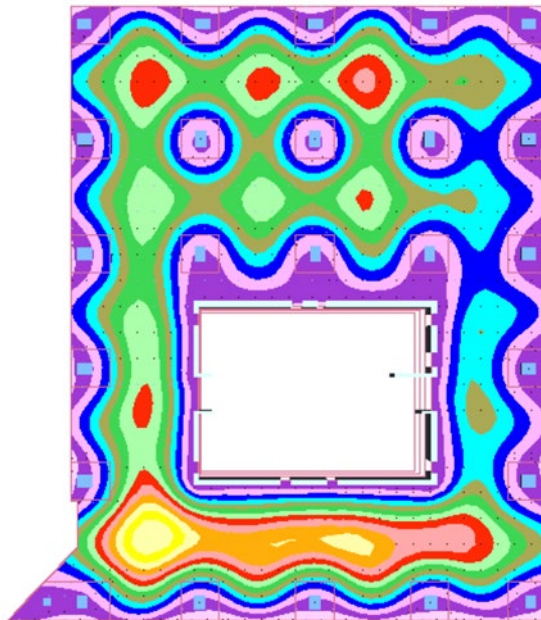


Figure 6-15 Analysis results of whole slab model

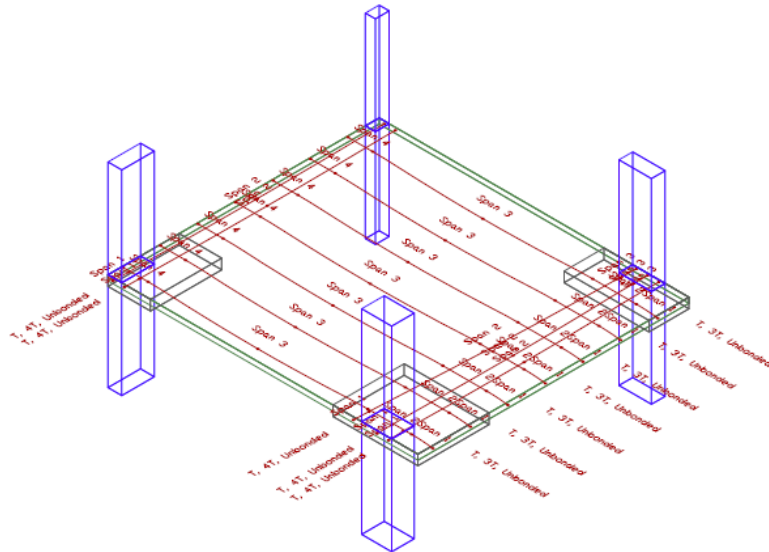


Figure 6-16 Modeling for partial slab

Table 6-2 Maximum deflection analysis for whole and partial slab models

Load combination	Whole slab model	Partial slab model
Self-weight	9.12 mm	9.11 mm
Self-weight + PT	4.56 mm	4.63 mm

6.4.2 Cycle of Construction

Three groups of shores are used in this building, and the main construction process related to the slab deflection, from pouring the slab concrete to removing shores above the target slab, is illustrated in **Figure 6-17**.

There are a total of eleven stages with four cycles (**Table 6-3**). The day on which concrete is poured on the target slab is defined as day 0. The bottom shoring group is removed on day 1 and the prestressing force is applied on day 9. Each cycle takes 12 days in the calendar date, without including the work days. On day 37, the shores on the target slab are eliminated, and the short-term deflection is determined.

6.4.3 Shoring

The shores are arranged as shown in **Figure 6-18**. The shores that are most used are PEP, which are made of aluminum, and are distributed overall on the slab. AS is also an aluminum shore that is placed near the drop panels. MP is a copper shoring, and a group of four MPs are used to support the center of each slab where the largest deflection occurs.

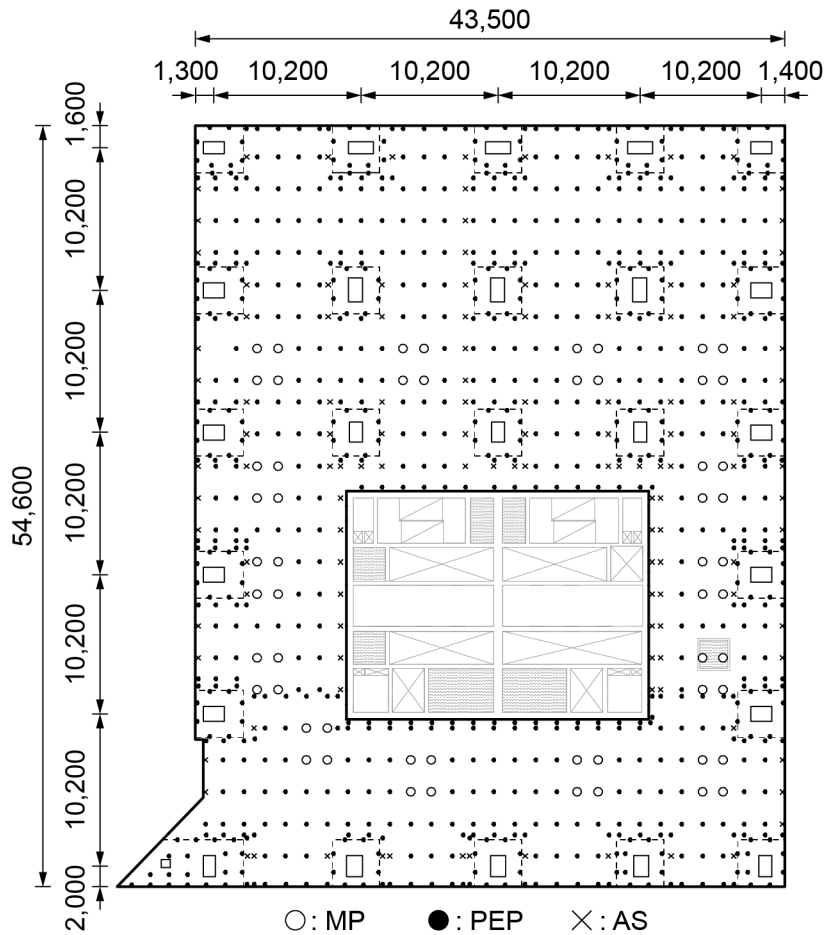


Figure 6-18 Shoring plan of standard floor [unit: mm]

Table 6-4 Material properties of shoring

	Weight [kg]	Elastic modulus, E [MPa]	Creep coefficient
MP	18.8	200,000	2.0
PEP	19.2	69,999	2.0
AS	17.9	69,999	2.0

The material properties of shoring are described in **Table 6-4**. In ADAPT, shoring is expressed as a circular pillar with a diameter of 100 mm. The unit weight was input by dividing the total weight with the volume of the circular column. The elastic modulus is set as 200,000 MPa for MP and 70,000 MPa for PEP and AS. The strength of the circular column is calculated automatically according to the elastic modulus.

6.4.4 Compressive Strength of Concrete

In KBC (2016), the compressive strength according to age is calculated using the following equations:

$$f_{cu}(t) = \beta_{cc}(t)f_{cu} \quad (6-1)$$

$$\beta_{cc}(t) = \exp \left[\beta_{sc} \left(1 - \sqrt{\frac{28}{t}} \right) \right] \quad (6-2)$$

where $f_{cu}(t)$ is the average compressive strength of concrete at age t ; $\beta_{cc}(t)$ is the correction coefficient according to age for concrete strength development; and β_{sc} is the influence coefficient on dry shrinkage according to cement type.

Otherwise, the equation for predicting concrete strength at age t [days] is given in ACI 209R (1992) by:

$$f_{cu}(t) = \frac{t}{\alpha + \beta t} f_{cu} \quad \text{[MPa]} \quad (6-3)$$

where α and β are constants.

The typical recommended values of β_{sc} , α , and β are given in **Table 6-5**, with the cement and curing types.

Table 6-5 Values of constants β_{sc} , α , and β

Cement type	I		II	III	
Type of curing	Moist cured	Steam cured	-	Moist cured	Steam cured
β_{sc}	0.35	0.15	0.40	0.25	0.12
α	4.00	1.00	-	2.30	0.70
β	0.85	0.95	-	0.92	0.98

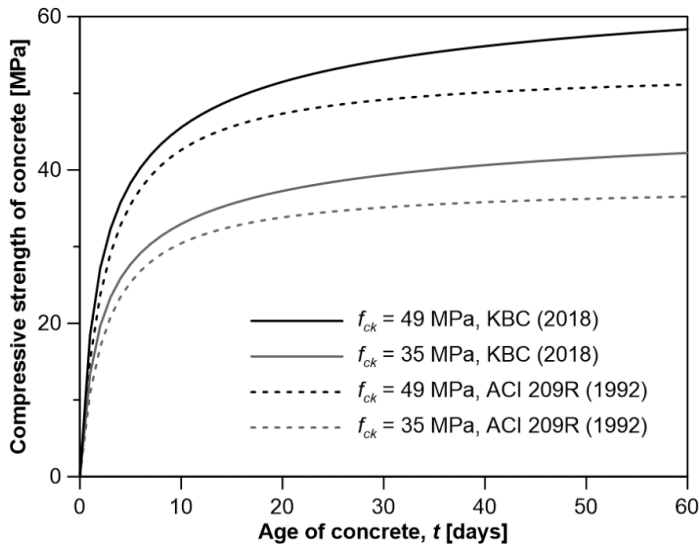


Figure 6-19 Compressive strength of concrete

For the slab and column, whose design strengths are 35 MPa and 45 MPa, respectively, the concrete strengths are expressed as shown in **Figure 6-19**. **Eq. (6-3)** is more conservative than **Eq. (6-1)**, but, **Eq. (6-1)**, defined by the domestic specification, is used for determining the compressive strength of concrete in the analysis.

6.4.5 Elastic Modulus of Concrete

Early-aged concrete

The elastic modulus of concrete can be calculated using **Eq. (6-4)** suggested in KBC (2016). The average compressive strength of concrete on the 28th day, f_{cu} , usually exceeds the design strength f_{ck} (**Eq. (6-5)**). The correction factor Δf varies the range of concrete strength as shown in **Eq. (6-6)**.

$$E_c = 0.077m_c^{1.5} \sqrt[3]{f_{cu}} \quad [\text{MPa}] \quad (6-4)$$

$$f_{cu} = f_{ck} + \Delta f \quad (6-5)$$

$$\Delta f = \begin{cases} 4 & [\text{MPa}] \quad (f_{ck} \leq 40) \\ 4 + 0.1(f_{ck} - 40) & [\text{MPa}] \quad (40 \leq f_{ck} \leq 60) \\ 6 & [\text{MPa}] \quad (f_{ck} \geq 60) \end{cases} \quad (6-6)$$

where E_c is the elastic modulus of concrete; m_c is the unit weight of concrete; f_{cu} is the average compressive strength of concrete at the age of 28 days; f_{ck} is

the design compressive strength of concrete; and Δf is the correction factor for concrete strength.

On the other hand, ACI 318 (2019) uses specified concrete strength for the calculation of elastic modulus.

$$E_c = 0.043m_c^{1.5} 4700\sqrt{f_c} \text{ [MPa]} \quad (6-7)$$

where f_c is the specified compressive strength of concrete.

However, the early-aged concrete is used for target building due to cold weather. Hong et al. (2010) found that **Eq. (6-4)** cannot reflect the elastic modulus of the early age concrete in Korea, and presented the following equation:

$$E_c = k_1\sqrt{f_c} \text{ [MPa]} \quad (6-8)$$

where k_1 is the proportional constant depending on the type of cement (4,050 for ordinary Portland cement).

The modulus of elasticity calculated using **Eqs. (6-4), (6-5), and (6-8)** are compared in **Figure 6-20**. The early-aged concrete has a lower elasticity than the normal concrete. In this analysis, **Eq. (6-8)** was applied to reflect the more realistic concrete properties and get more reasonable short-term deflections.

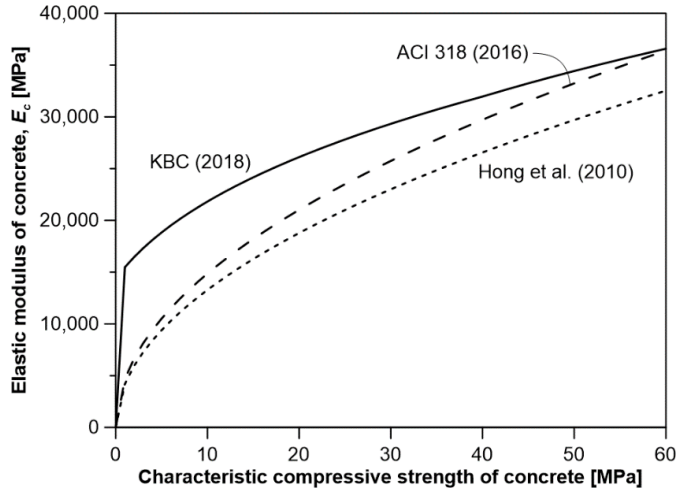


Figure 6-20 Elastic modulus of early-aged concrete

Equivalent age with curing temperature

The concrete age is not simply determined by the date of time but varies greatly depending on the curing temperature. Hansen and Pedersen (1977) offered the calculation of equivalent age by considering the curing temperature as follows:

$$t_e = \sum_0^t \exp\left[\frac{E_a}{R} \cdot \left(\frac{1}{T_s} - \frac{1}{T_a}\right)\right] \Delta t \quad [\text{days}] \quad (6-9)$$

$$E_a = \begin{cases} 33.5 & (T_a \geq 20 \text{ }^\circ\text{C}) \\ 33.5 + 1.47(20 - T_a) & (T_a < 20 \text{ }^\circ\text{C}) \end{cases} \quad [\text{KJ/mol}] \quad (6-10)$$

where t_e is the equivalent age; E_a is the apparent activation energy; R is the gas constant (8.314 J/mol·K); T_s is the reference temperature (293 K); and T_a [K] is the concrete temperature during the time Δt [days].

The curing rates according to **Eq. (6-6)** are summarized in the range 1 °C to 80 °C in **Table 6-6**. The reference temperature, when the curing rate is 100%, is 20 °C,

Table 6-7 is an example that shows how to calculate the equivalent concrete age. According to the Korea Meteorological Administration (KMA), the representative temperature during January 2016 was 0 °C. The first two days were set at 20 °C because thermal curing was performed until the formworks were demolded. After demolding, 0 °C was input for the remaining period. The equivalent age is the product of the curing rate and the duration. The cumulative equivalent age represents the equivalent age until the date.

For the slab (35 MPa) and column (45 MPa), the compressive strength and elastic modulus of the concrete are given in **Tables 6-8** and **6-9**, respectively. The equivalent age is determined by considering the curing temperature in the same way as in the example shown in **Table 6-7**. With **Eq. (6-1)** using the equivalent age, the concrete strength is calculated, and finally, the modulus of elasticity is defined with the equation by Hong et al. (2010).

Table 6-6 Curing rate coefficient according to temperature

Temp. [°C]	Curing rate [%]						
1	17.4	21	104.8	41	250.9	61	540.9
2	20.0	22	109.8	42	261.3	62	560.8
3	22.8	23	115.0	43	272.1	63	581.2
4	25.9	24	120.3	44	283.3	64	602.3
5	29.2	25	126.0	45	294.8	65	623.9
6	32.8	26	131.8	46	306.7	66	646.3
7	36.7	27	137.8	47	319.1	67	669.3
8	40.8	28	144.1	48	331.9	68	692.9
9	45.1	29	150.7	49	345.1	69	717.3
10	49.7	30	157.4	50	358.7	70	742.4
11	54.4	31	164.5	51	372.8	71	768.2
12	59.4	32	171.8	52	387.3	72	794.7
13	64.4	33	179.4	53	402.3	73	822.0
14	69.5	34	187.2	54	417.8	74	850.0
15	74.7	35	195.4	55	433.8	75	878.9
16	80.0	36	203.8	56	450.3	76	908.5
17	85.1	37	212.6	57	467.3	77	939.0
18	90.2	38	221.7	58	484.9	78	970.3
19	95.2	39	231.1	59	503.0	79	1002.4
20	100.0	40	240.8	60	521.7	80	1035.5

Table 6-7 Calculation example of cumulative equivalent curing duration

Temperature [°C]	20	0	0	0	0
Curing rate [%]	100.0	15.1	15.1	15.1	15.1
Duration [days]	2	7	3	12	12
Equivalent curing duration [days]	2.00	1.06	0.45	1.81	1.81
Calendar age [days]	2	9	12	24	36
Equivalent age [days]	2.00	3.06	3.51	5.32	7.13

Table 6-8 Elastic modulus of slab concrete (35 MPa)

Day [days]	Equivalent duration [days]	Concrete strength [MPa]	Elastic modulus [MPa]	Day [days]	Equivalent duration [days]	Concrete strength [MPa]	Elastic modulus [MPa]
1	1.0	12.0	14,012.5	31	6.4	26.6	20,894.9
2	2.0	17.6	17,008.0	32	6.5	26.8	20,958.6
3	2.2	18.2	17,294.7	33	6.7	26.9	21,020.4
4	2.3	18.8	17,556.8	34	6.8	27.1	21,080.2
5	2.5	19.3	17,797.8	35	7.0	27.2	21,138.3
6	2.6	19.8	18,020.3	36	7.1	27.4	21,194.7
7	2.8	20.3	18,226.8	37	7.3	27.5	21,249.4
8	2.9	20.7	18,419.0	38	7.4	27.7	21,302.6
9	3.1	21.1	18,598.6	39	7.6	27.8	21,354.4
10	3.2	21.5	18,766.9	40	7.7	27.9	21,404.7
11	3.4	21.8	18,925.2	41	7.9	28.1	21,453.7
12	3.5	22.2	19,074.3	42	8.0	28.2	21,501.4
13	3.7	22.5	19,215.2	43	8.2	28.3	21,547.9
14	3.8	22.8	19,348.5	44	8.3	28.4	21,593.3
15	4.0	23.1	19,475.0	45	8.5	28.5	21,637.5
16	4.1	23.4	19,595.2	46	8.6	28.7	21,680.6
17	4.3	23.7	19,709.7	47	8.8	28.8	21,722.7
18	4.4	23.9	19,818.9	48	8.9	28.9	21,763.8
19	4.6	24.2	19,923.1	49	9.1	29.0	21,803.9
20	4.7	24.4	20,022.9	50	9.2	29.1	21,843.2
21	4.9	24.7	20,118.4	51	9.4	29.2	21,881.5
22	5.0	24.9	20,210.0	52	9.6	29.3	21,919.0
23	5.2	25.1	20,297.9	53	9.7	29.4	21,955.7
24	5.3	25.3	20,382.5	54	9.9	29.5	21,991.6
25	5.5	25.5	20,463.8	55	10.0	29.6	22,026.7
26	5.6	25.7	20,542.2	56	10.2	29.7	22,061.1
27	5.8	25.9	20,617.7	57	10.3	29.8	22,094.8
28	5.9	26.1	20,690.6	58	10.5	29.9	22,127.9
29	6.1	26.3	20,761.0	59	10.6	29.9	22,160.2
30	6.2	26.5	20,829.1	60	10.8	30.0	22,191.9

Table 6-9 Elastic modulus of column concrete (45 MPa)

Day [days]	Equivalent duration [days]	Concrete strength [MPa]	Elastic modulus [MPa]	Day [days]	Equivalent duration [days]	Concrete strength [MPa]	Elastic modulus [MPa]
1	1.0	16.8	16,579.9	31	6.4	37.3	24,723.2
2	2.0	24.7	20,124.1	32	6.5	37.5	24,798.6
3	2.2	25.5	20,463.3	33	6.7	37.7	24,871.6
4	2.3	26.3	20,773.5	34	6.8	37.9	24,942.5
5	2.5	27.0	21,058.6	35	7.0	38.1	25,011.2
6	2.6	27.7	21,321.9	36	7.1	38.3	25,077.9
7	2.8	28.4	21,566.2	37	7.3	38.5	25,142.7
8	2.9	29.0	21,793.6	38	7.4	38.7	25,205.6
9	3.1	29.5	22,006.2	39	7.6	38.9	25,266.8
10	3.2	30.1	22,205.4	40	7.7	39.1	25,326.4
11	3.4	30.6	22,392.6	41	7.9	39.3	25,384.4
12	3.5	31.1	22,569.0	42	8.0	39.5	25,440.8
13	3.7	31.5	22,735.7	43	8.2	39.6	25,495.9
14	3.8	32.0	22,893.5	44	8.3	39.8	25,549.5
15	4.0	32.4	23,043.1	45	8.5	40.0	25,601.8
16	4.1	32.8	23,185.4	46	8.6	40.1	25,652.8
17	4.3	33.2	23,320.8	47	8.8	40.3	25,702.6
18	4.4	33.5	23,450.0	48	8.9	40.4	25,751.3
19	4.6	33.9	23,573.4	49	9.1	40.6	25,798.8
20	4.7	34.2	23,691.4	50	9.2	40.7	25,845.2
21	4.9	34.5	23,804.4	51	9.4	40.9	25,890.6
22	5.0	34.9	23,912.8	52	9.6	41.0	25,934.9
23	5.2	35.2	24,016.8	53	9.7	41.1	25,978.3
24	5.3	35.5	24,116.9	54	9.9	41.3	26,020.8
25	5.5	35.7	24,213.1	55	10.0	41.4	26,062.4
26	5.6	36.0	24,305.8	56	10.2	41.5	26,103.1
27	5.8	36.3	24,395.2	57	10.3	41.7	26,143.0
28	5.9	36.5	24,481.4	58	10.5	41.8	26,182.0
29	6.1	36.8	24,564.7	59	10.6	41.9	26,220.3
30	6.2	37.0	24,645.3	60	10.8	42.0	26,257.9

6.4.6 Analysis Results

In the previous sections, all the input data is determined. The deflection at each stage is analyzed with only one partial model, but having different properties depends on the time. **Table 6-10** and **Figure 6-21** show the deflection change over time with the ideal construction cycle, and the short-term deflection is 11.3 mm. On day 1, the bottom group of shoring is removed, but there is no change because the formwork is not disassembled. When the tendon is jacked, the deflection decreases; however, when the concrete is poured and shoring is eliminated, the deflection increases. In the final stage, when the shoring above the slab is removed, 62% of the maximum deflection (18.2 mm) is restored. This is predicted assuming that no cracks occur during the process due to post-tensioning and gross sectional properties are maintained.

Table 6-10 Deflection change of Nth floor slab along working procedure

Work process	Calendar day [days]	Deflection [mm]	Cumulative deflection [mm]
N th : concrete pouring	0	0	0
N-3 th : remove shoring	1	0	0
N th : jacking tendons	9	-3.7	-3.7
N+1 th : concrete pouring	12	8.6	4.9
N-2 th : remove shoring	13	5.9	10.8
N+1 th : jacking tendons	21	-1.4	9.4
N+2 th : concrete pouring	24	7.1	16.5
N-1 th : remove shoring	25	7.2	23.7
N+2 th : jacking tendons	33	-0.6	23.1
N+3 th : concrete pouring	36	6.4	29.5
N th : remove shoring	37	-18.2	11.3

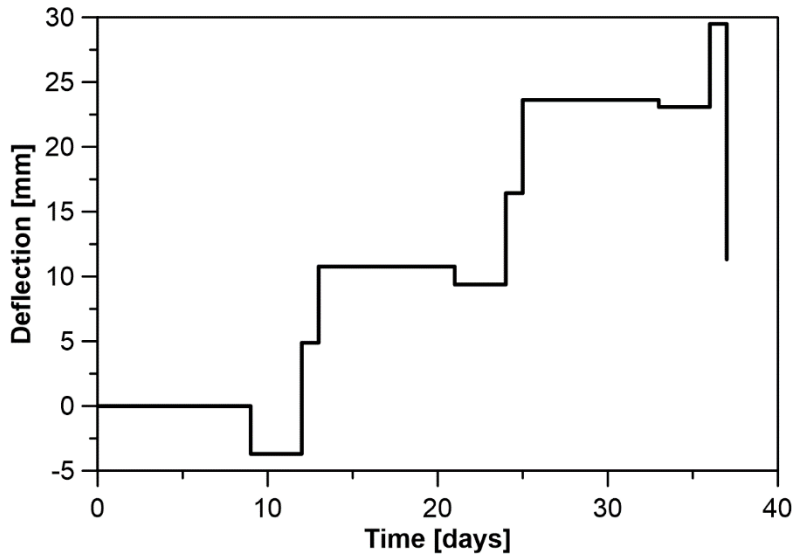


Figure 6-21 Analysis result of short-term deflection

6.4.7 Comparison of Monitoring and Analysis Results

The actual construction date is slightly different from the planned date. The properties on the actual day are used for each stage, and the results for 13F-A and 14F-B are summarized in **Table 6-11**. Also, **Figures 6-22** and **6-23** compare the measured results and the analytical predictions for 13F-A and 14F-A, respectively.

The maximum deflection of prediction for 13F-A is about 5 mm more than the measurement, but the short-term deflection is 1 mm less. When the N^{th} shoring is removed, the deflection decreased immediately in the analysis. However, in reality, 10 mm was restored on that day and the additional decrease of 3 mm took about 20

days. This may be due to the characteristics of the concrete, which takes time to restore elasticity.

Between the 30th and 38th days of the 14F-A, the displacement meter reached its limit and a horizontal section is observed in **Figure 6-23**. After the removal of shores, there was an immediate decrease in the deflection, and some of the deflection gradually decreased over a period of 10 days. The short-term deflections of the measured and predicted results was identical.

In the analysis, the concrete member is assumed as being in the elastic state. The measurement results, which are almost similar to the analysis, verify that the cracks are minimized with the PT effect and three groups of shoring.

Table 6-11 Deflection prediction for 13F-A and 14F-A

Work process	13F-A			14F-A		
	Calendar day [days]	Deflection [mm]	Cumulative deflection [mm]	Calendar day [days]	Deflection [mm]	Cumulative deflection [mm]
N th : concrete pouring	0	0	0	0	0	0
N-3 th : remove shoring	1	0	0	1	0	0
N th : jacking tendons	9	-3.7	-3.7	9	-3.7	-3.7
N+1 th : concrete pouring	12	8.6	4.9	12	8.6	4.9
N-2 th : remove shoring	13	5.9	10.8	13	5.9	10.8
N+1 th : jacking tendons	21	-1.4	9.4	21	-1.4	9.4
N+2 th : concrete pouring	24	7.1	16.5	24	7.1	16.5
N-1 th : remove shoring	25	7.2	23.7	25	7.2	23.7
N+2 th : jacking tendons	33	-0.6	23.1	33	-0.6	23.1
N+3 th : concrete pouring	36	6.4	29.5	36	6.4	29.5
N th : remove shoring	37	-18.2	11.3	37	-18.2	11.3

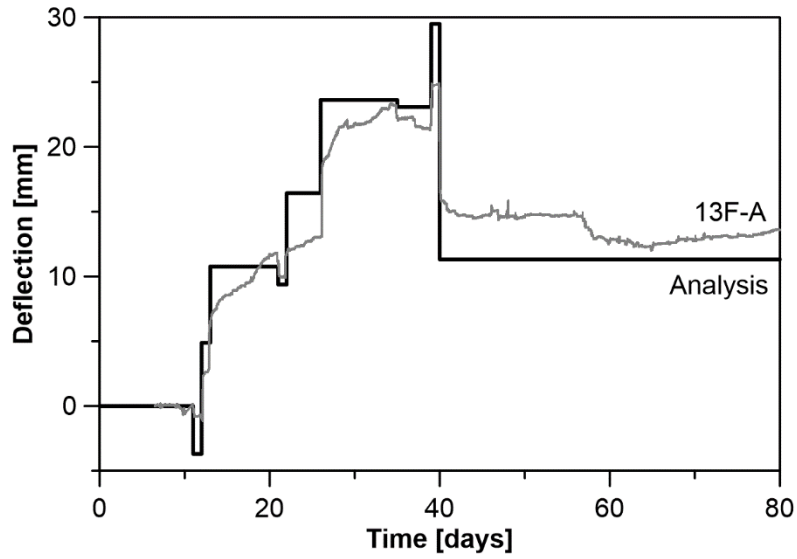


Figure 6-22 Comparison between analysis and measured data of 13F-A

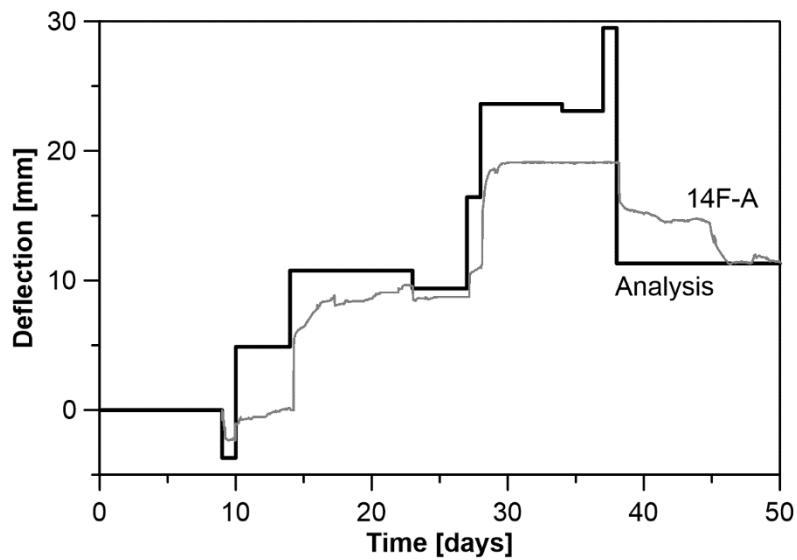


Figure 6-23 Comparison between analysis and measured data of 14F-A

6.5 Long-Term Deflection

The long-term deflection is proportional to the short-term deflection and can be expressed by using the following equation of KBC (2016):

$$\Delta_L = \Delta_S(1 + \lambda_\Delta) \quad (6-11)$$

$$\lambda_\Delta = \frac{\xi}{1 + 50\rho'} \quad (6-12)$$

where Δ_L is the long-term deflection; Δ_S is the short-term deflection; λ_Δ is the amplification factor; ξ is the time-dependent coefficient; and ρ' is the compression steel ratio.

6.5.1 Time-Dependent Factor

Eqs. (6-10) and (6-11) are defined based on the experimental results of the RC structures. Among these variables, only ξ is changeable. The ρ' is determined by design, and Δ_S is a result of the construction. The time-dependent coefficient for the RC slab, ξ_{RC} , is given as in **Table 6-12**.

To compare and normalize the measurement data, the deflections of 13F-A, 13FL-B, 14F-A, and 14F-C were divided by their respective short-term deflections (**Figure 6-24**). The short-term deflections' time was set to day 0. As compared to the data

measured for five months, the deflection ratio using ξ_{RC} was overestimated. For the PT slab, ξ_{PT} is suggested with the value as a blind prediction for further performance after five months monitoring.

Table 6-12 Time-dependent factor (ξ) for RC and PT slabs

Time [days]	ξ_{RC}	ξ_{PT} (suggestion)
90	1.0	0.8
180	1.2	0.95
360	1.4	1.1
1800	2.0	1.4

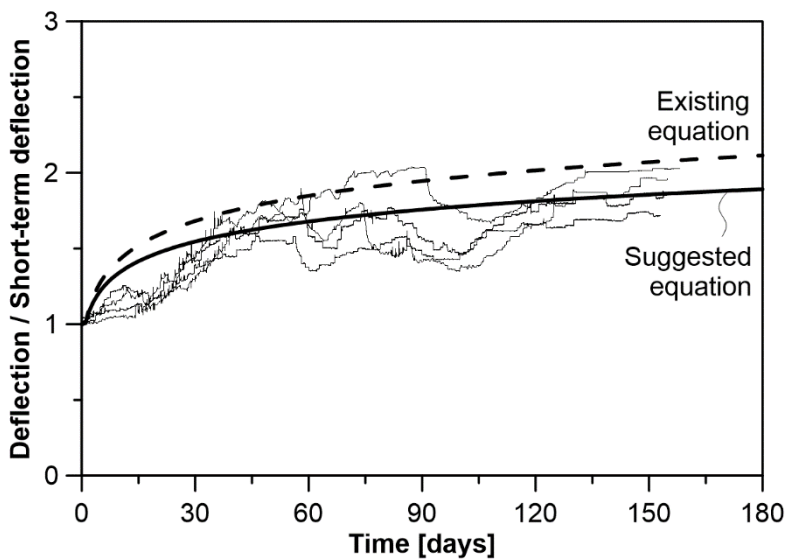


Figure 6-24 Comparison between existing and suggested time-dependent factors

6.5.2 Prediction of Long-Term Deflection

Figure 6-25 shows various methods that predict the long-term deflection using the measured result of 13F-A.

The most simple method for predicting long-term deflection is by using load combinations. Before analyzing the long-term deflection, the short-term deflection is obtained with a sustained load—the summation of self-weight (SW), post-tensioning (PT), dead load (DL), and 30% of the live load (LL). It is more than twice the deflection with only self-weight and PT. To get the long-term deflection, three times the sustained load and additional LLs are used as load combinations. The reason for using thrice the sustained load is that the long-term deflection of the RC slab after five years in **Eq. (6-11)** is three times that of the short-term deflection. The added LLs are for considering deflection due to extra load during construction or after moving in.

With the suggested coefficient ξ_{PT} , the prediction is better matched to the measurement results at over 900 days, confirming that the blind prediction was quite accurate and that the assumption of uncracked section due to PT was reasonable. The deflection is expected to be 27 mm at 5,000 days, which is much less than the allowable deflection ($L / 480 = 42.5$ mm) of KBC (2016).

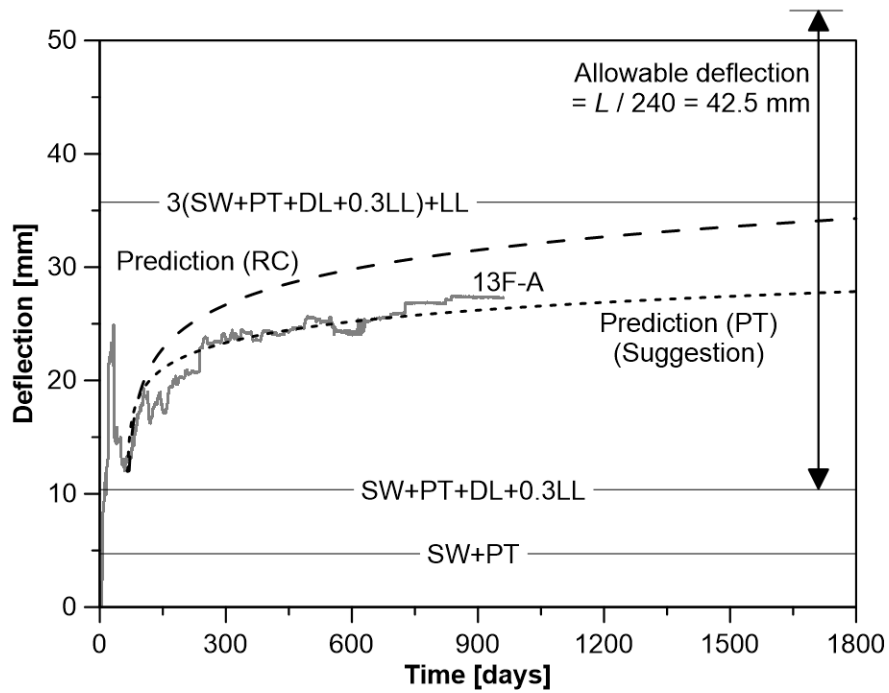


Figure 6-25 Various methods predicting long-term deflection

6.6 Summary

In order to monitor the long-term behavior of PT tendons with developed anchors in the actual building, the tendon stress and slab deflection were measured at the East Central Tower in Gangdong-gu, Seoul. A strand with fiber Bragg grating system is used for measuring the stress. Additionally, the deflection was measured at total six points (two floors for three different slab spans (corner, edge, interior)) in the same building over a period of three years and nine months.

Long-term deflection of the slab is proportional to short-term deflection, and a more accurate prediction of deflection can optimize PT design and reduce the cost of construction. The short-term deflection of the corner slab is predicted through the finite element analysis with the construction load and properties of the member that are known to change frequently during the construction process. However, sectional properties are fixed to gross-sectional properties.

The measurement and prediction results of short- and long-term deflections for PT slab are summarized as follows.

- 1) A 55-m strand was stressed up to 75% of the nominal tensile strength and decreased to about 73% after three months.
- 2) A 33-m strand had an initial stress of only 49% of the nominal tensile strength, but remained at an average 45% after three years.

- 3) The least deflection occurred in the interior slab, and the corner slab was deflected up to 44 mm.
- 4) The performance of PT slabs was better in deflection than RC slabs, even with longer span, verifying that the PT slab had minimal cracks.
- 5) The overall trend is similar to the measurement data. Especially, the predicted short-term deflection is relatively accurate with an error of less than 2 mm, which means that uncracked elastic analysis is reasonable for PT slab.
- 6) Based on the measured data, the value of time-dependent coefficient for PT slab is proposed, while the formula for calculating long-term deflection specifically pertains to the RC slab. The revised equation expresses the tendency of long-term deflection of PT slab better than the conventional formula.

These results demonstrate that long-term performance of the developed anchors has been satisfactory and did not adversely affect the deflection behavior.

Chapter 7. Application to Actual Buildings and Additional Research

The performance of the developed anchorage was verified by carrying out various tests mentioned in previous chapters. Furthermore, a patent for this anchor system was published in 2018 (Samsung_C&T & SNU_R&DB_Foundation, 2018). In addition to being used in PT buildings as its commercial purpose, the anchor was also used in additional experimental studies at Seoul National University to observe the behavior of PT members.

7.1 Application to Actual Buildings

The developed encapsulated post-tensioned anchor systems have been used for three residential buildings along with an office building in Korea. **Table 7-1** shows building names and the quantity of used anchors.

The first place used is Jayang-dong Raemian Premier Palace. It is a mixed-use apartment wherein two apartment buildings are connected with commercial and official facility (from 1st to 4th floors). The developed anchor system was used for one of two buildings, whereas the other one was built as RC structure.

On the other hand, Raemian Seocho Estige S used the PT anchor in all five apartment buildings. A total of 51,000 anchorages were utilized for this purpose, as shown in **Figure 7-1**.

In 2017, 1,400 anchors were applied to some slabs that needed the deflection control for the large dead load of equipment in Jeonju Eco-city Desian. The PT anchor system was used to achieve a high floor height with thin slab for one building of Knowledge Industrial Center of Pangyo Creative Economic Valley. No adverse reports or complaints have been received at all in terms of constructability and performance.

Table 7-1 Post-tensioned buildings with developed encapsulated anchors

Constructor	Building	Quantity	PT Construction
Samsung C&T	Jayang-dong Raemian Premier Palace (Apartments)	10,500	2016.05~2016.12
Samsung C&T	Raemian Seocho Estige S (Apartments)	51,000	2016.07~2017.04
Taeyoung E&C	Jeonju Eco-city Desian (Apartments), Block 7 and 12	1,400	2017.01~2017.05
Kolon Global	Knowledge Industrial Center of Pangyo Creative Economic Valley, Block F1	14,000	2017.10~2018.04



Figure 7-1 Application of developed anchor to Raemian Seocho Estige S project

7.2 Application to Research

Kwon (2016) conducted full-scale seismic tests to observe the behavior of exterior beam-column connections in accordance with the concrete strength. Three exterior joints and three roof level joints among total eight specimens used the unbonded PT system. The developed bare anchors were used as well (**Figure 7-2**). The PT specimens showed sufficient lateral deformation capacity and energy dissipation ability with very high joint shear demands.

The flexural behavior of seven two-span unbonded PT beams was verified under a four-point static loading condition (K. Kim, 2018). The variables included strand strength (2,400 and 1,860 MPa) and tendon profile (high and low). The developed encapsulated anchorage system was used for 1,860 MPa tendon. Test results demonstrated the flexural behavior and secondary moment effect of PT beams.



Figure 7-2 Unbonded tendons in specimen (Kwon, 2016)

Chapter 8. Summary and Conclusions

The United States or Europe mainly uses the strand with a diameter of 12.7 mm for post-tensioning (PT) method, while a 15.2-mm diameter strand is primarily used in Korea. An anchor for the Ø12.7 mm single-strand has a relatively small size, but the anchor using the Ø15.2-mm strand is large and inefficient. In this dissertation, a post-tensioned anchor for Ø15.2-mm unbonded single-strand tendon was developed to reflect the existing trend in domestic PT construction. In addition, its performance was verified through various tests.

The anchor is designed through finite element analysis, which investigates the maximum von Mises stress by varying the shape of bearing plate, body, and gusset. The shape is optimized to minimize this stress. In addition, the design is also determined in consideration of a jacking device, accessories, and workability. A bare anchor has the bearing plate of 125 mm×70 mm, and its height is 65 mm. The material of anchor casting is GCD500-7 and its sleeve can be fixed using threads.

ACI 423.7-14, on the other hand, requires the use of encapsulation system, which is highly resistant to corrosion. Although this is not mandatory in Korea, the encapsulated anchor was developed to improve the durability of PT tendons and buildings. As the plastic cover can be used to either substitute or fix the accessory, unnecessary parts of casting were removed. The height was decreased to 47.5 mm by eliminating the portions for the sleeve, pocket former, and end cap. The plastic

cover having a thickness of about 2 mm was made in a single piece, including a 145 mm long sleeve. The pocket former and the end cap can be screwed on the anchor head.

According to KCI-PS101, the anchor performance was confirmed with three kinds of tests; static load test, fatigue test, load transfer test. Static load tests were performed on the bare anchor and encapsulated anchor, respectively, to verify the anchorage behavior for the load greater than 95% of the strand's nominal tensile strength. The displacement of the wedge and the two wires of strand measured at the fixed end were less than 6 mm. In the fatigue test, the long-term performance of the developed anchor was examined by applying 2 million times of cyclic loads in the range of 156.6 kN and 167.7 kN at 3 Hz.

The load transfer test with rectangular concrete specimens verified the change of fracture strength based on the reinforcement details of the anchorage zone. A specimen which only has the auxiliary reinforcement withstands 1.62 times the nominal tensile strength of the strand. In the experiment which involves the use of three anchors, the performance with existing horizontal and U-shaped reinforcement was confirmed. In addition, it is experimentally verified that the use of spiral circular reinforcement increases the concrete binding force in the anchorage zone, thus resisting the bursting force.

Hydrostatic tests were conducted according to ACI 423.7-14 because there is no test at present that verifies the water tightness of the encapsulation system in Korea.

Though the water pressure was maintained over 8.6 kPa for 24 hours, no water flowed into the anchorage. Instead of carrying out rather existing performance tests which are complicate and time-consuming, a compression test and a jacking test were devised that could be performed easily in the field of construction. The compression test reflects the process of making the fixed end through compression, supporting the bearing plate and pushing the strand. For safety reasons, however, the test was stopped before reaching 400 kN. The misaligned wedges leveled themselves during seating and the final angle between two pieces of the wedge was within 4.1° .

Unlike the compression test, the jacking test is a method of verifying the anchorage performance by tensioning the strands. The jacking force was applied to the maximum capacity of device, and all the specimens withstood the load above the nominal tensile strength. However, the strand in one of the specimens was fractured due to excessively shifted (13 mm) wedges at a tension force of 275.3 kN.

Prior to applying the developed anchor to the actual building, the behavior and construction of the tendon were examined by conducting a mockup test. The specimen was a 6-m square two-way slab and its thickness was 230 mm. In one direction, six sets of two anchors were distributed; three and ten anchors were placed with a banded arrangement in the other direction. The tendon's behavior had no problem, and the wedge slip measured at some fixed ends was 4 to 6 mm. Since plastic breakage occurred during construction, the material of plastic cover and accessories was made softer to improve workability.

To monitor the long-term performance of PT tendon with developed anchors in the actual building, the tendon stress and slab deflection were measured at the East Central Tower in Gangdong-gu, Seoul. More specifically, the stress was measured using a strand with fiber Bragg grating system. A 55-m strand was stressed up to 75% of the nominal tensile strength and then decreased to about 73% after three months. A 33-m strand had an initial stress of only 49% of the nominal tensile strength, but remained at an average 45% after three years.

In the same building, the deflection was measured at total six points (two floors for three different slab spans (corner, edge, interior)) over a period of three years and nine months. The least deflection occurred in the interior slab, whereas the corner slab was deflected up to 44 mm. The PT slab exhibited improved performance in deflection than RC slabs, without showing any defect of the developed anchors.

Long-term deflection of the slab is also related to short-term deflection, and a more accurate prediction of deflection enables to optimize PT design while reducing the cost of construction. The short-term deflection of the corner slab (where the maximum deflection is expected to occur) is predicted using the finite element analysis program by applying the construction load and properties of the member that are known to change (hardening) during the construction process. Overall, the trend of the analyzed deflection is similar to the measurement data. Particularly, the predicted short-term deflection is relatively accurate with an error of less than 2 mm. This concludes that the use of uncracked section is reasonable for PT slab.

The formula for calculating long-term deflection specifically pertains to the RC slab. Based on the measurement results, a new time-dependent coefficient for PT slab is developed. The proposed equation expresses the tendency of long-term deflection of PT slab better than the conventional formula. Actual field application and monitoring of four tendons confirm that the anchor performance was satisfactory.

The anchorage developed in this dissertation is patented and has been applied to four buildings using developed anchors for all tendons, which also confirms the performance and practicality of the developed anchors in this study. It was also used in two previous seismic and ultimate gravity load studies, which re-verified the ultimate behavior of PT elements with developed anchors.

References

AASHTO. (2017a). *AASHTO LRFD Bridge Construction Specifications (LRFDCONS-4)*: American Association of State Highway Transportation Officials.

AASHTO. (2017b). *Bridge Design Specifications (LRFD-8)*: American Association of State Highway and Transportation Officials.

ACI Committee 209. (1992). *Prediction of Creep, Shrinkage, and Temperature Effects in Concrete Structures (ACI 209R)*: American Concrete Institute.

ACI Committee 301. (1989). *Specifications for Structural Concrete for Buildings (ACI 301)*: American Concrete Institute.

ACI Committee 301. (2016). *Specifications for Structural Concrete (ACI 301)*: American Concrete Institute.

ACI Committee 318. (1989). *Building Code Requirements for Structural Concrete (ACI 318) and Commentary (ACI 318R)*: American Concrete Institute.

ACI Committee 318. (2019). *Building Code Requirements for Structural Concrete (ACI 318) and Commentary (ACI 318R)*: American Concrete Institute.

ACI Committee 350. (2001). *Code Requirements for Environmental Engineering Concrete Structures and Commentary (ACI 350)*: American Concrete Institute.

ACI Committee 350. (2006). *Code Requirements for Environmental Engineering Concrete Structures and Commentary (ACI 350)*: American Concrete Institute.

ACI Committee 423. (2001). *Specification for Unbonded Single-Strand Tendons (ACI 423.6) and Commentary (ACI 423.6R)*: American Concrete Institute.

AIK. (2016). *Korean Building Code and Commentary (KBC)*: Architectural Institute of Korea.

Alga. (2001). *Alga Slab - Solutions for Post-Tensioned Slab*: Alga S.p.A. (in Italian)

Allen, A. H. (1981). *An Introduction to Prestressed Concrete*: Cement and Concrete Association.

Amsysco. (2010). *Amsysco Unbonded Post-Tensioning Systems, Service, Engineering*: Amsysco, Inc.

ASTM. (1984). *Standard Specification for Ductile Iron Castings (ASTM A536)*: American Society for Testing and Materials.

ASTM. (2008). *Standard Practice for Evaluating Degree of Rusting on Painted Steel Surfaces (ASTM D610)*: American Society for Testing and Materials.

ASTM. (2018). *Standard Specification for Low-Relaxation, Seven-Wire Steel Strand for Prestressed Concrete (ASTM A416M)*: American Society for Testing and Materials.

Berglund, A. (2011). *Criteria for Machinability Evaluation of Compacted Graphite Iron Materials: Design and Production Planning Perspective on Cylinder Block Manufacturing* (Doctoral Dissertation). KTH Royal Institute of Technology.

Chiang, K.-T., Chang, F.-P., and Tsai, D.-C. (2007). Modeling and Analysis of the Rapidly Resolidified Layer of SG Cast Iron in the EDM Process through the Response Surface Methodology. *Journal of Materials Processing Technology*, 182(1-3), 525-533.

Cho, A. S., Jo, Y. W., Jeon, B. K., and Kang, T. H.-K. (2015). Development and Performance Test for Unbonded Post-Tensioned Anchor. *Journal of the Korea Concrete Institute*, 27(1), 11-20. (in Korean)

Cho, A. S. and Kang, T. H.-K. (2017). Load Transfer Test of Spirally Reinforced Anchorage Zone for Banded Tendon Group. *Journal of the Korean Association for Spatial Structures*, 17(1), 59-67. (in Korean)

Cho, A. S. and Kang, T. H.-K. (2018a). Load-Carrying Performance and Hydrostatic Tests of Encapsulated Anchor Systems for Unbonded Post-Tensioning Single-Strands. *International Journal of Concrete Structures and Materials*, 12(1).

Cho, A. S. and Kang, T. H.-K. (2018b). A Review on Performance Test Methods for Post-Tensioned Anchor. *Proceedings of the Korea Concrete Institute Conference*, 30(1), 7-8. (in Korean)

Choat, R. and Prakash, O. (2017). Application of Post-Tensioning in Multi-Storey Buildings. *International Journal of Engineering Sciences & Research Technology*, 6(3), 242-245.

Chung, K. R. (2003). Unbonded Post-Tensioning Floor System Technology. *Magazine of the Korea Concrete Institute*, 15(2), 90-101. (in Korean)

Cramer, S. D. and Covino, B. S. (2005). *ASM Handbook - Corrosion: Materials* (Vol. 13B): American Society for Metals.

Cross, E. (2007). Post-Tensioning in Building Structures. *Concrete in Australia*, 33(4), 48-54.

Dinges, T. (2009). *The History of Prestressed Concrete: 1888 to 1963* (Master Thesis). Kansas State University.

DSI. (2004). *DYWIDAG Bonded Post-Tensioning Systems Using Strands*: DYWIDAG–Systems International.

DSI. (2009). *DYWIDAG Unbonded Mono-Strand Post-Tensioning Systems*: DYWIDAG–Systems International.

EOTA. (2002). *Guideline for European Technical Approval of Post-Tensioning Kits for Prestressing of Structures (ETAG 013)*: European Organisation for Technical Approvals.

EOTA. (2013). *European Technical Approval ETA-08/0012: Tensacciai Post-Tensioning System*: European Organisation for Technical Approvals.

Freyssinet. (2014). *Integrated Solutions for Building Prestressing by Post-Tensioning*: Soletanche Freyssinet.

Freyssinet, E. and Seailles, J. (1937). US Patent No. 2080074.

Grilec, K., Jakovljević, S., and Prusac, D. (2010). Erosion of Ductile Cast Iron with Quartz Particles. *Tehnički Vjesnik: Znanstveno-Stručni Časopis Tehničkih Fakulteta Sveučilišta U Osijeku*, 17(1), 17-22. (in Croatian)

Hafiz, M. (2001). Mechanical Properties of SG-Iron with Different Matrix Structure. *Journal of Materials Science*, 36(5), 1293-1300.

Hansen, P. F. and Pedersen, E. J. (1977). Maturity Computer for Controlled Curing and Hardening of Concrete. *Nordisk Betong*, 1, 21-25. (in Danish)

Hayes Industries. (2014). *Hydrostatic Test for Encapsulated Systems*: Hayes Industries, Ltd.

Hong, G.-H., Park, H.-G., Eum, T.-S., Mihn, J.-S., and Kim, Y.-N. (2010). Evaluation of Strength and Stiffness Gain of Concrete at Early-Ages. *Journal of the Korea Concrete Institute*, 22(2), 237-245. (in Korean)

ICC-ES. (2011). *Acceptance Criteria for Post-Tensioning Anchorages and Couplers of Prestressed Concrete (ICC-ES AC303)*: ICC Evaluation Service, LLC.

ICC-ES. (2018). *Precision SURE-LOCK® Post-Tension Anchorage and Coupling System and the HSM Post-Tensioning Anchorage System (ESR-2381)*: ICC Evaluation Service, LLC.

ICC-ES. (2019). *GTI Zero Void® Post-Tensioning System (ESR-2515)*: ICC Evaluation Service, LLC.

Jackson, P. H. (1888). US Patent No. 375999.

Joint ACI-ASCE Committee 423. (1996). *Recommendations for Concrete Members Prestressed with Unbonded Tendons (ACI 423.3R)*: American Concrete Institute.

Joint ACI-ASCE Committee 423. (2005). *Recommendations for Concrete Members Prestressed with Unbonded Tendons (ACI 423.3R)*: American Concrete Institute.

Joint ACI-ASCE Committee 423. (2014). *Specification for Unbonded Single-Strand Tendon Materials (ACI 423.7)*: American Concrete Institute.

Joint ACI-ASCE Committee 423. (2017). *Recommendations for Concrete Members Prestressed with Unbonded Tendons (ACI 423.3R)*: American Concrete Institute.

Kang, T. H.-K., Cho, A. S., Jo, Y.-W., and Jeon, B.-K. (2015). Development and Application of Anchor for Unbonded Tendon. *Magazine of the Korea Concrete Institute*, 27(3), 28-31. (in Korean)

Kasvayee, K. A. (2015). *Microstructure and Deformation Behaviour of Ductile Iron under Tensile Loading* (Doctoral Dissertation). Jönköping University.

- KCI. (2010). *Standard Concrete Specification and Commentary*: Korea Concrete Institute. (in Korean)
- KCI. (2013). *Architectural Post-Tensioning System (KCI PM105.1-13)*: Korea Concrete Institute. (in Korean)
- Kelley, G. S. (2001). A Short History of Unbonded Post-Tensioning Specifications. *Concrete Repair Bulletin, July/August 2001*, 10-13.
- Kelley, G. S. (2016). Specifications for Unbonded Post-Tensioning Tendons. *Concrete International*, 38(10), 35-39.
- KFCA. (2017). *Spheroidal Graphite Iron Castings (SPS-KFCA-D4302-5016)*: Korea Foundry Cooperative Association.
- Khosa, N. R. (2010). *Encapsulated Post-Tensioned Concrete for Corrosive and Non-Corrosive Environments*: Amsysco, Inc.
- Kim, K. (2018). *Experimental Study of 2-Span Continuous Beams with 2400 MPa Unbonded Tendons* (Master Thesis). Seoul National University.
- Kim, M. S., Ro, K. M., and Lee, Y. H. (2018). Anchorage Zone Reinforcement for Unbonded Post-Tensioned Circular Anchorage for Single Tendon. *Journal of Korean Association for Spatial Structures*, 18(3), 117-124. (in Korean)
- Kim, M. S., Ro, K. M., and Lee, Y. H. (2019). An Experimental Study on the Performance of One-Way Slab Using Unbonded Post-Tensioned Anchorage for

Single Tendon. *Journal of Korean Association for Spatial Structures*, 19(1), 45-51.
(in Korean)

Krauser, L. B. (2007). ACI and PTI Requirements for Encapsulation Systems. *PTI Journal*, 5(1), 49-54.

KSA. (2018). *Piano Wire Rods (KS D 3509)*: Korean Standards Association. (in Korean)

KSA. (2019). *Uncoated Stress-Relieved Steel Wires and Strands for Prestressed Concrete (KS D 7002)*: Korean Standards Association. (in Korean)

Kwon, B. U. (2016). *Seismic Tests of RC Exterior Beam-Column Joints with High-Strength Materials and Unbonded Tendons* (Master Thesis). Seoul National University.

Lampman, S. R. and DiMateo, N. (1996). *ASM Handbook: Fatigue and Fracture*: ASM International.

Leonhardt, F. (1964). *Prestressed Concrete; Design and Construction* (2 ed.): W. Ernst.

Millis, K. D., Gagnebin, A. P., and Pilling, N. B. (1949). US Patent No. 2485761.

Park, S.-S., Lim, D.-H., and Yang, D.-H. (1995). A Study on the Wedge-Type Anchorage Slip of Prestressed Concrete Structures. *Journal of the Architectural Institute of Korea*, 11(11), 193-201. (in Korean)

Pascual, M., Ferrer, C., and Rayón, E. (2009). Weldability of Spheroidal Graphite Ductile Cast Iron Using Ni / Ni-Fe Electrodes. *Revista de Metalurgia*, 45(5), 334-338.

PHI. (2016). *Concrete Stressing Products (PHI200)*: Precision-Hayes International.

PSI. (2015). *PT Cable Water Testing (Report No. 0204833)*: Professional Service Industries, Inc.

PTI. (1998). *Acceptance Standards for Post-Tensioning Systems (PTI M50.1)*: Post-Tensioning Institute.

PTI. (2000). *What Is Post-Tensioning?*: Post-Tensioning Institute.

PTI. (2006). *Post-Tensioning Manual (TAB.1)* (6 ed.): Post-Tensioning Institute.

PTI. (2010). *Specification for Unbonded Single Strand Tendons (PTI M10.2)*: Post-Tensioning Institute.

PTI. (2017). *Specification for Unbonded Single Strand Tendons (PTI M10.2)*: Post-Tensioning Institute.

QIT-Fer et Titane Inc. (2010). *A Design Engineer's Digest of Ductile Iron* (9 ed.): QIT-Fer et Titane Incorporated.

SAE. (2011). *Surface Texture Control (SAE J449)*: Society of Automotive Engineers International.

Samsung C&T and SNU R&DB Foundation. (2018). KR Patent No. 10-20180027840.

Slamova, K. (2012). Mapping Atmospheric Corrosion in Coastal Regions: Methods and Results. *Journal of Photonics for Energy*, 2(1).

Svensson, I. L. and Salomonsson, K. (2018). Mathematical Characterization of the Tensile Deformation Curve of Cast Iron Materials. *Materials Science Forum*, 925, 444-450.

Unkic, F., Glavas, Z., and Terzic, K. (2008). Utjecaj Broja Nodula na Žilavost Feritnog Nodularnog Lijeva. *Strojarstvo: Časopis za Teoriju i Praksu u Strojarstvu*, 50(4), 231-238. (in Croatian)

VSL. (2015). *VSL Strand Post-Tensioning Systems*: VSL International Ltd.

Walsh, K. Q. and Kurama, Y. C. (2009). *Behavior and Design of Unbonded Post-Tensioning Strand/Anchorage Systems for Seismic Applications (Report #NDSE-09-02)*: University of Notre Dame.

Walsh, K. Q. and Kurama, Y. C. (2010). Behavior of Unbonded Posttensioning Monostrand Anchorage Systems under Monotonic Tensile Loading. *PCI Journal*, 55(1), 97-117.

WJE. (2006). *SURE-LOCK® and SURE-LOCK® II Post-Tension Anchorage and Coupler Testing*: Wiss, Janney, Elstner Associates, Inc.

초 록

건축 포스트텐션(PT) 공법에 직경 15.2mm의 7연선 강연선을 사용하는 추세인 국내 시장과는 달리, 미국이나 유럽에서는 직경 12.7mm인 강연선을 주로 사용하고 있다. 정착장치 역시 12.7mm 강연선용 정착구는 상대적으로 작은 크기를 가지고 있지만, 15.2mm 강연선용 정착구는 크기가 최적화되어 있지 않아서 다소 비효율적이다. 본 논문에서는 이러한 현실을 반영하여 단일 비부착 강연선(직경 15.2mm)용 건축 포스트텐션 1구 정착구를 개발하였고, 각종 시험을 통해 성능을 검증한 후 실제 건축물에 적용한 일련의 과정을 담고 있다.

먼저 유한요소해석을 통해 정착판, 몸통, 거셋의 형태를 변화시켜가며 최대 폰 미세스 응력을 최소화하는 방향으로 형태를 최적화하였다. 또한, 긴장기의 사용이나 액세서리와의 결합, 시공성 등을 고려하여 주물 정착구를 개발하였다. 한편, ACI 423.7-14는 부식에 탁월한 캡슐화된(encapsulated) 정착장치를 사용하도록 규정하고 있다. 본 연구에서도 PT 텐던 및 건축물의 내구성을 증진시키기 위하여 캡슐화된 정착구를 개발하였다.

그 후 국내 시험방법인 KCI-PS101에 따라 정착구 성능시험을 수행하였다. 강연선 공칭인장강도의 95% 이상의 하중에 대한 정착장치 거동을 정하중시험을 통해 검증하였다. 피로시험에서는 정착장치의 장기사용에 대한 성능을 확인하였다. 하중전달시험에서는 정착구역의 보강상세에 따른 파괴강도의 변화를 확인하였다. 수밀시험은 ACI 423.7-

14의 방법에 따라 수행되었으며, 8.6 kPa의 수압을 24시간 동안 유지하였음에도 정착장치 내부로 물이 유입되지 않았다.

다소 복잡하고 많은 시간을 요구하는 성능시험을 대신하여, 현장에서 간단하게 수행할 수 있는 압축시험과 긴장시험을 또한 고안하였다. 압축시험은 압축을 통해 고정단을 만드는 과정을 반영한 것이며, 긴장시험은 강연선을 긴장하여 정착장치 성능을 검증하는 방법이다. 추가적으로, 개발된 정착장치를 실제 현장에 적용하기에 앞서 2방향 슬래브 목업 실험체를 통해 텐던의 거동과 시공성을 검토하였다.

실제 건물에서의 PT 텐던의 거동을 확인하기 위해, 광센서(fiber Bragg grating system)가 적용된 강연선을 이용해 장기응력을 측정하였으며, 슬래브의 단기처짐 및 장기처짐을 3년 9개월에 걸쳐 측정하였다. 시공 과정에서 수시로 변하는 시공하중과 부재의 물성치를 이용하여, 슬래브의 단기처짐을 유한요소해석을 통해 예측하였다. 측정한 처짐 데이터를 기반으로 PT 슬래브에 대한 시간의존계수값을 새로 제안하여 기존식보다 PT 슬래브의 장기처짐의 경향을 보다 잘 예측함을 확인하였다. 이 과정에서 비균열단면의 사용이 적절한 것으로 나타났고, 개발된 정착구 장기성능에 문제가 없음이 밝혀졌다.

본 논문에서 개발된 정착구는 특허를 받았으며, 현재까지 4개의 건물에 적용되었다. 또한 PT 부재의 거동을 확인하는 추가적인 극한실험 연구에도 두 차례 활용되었다.

주요어 : 정착구, 캡슐화, 포스트텐션, 비부착, 개발, 성능, 슬래브, 처짐

학 번 : 2014-21407

Acknowledgement

It is acknowledged that the academic advisor of this doctoral dissertation is Prof. Thomas Kang in the Department of Architecture & Architectural Engineering at Seoul National University.

I am deeply indebted to him for all his guidance and help.

감사의 글

우선 제가 건축구조의 길로 첫 발걸음을 떼는 것부터 시작해 연구자이자 공학자로 성장할 수 있게 지도해주신 강현구 교수님께 진심으로 감사를 드립니다. 교수님의 제자로서, 공학박사로서, 교수로서 앞으로 더욱 성장하고 발전하는 사람이 되겠습니다.

날카로운 통찰력을 보여주시며 항상 사람을 존중해주시는 홍성걸 교수님, 학부 지도교수님이셨고 학문에 대한 열의를 전달해주시는 이철호 교수님, 항상 애정 어린 관심을 주시며 연구를 진두지휘하시는 박홍근 교수님, 아낌없는 격려와 조언을 해주시는 서울시립대 김강수 교수님께 진심으로 감사를 드립니다. 평소 존경하던 훌륭한 교수님들께 학위 심사를 받을 수 있어 영광으로 생각하며, 교수님들의 존함과 명성에 누가 되지 않도록 노력하겠습니다.

또한, 학부 때부터 지도해주신 김광우 명예교수님, 이현수 교수님, 박문서 교수님, 여명석 교수님을 비롯한 서울대학교 건축학과의 모든 교수님들께도 감사드립니다. 또한 굳은 일에도 학생들의 편의를 위해 도와주시는 건축학과 사무실 직원 여러분께도 감사의 말씀을 전합니다.

본 논문의 핵심인 정착구 개발 연구를 시작할 수 있게 해주신 삼성물산(주) 전병갑 부장님 이하 주택ENG팀과 지앤수ENG(주) 최재관 사장님께 진심으로 감사의 말씀을 드립니다. 호서대학교 홍건호 교수님, (주)미래구조엔지니어링 김용남 대표님, (주)토탈피에스 정기남 대표님,

도탈피씨(주) 이승진 대표님과 정영광 부장님, (주)피티솔루션 박광옥 소장님과 허훈 이사님, 한국건설기술연구원 박영환 박사님과 김성태 박사님, 한국건설생활환경시험연구원(KCL) 박진영 선임연구원님, 이종석 선임연구원님과 김호룡 선임연구원님, 원우GTI(주) 원기철 대표님, (주)가엔테크 이창열 대표님 등 본 논문과 관련된 연구에 힘써주신 많은 분들께 감사드립니다. 그 외에도 심정욱 교수님, 김윤곤 교수님, 김진우 박사님, 포스코건설 연구인프라섹션팀 분들께도 감사의 인사를 전합니다.

프리스트레스트 콘크리트의 발전을 위해 힘써 주시는 한국콘크리트학회 PSC위원회 이재훈 교수님, 윤석구 교수님, 심별 위원장님, 김기현 대표님, 전세진 교수님, 김진국 교수님, 양준모 교수님, 이득행 교수님 이하 위원 여러분들께도 감사를 드립니다.

고성능구조공학연구실(Hi-performacne Structural Engineering Lab., HpSE) 2년차 때 보조연구원으로서 시작하여 석박사통합과정까지 총 7년이라는 시간을 보냈는데, 그 동안 함께 생활하며 고생했던 김상희 박사님, 이동주, 이주동 형, Marta Gil Perez, 권병운 형, 이수현, 이민선 누나, 정승용, 이주홍, 신형엽, 홍준기, 김경민, Fahimeh Yavartanoo, Hamidreza Alinejad Lashkariani, Andrew Nghiem, 안성룡, 성한석, 안병욱, 이동혁, 오형석, 김민규, 박수현, 박시영, Gabriela Renee Martinez Lara, Pauline Lin Li Lam에게 감사합니다. (Thank you all whom I met and worked with for seven years at HpSE.) 또한, 짧은 시간이지만 연구실에 함께 있으면서 많은 면에서도 도와주시고 격려해주신 김우석 교수님, 허영애 교수님, 홍성원 교수님, 정동혁 교수님께도 감사의 말씀을 전합니다.

임우영 교수님, 이지형 박사님을 비롯한 구조재료실험실 선후배 여러분, 박창희 박사님, 김성용 교수님을 비롯한 강구조내진설계연구실 선후배 여러분, 황현중 교수님, 김철구 교수님, 백장운 교수님, 학부 07학번 동기이기도 한 이호준 박사를 비롯한 건축구조시스템연구실 선후배 여러분들께 감사를 드립니다.

제가 연구원으로 시작할 때 함께 동기처럼 대해준 13학번 노주옥 누나, 서정일 형, 예쁜 천사가 된 이소영 누나, 박지현, 정수형, 소현준, 이유선, 김나은, 그리고 함께 대학원 생활을 시작한 14학번 정동현 형, 최정택 형, 김현진, 백길옥, 조정은 모두 감사합니다.

특히 이번 학기에 함께 학위심사를 받으면서 큰 힘이 되어준 김민수 박사님, 김대경 박사님께 감사드리며, 졸업을 축하드립니다.

이번에 졸업하는 한선진 박사를 비롯해 꾸준히 교류를 이어오고 있는 서울시립대학교 RC&PSC연구실 여러분, 그리고 류은미 박사를 비롯한 이화여자대학교 건축구조연구실 여러분들께 감사의 인사를 전합니다.

졸업 후에도 서로에게 의지하고 힘이 되어주는 조관우, 임용성, 김승범, 심우현을 비롯한 서울대학교 건축학과 07학번 동기들과 08학번 이종화, 김세훈, 노철오, 조정빈을 비롯한 건축학과 선후배들, 기숙사 생활로 동고동락했고 서로 좋은 일은 축하해주고 위로해주는 민족사관고등학교 9기 자연반 친구들, 그리고 15년도 넘었지만 그 모습 그대로인 신목중학교 친구들까지 모두 감사합니다.

철없던 시절 애정을 가지고 가르쳐주신 하동우 선생님, 항상 따뜻한 사랑으로 대해주신 김형화 선생님, 진심 어린 응원과 격려를 해주시는 기유경 대표님, 지치고 힘들 때면 친동생처럼 챙겨주신 조아라 누나와 이용재 형, 허경범, 이제호, 이향건 형, 김연수 교수님과 Spin 여러분, 김상진 선생님을 비롯한 L&B 스튜디오 김목반 여러분, 변서정 누나, 노진식 선생님, 이민선 선생님, 전재린 선생님, Appel 여러분, 장세진 선생님, 이해인 선생님, 정동욱과 김용구를 비롯한 Noitamina 여러분, Mediance 여러분, 박재훈 선생님 및 제자분들, 이영하 선생님, 이영란 선생님과 조승호 선생님, 김승연 사장님까지 마음 깊이 감사합니다.

마지막으로 세상 누구보다도 사랑하는 가족들이 있었기에 힘들어도 버틸 수 있었고 지금의 제가 있습니다. 가정의 든든한 기둥이신 존경하는 아버지(조대연), 누구보다 먼저 가족들을 위해 희생을 마다하지 않으셨던 어머니(이은실), 책임감 많은 만형이면서도 동생을 배려하고 응원해준 형님(조성인), 우리 형을 사랑해주고 언제나 밝은 에너지를 주시는 형수님(김지윤), 조카 뿌니, 하늘에서 지켜보고 계실 친할머니와 아직 정정하신 외할머니를 비롯한 친가/외가 친척 어르신들과 사촌들, 조카들까지 모두 사랑하고, 감사합니다. 또한 항상 기도해주시고 따뜻한 응원을 보내주시는 형수님의 가족분들께도 감사드립니다.

이렇게 많은 분들의 도움 없이는 여기까지 오지 못했을 것입니다. 여기에 미처 다 적지 못하였지만, 이 외에도 수 많은 분들과의 인연이 지금의 저에게 영향을 미쳤다는 것을 기억하고 있습니다. 항상 감사한

마음을 가지고, 앞으로 저도 누군가에게 도움을 주며 사회에 이바지하는 사람이 되도록 노력하겠습니다.

모든 분들이 하시는 일이 잘 되시고 항상 건강하길 기원하며, 다시 한번 진심으로 감사의 말씀을 전합니다.

감사합니다.

2020년 2월

조아서